

PROCESSING AND NANOSTRUCTURE INFLUENCES ON MECHANICAL
PROPERTIES OF THERMOELECTRIC MATERIALS

By

Robert David Schmidt

A DISSERTATION

Submitted to
Michigan State University
in partial fulfillment of the requirements
for the degree of

Materials Science and Engineering – Doctor of Philosophy

2014

ABSTRACT

PROCESSING AND NANOSTRUCTURE INFLUENCES ON MECHANICAL PROPERTIES OF THERMOELECTRIC MATERIALS

By

Robert David Schmidt

Thermoelectric (TE) materials are materials that can generate an electric current from a thermal gradient, with possible service in recovery of waste heat such as engine exhaust. Significant progress has been made in improving TE conversion efficiency, typically reported according to the figure of merit, ZT , with several recent papers publishing ZT values above 2. Furthermore, cost reductions may be made by the use of lower cost elements such as Mg, Si, Sn, Pb, Se and S in TE materials, while achieving ZT values between 1.3 and 1.8.

To be used in a device, the thermoelectric material must be able to withstand the applied thermal and mechanical forces without failure. However, these materials are brittle, with low fracture toughness typically less than $1.5 \text{ MPa-m}^{1/2}$, and often less than $0.5 \text{ MPa-m}^{1/2}$. For comparison, window glass is approximately $0.75 \text{ MPa-m}^{1/2}$. They have been optimized with nanoprecipitates, nanoparticles, doping, alterations in stoichiometry, powder processing and other techniques, all of which may alter the mechanical properties.

In this study, the effect of SiC nanoparticle additions in Mg_2Si , SnTe and Ag nanoparticle additions in the skutterudite $\text{Ba}_{0.3}\text{Co}_4\text{Sb}_{12}$ on the elastic moduli, hardness and fracture toughness are measured. Large changes ($\sim 20\%$) in the elastic moduli in SnTe_{1+x} as a function of x at 0 and 0.016 are shown. The effect on mechanical properties of doping and precipitates of CdS or ZnS in a PbS or PbSe matrix have been reported.

Changes in sintering behavior of the skutterudite with the Ag nanoparticle additions were explored. Possible liquid phase sintering, with associated benefits in lower processing temperature, faster densification and lower cost, has been shown. A technique has been proposed for determining additional liquid phase sintering aids in other TE materials.

The effects of porosity, grain size, powder processing method, and sintering method were explored with YbAl_3 and $\text{Ba}_{0.3}\text{Co}_4\text{Sb}_{12}$, with the porosity dependence of the elastic moduli reported. Only one other TE material has the porosity dependence of the elastic moduli previously reported in the literature, lead-antimony-silver-tellurium (LAST), and the effect of different powder processing and sintering methods has never been reported previously on TE materials.

ACKNOWLEDGEMENTS

I would like to acknowledge my advisor, Professor Eldon Case, for his patient advising and teaching throughout the work on this dissertation. Particular thanks to Professor Eldon D. Case for directing the projects and keeping everything moving, advising in all the experiments, and extensive assistance in advancing my writing.

Thank you to Professor Timothy Hogan, Professor Donald Morelli and Professor Jeffrey Sakamoto for their work on this dissertation, the use of their labs for portions of the research, and for their work on my dissertation committee.

I would like to acknowledge all my co-authors on the papers in this study, my lab mates, Jennifer Ni, Xiaofeng Fan, Cheng-Yun Liu, undergrad lab assistants Patricia Bordon Sarac, Miguel Valdes Tabernero, Andreia Ditzel Facci, Alex Zettler, Miguel Martinez Calderon, Luis Gonzalez Guerrero, Jesse Giles III, and summer high school honors student Zayra Lobo. Thank you to Karl Dersch for all of the PECS sintering of specimens.

Thank you to the High Temperature Materials Laboratory at Oak Ridge National Laboratory. I would like to acknowledge the director, Edgar Lara-Curzio, for his support on the study of the SnTe thermoelectric materials, and making the resources of the laboratory available for use. I would like to acknowledge my primary contact for the user proposal, Rosa Trejo.

Thank you to Professor Stanley Flegler, Carol Flegler and Abigail Vanderberg at the Center for Advanced Microscopy for their advice, maintenance and work with the scanning electron microscopes used in this dissertation.

I would like to acknowledge the financial support of the Department of Energy, Revolutionary Materials for Solid State Energy Conversion Center, an Energy Frontiers Research Center funded by the U.S. Department of Energy, Office of Science, Office of Basic Energy Sciences under award number DE-SC0001054, for the funding for the research within this dissertation.

TABLE OF CONTENTS

LIST OF TABLES	vii
LIST OF FIGURES	xi
1 Introduction.....	1
1.1 Applications of thermoelectric materials	1
1.2 Thermoelectric efficiency	2
1.3 Mechanical properties of thermoelectric materials	3
1.3.1 Elastic moduli	7
1.3.2 Fracture toughness	8
1.4 Porosity effects on mechanical properties	9
1.5 Temperature effects on mechanical properties	10
1.6 Sintering of thermoelectric materials.....	11
REFERENCES	12
2 Experimental Procedure.....	21
2.1 Material preparation.....	21
2.2 Crushing, grinding, sieving and regrinding (CGSR) process	22
2.3 Milling of CGSR powder.....	23
2.3.1 Planetary ball milling.....	23
2.3.2 Vibratory ball milling	24
2.4 Incorporation of nanoparticles	26
2.5 Sintering of powders	26
2.5.1 Hot press sintering	26
2.5.2 Pulsed electric current sintering.....	27
2.6 Sintered specimen preparation.....	28
2.7 Mounting of specimens.....	28
2.7.1 Thermoplastic mounting of specimens	28
2.7.2 Thermoplastic dismounting of specimens	29
2.7.3 Epoxy mounting of specimens.....	29
2.8 Specimen cutting.....	30
2.9 Specimen polishing.....	30
2.10 Mass, dimensions and density.....	33
2.11 Resonant ultrasound spectroscopy.....	33
2.12 Hardness and fracture toughness by Vickers indentation	39
2.13 X-ray diffraction	42
2.14 Scanning electron microscopy imaging and energy dispersive x-ray spectroscopy	42
2.14.1 Grain size measurement from fractured surface images.....	43
REFERENCES	45

3 Room temperature mechanical properties of polycrystalline YbAl ₃ , a promising low temperature thermoelectric material	48
Abstract	48
3.1 Introduction.....	49
3.2 Experimental procedure	51
3.2.1 Materials and specimen preparation	51
3.2.2 Microstructural characterization	54
3.2.3 Hardness testing	55
3.2.4 Elastic modulus measurements	55
3.2.5 Fracture toughness measurements	56
3.3 Results and Discussion	57
3.3.1 Microstructural characterization	57
3.3.2 Hardness.....	62
3.3.3 Fracture Toughness.....	65
3.3.4 Elastic modulus.....	67
3.3.5. Acoustic wave speeds and the Debye temperature	76
3.3.6 Mechanical properties as a function of processing technique	78
3.4 Summary and Conclusions	79
ACKNOWLEDGEMENTS	80
REFERENCES	81
4 Room-Temperature Mechanical Properties and Slow Crack Growth Behavior of Mg ₂ Si Thermoelectric Materials	86
Abstract	86
4.1 Introduction.....	87
4.2 Experimental procedure	89
4.3 Results and Discussion	93
4.4 Conclusions.....	99
ACKNOWLEDGEMENTS	99
REFERENCES	101
5 Mechanical properties of Mg ₂ Si thermoelectric materials with the addition of 0 to 4 volume percent silicon carbide nanoparticles (SiC _{NP})	105
Abstract	105
5.1 Background	105
5.2 Experimental Procedure.....	110
5.2.1 Materials and Specimen Preparation	110
5.2.2 Elasticity Measurements	111
5.2.3 Hardness and toughness measurements	111
5.2.4 Microscopy	112
5.3 Results and Discussion	112
5.3.1 Microstructural analysis.....	112
5.3.1.1 Starting material density and microstructure	114
5.3.2 Elasticity results.....	117
5.3.2.1 Elasticity and SiC _{NP} addition	117

5.3.2.2 Elasticity and porosity.....	120
5.3.3 Hardness and Toughness Results.....	121
5.3.3.1 Crack bridging and toughness.....	126
5.4 Conclusions.....	126
ACKNOWLEDGEMENTS.....	126
REFERENCES	128
 6 Influence of silver nanoparticle addition, porosity and processing technique on the mechanical properties of $\text{Ba}_{0.3}\text{Co}_4\text{Sb}_{12}$ skutterudites.....	133
Abstract.....	133
6.1 Introduction.....	134
6.2 Experimental procedure	137
6.2.1 Materials and Specimen Preparation	137
6.2.2 Elasticity Measurements	138
6.2.3 Hardness and toughness measurements	140
6.2.4 Energy-dispersive X-ray spectroscopy and microscopy.....	141
6.3 Results and Discussion	149
6.3.1 Microstructural and chemical analysis.....	149
6.3.1.1 Microstructure of the Ag_{NP} and Ag agglomerates	149
6.3.1.2 Porosity and grain size and relationship to the processing technique.....	152
6.3.2 Chemical analysis	153
6.3.2.1 Chemistry of the Ag_{NP} and Ag agglomerates	153
6.3.2.2 Sintering behavior changes and scavenging of Sb.....	156
6.3.2.3 Possible significance to other thermoelectric material systems.....	157
6.3.3 Elasticity results.....	158
6.3.3.1 Elasticity as a function of Ag_{NP} addition	158
6.3.3.2 Elastic moduli and porosity	161
6.3.3.3 Elastic moduli and grain size/processing effects	164
6.3.4 Hardness and fracture toughness results	166
6.3.4.1 Hardness and toughness as a function of Ag addition	166
6.3.4.2 Hardness and fracture toughness as function of porosity	168
6.3.4.2.1 Hardness as function of porosity.....	168
6.3.4.2.2 Fracture toughness as function of porosity	169
6.3.4.3 Hardness and fracture toughness as a function of load.....	170
6.3.4.4 Hardness and fracture toughness results as a function of grain size.....	172
6.3.4.4.1 Hardness results as a function of grain size	172
6.3.4.4.2 Fracture toughness results as a function of grain size.....	173
6.4 Summary and conclusions	175
ACKNOWLEDGEMENTS.....	176
REFERENCES	177
 7 High temperature elastic moduli of thermoelectric $\text{SnTe}_{1+x-y}\text{SiC}$ nanoparticulate composites.....	187
Abstract.....	187
7.1 Introduction.....	188

7.2 Experimental procedure	190
7.2.1 Specimen Preparation	190
7.2.2 Specimen characterization	192
7.2.3 High temperature Resonant Ultrasound Spectroscopy measurements	193
7.3 Results and Discussion	194
7.3.1 Microstructural analysis	194
7.3.2 Elastic modulus as a function of temperature, matrix composition and SiC_{NP} volume fraction	201
7.3.2.1 Bilinear model of elastic modulus versus temperature	205
7.3.2.2 Effects of chemical composition and porosity on elastic moduli of the $\text{SnTe}_{1+\text{X}}$ matrix	210
7.3.2.3 Comparison of the Young's modulus versus elasticity behavior of polycrystalline $\text{SnTe}_{1+\text{X}}$ to the literature	215
7.3.2.4 Effect of volume fraction of SiC_{NP} on the elastic moduli of the $\text{SnTe}_{1+\text{X}}$ - SiC_{NP} composites	217
7.5 Summary and conclusions	220
ACKNOWLEDGEMENTS	221
REFERENCES	222
 8 Mechanical properties of lower-cost, earth-abundant chalcogenide thermoelectric materials, PbSe and PbS, with additions of 0 to 4% CdS or ZnS	228
Abstract	228
8.1 Introduction	229
8.2 Experimental procedure	231
8.2.1 Materials and Specimen Preparation	231
8.2.2 Elasticity Measurements	232
8.2.3 Hardness and toughness measurements	234
8.2.4 Microscopy and X-ray diffraction	234
8.3 Results and Discussion	235
8.3.1 Microstructural analysis	235
8.3.2 Elasticity results	245
8.3.3 Hardness results	248
8.4 Discussion	248
8.4.1 Microstructural analysis	248
8.4.2 Elasticity analysis	250
8.4.3 Hardness analysis	254
8.5 Conclusions	257
ACKNOWLEDGEMENTS	258
REFERENCES	259
 9 Summary and Conclusions	267
9.1 Porosity dependence and processing method independence of elastic moduli	267
9.1.1 Grain size and processing method independence of elastic moduli	268
9.2 Sintering aids and TE materials	268
9.3 Elastic moduli of TE materials with nanoparticle or nanoprecipitate additions ...	269

9.4 Fracture toughness and slow crack growth in Mg ₂ Si and other TE materials	270
REFERENCES	272
10 Future work	274
REFERENCES	276
APPENDICES	278
APPENDIX A. Effect of nanoparticle addition on the elastic modulus of a composite material	279
APPENDIX B. Standard operating procedure for HT-RUS furnace.....	283
APPENDIX C. Machine drawings of the HT-RUS equipment.....	303
REFERENCES	362

LIST OF TABLES

Table 2.1	32
A series of diamond grit pastes were used to polish the specimens. A grit size may be skipped, with additional polishing time on the next smaller diamond grit size to compensate.	
Table 3.1	53
The HP and PECS processing parameters for the YbAl ₃ specimens included in this study.	
Table 3.2	58
Specimen label, densification method (hot pressed, HP, or pulsed electric current sintering, PECS), mass, dimensions and mass density of each of the YbAl ₃ specimens included in this study.	
Table 3.3	58
The number of indentations, indentation load and mean hardness, $\langle H \rangle$, of the YbAl ₃ specimens and porosity, P . In each case, the loading time was 10 s. The porosity reported is the average as measured from the disc and bar specimen geometries.	
Table 3.4	66
For YbAl ₃ specimens included in this study, the fracture toughness, K_C , measured by Vickers indentation, including the applied load, specimen grain size and volume fraction porosity, P . The K_C was obtained from the mean of 10 indentations per specimen.	
Table 3.5	69
The fitting parameters obtained from the least-squares fit of the appropriate elastic modulus to Eqs. (5a) – (5c). The coefficient of determination, R^2 , is given for each of the fitted equations.	
Table 3.6	69
A comparison of this study's experimentally determined values of elastic moduli (E , Young's modulus, G , shear modulus, B , bulk modulus and ν , Poisson's ratio) for YbAl ₃ with calculated and experimental values of other trialuminide materials, R-Al ₃ , from the literature for R = Yb, Sc, Tm, or Zr [Sa 2011, Zhou 2010, Tao 2008, Hyland 1991, Fu 1990, Xu 1990, Jahnatek 2007].	

Table 3.7	75
For the seven YbAl_3 specimens included in this study, N , the number of RUS resonant peaks measured, the RMS error in RUS, the Young's modulus, E , shear modulus, G , Poisson's ratio, ν , longitudinal and shear velocity, V_L and V_S , acoustic Debye temperature, θ_D , and porosity, P , were measured. The RUS analysis on each specimen was performed on the tripod configuration (Fig. 3.1a).	
Table 3.8	77
The fitting parameters obtained from the least-squares fit of the V_L and V_S versus P data to Eqs. (6a) and (6b), respectively, with the coefficient of determination, R^2 .	
Table 4.1	88
The Mg_2Si specimens used in this study for Vicker's hardness, H , fracture toughness, K_{IC} , Young's modulus, E , shear modulus, G , Poisson's ratio, ν , and acoustic debye temperature, θ_D , measurements. The Mg_2Si pieces were reduced using a (1) mechanical mortar and pestle until all powder passed through a 53 μm sieve and then either densified or further reduced using a (2) planetary mill at 150 rpm for 3 hours. For indentation the specimens were polished to 1 μm diamond grit, further details are available elsewhere [Ni 2010]. Due to reactions with water [Aesar], the specimens were cleaned using ethanol instead of water between polishing grit sizes.	
Table 4.2	92
The density, Young's modulus, E , shear modulus, G , Poisson's ratio, ν , and Debye temperature, θ_D , from this study compared with the literature. The moduli were determined using resonant ultrasound spectroscopy, RUS, first principle calculation, FPC, resonance technique, RT, and compression.	
Table 4.3	95
A comparisons of Vickers hardness, H , and fracture toughness, K_{IC} , from this study to the literature. For the PECS processed specimens in this study, the H and K_{IC} was determined using at least 10 indentations per load with one standard deviation reported as error. For cast specimens in literature, Milekhine et al. measured at least 10 indentations per load [Milekhine 2002] and Li et al. measured 5 indentations [Li 1993].	

Table 4.4	98
No significant slow crack growth occurred for the six Vickers indentation cracks listed below for specimen Mg ₂ Si-01, where the radial crack lengths were monitored for up to 3 days (Fig. 4.5). For the radial crack length measurements performed over the entire time range, the measured crack lengths did not depart significantly from the mean length of each crack, as indicated by the coefficient of variation (CV, standard deviation/mean), where CV ranges from about 1.4% to 5%.	
Table 5.1	109
The fracture toughness, K_{IC} , has been improved in brittle materials, including the thermoelectric Bi ₂ Te ₃ , by the addition of SiC nanoparticles.	
Table 5.2	109
Doped Mg ₂ Si-based thermoelectric materials with ZT near 1 have been reported. These reasonable ZT values for a thermoelectric material support the use of Mg ₂ Si as a model system.	
Table 5.3	115
Specimens in this study were either milled by planetary ball mill (PM) or vibratory mill (VM), with up to 4 vol% SiC _{NP} additions, then sintered by pulsed electric current sintering to produce specimens with a density (ρ) of 2.00 g/cm ³ or greater for all specimens except VM-0SiC-2. The average grain size (GS) by the lineal intercept method are a function of the milling method, and not a function of SiC _{NP} additions.	
Table 5.4	119
The Young's modulus, E , shear modulus, G , and density, ρ , for the specimens in this study, as compared to the range of E , G and ρ in a previous study on three Mg ₂ Si specimens produced by the same vendor.	
Table 6.1	139
Specimens of skutterudite Ba _{0.3} Co ₄ Sb ₁₂ used in this study varied based on Ag _{NP} addition, sintering procedure and temperature, resulting porosity, and powder processing. Specimens VM-PECS-673, VM-PECS-723 and VM-PECS-773 were reprocessed from specimens PM-HP-673, PM-HP-773 and PM-HP-873 by grinding and powder processing by vibratory milling, and sintering by PECS.	
Table 6.2	154
Results of EDS scan using Point ID mode on two as-received Ag _{NP} agglomerates.	

Table 6.3	154
Results of EDS scan using Point ID mode on specimen PM-HP-873-Ag. Spacing between spots is approximately 5 to 10 μm (Figure 6.4e). Ag areas examined are 1-3 μm in diameter.	
Table 6.4	154
Results of EDS scan using Point ID mode on specimen PM-HP-773-Ag. Spacing between spots is approximately 4 μm (Figure 6.4c). Ag area examined approximately 1-3 μm in diameter.	
Table 6.5	154
Results of EDS scan using Point ID mode on specimen PM-HP-673-Ag. Spacing between spots is approximately 5 to 10 μm (Figure 6.4a). Ag area examined is approximately 20 μm in diameter.	
Table 6.6	160
The linear decrease in elastic moduli, E , G , and B , according to equation (5b), for this study of $\text{Ba}_{0.3}\text{Co}_4\text{Sb}_{12}$ is consistent with the limited information available in the literature for porosity dependence of elastic moduli for thermoelectric materials [Schmidt 2013a; Ni 2009].	
Table 6.7	165
For CoSb_3 -based thermoelectric materials, a comparison of the K_C results from this study with the literature, including the porosity, P , the grain size, GS , of the specimens and the K_C measurement technique [Ravi 2009; Eilertsen 2013; Rogl 2011].	
Table 7.1	191
For each of the six $\text{SnTe-SiC}_{\text{NP}}$ specimens included in this study, the volume fraction SiC_{NP} addition, specimen mass, dimensions, mass density, porosity, P , and mean grain size. Specimens were prepared from one of two starting ingots, designated A or B in the specimen label.	
Table 7.2	200
For SiC_{NP} clusters identified by electron backscatter images for specimen $\text{SnTe}(x = 0)\text{V}0.04$ (Fig. 6), the SEM magnification, the area of the field of view of the micrograph, along with the number, number density, and size range of the SiC_{NP} clusters	
Table 7.3	203
For the six $\text{SnTe-SiC}_{\text{NP}}$ specimens included in this study, results of a least squares fit to equation (4a) for the Young's modulus, E , versus temperature, T , data and to equation (4b) for the shear modulus, G , versus T , data. The coefficients of determination for the fit of the E versus T and the G versus T data are given by R_E^2 and R_G^2 , respectively	

Table 7.4	206
For two separate temperature ranges, RT – 543 K, and 543 K – 663 K, the E versus T was fit to equation (4a).	
Table 7.5	206
Comparison of Δb , equation (6), for this study and LAST [Ren 2010].	
Table 7.6	211
Fractional changes in Young’s modulus, E , shear modulus, G , and hardness H as a function of changes in composition from n_1 to n_2 [this study, [Kawaharada 2004; Ravinder 2001; Schenk 1998].	
Table 7.7	214
In order to compare the room temperature experimental values of Young’s modulus, E_{exp} , and shear modulus, G_{exp} , for this study’s specimens without SiC _{NP} additions to the single crystal values of E_0 and G_0 values from SnTe from the literature [Beattie 1969; Simmons 1971], equations (7c) and (7d) were used to calculate porosity corrected values for the single crystal data using the modulus-porosity slope data for two thermoelectric materials, namely YbAl ₃ ($b_{PE} = 2.34$, $b_{PG} = 2.38$) and LAST ($b_{PE} = 3.5$, $b_{PG} = 3.5$) [Schmidt 2013; Ni 2009]. This study’s experimental E_{exp} and G_{exp} values for the tellurium rich specimen, SnTe(x=0.016)V0, are in the best agreement with the range of porosity corrected values E_{CORR} and G_{CORR} .	
Table 7.8	216
Comparison of the Young’s modulus, E , versus temperature behavior for a variety of brittle materials, SnTe [this study], PbTe [Houston 1968; Simmons 1971; Ren 2010], and selected skutterudite TE materials [Schmidt 2012; Ravi 2008]. The parameters E_{RT} and b_{RT} were obtained via a least-squares fit of each of the data sets to equation (4a). The coefficient of determination, R^2 , was equal to or greater than 0.98 for each data set, indicating that equation (4a) describes the E versus temperature behavior well.	
Table 8.1	236
Composition, theoretical density, ρ_{theo} , measured density, ρ_{meas} , volume fraction porosity, P , average grain size, $\langle GS \rangle$, typical observed inclusion size range, $Incl$, and mode mixity, M (equation 3) for the PbS- based specimens included in this study.	

Table 8.2	237
Composition, theoretical density, ρ_{theo} , measured density, ρ_{meas} , volume fraction porosity, P , average grain size, $\langle GS \rangle$, typical observed inclusion size range, $Incl$, and mode mixity, M (equation 3) for the PbSe-based specimens included in this study.	
Table 8.3	244
EDS results from four area scans of a polished PbS specimen, indicating a higher concentration of Pb than S.	
Table 8.4	252
The Young's modulus, E , the shear modulus, G , and the Poisson's ratio measured in this study for the polycrystalline undoped PbSe and undoped PbS specimens compared with the aggregate average values of E and G computed from the Hashin and Shtrikman bounds, $\langle H-S \rangle$ [Simmons 1971] for single crystal elasticity from the literature [Dalven 1969, Bhagavantam 1951, Lippmann 1971, Hellwege 1979].	
Table 8.5	255
In general, hardness, H , is grain size dependent, and the single crystal hardness results from Bloem and Kröger [Bloem 1955] are expected to have a lower hardness than the other, polycrystalline specimens in this table. The grain size for the PbS and PbSe was not listed by Darrow [Darrow 1969]. Average grain sizes for all specimens in this study are between 1.8 μm and 18.7 μm , listed in Tables 8.1 and 8.2.	
Table A.1.....	255
For spherical metallic particle additions to brittle matrices [Fujieda 2012; Hasselman 1965], comparison of the measured composite modulus, E_C , with the values predicted by the four models given in this appendix (rule of mixtures, ROM, Reuss constant strain, RCS, Hashin particulate, HP, and Halpin-Tsai, HT [Schmidt 2013b]). E_m is the Young's modulus of the matrix material [Fujieda 2012; Hasselman 1965] and E_r is the Young's modulus of the reinforcing material [Lowrie 1967; Macfarlane 1965; Neighbours 1958; Chang 1966].	

LIST OF FIGURES

Figure 1.1	6
Schematic of a thermoelectric couple, indicating current flow when placed in a temperature gradient.	
Figure 2.1	36
Typical setup of tripod arrangement of RUS transducers, with specimen on top and the transducer tips near the edge of the specimen.	
Figure 2.2	36
RUS spectrum from PbSe specimen. Each sharp peak in intensity represents a mechanical resonance at the driven frequency.	
Figure 2.3	37
RUS analysis software, showing setup of initial conditions for a PbSe specimen.	
Figure 2.4	38
Sample output file from a CylModel RUS analysis, truncated to show only the first 12 resonance peaks. Note that resonance frequency 10, 191.681 kHz, was not included in the analysis to improve the error. The “chisquare increased 2% by...” section includes the highlighted values of A , 0.47, and of D , 0.11, used in the determination of the uncertainties, dc_{11} and dc_{44} .	
Figure 2.5	41
Schematic representation of Vickers indentation, illustrating the indentation impression dimensions, $2a$, and the radial crack length dimensions, $2c$.	
Figure 3.1	58
Photographs of tripod and bipod transducer stages for the RUS measurements of elastic modulus performed in this study.	
Figure 3.2	59
SEM micrographs of fracture surfaces and polished surfaces of YbAl_3 specimens included in this study. The ovals indicate more porous regions neighboring more dense areas that occur in the two HP specimens (Fig. 3.2a and b) as well as the PECS specimen intentionally processed to give high porosity (Fig. 3.2e).	

Figure 3.3	60
The fractured surfaces of specimens YbAl ₃ -B and YbAl ₃ -E exhibited lower porosity regions surrounded by channels of higher porosity in (a) and (b), both with similar porosity but each sintered by a different method. In contrast, specimen YbAl ₃ -D, shown in (c), exhibited a uniform density throughout.	
Figure 3.4	64
The hardness, H , versus volume fraction porosity, P , for the YbAl ₃ specimens included in this study. The solid line represents a least-squares fit to Eq. (4b).	
Figure 3.5	70
For the YbAl ₃ specimens included in this study, the RUS measurement results for (a) the Young's modulus, E , shear modulus, G , bulk modulus, B as a function of P and (b) Poisson's ratio as a function of P . The solid lines in Fig. 3.5a represent least-squares fits to Eqs. (5a), (5b) and (5c) for the Young's modulus, shear modulus and bulk modulus, respectively.	
Figure 3.6	71
The RUS mechanical vibration spectra for the two-transducer stage and tripod specimen stage.	
Figure 3.7	77
From the RUS measurements of the YbAl ₃ specimens included in this study, (a) shear and longitudinal wave speeds as a function of P , where the solid lines in represent least-squares fits to Eq. (6a) and (6b) for the longitudinal and shear velocities, respectively. (b) the effective Debye temperature as a function of P , where the solid line represents a least-squares fit to Eq. (9).	
Figure 4.1	88
The time–temperature and time–pressure profiles used in the PECS processing of each of the Mg ₂ Si specimens included in this study.	
Figure 4.2	91
X-ray diffraction of planetary-milled Mg ₂ Si powder with peaks compared with the literature for MgO [Hazen 1976] and Mg ₂ Si [Owen 1923].	

Figure 4.3	91
Fractured surface of specimens (a) Mg ₂ Si-01 and (b) Mg ₂ Si-05, PECS processed from planetary mill and mechanical mortar and pestle Mg ₂ Si powder, respectively. Cleavage steps show mixed- mode fracture, with both intergranular and transgranular fracture present. Entrapped pores visible at grain boundaries were approximately 1 µm to 3 µm diameter with polygonal shape. The dark areas between grains are porosity within the specimens, typically around 1 µm or less in diameter.	
Figure 4.4	92
Typical Vickers indentation crack systems for specimens Mg ₂ Si-01 and Mg ₂ Si-05, which display indentation impressions, little chipping or spalling, and a fully developed radial crack system.	
Figure 4.5	97
For specimen Mg ₂ Si-01, plots of radial crack length versus time for six Vickers indentation crack systems loaded at 2.94 N. In figures (b) and (e), a radial crack popped in within 1 min to 5 min following the initial indentation event. The average crack length and one standard deviation variation is indicated by solid and dashed lines, respectively, for each indentation crack. The crack length may vary significantly between indentations, resulting in the uncertainties in the reported K_{IC} values in Table 4.3.	
Figure 5.1	113
Planetary milled Mg ₂ Si powder exhibited typical particle sizes of sub-micron to 5 µm in SEM. The powder has a surface area of 4.4 m ² /g measured by BET, or approximately 0.7 µm average particle size.	
Figure 5.2	113
Vibratory milled Mg ₂ Si powder exhibited typical particle sizes of 0.2 µm to 2 µm in SEM.	
Figure 5.3	116
For Mg ₂ Si fracture surfaces, transgranular fracture dominate in all specimens. The PM specimens (a-c) with varying amounts of SiC _{NP} addition did not show any appreciable difference in grain size, although changing to VM processing significantly reduced the grain size (d). Note the difference in scale between the PM images (a-c) and the VM image (d).	

Figure 5.4	118
The Young's modulus (a, b) and shear modulus (c, d) of Mg_2Si varied primarily due to small variations in density. The variation in vol. % SiC_{NP} did not significantly affect the moduli, regardless of if the specimens were planetary milled (a, c) or vibratory milled (b, d).	
Figure 5.5	118
The Young's modulus, E , decreases linearly with porosity for the set of 13 specimens in this study.	
Figure 5.6	122
The hardness, (a) and (b) is not a function of the milling procedure or the vol% SiC_{NP} , but less scatter was observed in the (b) vibratory milled specimens than the (a) planetary ball milled specimens. The fracture toughness exhibited a maximum at 1 vol% SiC_{NP} for the (c) planetary ball milled specimens, but the fracture toughness is not a function of vol% SiC_{NP} for the (d) vibratory milled specimens. Open symbols in (b) and (d) indicate a specimen with lower density of 1.93 g/cm^3 , relative to the 2.00 to 2.06 g/cm^3 for all other specimens in this study.	
Figure 5.7	124
Crack bridging, in PM Mg_2Si was commonly observed in radial cracks for all the Mg_2Si specimens in this study.	
Figure 5.8	125
Crack bridges were commonly observed in VM specimens regardless of SiC_{NP} addition. Crack bridging in radial cracks was not eliminated by reducing grain size through VM processing. Spotting is from oil residue on the surface of the specimen.	
Figure 6.1	139
RUS spectrum from specimen PM-HP-873-Ag, $P = 0.05$ with Ag_{NP} . The elastic moduli of each of the specimens in this study are calculated from the specimen mass, dimensions, shape, and resonant frequencies. Each peak in the spectrum represents a mechanical resonance at that frequency	
Figure 6.2	142
Silver nanoparticles exhibited agglomerates of $10 \mu\text{m}$ or greater (a-c), but consisting of individual grains or particles consistent with the manufacturer claimed average particle size of $20\text{-}40 \text{ nm}$ (d)	

Figure 6.3	143
<p>Polished surfaces of specimen PM-HP-873-Ag, both in secondary electron images (a) and backscatter images (b). Porosity is observed between larger grains (a and b), but also with areas of Ag visible in backscatter as bright areas (b), due to the higher average atomic weight of the silver rich regions. The abundance of Ag and the relative deficiency of Co or Sb in the bright areas of the backscatter image (b) is confirmed by energy-dispersive x-ray spectroscopy maps (c-e)</p>	
Figure 6.4	144
<p>For each of the hot pressed specimens with Ag_{NP} additions, an EDS line scan was performed and point ID locations were chosen. For PM-HP-673-Ag, a cut surface was used (a) because the specimen was not successfully polished. For PM-HP-773-Ag and PM-HP-873-Ag, polished surfaces were examined (c and e). The line scan for PM-HP-673-Ag (b) indicated only silver present except for two regions in the silver where antimony and cobalt were present in concentrations consistent with skutterudite particles. In contrast, the line scan for PM-HP-773-Ag (d) and PM-HP-873-Ag (f) indicated the presence of antimony in the silver-rich locations. No silver was observed in the matrix outside of the silver-rich locations</p>	
Figure 6.5	145
<p>The microstructure of Ba_{0.3}Co₄Sb₁₂, without Ag addition, changed as a function of sintering temperature. For (a) a sintering temperature of 673 K, microstructure and porosity, P, are consistent with a specimen with little to no observed sintering or densification. After sintering at 773 K (b), only minimal densification and neck formation are observed. Hot pressing at 873 K (c) enhanced both grain growth and densification in the specimen without Ag nanoparticles, however, the microstructure still is observed to be very porous, consistent with measurement of P = 0.16</p>	
Figure 6.6	146
<p>The microstructure of Ba_{0.3}Co₄Sb₁₂ with 0.5 wt% Ag_{NP} addition changed as a function of sintering temperature. At 673 K (a), little to no sintering is observed in the microstructure. Hot pressing at 773 K (b) resulted in limited grain growth and densification, with necks observed between the grains but significant porosity observed, consistent with early stage sintering. The porosity for the specimen with Ag nanoparticles sintered at 873 K (c) is the lowest (P = 0.03) of all the specimens in this study</p>	

Figure 6.7	147
Fracture surface images of reprocessed material sintered by PECS exhibit dense regions surrounded by regions of higher porosity. All regions of the specimens exhibit similar grain sizes. The porous areas decrease as the sintering temperature increased from (a) 673 K, to (b) 723 K, to 773 K	
Figure 6.8	148
After reprocessing by SPEX milling and sintering by PECS, the samples exhibit a unimodal, sub-micron grain size distribution.	
Figure 6.9	151
Hand milling of Ag _{NP} agglomerates in ethanol were not observed to reduce the size of the nanoparticle agglomerates. After hand milling, silver nanoparticle agglomerates of 10 μ m or greater were typically observed, similar to the size of agglomerates for the as received Ag _{NP} . Several faces of the agglomerates appear to be deformed after hand milling	
Figure 6.10	159
The (a) Young's modulus, E, (b) shear modulus, G, and (c) bulk modulus, B, are each a function of porosity. In each figure, the solid lines represent a least-squares fit to equation (5b). The Poisson's ratio (d) is observed to be a weak function of porosity. The elastic moduli were not observed to be a function of the addition of 0.5 wt% Ag _{NP} or of reprocessing	
Figure 6.11	163
The elastic moduli for the exact composition of skutterudite in this study are not recorded in literature, however the moduli for specimens of similar composition [Zhang 2010] are consistent with the porosity dependent elastic moduli relationships observed in this study. Filled symbols indicate specimens with 0.5 wt% Ag _{NP} , unfilled for specimens without any Ag _{NP} , and half-filled symbols for reprocessed specimens without any Ag _{NP} . The solid lines represent a least squares fit to equation (5b) of the data in this study	

Figure 6.12	167
<p>The (a) hardness and (b) fracture toughness for the hot pressed specimens with Ag_{NP}, filled symbols, the hot pressed specimens without Ag_{NP}, open symbols, and the reprocessed PECS specimens without Ag_{NP}, half-filled symbols, from Vickers indentation at four loads, 9.8 N, 4.9 N, 2.94 N, and 1.96 N. Full radial cracks were not observed on the specimens at 1.96 N load and therefore no fracture toughness values are available at 1.96 N load. The hot pressed specimens sintered at 673 K were not able to be polished and were not tested. The solid lines in the figure (a) represent hardness for the reprocessed specimens were fit to equation (6) separately from the hot pressed specimens because hardness is a function of grain size. Fracture toughness, figure (b), was not observed to be a function of either porosity or load, as plotted by the average (solid) and standard deviation (dotted) lines, with an average K_C for all 7 specimens of $1.0 \pm 0.2 \text{ MPa-m}^{1/2}$</p>	
Figure 6.13	171
<p>For each of the specimens, a plot of $c^{3/2}$ versus load, F, was used to determine the suitability of the fracture toughness by Vickers indentation. For 5 of 7 specimens, the coefficient of determination, R², for a linear regression to equation (7) through the data points is 0.99 or greater, with an R² of 0.98 for specimen VM-PECS-773, and 0.84 for specimen PM-HP-773. Note specimen PM-HP-773 also has a low fracture toughness measurement at 2.94 N load. All specimens were measured at three loads, except VM-PECS-673 and VM-PECS-773 with a fourth measurement at a Vickers indentation load of 1.96 N</p>	
Figure 7.1	191
<p>Processing parameters (temperature and die pressure) as a function of time for the PECS densification of the SnTe-SiC_{NP} specimens included in this study.</p>	
Figure 7.2	195
<p>For SnTe specimen A-06 (0 vol% SiC_{NP}), (a) fractured specimen surface and (b) polished specimen surface.</p>	
Figure 7.3	195
<p>The as-received SiC_{NP} consisted of particles roughly 50 nm across agglomerated into clusters ranging in size from approximately 100 nm to 20 μm.</p>	

Figure 7.4	195
(a) After grinding in an alumina mortar and pestle for 5 min in ethanol, the SiC _{NP} exhibited agglomerations of particles ranging from sub-micron to ~10 μ m diameter. (b) The agglomerations consisted primarily of nanoparticles with diameter less than 100 nm, but with an occasional micron-scale particle. The size distribution of the agglomerates after manual grinding was similar to that observed prior to manual grinding (Figure 7.3).	
Figure 7.5	197
Fractured specimen surface images for (a) specimen SnTe (x = 0)V0 with no SiC _{NP} added, and for (b) SnTe (x = 0)V0.01, (c) SnTe(x = 0)V0.02, (d) SnTe(x = 0)V0.03, and (e) SnTe(x = 0)V0.04. In (b) – (e), the location of SiC _{NP} clusters is indicated by arrows.	
Figure 7.6	199
Specimen SnTe(x = 0)V0, with no added SiC _{NP} , shows no surface features other than surface debris in both (a) a secondary electron image (SEI) and in (b) a backscattered electron image. Specimen SnTe(x = 0)V0.04 with 0.04 vol fraction SiC _{NP} addition shows a difference between the (c) secondary electron image and (d) the backscattered electron image, with the image in the backscattered electron mode showing dark regions indicating likely SiC _{NP} clusters at or near the specimen surface.	
Figure 7.7	200
A backscattered electron image of a polished surface of specimen SnTe(x = 0)V0.04 indicates darker regions with a lower average atomic weight, likely composed primarily of the SiC _{NP} . Using EDS, silicon was detected at the location of spectrum one, at approximately 13 at%, but not at spectrum two, with <1 at%, confirming that the dark regions contain a high concentration of the SiC _{NP} . The specimen was osmium coated prior to imaging to reduce localized charging.	
Figure 7.8	202
The Young's modulus versus temperature for the six SnTe–SiC _{NP} specimens included in this study. For each specimen, there is no observable hysteresis between the heating and cooling curves indicating the lack of significant microcracking or bloating over the test temperature range (room temperature to 663 K). The error bars are smaller than the plotting symbols for each modulus value in (a–f).	

Figure 7.9	203
Schematic representation of the bilinear Young's modulus, E , versus temperature, T , behavior showing T_{KINK} and the associated slope change in the E versus T curve.	
Figure 7.10	204
The residuals (equation 5) representing the difference between the experimental Young's modulus data and the modulus values predicted from the least-squares fit of the E versus T data to equation (4). The dashed lines at 0.05 GPa are a guide, representing roughly $\pm 0.01 E_{RT}$, where E_{RT} is defined as the room temperature intercept of the modulus–porosity relationship given by equation (4a). A change in the E versus T slope occurs at approximately 543 K (T_{KINK}).	
Figure 7.11	208
Unlike Figure 7.10, the residuals represent the difference between the experimental data and the least-squares fit performed to equation (4) in a piecewise manner, that is least-squares fits were performed separately for the two temperature intervals (i) T_{RT} to T_{KINK} and (ii) T_{KINK} to the maximum test temperature. As in Figure 7.10, the dashed lines at 0.05 GPa represent roughly $\pm 0.01 E_{RT}$, where E_{RT} is defined as the room temperature intercept of the modulus–porosity relationship given by equation (4a). In (a) – (f), the vertical line at 543 K represents T_{KINK} , the temperature at which the change in the E versus T slope occurs.	
Figure 7.12	219
Comparison of the experimental Young's modulus, E , results for the composites $\text{SnTe}_{1+x}-y\text{SiC}$ ($y = 0.0$ to 0.04) with the four composite models given by equations (8) – (12). Also plotted are the values of E corrected to zero porosity using equation (7a).	
Figure 8.1	233
RUS scan of PbSe specimen	
Figure 8.2	238
Fracture surfaces of PbS specimens indicate primarily transgranular fracture in undoped PbS (a) changing to intergranular fracture for the Na-doped PbS specimen (b). With 1% to 4% addition of CdS, the fracture mode changes to primarily transgranular fracture (b, d), and with 1% to 4% addition of ZnS, the fracture mode changes to mixed, with majority transgranular and minority intergranular (c, e). Note the bright areas in images (c) and (e) are the ZnS precipitates.	

Figure 8.3	239
Fracture surfaces of PbSe specimens indicate primarily intergranular fracture for the pure PbSe specimen, the Na-doped PbSe specimen, and the specimens with 1% addition of CdS or ZnS (a-c). With 2% to 4% addition of CdS or ZnS, the fracture mode changes to primarily transgranular fracture (d-f), although significant intergranular fracture was also observed in the specimen with 4% ZnS (f). Note the bright areas in images (d) and (f) are the ZnS precipitates	
Figure 8.4	240
Secondary images of the polished specimens show isolated, micron scale spherical porosity and minor scratches from polishing. In the specimens with 4% CdS or ZnS, precipitates of sub-micron up to approximately 15 μm were observed, particularly in backscatter electron (BSE) mode. The images of polished PbS in both secondary electron (SE) and BSE mode (a and b) only exhibit spherical pores $\sim 1\ \mu\text{m}$, with no evidence of precipitates, consistent with the material having no additions of CdS or ZnS.	
Figure 8.5	242
Observed in backscatter, precipitates of CdS were up to $\sim 4\ \mu\text{m}$, with some micron scale precipitates with geometry of rods or plates and sharp facets consistent with crystallographic alignment.	
Figure 8.6	242
Some ZnS inclusions in PbS resembled stacked plates.	
Figure 8.7	244
XRD pattern of the sintered PbS specimen.	
Figure 8.8	246
The E and G of the undoped PbS and PbSe were higher than the Na-doped PbS and PbSe. The E and G of undoped PbS are likely higher due to reduced porosity (pure PbS $P = 0.008$, all other PbS $P = 0.031$ to 0.050), while the E and G of undoped PbSe are likely higher due to doping effects. Only small changes in E and G were noted in Na-doped PbS and PbSe with addition of up to 4% CdS or ZnS, with. Only small variability in the v noted in PbS with addition of CdS or ZnS. The v of PbSe increased with the addition of CdS or ZnS. Solid line is average and dotted line is standard deviation of the specimens with 1% to 4% CdS or ZnS addition.	

Figure 8.9	247
No measurable change in hardness was noted in PbS with addition of up to 4% CdS or ZnS. Hardness of PbSe increased from 0.5 GPa to 0.8 GPa with the addition of either CdS or ZnS. The scatter in the fracture toughness data of PbS increased with increasing CdS or ZnS content. No change in the fracture toughness of PbSe was noted.	
Figure B.1.	284
The top of the furnace has exposed leads to power the heating elements with up to 120 VAC electricity. Do not operate the furnace with these leads exposed.	
Figure B.2.	285
Note feedthroughs for the thermocouples (left arrow) and heating element power (right arrow). These feedthroughs and the wires from them should not touch the base or the sides of the bell jar when closed.	
Figure B.3.	285
Braided insulation must be in place around the conductors to the heating elements to prevent a short.	
Figure B.4.	286
The o-ring and the base of the bell jar may have some debris, particularly from the furnace refractories. The debris is abrasive, and may inhibit a proper seal between the bottom and side of the bell jar. The debris should be removed and appropriate grease reapplied to the o-ring prior to operation.	
Figure B.5.	287
Controls and power supply for furnace. Note the high voltage power supply is activated with the red button, and indicated with a red light. Power for the transducers is provided by a 110 VAC circuit, turned on with a toggle switch and indicated with a green light.	
Figure B.6.	288
Blue hoses for gas in and gas out (front bottom) and for coolant water in and out (behind valves) should be inspected for damage such as abrasion or holes.	
Figure B.7.	288
The bubbler (arrow), with the hose extending out, should be filled to cover the end of the hose with liquid to prevent air from entering the hose.	
Figure B.8.	289
Debris can be seen on the screen in the feed-through leading to the vacuum pump.	

Figure B.9.	290
The three transducers are mounted to copper blocks on the chiller plates underneath the furnace. The mount swivels to allow the angle of the transducer to be adjusted.	
Figure B.10.	291
Molybdenum sheets to be used as baffles.	
Figure B.11.	291
Molybdenum baffle being inserted around buffer rods.	
Figure B.12.	292
Front SALI board of inner furnace.	
Figure B.13.	292
Front SALI board of inner furnace, inserted into position.	
Figure B.14.	292
Front refractory bricks of outer furnace.	
Figure B.15.	292
Front refractory bricks of outer furnace, inserted into position.	
Figure B.16.	293
Hoist and controls to operate up and down. Note the hoist is mounted to a rail for movement left and right, and that the chain has some slack when the bell jar is in position.	
Figure B.17.	294
Clamps for the bell jar. The same clamps are used to secure the top and base of the bell jar.	
Figure B.18.	294
High vacuum valves below the furnace. The gas in and gas out valves should be closed before pumping down the bell jar chamber.	
Figure B.19.	295
Flow control panel, with flow controls and bypass for the inert gas in and out of the bell jar and the coolant water from the chiller to the base of the transducers.	
Figure B.20.	296
From left, the furnace over temperature limit controller, furnace temperature controller, and the transducer over temperature limit controller.	

Figure B.21.	297
Furnace temperature controller, from left, in run mode, selecting set point 1, and setting set point 1 to 60°C.	
Figure B.22.	297
208 VAC power switch with red indicator light on, and 110 VAC power switch with green indicator on.	
Figure B.23.	298
Ammeter and voltmeter for heaters. Resistance decreases with temperature, and the current should be monitored to not exceed 20 A. Operate heater elements at less than 60 V for new elements, less than 120 V for elements that have aged due to use.	
Figure B.24.	298
Heater ammeter, heater voltmeter, and variac output knob on control box.	
Figure B.25.	299
Bell jar at rest on side table and furnace opened. There should be some slack in the chain, allowing all the weight of the bell jar to rest on the table.	
Figure B.26.	301
RUS transducer mount components.	
Figure B.27.	302
The spiral cut hot zone of the heating elements should be completely contained within the furnace. The power connections to the heating elements should be outside the furnace.	
Figure B.28.	303
Terminal strip on back of furnace for R-type thermocouples, with thermocouple wires extending into the furnace.	
Figure C.1.	303
Gantry and full assembly.	
Figure C.2.	304
Gantry and full assembly BOM.	
Figure C.3.	305
Gantry.	
Figure C.4.	306
Gantry BOM.	

Figure C.5.	307
Full assembly.	
Figure C.6.	308
Full assembly BOM.	
Figure C.7.	309
Bar clamp.	
Figure C.8.	310
Bar clamp.	
Figure C.9.	311
Bell jar base.	
Figure C.10.	312
Bell jar base assembly.	
Figure C.11.	313
Bell jar base assembly BOM.	
Figure C.12.	314
Bell jar base weldment.	
Figure C.13.	315
Bell jar base weldment BOM.	
Figure C.14.	316
Bell jar top.	
Figure C.15.	317
Cold plate mount 1.	
Figure C.16.	318
Cold plate mount 2.	
Figure C.17.	319
Flange tube.	
Figure C.18.	320
Furnace box.	
Figure C.19.	321
Furnace box BOM.	

Figure C.20.	322
Furnace support plate.	
Figure C.21.	323
Heater support 2.	
Figure C.22.	324
Heater support.	
Figure C.23.	325
Inner furnace back SALI board.	
Figure C.24.	326
Inner furnace base SALI board.	
Figure C.25.	327
Inner furnace front SALI board.	
Figure C.26.	328
Inner furnace side SALI board.	
Figure C.27.	329
Inner furnace top SALI board.	
Figure C.28.	330
Inner furnace.	
Figure C.29.	331
Inner furnace BOM.	
Figure C.30.	332
Outer furnace base center.	
Figure C.31.	333
Outer furnace base left.	
Figure C.32.	334
Outer furnace base right.	
Figure C.33.	335
Outer furnace base.	
Figure C.34.	336
Outer furnace base BOM.	

Figure C.35.	337
Outer furnace front 2.	
Figure C.36.	338
Outer furnace front.	
Figure C.37.	339
Outer furnace side 2.	
Figure C.38.	340
Outer furnace side.	
Figure C.39.	341
Outer furnace top center.	
Figure C.40.	342
Outer furnace top left.	
Figure C.41.	343
Outer furnace top right.	
Figure C.42.	344
Outer furnace top.	
Figure C.43.	345
Outer furnace top BOM.	
Figure C.44.	346
Bell jar top.	
Figure C.45.	347
RUS and furnace.	
Figure C.46.	348
RUS clamp.	
Figure C.47.	349
RUS mount assembly.	
Figure C.48.	350
RUS mount assembly BOM.	
Figure C.49.	351
RUS mount.	

Figure C.50.	352
RUS support leg.	
Figure C.51.	353
RUS support plate.	
Figure C.52.	354
RUS support.	
Figure C.53.	355
Splash shield mount.	
Figure C.54.	356
Splash shield.	
Figure C.55.	357
Standoff.	
Figure C.56.	358
Table top.	
Figure C.57.	359
Transducer cold cap.	
Figure C.58.	360
Valve assembly.	
Figure C.59.	361
Valve mount.	

1 Introduction

Bulk thermoelectric (TE) materials have been developed with increasing figure of merit, ZT, with some near or exceeding ZT of 2 [Biswas 2012; Heremans 2008], and with improvements in the ZT made by the incorporation of nanoparticles [Androulakis 2007; Zhao 2012a; Zhou 2008a; Alleno 2009; Ji 2007] or nanostructured bulk materials [Toprak 2004; Mi 2008]. While the mechanical properties of many of the undoped TE materials without nanoparticles or nanostructures have been measured and published, doping [Gelbstein 2008], alloying [Gelbstein 2008; Darrow 1969], and incorporation of nanoparticles [Zhao 2008; Kvetková 2013] or nanoprecipitates [Ni 2010; Ren 2010] have each been shown to change the mechanical properties such as hardness or elastic moduli. In addition, the hardness and elastic moduli of TE materials are a function of porosity [Ni 2009]. Furthermore, porosity may be structured similar to particles and precipitates to engineer the properties of the material, such as has been done to improve fatigue life in thermal barrier coatings [Giolli 2009], to improve the operational life of a TE device.

As the TE materials are optimized to achieve a high figure of merit, the mechanical properties of the materials also need to be tested. Furthermore, the mechanical properties may be optimized without significant change to the ZT such as by additions of silicon carbide nanoparticles, or in some cases, improving the ZT by the addition of nanoparticles [Zhao 2008]. Thus, the mechanical properties of TE materials must be tested and optimized together with the ZT.

1.1 Applications of thermoelectric materials

Thermoelectric materials are capable of being used for either power generation from a temperature gradient or for producing a temperature gradient by applying an

electrical potential. TE materials such those based on Mg_2Si [Gao 2014], SnTe [Vedeneev 1998; Gelbstein 2009; Leontyev 2012; Gojaev 2010], PbS [Zhao 2012b], PbSe [Zhao 2013], and CoSb_3 -based skutterudites [Chubilleau 2012; Salvador 2009; Yang 2007; Nolas 1999] are considered candidate materials for waste heat recovery, such as from automotive exhaust heat. Other TE materials such as YbAl_3 -based compounds are being developed as possible cryogenic Peltier coolers [Lehr 2013a; Lehr 2013b].

TE materials for waste heat recovery applications are subject to stresses from multiple sources when placed in service. For waste heat recovery, the hot side of a TE device would be placed in thermal contact with a source of heat, from sources such as automotive or other engine exhaust, industrial boilers, or metal refineries. The waste heat source is typically not at constant temperature, subjecting the device to stresses caused by thermal gradients, thermal expansion mismatch, thermal transients, in addition to externally applied stresses. In order to understand the mechanical response to these stresses, the mechanical properties of fracture toughness, hardness and elastic moduli must be understood. In addition, the material must be examined for reactions such as decomposition or bloating for the possible operating temperature range.

1.2 Thermoelectric efficiency

Thermoelectric (TE) materials are typically brittle materials, heavily doped semiconductor devices or semimetals, which may be used in either power generation or heating or cooling. Typically, the efficiency of a TE material is characterized by the dimensionless figure of merit, ZT , defined as [Tritt 2011; Bux 2010]

$$ZT = \frac{S^2 \sigma}{\kappa} T \quad (1.1)$$

where S is Seebeck coefficient, σ is the electrical conductivity, T is temperature, and κ is thermal conductivity. In heat recovery, the efficiency of a TE device, η , is defined as [Tritt 2011; Bux 2010]

$$\eta = \frac{T_H - T_C}{T_H} \left(\frac{\sqrt{1 + ZT} - 1}{\sqrt{1 + ZT} + \frac{T_C}{T_H}} \right) \quad (1.2)$$

where T_H is the hot side temperature and T_C is the cold side temperature. The η for the TE material is proportional to the Carnot efficiency, η_C [Tritt 2011].

$$\eta_C = \frac{T_H - T_C}{T_H} \quad (1.3)$$

From equations (1.2) and (1.3), it is seen that in order to achieve the efficiency closest to Carnot in a TE device, the ZT must be maximized.

Improvements in ZT have incorporated one of several processes, including atomic scale doping or substitution [Gelbstein 2008; Zhu 2009; Zhao 2012b], creation of nanostructured bulk materials [Toprak 2004; Mi 2008; Hsu 2004; Zhu 2009], incorporation of nanoparticles [Androulakis 2007; Zhao 2012a; Zhou 2008a; Alleno 2009; Ji 2007], or a combination of atomic, nanostructural, and microstructural length scale modifications [Biswas 2012]. Until the mid-1990's, the practical limit for ZT was 1 [Tritt 2011], although recent advancements have demonstrated bulk TE materials with $ZT > 2$, such as PbTe-based compounds [Biswas 2012] and SnSe [Zhao 2014], along with several other TE materials with $ZT > 1$, such as skutterudites with ZT of 1.7 [Shi 2011], PbSe with ZT of 1.6 [Zhao 2013], and PbS with ZT of 1.3 [Zhao 2012b].

1.3 Mechanical properties of thermoelectric materials

TE materials are typically incorporated into thermoelectric modules, where a series of TE materials in the form of legs (Figure 1.1) are electrically connected in series,

but each leg is thermally in parallel [Bux 2010]. Thus, each leg of a TE module is subject to the same temperature gradient individually, but the failure of a single TE leg will result in the failure of an entire module of 10's or 100's of legs. Therefore, understanding the mechanical stresses that develop due to thermal gradients, thermal transients, and applied external loads, and how the material will respond to the stresses are critically important to a reliable TE device.

The ZT of a TE material is a function of temperature, and therefore different materials achieve maximum efficiency at different temperature ranges. Maximizing efficiency depends on the material choice as well as the operational temperature. An improvement may also be made by segmenting a TE leg, using different TE materials within a leg based on the expected temperature at a section of a leg [Crane 2009]. For example, replacing a part of a Bi_2Te_3 leg with either TAGS $[(\text{AgSbTe}_2)_{1-x}(\text{GeTe})_x]$ or PbTe on the high temperature side of the leg, depending on whether the leg was p-type or n-type doped, was used to fabricate a TE generator with $\eta > 0.1$ for a temperature difference of 500°C [Crane 2009]. A segmented design requires additional modeling to ensure mechanical reliability because of the added complexity of two TE materials in a single leg [Crane 2009].

Numerical simulation of the mechanical response of TE materials requires knowledge of the mechanical properties, such as elastic moduli, hardness or fracture toughness of the material [Kardestuncer 1987]. These mechanical properties are typically not measured for any case of optimized TE materials. The only published elastic moduli for TE materials are typically for undoped or single crystal case, such as elastic moduli in SnTe [Beattie 1969] or PbS [Dalven 1969; Bhagavantam 1951], which may not be

comparable to doped or otherwise optimized TE materials. Thus, to understand the mechanical response and to run simulation results, the mechanical properties, including elastic moduli, hardness, and fracture toughness, must be measured on the optimized TE material.

The calculation of thermal stresses in a temperature transient may be demonstrated with the simplified case of a flat plate. The maximum surface stress on a flat plate, S_{max} , is a function of the temperature-dependent Young's modulus, $E(T)$, Poisson's ratio, $\nu(T)$, thermal expansion, $\alpha(T)$, and a function of the Biot modulus, $f(Bi)$, where [Case 2012]

$$S_{max} = \frac{E(T)}{1 - \nu(T)} \alpha(T) \cdot \Delta T \cdot f(Bi) \quad (1.4)$$

The function $f(Bi)$ increases monotonically with increasing Biot modulus Bi , where $Bi = ah/\kappa$, and a is the characteristic dimension of the specimen, h is the surface heat transfer coefficient and κ is the thermal conductivity of the specimen. In this case, the elastic moduli, $E(T)$ and $\nu(T)$, and thermal expansion, $\alpha(T)$, are required mechanical/thermal properties to determine the stress in the material.

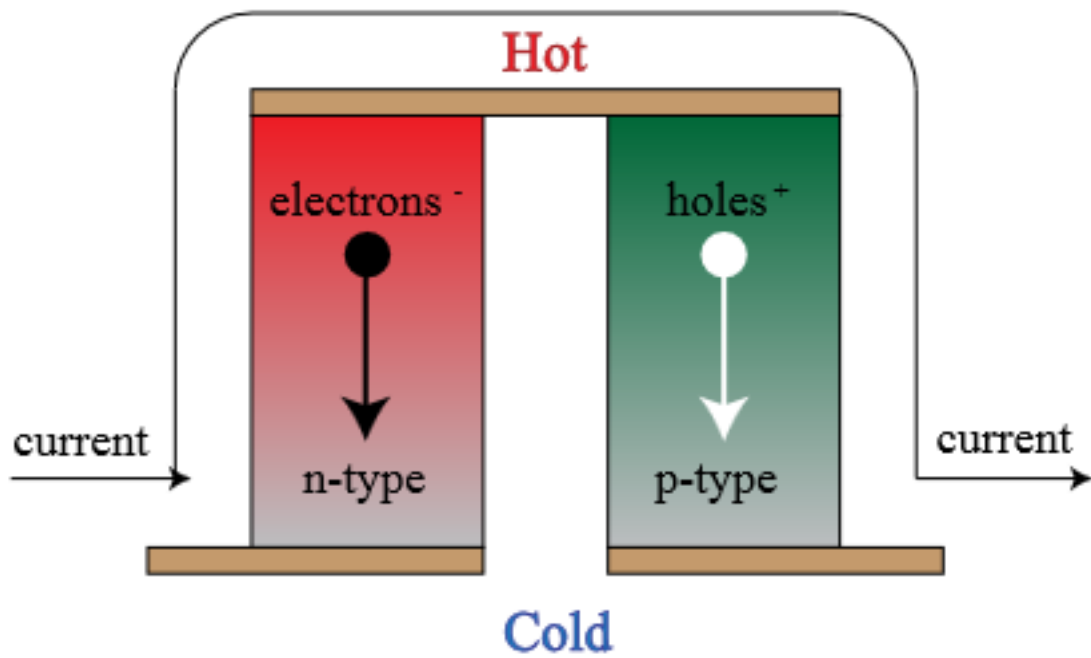


Figure 1.1. Schematic of a thermoelectric couple, indicating current flow when placed in a temperature gradient.

1.3.1 Elastic moduli

The elastic moduli of a specimen are required to determine the elastic response of a material to a given stress. The moduli may change as a material system is optimized as a TE material, such as by the addition of particles or precipitates, or through dopants. Additions of dopants and elements to produce solid-state precipitates have been commonly applied to thermoelectric materials. Lead telluride-based thermoelectrics have achieved record efficiencies in part by using this technique [Zhao 2013]. Also, if microcrack damage is accumulated, through thermal cycling or mechanical loading, the microcrack-induced reduction in E may be used to monitor the extent of the microcrack damage, as has been previously shown for non-TE materials [Fan 2012; Case 1993; Ghassemi Kakroudi 2009].

For the elastic moduli, additions of well-connected, insoluble nanoparticles may be modeled several ways, including rule of mixtures [Hashin 1962], constant strain [Hashin 1962], Hashin particulate composite model [Bedolla 2012; Couturier 1997; Hashin 1962], and Halpin-Tsai composite [Halpin 1992]. Each of these models ignores the possible effects of the size of nanoparticles within a matrix, but only the rule of mixtures model predicts a significant change in elastic modulus for small additions of nanoparticles.

Additions of silver nanoparticles (Ag_{NP}) have improved the ZT of barium-filled skutterudite by 30% [Zhou 2012], which raised interest in examining the mechanical properties of the material. The Young's modulus of silver and CoSb_3 -based skutterudite are not dramatically different ($E = 82$ GPa for Ag [Neighbours 1958; Chang 1966], $E = 109$ GPa to 148 GPa for SKD [Rogl 2011]). Therefore, addition of 0.5 wt% silver to skutterudite should not change the E significantly, if the models for additions insoluble

nanoparticles are accurate [Hashin 1962; Bedolla 2012; Couturier 1997; Halpin 1992]. However, addition of 0.5 wt% silver to skutterudite was accompanied by a modest increase in Seebeck along with the expected change in electrical conductivity [Zhou 2012]. The change in Seebeck could indicate the nanoparticle additions are not be completely insoluble, and therefore there may be a change in the mechanical properties of the TE material as well that the models would not predict.

The addition of silicon carbide nanoparticles (SiC_{NP}) or precipitates to a TE material may improve various material properties, such as acting as a scattering site to reduce the thermal conductivity [Zhou 2008b; Li 2006], or to inhibit bloating and creep behavior [Ni 2013]. The ZT of Bi_2Te_3 was improved from 0.99 to 1.04, while the hardness, fracture toughness and E were each increased by the addition of 0.1 vol% to 1.0 vol% SiC_{NP} [Zhao 2008], demonstrating the possibilities of SiC_{NP} or other particle additions to TE materials.

Dopants, as well as solid solution changes or modifications to stoichiometry, may have a strong influence on the elastic moduli. In a review by Ren et al., ratios between the maximum and minimum moduli, $E_{\text{max}}/E_{\text{min}}$ and $B_{\text{max}}/B_{\text{min}}$, of up to 3 were observed for changes in solid solution [Ren 2007]. If additions such as Ag_{NP} or SiC_{NP} form a solid solution with a TE material, or if the composition of the TE material is otherwise altered, the mechanical properties of the TE material could have significant changes.

1.3.2 Fracture toughness

In order to create a reliable TE device, the TE material must withstand the environmental stresses and the cycling of the intended application without failure. In general, TE materials are brittle, including Zn_4Sb_3 [Ueno 2005], CoSb_3 [Salvador 2009,

Yang 2009a], PbTe [Salvador 2009], and lead antimony silver tellurium compounds (LAST) [Ren 2006]. This generally implies that the mechanical failure mode of TE materials is fracture, similar to ceramics [Kingery 1976]. The conditions under which crack propagation may occur from a flaw of size a [Rice 1998] are

$$\sigma_{fract} = \frac{YK_C}{\sqrt{a}} \quad (6)$$

where σ_{fract} is the fracture stress, K_C is the fracture toughness of a material, and Y is a shape factor based upon the geometry of the flaw. Therefore, K_C is a necessary material property a designer requires to minimize the risk of fracture in a device.

Unfortunately, the K_C of TE materials is typically low, between 0.5 and 1.5 MPa-m^{1/2} or less [Eilertsen 2013; Fan 2012; Ni 2013]. However, fracture toughness may be changed by the addition of particles or second phases. The fracture toughness of Bi₂Te₃ was increased from 1.14 MPa-m^{1/2} to 1.35 MPa-m^{1/2} by the addition of 0.1 vol% SiC_{NP} [Zhao 2008]. Furthermore, additions of nanoparticles may influence fracture mode or sintering behavior [Mukhopadhyay 2010; Ni 2013], and a fracture mode change has been accompanied by either an increase [Mukhopadhyay 2010; Kawabata 1977; Karakasidis 2011] or decrease [Yamada 2010; Jang 2010] in K_C .

1.4 Porosity effects on mechanical properties

The addition of porosity to a specimen may have profound effects. The elastic modulus of several TE materials drops off according to an empirically derived exponential relationship,

$$E = E_0 \exp(-bP) \quad (1.4a)$$

where E is Young's modulus, E_0 is the modulus of theoretically dense specimen, P is volume fraction porosity, and b is a fitting parameter, commonly observed to be between 2 and 6 for a wide range of solid materials [Rice 1998]. This exponential relationship may be extended to include the shear modulus, G , and bulk modulus, B , of TE materials [Ni 2009], as well as hardness, H [Ni 2011; Ren 2008], as the general equation

$$A = A_0 \exp(-bP) \quad (1.4b)$$

where A represents the property E , G , B , or H [Rice 1998]. If the term bP is small, the equation may be linearized by using the first two terms of the Taylor series expansion of the exponential to give

$$A = A_0(1 - bP) \quad (1.4c)$$

For the materials in this study, this linear approximation is appropriate for the data.

The fracture toughness of a brittle material may increase, decrease or remain constant with increasing porosity [Rice 1995]. In particular, an evaluation including Al_2O_3 , B_4C and Si_3N_4 at $P = 0.1$ to $P = 0.15$ indicated K_{IC} values as high or higher than at $P = 0$ [Rice 1995]. The maintenance of K_{IC} values with increasing P may be due to the pore blunting or deflecting the crack tip [Case 2012].

1.5 Temperature effects on mechanical properties

The elastic moduli decreases with increasing temperature. For temperatures greater than 0.3 to 0.5 of the Debye temperature, the temperature-dependent change may be represented by [Schmidt 2012]

$$E(T) = E_{RT} [1 - b_{TE}(T - T_{RT})] \quad (1.5a)$$

$$G(T) = G_{RT} [1 - b_{TG}(T - T_{RT})] \quad (1.5b)$$

where E_{RT} and G_{RT} are the room temperature Young's and shear moduli respectively, and the constants b_{TE} and b_{TG} are experimentally measured fitting factors. A change in the slope, b_{TE} and b_{TG} , indicates a change within the material, such as the onset of grain boundary sliding or an order-disorder transition [Schmidt 2012; Ren 2009; Wachtman 2009]. These changes within a material may be significant, and in some cases may be controlled by particle additions to the material [Schmidt 2012].

1.6 Sintering of thermoelectric materials

Typically, thermoelectric materials are fabricated by sintering of a powder processed ingot, either by hot pressing (HP) or pulsed electric current sintering (PECS) [Ni 2011]. These two methods of sintering both may produce dense specimens, but the microstructure, including pore shape and distribution, grain size and grain growth, may vary considerably [Ni 2011]. The HP method is well established, but the PECS method may permit consolidation in considerably shorter time, reducing cost of sintering and reducing time for grain growth [Savary 2012; Recknagel 2007; Zhao 2012b; Biswas 2012]. Additionally, the use of sintering aids to create a small, $< 1\%$, amount of liquid phase at sintering temperature may permit the use of lower sintering temperature and shorter time to densify a specimen [Barsoum 2003].

For TE materials, the mechanical properties of elastic moduli, hardness and fracture toughness for specimens sintered by each of HP and PECS have not previously been explored. Furthermore, additions of sintering aids have not been explored for Sb-based skutterudite TE materials, nor for most TE materials. The exploring of sintering aids and creating a process for the development of new sintering aids may improve the sintering time and cost [Barsoum 2003].

REFERENCES

REFERENCES

- [Alleno, Chen, Chubilleau, Lenoir, Rouleau, Trichet, Villeroy 2009] Alleno, E., Chen, L., Chubilleau, C., Lenoir, B., Rouleau, O., Trichet, M.F., Villeroy, B. Thermal Conductivity Reduction in CoSb₃–CeO₂ Nanocomposites. *Journal of Electronic Materials* 39 (2009) 1966–1970.
- [Androulakis, Lin, Kong, Uher, Wu, Hogan, Cook, Caillat, Paraskevopoulos, Kanatzidis 2007] Androulakis, J., Lin, C.-H., Kong, H.-J., Uher, C., Wu, C.-I., Hogan, T., Cook, B.A., Caillat, T., Paraskevopoulos, K.M., Kanatzidis, M.G. Spinodal decomposition and nucleation and growth as a means to bulk nanostructured thermoelectrics: enhanced performance in Pb(1-x)Sn(x)Te-PbS. *Journal of the American Chemical Society* 129 (2007) 9780–8.
- [Barsoum 2003] Barsoum, M.W. *Fundamentals of Ceramics*. Taylor & Francis Group, New York, 2003.
- [Beattie 1969] Beattie, A.G. Temperature Dependence of the Elastic Constants of Tin Telluride. *Journal of Applied Physics* 40 (1969) 4818.
- [Bedolla, Lemus-Ruiz, Contreras 2012] Bedolla, E., Lemus-Ruiz, J., Contreras, A. Synthesis and characterization of Mg-AZ91/AlN composites. *Materials and Design* 38 (2012) 91–98.
- [Bhagavantam, Rao 1951] Bhagavantam, S., Rao, T. Elastic constants of galena. *Nature* 168 (1951) 42.
- [Biswas, He, Blum, Wu, Hogan, Seidman, Dravid, Kanatzidis 2012] Biswas, K., He, J., Blum, I.D., Wu, C.-I., Hogan, T.P., Seidman, D.N., Dravid, V.P., Kanatzidis, M.G. High-performance bulk thermoelectrics with all-scale hierarchical architectures. *Nature* 489 (2012) 414–8.
- [Bux, Fleurial, Kaner 2010] Bux, S.K., Fleurial, J.-P., Kaner, R.B. Nanostructured materials for thermoelectric applications. *Chemical communications (Cambridge, England)* 46 (2010) 8311–24.
- [Case 2012] Case, E.D. Thermo-mechanical properties of thermoelectric materials. In: D.M. Rowe, ed., *Thermoelectrics and its Energy Harvesting: Modules, Systems and Applications*. CRC Press, Boca Raton, Florida, 2012, 581.
- [Case, Kim 1993] Case, E.D., Kim, Y. The effect of surface-limited microcracks on the effective Young's modulus of ceramics. *Journal of Materials Science* 28 (1993) 1885–1900.

- [Chang, Himmel 1966] Chang, Y.A., Himmel, L. Temperature Dependence of the Elastic Constants of Cu, Ag, and Au above Room Temperature. *Journal of Applied Physics* 37 (1966) 3567–3572.
- [Chubilleau, Lenoir, Masschelein, Dauscher, Candolfi, Guilmeau, Godart 2012] Chubilleau, C., Lenoir, B., Masschelein, P., Dauscher, a., Candolfi, C., Guilmeau, E., Godart, C. High temperature thermoelectric properties of CoSb₃ skutterudites with PbTe inclusions. *Journal of Materials Science* 48 (2012) 2761–2766.
- [Couturier, Ducret, Merle, Disson, Joubert 1997] Couturier, R., Ducret, D., Merle, P., Disson, J.P., Joubert, P. Elaboration and characterization of a metal matrix composite: Al/AlN. *Journal of the European Ceramic Society* 17 (1997) 1861–1866.
- [Crane, Kossakovski, Bell 2009] Crane, D.T., Kossakovski, D., Bell, L.E. Modeling the Building Blocks of a 10% Efficient Segmented Thermoelectric Power Generator. *Journal of Electronic Materials* 38 (2009) 1382–1386.
- [Dalven 1969] Dalven, R. A review of the semiconductor properties of PbTe, PbSe, PbS and PbO. *Infrared physics* 9 (1969) 141–184.
- [Darrow, White, Roy 1969] Darrow, M., White, W., Roy, R. Micro-indentation hardness variation as a function of composition for polycrystalline solutions in the systems PbS/PbTe, PbSe/PbTe, and PbS/PbSe. *Journal of Materials Science* 4 (1969) 313–319.
- [Eilertsen, Subramanian, Kruzic 2013] Eilertsen, J., Subramanian, M. a., Kruzic, J.J. Fracture toughness of Co₄Sb₁₂ and In_{0.1}Co₄Sb₁₂ thermoelectric skutterudites evaluated by three methods. *Journal of Alloys and Compounds* 552 (2013) 492–498.
- [Fan, Case, Ren, Shu, Baumann 2012] Fan, X., Case, E.D., Ren, F., Shu, Y., Baumann, M.J. Part II: fracture strength and elastic modulus as a function of porosity for hydroxyapatite and other brittle materials. *Journal of the mechanical behavior of biomedical materials* 8 (2012) 99–110.
- [Gao, Berkun, Schmidt, Luzenski, Lu, Bordon Sarac, Case, Hogan 2014] Gao, P., Berkun, I., Schmidt, R.D., Luzenski, M.F., Lu, X., Bordon Sarac, P., Case, E.D., Hogan, T.P. Transport and Mechanical Properties of High-ZT Mg_{2.08}Si_{0.4-x}Sn_{0.6}Sb_x Thermoelectric Materials. *Journal of Electronic Materials* 43 (2014) 1790–1803.
- [Gelbstein 2009] Gelbstein, Y. Thermoelectric power and structural properties in two-phase Sn/SnTe alloys. *Journal of Applied Physics* 105 (2009) 023713.

- [Gelbstein, Gotesman, Lishzinker, Dashevsky, Dariel 2008] Gelbstein, Y., Gotesman, G., Lishzinker, Y., Dashevsky, Z., Dariel, M.P. Mechanical properties of PbTe-based thermoelectric semiconductors. *Scripta Materialia* 58 (2008) 251–254.
- [Ghassemi Kakroudi, Yeugo-Fogaing, Huger, Gault, Chotard 2009] Ghassemi Kakroudi, M., Yeugo-Fogaing, E., Huger, M., Gault, C., Chotard, T. Influence of the thermal history on the mechanical properties of two alumina based castables. *Journal of the European Ceramic Society* 29 (2009) 3197–3204.
- [Giolli, Scrivani, Rizzi, Borgioli, Bolelli, Lusvarghi 2009] Giolli, C., Scrivani, a., Rizzi, G., Borgioli, F., Bolelli, G., Lusvarghi, L. Failure Mechanism for Thermal Fatigue of Thermal Barrier Coating Systems. *Journal of Thermal Spray Technology* 18 (2009) 223–230.
- [Gojaev, Murguzov, Mamedov, Abdurragimov 2010] Gojaev, E.M., Murguzov, M.I., Mamedov, I.M., Abdurragimov, a. a. Synthesis and properties of SnTe-PrTe solid solutions. *Inorganic Materials* 46 (2010) 1061–1064.
- [Halpin 1992] Halpin, J.C. *Primer on composite materials analysis*. Technomic Publishing Company, Inc., Lancaster, Pennsylvania, 1992.
- [Hashin 1962] Hashin, Z. The Elastic Moduli of Heterogeneous Materials. *Journal of Applied Mechanics* 29 (1962) 143–150.
- [Heremans, Jovovic, Toberer, Saramat, Kurosaki, Charoenphakdee, Yamanaka, Snyder 2008] Heremans, J.P., Jovovic, V., Toberer, E.S., Saramat, A., Kurosaki, K., Charoenphakdee, A., Yamanaka, S., Snyder, G.J. Enhancement of thermoelectric efficiency in PbTe by distortion of the electronic density of states. *Science (New York, N.Y.)* 321 (2008) 554–7.
- [Hsu, Loo, Guo, Chen, Dyck, Uher, Hogan, Polychroniadis, Kanatzidis 2004] Hsu, K.F., Loo, S., Guo, F., Chen, W., Dyck, J.S., Uher, C., Hogan, T., Polychroniadis, E.K., Kanatzidis, M.G. Cubic AgPb(m)SbTe(2+m): bulk thermoelectric materials with high figure of merit. *Science (New York, N.Y.)* 303 (2004) 818–21.
- [Jang, Kim, Han, Seo, Hong, Woo, Sakka 2010] Jang, B.-K., Kim, S.-Y., Han, I.-S., Seo, D.-W., Hong, K.-S., Woo, S.-K., Sakka, Y. Influence of uni and bi-modal SiC composition on mechanical properties and microstructure of reaction-bonded SiC ceramics. *Journal of the Ceramic Society of Japan* 118 (2010) 1028–1031.
- [Ji, He, Alboni, Su, Gothard, Zhang, Tritt, Kolis 2007] Ji, X., He, J., Alboni, P., Su, Z., Gothard, N., Zhang, B., Tritt, T.M., Kolis, J.W. Thermal conductivity of CoSb₃ nano-composites grown via a novel solvothermal nano-plating technique. *physica status solidi RRL – Rapid Research Letters* 1 (2007) 229–231.

- [Karakasidis, Charitidis 2011] Karakasidis, T.E., Charitidis, C. a. Influence of nano-inclusions' grain boundaries on crack propagation modes in materials. *Materials Science and Engineering: B* 176 (2011) 490–493.
- [Kardestuncer, Norrie 1987] Finite element handbook. McGraw-Hill, New York, 1987.
- [Kawabata, Izumi 1977] Kawabata, T., Izumi, O. The relationship between fracture toughness and transgranular fracture in an Al-6.0% Zn-2.5% Mg alloy. *Acta Metallurgica* 25 (1977) 505–512.
- [Kingery, Bowen, Uhlman 1976] Kingery, W.D., Bowen, H.K., Uhlman, D.R. *Introduction to Ceramics*. John Wiley & Sons, New York, 1976.
- [Kvetková, Duszová, Kašiarová, Dorčáková, Dusza, Balázs 2013] Kvetková, L., Duszová, A., Kašiarová, M., Dorčáková, F., Dusza, J., Balázs, C. Influence of processing on fracture toughness of Si₃N₄+graphene platelet composites. *Journal of the European Ceramic Society* 33 (2013) 2299–2304.
- [Lehr, Morelli 2013a] Lehr, G.J., Morelli, D.T. Thermoelectric Properties of Yb_{1-x}(Er,Lu)_x Al₃ Solid Solutions. *Journal of Electronic Materials* 42 (2013) 1697–1701.
- [Lehr, Morelli, Jin, Heremans 2013b] Lehr, G.J., Morelli, D.T., Jin, H., Heremans, J.P. Enhanced thermoelectric power factor in Yb_{1-x}Sc_xAl₂ alloys using chemical pressure tuning of the Yb valence. *Journal of Applied Physics* 114 (2013) 223712.
- [Leontyev, Ivanova, Bente, Gremenok 2012] Leontyev, V.G., Ivanova, L.D., Bente, K., Gremenok, V.F. Fabrication of bulk materials from fine particles of PbTe-SnTe solid solutions prepared through thermal decomposition of salts. *Inorganic Materials* 48 (2012) 991–996.
- [Li, Liu 2006] Li, J.-F., Liu, J. Effect of nano-SiC dispersion on thermoelectric properties of Bi₂Te₃ polycrystals. *Physica Status Solidi (a)* 203 (2006) 3768–3773.
- [Mi, Zhao, Zhu, Tu 2008] Mi, J.L., Zhao, X.B., Zhu, T.J., Tu, J.P. Thermoelectric properties of Yb_{0.15}Co₄Sb₁₂ based nanocomposites with CoSb₃ nano-inclusion. *Journal of Physics D: Applied Physics* 41 (2008) 205403.
- [Mukhopadhyay, Chakravarty, Basu 2010] Mukhopadhyay, A., Chakravarty, D., Basu, B. Spark Plasma-Sintered WC-ZrO₂-Co Nanocomposites with High Fracture Toughness and Strength. *Journal of the American Ceramic Society* 1763 (2010) 1754–1763.
- [Neighbours, Alers 1958] Neighbours, J., Alers, G. Elastic constants of silver and gold. *Physical Review* 885 (1958) 707–712.

- [Ni, Case, Khabir, Stewart, Wu, Hogan, Timm, Girard, Kanatzidis 2010] Ni, J.E., Case, E.D., Khabir, K.N., Stewart, R.C., Wu, C.-I., Hogan, T.P., Timm, E.J., Girard, S.N., Kanatzidis, M.G. Room temperature Young's modulus, shear modulus, Poisson's ratio and hardness of PbTe–PbS thermoelectric materials. *Materials Science and Engineering: B* 170 (2010) 58–66.
- [Ni, Case, Schmidt, Wu, Hogan, Trejo, Lara-Curzio, Kanatzidis 2013] Ni, J.E., Case, E.D., Schmidt, R.D., Wu, C.-I., Hogan, T.P., Trejo, R.M., Lara-Curzio, E., Kanatzidis, M.G. Fracture mode, microstructure and temperature-dependent elastic moduli for thermoelectric composites of PbTe–PbS with SiC nanoparticle additions. *Philosophical Magazine* 93 (2013) 4412–4439.
- [Ni, Case, Stewart, Wu, Hogan, Kanatzidis 2011] Ni, J.E., Case, E.D., Stewart, R., Wu, C.-I., Hogan, T.P., Kanatzidis, M.G. Bloating in (Pb_{0.95}Sn_{0.05}Te)_{0.92}(PbS)_{0.08-0.055}PbI₂ Thermoelectric Specimens as a Result of Processing Conditions. *Journal of Electronic Materials* 41 (2011) 1153–1158.
- [Ni, Ren, Case, Timm 2009] Ni, J.E., Ren, F., Case, E.E.D., Timm, E.J.E. Porosity dependence of elastic moduli in LAST (lead–antimony–silver–tellurium) thermoelectric materials. *Materials Chemistry and Physics* 118 (2009) 459–466.
- [Nolas, Morelli, Tritt 1999] Nolas, G.S., Morelli, D.T., Tritt, T.M. SKUTTERUDITES: A Phonon-Glass-Electron Crystal Approach to Advanced Thermoelectric Energy Conversion Applications. *Annual Review of Materials Science* 29 (1999) 89–116.
- [Recknagel, Reinfried, Höhn, Schnelle, Rosner, Grin, Leithe-Jasper 2007] Recknagel, C., Reinfried, N., Höhn, P., Schnelle, W., Rosner, H., Grin, Y., Leithe-Jasper, a. Application of spark plasma sintering to the fabrication of binary and ternary skutterudites. *Science and Technology of Advanced Materials* 8 (2007) 357–363.
- [Ren, Case, Ni, Timm 2009] Ren, F., Case, E.D., Ni, J.E., Timm, E.J. Temperature-dependent elastic moduli of lead telluride-based thermoelectric materials. (2009) 37–41.
- [Ren, Case, Timm, Lara-Curzio, Trejo 2010] Ren, F., Case, E.D., Timm, E.J., Lara-Curzio, E., Trejo, R.M. Anomalous temperature-dependent Young's modulus of a cast LAST (Pb–Sb–Ag–Te) thermoelectric material. *Acta Materialia* 58 (2010) 31–38.
- [Ren, Case, Timm, Schock 2007] Ren, F., Case, E.D., Timm, E.J., Schock, H.J. Young's modulus as a function of composition for an n-type lead–antimony–silver–telluride (LAST) thermoelectric material. *Philosophical Magazine* 87 (2007) 4907–4934.

- [Ren, Case, Timm, Schock 2008] Ren, F., Case, E.D., Timm, E.J., Schock, H.J. Hardness as a function of composition for n-type LAST thermoelectric material. *Journal of Alloys and Compounds* 455 (2008) 340–345.
- [Rice 1995] Rice, R.W. Comment on “Effective elastic moduli of porous ceramic materials.” *Journal of the American Ceramic Society* 78 (1995) 1711.
- [Rice 1998] Rice, R.W. *Porosity of Ceramics*. Marcel Dekker, New York, 1998.
- [Rogl, Rogl 2011] Rogl, G., Rogl, P. Mechanical Properties of Skutterudites. *Science of Advanced Materials* 3 (2011) 517–538.
- [Salvador, Yang, Shi, Wang, Wereszczak, Kong, Uher 2009] Salvador, J.R., Yang, J., Shi, X., Wang, H., Wereszczak, a. a., Kong, H., Uher, C. Transport and mechanical properties of Yb-filled skutterudites. *Philosophical Magazine* 89 (2009) 1517–1534.
- [Savary, Gascoin, Marinel, Heuguet 2012] Savary, E., Gascoin, F., Marinel, S., Heuguet, R. Spark plasma sintering of fine Mg₂Si particles. *Powder Technology* 228 (2012) 295–300.
- [Schmidt, Case, Ni, Sakamoto, Trejo, Lara-Curzio 2012] Schmidt, R.D., Case, E.D., Ni, J.E., Sakamoto, J.S., Trejo, R.M., Lara-Curzio, E. Temperature-dependent Young’s modulus, shear modulus and Poisson’s ratio of p -type Ce_{0.9} Fe_{3.5} Co_{0.5} Sb₁₂ and n -type Co_{0.95} Pd_{0.05} Te_{0.05} Sb₃ skutterudite thermoelectric materials. *Philosophical Magazine* 92 (2012) 727–759.
- [Shi, Yang, Salvador, Chi, Cho, Wang, Bai, Yang, Zhang, Chen 2011] Shi, X., Yang, J., Salvador, J.R., Chi, M., Cho, J.Y., Wang, H., Bai, S., Yang, J., Zhang, W., Chen, L. Multiple-filled skutterudites: high thermoelectric figure of merit through separately optimizing electrical and thermal transports. *Journal of the American Chemical Society* 133 (2011) 7837–46.
- [Toprak, Stiewe, Platzek, Williams, Bertini, Muller, Gatti, Zhang, Rowe, Muhammed 2004] Toprak, M.S., Stiewe, C., Platzek, D., Williams, S., Bertini, L., Muller, E., Gatti, C., Zhang, Y., Rowe, M., Muhammed, M. The Impact of Nanostructuring on the Thermal Conductivity of Thermoelectric CoSb₃. *Advanced Functional Materials* 14 (2004) 1189–1196.
- [Tritt 2011] Tritt, T.M. Thermoelectric Phenomena, Materials, and Applications. *Annual Review of Materials Research* 41 (2011) 433–448.
- [Vedeneev, Krivoruchko, Sabo 1998] Vedeneev, V.P., Krivoruchko, S.P., Sabo, E.P. Tin telluride based thermoelectrical alloys. *Semiconductors* 32 (1998) 241–244.

- [Wachtman, Cannon, Matthewson 2009] Wachtman, J.B., Cannon, W.R., Matthewson, M.J. *Mechanical Properties of Ceramics*. Wiley-Vch, Hoboken, N.J., 2009.
- [Yamada, Sekine, Kumazawa, Tanabe 2010] Yamada, M., Sekine, K., Kumazawa, T., Tanabe, Y. Relationship between the cone crack and fracture mode in ceramics under high-velocity-projectile impact. 96 (2010) 903–908.
- [Yang, Meisner, Pedersen 2007] Yang, J., Meisner, G.P., Pedersen, B.L. Low temperature transport and structural properties of misch-metal-filled skutterudites. (2007) 1–7.
- [Zhao, Hao, Lo, Wu, Zhou, Lee, Li, Biswas, Hogan, Uher, Wolverton, Dravid, Kanatzidis 2013] Zhao, L.-D., Hao, S., Lo, S.-H., Wu, C.-I., Zhou, X., Lee, Y., Li, H., Biswas, K., Hogan, T.P., Uher, C., Wolverton, C., Dravid, V.P., Kanatzidis, M.G. High thermoelectric performance via hierarchical compositionally alloyed nanostructures. *Journal of the American Chemical Society* 135 (2013) 7364–70.
- [Zhao, He, Hao, Wu, Hogan, Wolverton, Dravid, Kanatzidis 2012a] Zhao, L.-D., He, J., Hao, S., Wu, C.-I., Hogan, T.P., Wolverton, C., Dravid, V.P., Kanatzidis, M.G. Raising the thermoelectric performance of p-type PbS with endotaxial nanostructuring and valence-band offset engineering using CdS and ZnS. *Journal of the American Chemical Society* 134 (2012) 16327–36.
- [Zhao, He, Wu, Hogan, Zhou, Uher, Dravid, Kanatzidis 2012b] Zhao, L.-D., He, J., Wu, C.-I., Hogan, T.P., Zhou, X., Uher, C., Dravid, V.P., Kanatzidis, M.G. Thermoelectrics with earth abundant elements: high performance p-type PbS nanostructured with SrS and CaS. *Journal of the American Chemical Society* 134 (2012) 7902–12.
- [Zhao, Lo, Zhang, Sun, Tan, Uher, Wolverton, Dravid, Kanatzidis 2014] Zhao, L.-D., Lo, S.-H., Zhang, Y., Sun, H., Tan, G., Uher, C., Wolverton, C., Dravid, V.P., Kanatzidis, M.G. Ultralow thermal conductivity and high thermoelectric figure of merit in SnSe crystals. *Nature* 508 (2014) 373–7.
- [Zhao, Zhang, Li, Zhou, Liu, Liu 2008] Zhao, L.-D., Zhang, B.-P., Li, J.-F., Zhou, M., Liu, W.-S., Liu, J. Thermoelectric and mechanical properties of nano-SiC-dispersed Bi₂Te₃ fabricated by mechanical alloying and spark plasma sintering. *Journal of Alloys and Compounds* 455 (2008) 259–264.
- [Zhou, Li, Kita 2008a] Zhou, M., Li, J.-F., Kita, T. Nanostructured AgPb(m)SbTe(m+2) system bulk materials with enhanced thermoelectric performance. *Journal of the American Chemical Society* 130 (2008) 4527–32.

- [Zhou, Li, Kita 2008b] Zhou, M., Li, J.-F., Kita, T. Nanostructured AgPb(m)SbTe(m+2) system bulk materials with enhanced thermoelectric performance. *Journal of the American Chemical Society* 130 (2008) 4527–32.
- [Zhou, Wang, Zhang, Chi, Su, Sakamoto, Uher 2012] Zhou, X., Wang, G., Zhang, L., Chi, H., Su, X., Sakamoto, J., Uher, C. Enhanced thermoelectric properties of Ba-filled skutterudites by grain size reduction and Ag nanoparticle inclusion. *Journal of Materials Chemistry* 22 (2012) 2958.
- [Zhu, Lee, Lan, Wang, Joshi, Wang, Yang, Vashaee, Guilbert, Pillitteri, Dresselhaus, Chen, Ren 2009] Zhu, G., Lee, H., Lan, Y., Wang, X., Joshi, G., Wang, D., Yang, J., Vashaee, D., Guilbert, H., Pillitteri, a., Dresselhaus, M., Chen, G., Ren, Z. Increased Phonon Scattering by Nanograins and Point Defects in Nanostructured Silicon with a Low Concentration of Germanium. *Physical Review Letters* 102 (2009) 196803.

2 Experimental Procedure

2.1 Material preparation

For the YbAl_3 (chapter 3), Mg_2Si (chapters 4 and 5), $\text{Ba}_{0.3}\text{Co}_4\text{Sb}_{12}$ (chapter 6), SnTe (chapter 7), and PbS and PbSe -based thermoelectric materials (chapter 8) in this dissertation, ingots or lump material were prepared from high purity elemental powders at Michigan State University, Northwestern University, University of Michigan, or by Alfa Aesar.

YbAl_3 ingots (chapter 3) were arc melted at Michigan State University in an Al flux under argon, with each ingot melted at least 5 times to ensure homogeneity. The excess Al was removed by crushing the ingot and etching the Al with a 5 M solution of NaOH for 24 h. The etched powder was passed through a 100-mesh (149 μm) sieve before powder processing or sintering.

The Mg_2Si lump material (chapters 4 and 5) was commercially prepared (45518, Alfa Aesar, Ward Hill, MA) from high purity elements (99.99% metals basis). The lump material was crushed, ground, sieved and reground (CGSR), as described in section 2.2.

Barium-doped skutterudite ingots, $\text{Ba}_{0.3}\text{Co}_4\text{Sb}_{12}$ (chapter 6), were fabricated from elemental Ba (pieces, 99.9% pure), Co (powder 99.5% pure), and Sb (shot 99.999% pure), by sealing the elements in evacuated carbon coated quartz ampoules, heated to 1373 K for 5 h, quenched, then annealing at 1023 K for 7 days. The skutterudite ingot produced was processed by CGSR, as described in section 2.2.

SnTe (chapter 7) ingots were prepared by combining high purity elemental powders of Sn (Plamaterials purity 99.999 %) and Te (5 N Plus Inc., purity 99.999 %) in a quartz ampoule and sealed under vacuum. The sealed tubes were heated to either 1273

K for 10 h or 1148 K for 12 h, then quenched. The ingot material produced was processed by CGSR, as described in section 2.2.

Na-doped PbS and PbSe ingots (chapter 8) with x% CdS/ZnS, where the at fraction $x = 1, 2, 3$ and 4, were produced by sealing high purity elements in evacuated carbon coated quartz ampoules and heating to 1473 K for 4 h, then quenched. The resulting ingots were crushed, and the crushed powder was passed through a 53 μm sieve before sintering.

2.2 Crushing, grinding, sieving and regrinding (CGSR) process

The Mg_2Si lump, $\text{Ba}_{0.3}\text{Co}_4\text{Sb}_{12}$ sintered billets for reprocessing and SnTe ingot (chapters 4 – 7) were crushed, ground, sieved and reground (CGSR), using a process originally developed for another TE material, LAST (lead-antimony-silver-tellurium) [Pilchak 2007], and previously used for $\text{Pb}_{0.95}\text{Sn}_{0.05}\text{Te-PbS}$ 8% [Ni 2010] and other Sb-based skutterudites [Schmidt 2011]. All CGSR processing was performed in a glove box under argon (Omni-Lab double glove box) equipped with an oxygen sensor and a moisture sensor (Vacuum Atmospheres Company, Hawthorne, CA).

The lump or ingot material was ground for 5 minutes in a WC-lined mechanical mortar and pestle machine (Retsch RM200, Retsch GmbH, Haan, Germany). The powder was transferred to a sieve, 53 μm ASTM E 11 sieve (60.150.000053, Retsch GmbH, Haan, Germany) for the Mg_2Si and SnTe, or 75 μm sieve (60.150.000075, Retsch GmbH) for the $\text{Ba}_{0.3}\text{Co}_4\text{Sb}_{12}$, with a bottom collector pan (697203050, Retsch GmbH). The top of the sieve was covered with a sheet of aluminum foil to limit possible contamination, and then the ground powder was passed through the sieve on a shaker table (AS 200, Retsch GmbH) for 5 to 15 minutes. The sieved powder was collected and

stored in glass scintillation vials (RPI 121000, Research Products International Corp., Mt. Prospect, IL), and the powder that did not pass was returned to the mortar for regrinding. Up to 5 grindings were performed per batch of powder to pass the ground lump or ingot through the sieve.

Sieves were cleaned between uses with different material systems or when the amount of ground powder noticeably decreased to indicate clogging. The sieve was placed in an ultrasonic cleaner (VWR, 98000-336) with RO water and detergent. A drop of ethanol was used to break the water surface tension and remove any large bubbles trapped under the mesh before cleaning. The ultrasonic cleaner was run for 5 minutes, the screen was rinsed with ethanol and RO water, then dried in a 353 K oven for 20 to 30 minutes.

2.3 Milling of CGSR powder

The CGSR powder was milled by one of two methods, planetary ball milling or vibratory milling.

2.3.1 Planetary ball milling

Planetary ball milling (PM) was performed on Mg_2Si CGSR powder and SnTe CGSR powder in the same glove box under argon (Omni-Lab double glove box) as the CGSR processing of powder was performed, allowing the material to remain in the same argon atmosphere for the entire powder processing process.

The CGSR powder was milled in 10–30 g batches with 100 g of 10-mm diameter spherical alumina media at 150 rpm for 3 h (planetary mill PM100 and 250 mL alumina jar 01.462.0221, Retsch GmbH, Haan, Germany). The powder was collected from the mill by transferring the contents of the mill jar to a coarse sieve (60.150.000, Retsch

GmbH) stacked on a bottom collector pan (697203050, Retsch GmbH). The jar was scraped down with a metal spatula (82027-532, VWR, Radnor, PA) to collect material caked to the walls of the jar. The top of the sieve was covered with a sheet of aluminum foil, then the loose powder on the media was removed on a shaker table for 5 to 15 minutes. The milled powder was collected and stored in glass scintillation vials.

Cleaning of the PM jar and media was performed when changing the TE material milled, or when the jar was removed from the glove box. If the jar was used for Mg_2Si , the jar and media were first soaked overnight in reverse osmosis (RO) water, then rinsed with diluted HCl and RO water to reduce the possibility of a significant reaction between the TE material and the cleaning chemicals. The PM jar and media were cleaned using aqua regia (3-4 parts HCl: 1 part HNO_3) in a fume hood while wearing appropriate personal protective equipment. The media and jar were soaked in aqua regia until no remaining TE material was visible, and for at least 20 minutes. Stirring and applying of aqua regia was performed with disposable plastic pipets (14670-147, VWR). The used aqua regia was disposed of in a vented container. The media and jar were thoroughly rinsed with RO water, filling the jar multiple times with RO water, before air drying.

2.3.2 Vibratory ball milling

Vibratory ball milling (VM) was performed on Mg_2Si CGSR powder (chapter 5), $\text{Ba}_{0.3}\text{Co}_4\text{Sb}_{12}$ CGSR powder (chapter 6), and YbAl_3 sieved powder (chapter 3). For the Mg_2Si CGSR powder and $\text{Ba}_{0.3}\text{Co}_4\text{Sb}_{12}$ CGSR powder, each batch of powder (5 g for Mg_2Si , 7.1 g for $\text{Ba}_{0.3}\text{Co}_4\text{Sb}_{12}$) was milled in a WC mill jar with two 11.2 mm WC spheres and four 7.9 mm WC spheres, sealed with Viton gaskets (WC mill jar set 8004, WC media 5004A, Viton gasket 39322, SPEX Sample Prep, Metuchen, NJ). The mill jar

was filled and sealed in an argon glove box, then the cap was wrapped with electrical tape (Super 88, 3m, St. Paul, MN), and a layer of Parafilm “M” wrapped around the entire jar (PM-996 Pechiney Plastic Packaging, Menasha WI) to prevent air from entering the jar. The powder, sealed in the mill jar with the media, was removed from the glove box, then milled for 10 minutes in a vibratory mill (8000M SPEX SamplePrep). The sealed mill jar was returned to the glove box after milling and opened to collect the powder. The oxygen concentration in the glove box did not change when the mill jar was opened, with a meter sensitivity of ± 0.1 ppm, indicating the mill jar remained sealed during milling. The milled powder was collected and stored in glass scintillation vials.

For the YbAl_3 sieved powder, the powder was VM in a stainless steel jar with stainless steel media. The powder was loaded into the jar in air, thus no electrical tape or parafilm was necessary to seal the jar.

Cleaning of the VM jar and media was performed when changing the TE material milled, or when the jar was opened while removed from the glove box. For cleaning, the jar and media were filled to approximately 1 cm depth with play sand and milled for 10 minutes. The milled sand was removed, the jar disassembled and rinsed with RO water and ethanol, and the Viton gaskets wiped down with a Kim-wipe (Kimberly Clark 34155, Neenah, Wisconsin) and ethanol. The jar and gaskets were reassembled, the jar filled with approximately 1 cm of play sand, then with ethanol to the top of the sand and milled for a second 10 minutes. The jar was cleaned out, rinsed and gaskets wiped down again before reassembly. The jar was filled with approximately 1 cm of ethanol and milled for a third 10 minutes. The jar was cleaned out, rinsed and gaskets wiped down a third time before final reassembly. A separate set of Viton gaskets were used for each material

system milled in the jar. The Viton gaskets were changed during final reassembly if necessary.

2.4 Incorporation of nanoparticles

Silicon carbide nanoparticles (SiC_{NP}) from one of two vendors, with vendor-specified average particle size between 45 nm and 55 nm (44646, Lot number E15T018, Alfa Aesar) or 50 nm to 60 nm (4621HW, Lot #4621-110209, Nanostructured & Amorphous Materials Inc., Houston, TX) were incorporated into PM powder of SnTe (chapter 7) and Mg_2Si (chapter 4) by PM at 120 RPM for 3 h, and into CGSR powder of Mg_2Si by VM for 10 min. Other than the addition of SiC_{NP} , and the change in PM speed and time, all PM and VM processing was identical to the processing

Silver nanoparticles (Ag_{NP}) with a vendor specified purity of 99.9% and a vendor-specified size range of from 20 nm to 40 nm (45509, Alfa Aesar, Ward Hill MA), were dispersed into the $\text{Ba}_{0.3}\text{Co}_4\text{Sb}_{12}$ powder by PM at 300 rpm for 15 min (chapter 6).

2.5 Sintering of powders

Sintering of powders to make bulk specimens was performed by either hot press (HP) or by pulsed electric current sintering (PECS).

2.5.1 Hot press sintering

Hot press (HP) sintering was employed for the sieved YbAl_3 (chapter 3) and PM $\text{Ba}_{0.3}\text{Co}_4\text{Sb}_{12}$ powder (chapter 6).

HP Sintering of the $\text{Ba}_{0.3}\text{Co}_4\text{Sb}_{12}$ powder (chapter 6) was performed in an argon glove box with a graphite die and a custom-built hot press. The graphite die was lined with grafoil (Graftech International, Lakewood, OH) to prevent the powders from sticking to the die. The temperature was monitored by K-type thermocouple and adjusted

manually by varying power supplied to a resistance coil heating element in a spiral surrounding the die. A manual hydraulic press was maintained at the desired pressure during the HP cycle.

HP specimens of YbAl_3 (chapter 3) were pressed by Edward J. Timm in a 22 mm diameter graphite die at 973 K for 1 hour under at 70 MPa (Hot press model HP200-14020-23G by Thermal Technologies LLC, Santa Rosa, CA).

2.5.2 Pulsed electric current sintering

Pulsed electric current sintering (PECS) was employed for the VM YbAl_3 powder (chapter 3), CGSR, PM and VM Mg_2Si powders (chapters 4 and 5), VM $\text{Ba}_{0.3}\text{Co}_4\text{Sb}_{12}$ powder (chapter 6), PM SnTe powder (chapter 7), and the CGSR PbS and PbSe powders (chapter 8).

Specimens were densified by pulsed electric current sintering (SPS Model 10-3, Thermal Technology LLC, Santa Rosa, CA) in a 12.7 mm or 20 mm diameter graphite die lined with grafoil. Powder was added to the die in an argon glove box and manually tamped down with the punch of the die. The loaded die was transferred to the PECS machine, and then the PECS chamber was evacuated with a roughing pump. The PECS chamber was backfilled with argon, then the sintering cycle was run from automated control software for the desired temperature and pressure ramp rate and hold time as specified for the individual specimens (see chapters 3-8). After cooling, the die was removed from the PECS chamber and the specimen removed. Overhanging grafoil may be cut with a razor blade to aid in removal of the specimen from the die.

2.6 Sintered specimen preparation

After sintering, the specimens remained covered with a grafoil layer requiring removal. The bulk of the grafoil was removed with a #10 or #11 scalpel (372610 or 372611, Aspen Surgical Products, Caledonia, MI) by hand. The remaining grafoil on a rough sintered specimen surface was primarily removed by hand sanding until most of the rough surface was no longer visible using 600 to 1200 grit sand paper with adhesive back, adhered to an aluminum plate. For the Mg_2Si specimens, the sand paper was wetted with ethanol due to an incompatibility between the Mg_2Si and water. For all other specimens, the sand paper was wetted with RO water.

Final cleaning of grafoil was performed with a Pyrex 50 mL beaker filled with 20 to 30 mL of ethanol (Mg_2Si specimens) or a solution of 1% liquid detergent (Liquinox detergent, Alconox, White Plains, NY) in RO water. The beaker was placed in an ultrasonic cleaner (Ultramet III, Buehler, Evanston, IL) until the grafoil was removed, 5 to 30 minutes.

2.7 Mounting of specimens

Specimens were mounted for cutting or polishing by thermoplastic or by epoxy.

2.7.1 Thermoplastic mounting of specimens

Specimens were mounted with thermoplastic (CrystalBond 509, EMS, Hatfield, PA) to a glass slide for cutting or to aluminum stubs for polishing. The glass slide or stub, pieces of thermoplastic and specimen were heated simultaneously, starting with a room-temperature hot plate, to the softening point of the thermoplastic over 5 to 30 minutes. The slow heating rate was used to avoid introducing a thermal shock to the specimen. The specimen was placed into the softened thermoplastic such that the desired

side was flat against the slide or stub with only a thin layer of thermoplastic between, and the thermoplastic extended at least half the distance up the sides of the specimen.

Additional small pieces of thermoplastic may be added if necessary to reach the required distance for specimen support. The heat was removed and the mounted specimen air cooled to room temperature.

2.7.2 Thermoplastic dismounting of specimens

Dismounting of thermoplastic mounted specimens was performed by slowly reheating the mounted specimen on a hot plate, then removing the softened thermoplastic from the specimen with a metal spatula. The roughly cleaned specimen was slowly cooled to room temperature.

Final cleaning of the specimen was done with acetone in a fume hood. A KimWipe with acetone was used to remove the bulk of the thermoplastic film by hand. The specimen was then soaked in approximately 10 to 20 mL of acetone in a 50 mL Pyrex beaker for approximately 5 minutes. The specimen was removed from the soak, rinsed with a spray of acetone while held in a clean KimWipe, then soaked in a second 50 mL Pyrex beaker of approximately 10 to 20 mL clean acetone for another 5 minutes. The specimen was removed from the second soak, rinsed with a spray of acetone while held in a clean KimWipe, then air dried on a clean and dry KimWipe. If any film of thermoplastic was observed, the final cleaning was repeated.

2.7.3 Epoxy mounting of specimens

Small or irregular pieces of specimens for polishing and indentation were mounted in epoxy. Ring forms (Black Bakelite Ring Forms #811-221, Leco, St Joseph, MI) were placed on an aluminum plate that had been sprayed with mold release (3470

Reliable Release, Crown, Woodstock, IL). Specimens for mounting were placed in each ring form. The manufacturer specified ratio of epoxy resin and hardener (Epoxicure Resin and Epoxicure Hardener, Buehler, Evanston, IL) were measured by weight on an electronic balance (Adventurer AR2140, Ohaus Corp, Pine Brook, NJ) in a disposable medicine cup to produce 20-30 mL of epoxy. The resin and hardener were mixed by hand with a wooden stir stick until swirls of separate resin or hardener were no longer visible. The ring forms were filled to approximately 2/3 full with the mixed epoxy, and any bubbles that formed around the specimen were dislodged with the stir stick to dissipate at the surface. A steel weight was sprayed with mold release and placed on top of the ring forms to limit epoxy seepage out from the bottom of the ring forms. The epoxy was cured for at least 1 day. After curing, the epoxy was engraved with the specimen name using a rotary tool. Any epoxy that leaked out was cut from the sides of the ring forms.

2.8 Specimen cutting

Specimens mounted on a glass slide were cut on a low speed diamond saw (Isomet Low Speed Saw, Buehler, Evanston, IL) with a cutting oil bath (VP-50 cutting oil, part number 811-024, Leco Corporation, St. Joseph, MI) set at a cutting speed between 3 and 4. Counterweights were adjusted to cut through a 10 mm specimen in approximately 15 to 30 minutes.

2.9 Specimen polishing

Mounted specimens were polished on an automatic polishing machine (Leco Vari/Pol VP-50, Leco Corporation, St. Joseph, MI). Specimens were mounted in a 12-position specimen holder, with 3 or 4 specimens polished at a time. A series of diamond

grit pastes (Table 2.1) were used to polish the specimens prior to indentation or scanning electron microscope (SEM) imaging of polished surfaces.

The diamond grit was applied in a spiral dot pattern to a WhiteTec polishing pad (White Tec #812-454, Leco, St. Joseph, MI) mounted to a 12-inch polishing wheel. The wheel was wetted with diamond compound extender (Microid Diamond Compound Extender #811-004, Leco, St. Joseph, MI). The specimens were polished for 3 to 120 minutes at each grit size, until the specimens were flat and no scratches from the previous grit size were present (e.g., polishing with 6 μm grit is complete when no scratches are visible that were present after polishing with 9 μm grit).

When polishing is complete for a specific grit size, the specimens and the mounting wheel were cleaned to remove all polishing grit prior to the next polishing step. All specimens except Mg_2Si were cleaned by rinsing with tap water, then cleaning in an ultrasonic cleaner (B3500A-MT, VWR International, West Chester, PA) with a solution of 1% detergent (Liquinox detergent, Alconox) in RO water for 10 minutes. The specimens were then manually cleaned with cotton tipped applicators and ethanol before final rinse with RO water. For the Mg_2Si specimens, the cleaning was performed exclusively by hand with cotton tipped applicators and ethanol with an ethanol rinse due to a reaction between Mg_2Si and water.

Table 2.1. A series of diamond grit pastes were used to polish the specimens. A grit size may be skipped, with additional polishing time on the next smaller diamond grit size to compensate.

Nominal Diamond Grit Size	Diamond Grit Size Range	Manufacturer	Part Number
67 μm	54-80 μm	Warren Superabrasives, Anaheim, CA	54-80MB MUS 20gm
35 μm	Not listed	Warren Diamond Powder Company, Olyphant, PA	#35 MUS MB 20G
9 μm	Not listed	Leco Corporation, St. Joseph, MI	810-913
6 μm	Not listed	Warren Diamond Powder Company, Olyphant, PA	#6 MUS MB 20G
1 μm	Not listed	Leco Corporation, St. Joseph, MI	810-870
0.5 μm	Not listed	Leco Corporation, St. Joseph, MI	810-868

2.10 Mass, dimensions and density

Specimens of cylinder or parallelepiped geometry were measured to determine mass and dimensions, and calculate density. The mass and dimensions were used in later resonant ultrasound spectroscopy measurements (see section 2.11) and density was used in the analysis of mechanical property measurements.

Each of the dimensions of a specimen were determined by 5 measurements with micrometers (293-832, Mitutoyo, Japan), one measurement on each corner and one in the center or similar pattern, and the 5 measurements averaged. Specimen mass was measured by electronic balance (Adventurer AR2140, OHAUS, Pine Brook IL).

2.11 Resonant ultrasound spectroscopy

The Young's modulus, E , shear modulus, G , and Poisson's ratio, ν , of the specimens were determined by resonant ultrasound spectroscopy (RUS). In RUS, the resonant frequencies of a specimen are measured across a range of frequencies. These measured resonant frequencies are a function of the specimen mass, dimensions, geometry and elastic moduli [Migliori 1997; Ren 2009a].

The resonant frequencies were measured with a commercial RUS system (RUSpec, Quasar International, Albuquerque, NM) by placing the specimen on either a tripod arrangement of transducers (Figure 2.1) or between two transducers across a body diagonal. The range of frequencies was set to begin measurement before the first resonance frequency, and record at least 40 resonance frequencies (Figure 2.2). Four measurements of the resonance frequency spectrum were taken per specimen, two per side for the tripod arrangement, and once for each body diagonal for the two transducer arrangement. Some resonance frequencies may be missing or poorly measured for one

position, possibly due to contact issues between the specimen and the transducer or other causes [Ren 2009b], but more visible in another scan. The scan with the clearest representation of resonance frequencies was chosen for analysis.

Analysis was performed with commercial software (Figure 2.3) for either a parallelepiped geometry specimen (RPModel version 2.68b, Quasar International) or a disk shaped specimen (CylModel version 2.68b, Quasar International). The measured mass and dimensions, and an initial guess for the stiffness, c_{11} and c_{44} for isotropic specimens, were entered, the desired number of calculated resonance frequencies, the convergence rate (typically set to 0.5), the polynomial order (typically set to 12), and the fit dimensions option set (typically unused). The calculated resonance frequencies were matched to measured resonance frequencies from the spectrum (Figure 2.2), and the model was fit to the results through an iterative process. Typically, at least 12 peaks were included on the first fit of the model. Additional peaks may be added or removed from the analysis and rerun the model fit to improve the output results.

For elastically isotropic specimens, the elastic moduli are calculated from the stiffness as [Ren 2009b]

$$E = \frac{c_{44}(3c_{11}-4c_{44})}{c_{11}-c_{44}} \quad (2.1)$$

$$G = c_{44} \quad (2.2)$$

$$\nu = \frac{c_{11}-2c_{44}}{2(c_{11}-c_{44})} \quad (2.3)$$

The output of the RUS model includes information on the confidence of fit. From the output information, the uncertainties dc_{11} and dc_{44} in the measurement of c_{11} and c_{44} correspond to the 95% confidence levels calculated by the RUS model software [Ren

2009b]. The dc_{11} and dc_{44} values are computed from the first and last values, A and D , under the “chisquare increased 2% by...” section of the RUS output file, as indicated in

Figure 2.4. The dc_{11} and dc_{44} values are used to compute dE , dG , and dv .

$$dc_{11} = \frac{A}{100} c_{11} \quad (2.4)$$

$$dc_{44} = \frac{D}{100} c_{44} \quad (2.5)$$

$$dE = \sqrt{\left(\frac{c_{44}}{c_{11}-c_{44}}\right)^4 dc_{11}^2 + \frac{(3c_{11}^2-8c_{11}c_{44}+4c_{44}^2)^2}{(c_{11}-c_{44})^4} dc_{44}^2} \quad (2.6)$$

$$dG = dc_{44} \quad (2.7)$$

$$dv = \sqrt{\frac{c_{44}^2 dc_{11}^2 + c_{11}^2 dc_{44}^2}{4(c_{11}-c_{44})^4}} \quad (2.8)$$

The output of equations (2.6-2.8) are reported as the error for the RUS measurements of E , G and ν , respectively.

Additional details of the RUS theory are provided in a comprehensive book by Migliori and Sarrao [Migliori 1997].



Figure 2.1. Typical setup of tripod arrangement of RUS transducers, with specimen on top and the transducer tips near the edge of the specimen.

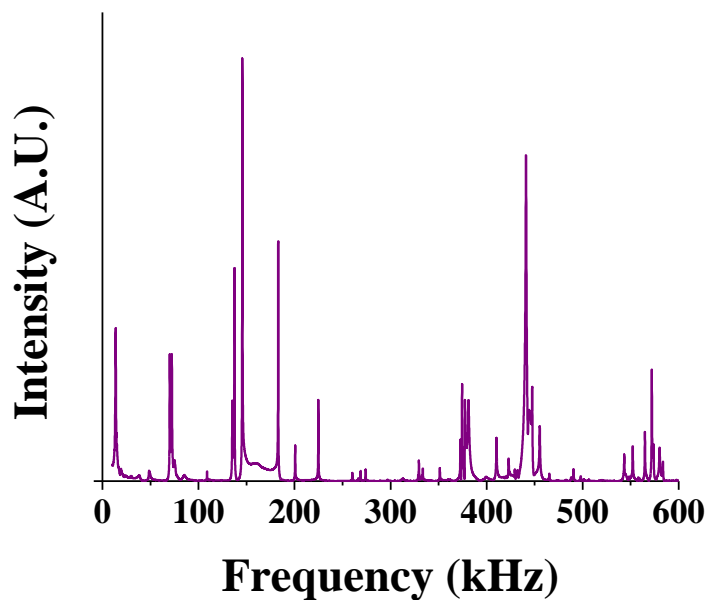


Figure 2.2. RUS spectrum from PbSe specimen. Each sharp peak in intensity represents a mechanical resonance at the driven frequency.

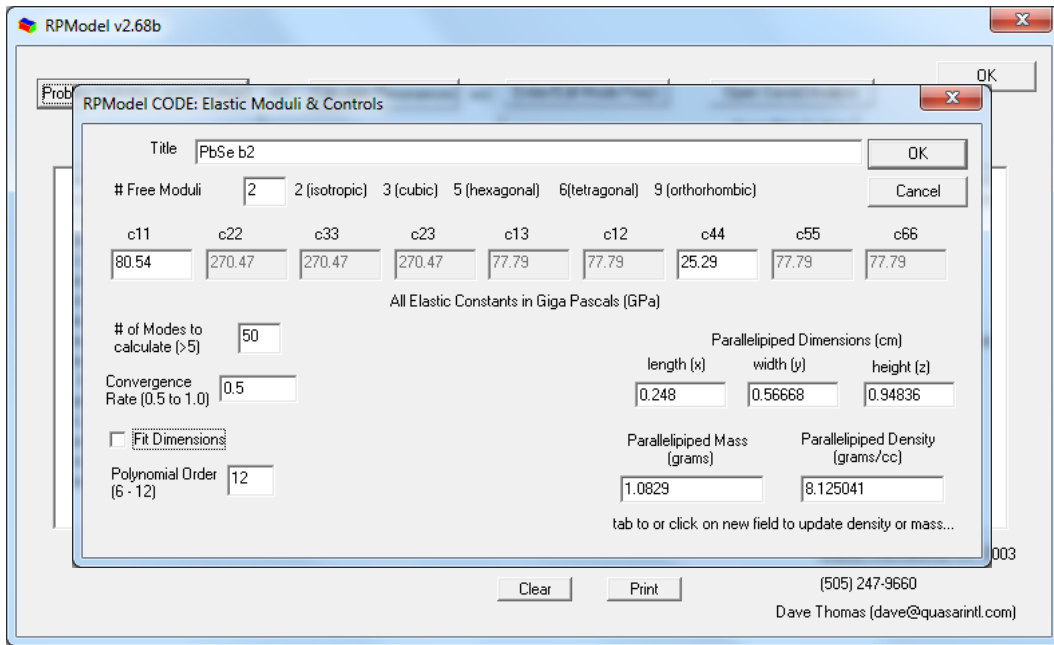


Figure 2.3. RUS analysis software, showing setup of initial conditions for a PbSe specimen.

```

Cylinder Calculation Report
This Report was prepared on 12/18/12 14:35:52 Eastern Standard Time
PbSe
Elastic Moduli Analysis is completed.
free moduli are c11 and c44
Poly Order = 12, Mass = 0.639300 gm, Density = 7.647000 g/cc
Convergence Rate = 0.500000

n      fmeas(kHz) fcalc(kHz) %err   wt      k   i   df/d(moduli)
1       65.404     65.227  -0.27% 1.0     6   2   0.05  0.95
2       65.404     65.227  -0.27% 1.0     4   1   0.05  0.95
3      100.989    101.377   0.38% 1.0     6   3   0.59  0.41
4      131.858    132.144   0.22% 1.0     2   1   0.07  0.93
5      131.858    132.144   0.22% 1.0     8   1   0.07  0.93
6      159.460    160.289   0.52% 1.0     3   1   0.01  0.99
7      159.460    160.289   0.52% 1.0     5   1   0.01  0.99
8      183.645    184.620   0.53% 1.0     7   2   0.19  0.81
9      183.645    184.620   0.53% 1.0     1   2   0.19  0.81
10     186.862    191.681   2.58% 0.0     2   2   0.41  0.59
...
Bulk Modulus= 38.252000 GPa

c11      c22      c33      c23      c13      c12      c44      c55      c66
67.76    67.76    67.76    23.50    23.50    23.50    22.13    22.13    22.13

Young's Modulus= 55.657217 GPa
Shear Modulus= 22.130000 GPa
Poisson's Ratio = 0.257506
Longitudinal Velocity (c11)= 2.976742 mm/us
Shear Velocity (c44)= 1.701160 mm/us

Xdiam= 0.792070 cm, Ydiam= 0.792070 cm, Height= 0.169670 cm

loop# 6, rms error= 0.3210%, changed by -0.0000005%

length of gradient vector= 0.000006 blamb= 0.000000

eigenvalues      eigenvectors
    1.15562      1.00 0.05
    211.91354     -0.05 1.00

chisquare increased 2% by the following % changes in independent
parameters
    0.47 -0.07
    0.00 0.11

```

Figure 2.4. Sample output file from a CylModel RUS analysis, truncated to show only the first 10 resonance peaks. Note that resonance frequency 10, 191.681 kHz, was not included in the analysis to improve the error. The “chisquare increased 2% by...” section includes the highlighted values of A , 0.47, and of D , 0.11, used in the determination of the uncertainties, dc_{11} and dc_{44} .

2.12 Hardness and fracture toughness by Vickers indentation

Vickers indentations were performed with a Buehler microindenter (Buehler Semimacro Indenter, Lake Bluff, IL) and a Shimadzu hardness tester (Shimadzu HMV-2000, Kyoto, Japan). The indenter machines were calibrated by use of a steel standard (761-048, Yamamoto Scientific Tools Lab, Co LTD, Japan), and a correction factor, ζ , of 0.95 to 1.00 for the Shimadzu hardness tester and 0.99 to 1.02 for the Buehler microindenter was calculated. The correction factor was multiplied by the measured hardness values for the specimens.

Vickers indentations typically produce an indentation impression as well as a set of radial cracks. If cracks are present, the dimensions of the cracks are the largest feature size of the indentation, and if cracks are not present, the dimensions of the indentation impression are the largest feature. Indentations were separated from the edges of the specimen and from other indentations by a minimum of 5x the largest feature of the indentation. This separation distance is inclusive of a minimum thickness for the specimen. Typically, the indentations were 1.0 mm from any edge and 0.5 mm from the nearest indentation.

Hardness was calculated from the Vickers indentation impression (Figure 2.5), $2a$,

$$H = \zeta \frac{1.8544P}{(2a)^2} \quad (2.9)$$

where P is the applied load, ζ is the indenter correction factor, and 1.8544 is a geometric factor for the angle of the pyramidal Vickers indenter tip [Wachtman 2009].

Radial cracks from Vickers indentations, $2c$ (Figure 2.5), may be used to estimate the fracture toughness, K_{IC} . As Vickers indentations is not purely mode one fracture toughness measurement, but rather an estimate, the designation of K_C shall be used when referencing fracture toughness in general rather than mode one fracture toughness, and for values of fracture toughness determined by Vickers indentation. The K_C was determined by [Wachtman 2009]

$$K_C = \xi \frac{(E/H)^{1/2} P}{c^{3/2}} \quad (2.10)$$

where ξ is a calibration factor set to 0.0016 [Anstis 1981], E is the Young's modulus for the specimen as determined by RUS analysis (see section 2.11), and P is the applied load.

The indentation method is not without controversy, with the assumption of the crack shape and plastically deformed zone being both revised and expanded [Anstis 1981; Dukino 2006] and questioned [Eilertsen 2013; Quinn 2007], with Quinn and Bradt stating, “the VIF technique is not suitable for the measurement of the fracture toughness, K_{IC} , or any other form of the fracture resistance of ceramics or other brittle materials” [Quinn 2007]. It should be noted that some of the indentations used to question the indentation method in Eilertson et al. [Eilertsen 2013] have crack systems that are not suitable for determination of K_C by Vickers indentation, as illustrated by Anstis et al. [Anstis 1981], and simply illustrate that the use of poorly developed radial cracks produce poor results for K_C . Regardless, the Vickers indentation method for determination of K_C is a common test with particular value for specimens where other methods of measuring K_C are not possible or practical [Wachtman 2009; Walker 2011; Ni 2010; Zhao 2008; Anstis 1981; Evans 1976].

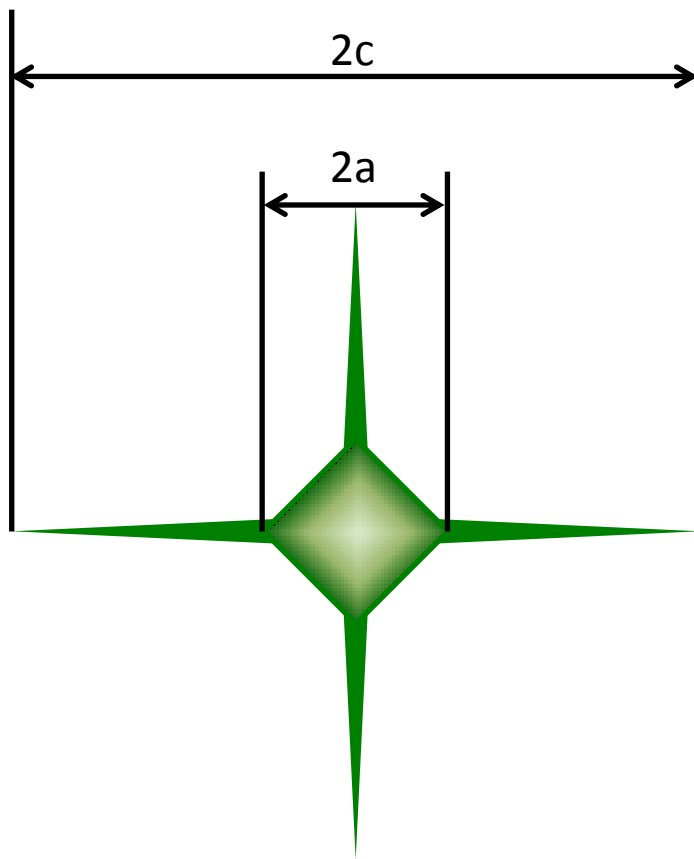


Figure 2.5. Schematic representation of Vickers indentation, illustrating the indentation impression dimensions, $2a$, and the radial crack length dimensions, $2c$.

2.13 X-ray diffraction

X-ray diffraction (XRD) analysis was performed on YbAl₃ (chapter 3), Mg₂Si (chapter 4), SnTe (chapter 7), and PbS (chapter 8) to verify phase, determine lattice parameter, and detect possible contamination. Diffraction was performed with a benchtop XRD machine (Miniflex II, Cu K α radiation, Rigaku, Tokyo, Japan) on powder SnTe and powder YbAl₃, or with a rotating stage free-standing XRD machine (Bruker Davinci Diffractometer) at the Michigan State University Center for Crystallographic Research on powder Mg₂Si and sintered PbS. Both XRD machines use a Cu K α radiation source.

Reitveld refinement and phase determination was performed with commercial software (HighScorePlus version 3.0c, PANalytical B.V., Almelo, The Netherlands) and patterns from the crystallography open database [Gražulis 2012; Gražulis 2009].

2.14 Scanning electron microscopy imaging and energy dispersive x-ray spectroscopy

Scanning electron microscopy (SEM) imaging permits the examination of micrometer- and nanometer-scale features such as determining size or morphology of particles, pores, and grains, determination of differences in average atomic weight by backscatter imaging, and determining distribution of particles, pores, or grains. For these reasons, SEM imaging was performed on each of the six studies in this dissertation.

The SEMs used in this study (6400, 6610LV, and 7500F, JEOL Ltd., Japan) at the Center for Advanced Microscopy, Michigan State University were operated at an average working distance of 15 mm (6400 and 6610LV) or 8 mm (7500F) and an accelerating voltage of 15 kV, unless specified.

Powder specimens were mounted with carbon paint (05006-AB, SPI Supplies, West Chester, PA), and sintered specimens were mounted with epoxy and carbon paint, or with carbon tape. Prior to imaging, each specimen was blown off with compressed air (22531093, OfficeMax) to remove loose powder or dust on the surface.

Energy dispersive x-ray spectroscopy (EDS) was performed primarily with the 6610LV SEM because the tungsten filament and detector are capable of recording higher counts than the 7500F SEM. The 7500F SEM was used for EDS on only the PM-HP-673-Ag specimen (chapter 6) because the higher resolution of the 7500F SEM permitted locating the necessary areas for EDS detection more readily than was possible on the 6610LV.

2.14.1 Grain size measurement from fractured surface images

Fractured surfaces were used to determine average grain sizes by the linear intercept method [ASTM-Standard-E112-13 2014] in specimens with unimodal grain size distributions. Specimens with bimodal grain size distributions are not appropriate for measurement by lineal intercept method. A fractured surface image with approximately 10-30 grains along the length and clearly visible grain boundaries was chosen for analysis. In the linear intercept method, a line of measured length is drawn in a random orientation across a fractured surface image, and the number of grain boundaries the line intercepts was summed. Additional lines were drawn until the number of intercepts counted was greater than 200, typically about 10 to 15 lines. The total length of the lines was scaled according to the printed scale bar on the image, and divided by the total number of intercepts to determine an average line length between intercepts. The average

line length was multiplied by the stereographic projection factor, 1.5, to determine the average grain size of the specimen.

REFERENCES

REFERENCES

- [Anstis, Chantikul, Lawn, Marshall 1981] Anstis, G., Chantikul, P., Lawn, B., Marshall, D. A critical evaluation of indentation techniques for measuring fracture toughness: I, direct crack measurements. *Journal of the American Ceramic Society* 64 (1981) 533–538.
- [ASTM-Standard-E112-13 2014] ASTM-Standard-E112-13. Standard Test Methods for Determining Average Grain Size. In: *ASTM Volume 03.01 Metals Mechanical Testing; Elevated and Low Temperature Tests; Metallography*. ASTM International, West Conshohocken, PA, 2014.
- [Dukino, Swain 2006] Dukino, R.D., Swain, M. V. Comparative Measurement of Indentation Fracture Toughness with Berkovich and Vickers Indenters. 2 (2006) 3299–3304.
- [Eilertsen, Subramanian, Kruzic 2013] Eilertsen, J., Subramanian, M. a., Kruzic, J.J. Fracture toughness of Co₄Sb₁₂ and In_{0.1}Co₄Sb₁₂ thermoelectric skutterudites evaluated by three methods. *Journal of Alloys and Compounds* 552 (2013) 492–498.
- [Evans, Charles 1976] Evans, A., Charles, E. Fracture toughness determinations by indentation. *Journal of the American Ceramic ...* (1976) 371–372.
- [Gražulis, Chateigner, Downs, Yokochi, Quirós, Lutterotti, Manakova, Butkus, Moeck, Le Bail 2009] Gražulis, S., Chateigner, D., Downs, R.T., Yokochi, a F.T., Quirós, M., Lutterotti, L., Manakova, E., Butkus, J., Moeck, P., Le Bail, A. Crystallography Open Database - an open-access collection of crystal structures. *Journal of applied crystallography* 42 (2009) 726–729.
- [Gražulis, Daškevič, Merkys, Chateigner, Lutterotti, Quirós, Serebryanaya, Moeck, Downs, Le Bail 2012] Gražulis, S., Daškevič, A., Merkys, A., Chateigner, D., Lutterotti, L., Quirós, M., Serebryanaya, N.R., Moeck, P., Downs, R.T., Le Bail, A. Crystallography Open Database (COD): an open-access collection of crystal structures and platform for world-wide collaboration. *Nucleic acids research* 40 (2012) D420–7.
- [Migliori, Sarrao 1997] Migliori, A., Sarrao, J.L. *Resonant Ultrasound Spectroscopy: Applications to Physics, Materials Measurements, and Nondestructive Evaluation*. Wiley-Vch, New York, 1997.
- [Ni, Case, Khabir, Stewart, Wu, Hogan, Timm, Girard, Kanatzidis 2010] Ni, J.E., Case, E.D., Khabir, K.N., Stewart, R.C., Wu, C.-I., Hogan, T.P., Timm, E.J., Girard, S.N., Kanatzidis, M.G. Room temperature Young's modulus, shear modulus, Poisson's

ratio and hardness of PbTe–PbS thermoelectric materials. *Materials Science and Engineering: B* 170 (2010) 58–66.

[Pilchak, Ren, Case, Timm, Schock, Wu, Hogan 2007] Pilchak, A.L., Ren, F., Case, E.D., Timm, E.J., Schock, H.J., Wu, C.-I., Hogan, T.P. Characterization of dry milled powders of LAST (lead–antimony–silver–tellurium) thermoelectric material. *Philosophical Magazine* 87 (2007) 4567–4591.

[Quinn, Bradt 2007] Quinn, G.D., Bradt, R.C. On the Vickers Indentation Fracture Toughness Test. *Journal of the American Ceramic Society* 90 (2007) 673–680.

[Ren, Case, Ni, Timm, Lara-Curzio, Trejo, Lin, Kanatzidis 2009a] Ren, F., Case, E.D., Ni, J.E., Timm, E.J., Lara-Curzio, E., Trejo, R.M., Lin, C.-H., Kanatzidis, M.G. Temperature-dependent elastic moduli of lead telluride-based thermoelectric materials. *Philosophical Magazine* 89 (2009) 143–167.

[Ren, Case, Ni, Timm, Lara-Curzio, Trejo, Lin, Kanatzidis 2009b] Ren, F., Case, E.D., Ni, J.E., Timm, E.J., Lara-Curzio, E., Trejo, R.M., Lin, C.-H., Kanatzidis, M.G. Temperature-dependent elastic moduli of lead telluride-based thermoelectric materials. *Philosophical Magazine* 89 (2009) 143–167.

[Schmidt, Case, Ni, Sakamoto, Trejo, Lara-curzio, Payzant, Kirkham 2011] Schmidt, R., Case, E., Ni, J., Sakamoto, J., Trejo, R., Lara-curzio, E., Payzant, E., Kirkham, M. Characterization of the mechanical properties of two n-type and one p-type Sb-based skutterudite thermoelectric compounds. 2011.

[Wachtman, Cannon, Matthewson 2009] Wachtman, J.B., Cannon, W.R., Matthewson, M.J. *Mechanical Properties of Ceramics*. Wiley-Vch, Hoboken, N.J., 2009.

[Walker, Marotto, Rafiee, Koratkar, Corral 2011] Walker, L.S., Marotto, V.R., Rafiee, M. a, Koratkar, N., Corral, E.L. Toughening in graphene ceramic composites. *ACS nano* 5 (2011) 3182–90.

[Zhao, Zhang, Li, Zhou, Liu, Liu 2008] Zhao, L.-D., Zhang, B.-P., Li, J.-F., Zhou, M., Liu, W.-S., Liu, J. Thermoelectric and mechanical properties of nano-SiC-dispersed Bi₂Te₃ fabricated by mechanical alloying and spark plasma sintering. *Journal of Alloys and Compounds* 455 (2008) 259–264.

3 Room temperature mechanical properties of polycrystalline YbAl₃, a promising low temperature thermoelectric material

Robert D. Schmidt, Eldon D. Case, Gloria J. Lehr, Donald T. Morelli
Chemical Engineering and Materials Science Department,
Michigan State University, East Lansing, MI, 48824
Published in: Intermetallics 35 (2013) 15-24.

Abstract

Intermetallic YbAl₃ in the L₁₂ (AuCu₃) phase is a promising material for low temperature thermoelectric applications. However, there is no experimental data in the literature on the mechanical properties of YbAl₃, although the design and development of thermoelectric modules incorporating YbAl₃ will require mechanical property data. Using resonant ultrasound spectroscopy (RUS), the room temperature Young's modulus, shear modulus, bulk modulus and Poisson's ratio were determined as a function of volume fraction porosity, P, for specimens densified by both hot pressing (HP) and pulsed electric current sintering (PECS) polycrystalline specimens, where P ranged from 0.030 to 0.233 and mean grain sizes ranged from 0.5 to 1.4 μm . In addition, the longitudinal and acoustic wave speeds and the Debye temperature were measured. Using Vickers indentation, the hardness and fracture toughness of the specimens were also measured. Despite microstructural differences between the HP and PECS-processed specimens, the porosity dependence of the mechanical properties was a function of the total volume fraction porosity, P, independent of the details of the size and spatial distribution of pores within individual specimens.

Keywords: A. aluminides, B. elastic properties, mechanical properties at ambient temperature

3.1 Introduction

Research directed at developing more efficient thermoelectric (TE) materials has surged in the last decade with hopes that applications in thermoelectric power generation may be realized on a large scale. TE devices convert heat directly to electricity using the Seebeck effect. The efficiency of conversion depends on the dimensionless thermoelectric figure of merit:

$$ZT = \frac{\alpha^2 \sigma}{\kappa} T = \frac{PF}{\kappa} T \quad (1)$$

In this equation, α is the Seebeck coefficient, σ the electrical conductivity, and κ the thermal conductivity of the material; PF is termed the power factor. Historically, the best TE materials have exhibited ZT values not exceeding unity. Recent research has successfully demonstrated higher values of the figure of merit, most notably in bulk nanostructured chalcogenides [Biswas 2011] and filled skutterudite [Shi 2011] compounds, which exhibit ZT values in the range of 1.6-1.8 above 600 K.

Another application of thermoelectricity involves solid state heating and cooling using the Peltier effect. In contrast to the very promising developments in the high temperature range, new materials for Peltier cooling at room temperature and below have received relatively little attention. One interesting and promising material for Peltier cooling is the intermetallic compound YbAl_3 . This compound exhibits a power factor some five to ten times that of bismuth telluride [Van Daal 1974; Rowe 2002; Mahan 1998] (the state of the art material for TE cooling), but does not possess high ZT due to its high thermal conductivity. Thermal conductivity reduction in YbAl_3 -based materials is a current area of focus of our research.

While it is self-evident that the electronic and thermal transport properties of a material are important parameters in determining its suitability in a TE application, equally important, yet often underappreciated, is an understanding of the mechanical properties. By the very nature of their application, TE materials can be subjected to large thermal gradients, temperature cycling, and thermal shock.

In this study, the room temperature mechanical properties (elasticity, hardness and fracture toughness) were measured as a function of volume fraction porosity, P , for polycrystalline intermetallic YbAl_3 specimens in the L1_2 phase. The specimens were densified by either hot pressing (HP) or pulsed electric current sintering (PECS). Resonant Ultrasound Spectroscopy (RUS) was used to measure the room temperature elastic moduli, including Young's modulus, shear modulus, bulk modulus and Poisson's ratio. The elastic moduli are required for stress and strain modeling of any solid which in turn is critical in the design of thermoelectric modules that will be subjected to both thermal gradients and thermal transients. Also, the longitudinal and acoustic wave speeds of YbAl_3 were measured by RUS. The wave speeds were in turn used to compute the acoustic Debye temperature which is related to thermal conductivity. Hardness, which is a measure of the resistance of a material to plastic deformation and scratching, was measured by Vickers indentation. Finally, the fracture toughness, K_C , was estimated using the length of radial cracks induced by Vickers indentation, where K_C measures the resistance to slow crack growth.

The mechanical properties were characterized as a function of porosity for two reasons. First, extrapolation of the experimental modulus versus temperature data to $P = 0$ allows the direct comparison to theoretical modulus calculations by techniques such as

density functional theory. Second, determining the modulus-porosity relationship allows comparison of the data from this study to other experimental studies by other researchers for specimens with differing P values.

3.2 Experimental procedure

3.2.1 Materials and specimen preparation

Only two binary phases exist in the Yb-Al phase diagram [Massalski 1987]: YbAl_2 and YbAl_3 . YbAl_3 can be difficult to synthesize in single phase form due to the peritectic nature of the phase transformation at the 1:3 Yb:Al ratio. Samples which are arc-melted at this composition invariably contain mixtures of YbAl_3 , Al, and the high-melting point YbAl_2 phase which cannot be removed even after extended annealing. Single crystals of pure YbAl_3 have been synthesized by growth in an Al flux [Canfield 1992]; the excess Al prevents the formation of the YbAl_2 phase. Unfortunately, the crystals so obtained are too small for mechanical property measurements.

We have successfully synthesized pellets of YbAl_3 of up to 2.54 cm in diameter by a combination of a novel arc-melting procedure and either HP or PECS. In order to obtain pure YbAl_3 phase material, we applied the concept of growth of YbAl_3 in an Al flux to the arc-melting process. Starting materials (Al 99.999% - ULVAC and Yb 99.9% - Alfa Aesar) were arc melted on a water-cooled copper hearth under argon with the nominal composition YbAl_7 . Each ingot was melted and flipped at least 5 times to ensure homogeneity.

This process resulted in a polycrystalline ingot comprised of a mixture of YbAl_3 and Al phases, as determined by X-ray diffraction (Rigaku MiniFlex II with Cu K_α radiation). Just as in the growth of single crystals in an Al flux, the excess Al present in

the arc-melting process inhibits the formation of the undesirable YbAl_2 phase. To remove the pure Al phase, the ingots were broken into small pieces and etched in a 5M NaOH bath for 24 hours. The pieces were then rinsed in a series of H_2O baths to remove any remnant NaOH, heated on a hotplate for 10-15 minutes to dry, and then ground into powder using a mortar and pestle. The powder was then sieved through a 100-mesh screen. Particles larger than this were returned to the NaOH bath and the process was repeated. The sieved powder was ball milled in a vibratory mill using stainless steel media.

Prior to densification, the powder so obtained was determined by x-ray diffraction to be single phase YbAl_3 (cubic AuCu_3 structure with lattice constant of 0.4205 nm, in agreement with literature values [Rowe 2002; Havinga 1973]). The powder was then sieved again through a 100-mesh screen. Two densification techniques were used, HP and PECS, and the processing conditions are summarized in Table 3.1. The HP specimens were pressed in a 22 mm diameter graphite die at 973 K for 1 hour under at 70 MPa (Hot press model HP200-14020-23G by Thermal Technologies LLC, Santa Rosa, CA). The PECS samples were pressed in a 12.7 mm diameter graphite die at 1023 K to 1073 K for 1 hour at a pressure of 60 MPa (Model 10, Series 4 by Thermal Technologies LLC, Santa Rosa, CA). X-ray diffraction on the densified pellets again revealed predominantly single phase material. Several low intensity peaks, however, did not index to the AuCu_3 phase, but rather matched fairly closely those of $\text{Yb}_3\text{Al}_5\text{O}_{12}$, suggesting a slight amount of this phase exists as an impurity in the pressed pellets.

Table 3.1. The HP and PECS processing parameters for the YbAl₃ specimens included in this study.

Specimen	Densification technique	Sintering time (min)	Sintering temperature (K)	Pressure (MPa)	Specimen diameter (mm)
YbAl ₃ -A	HP	75	1053	60	22
YbAl ₃ -B	HP	60	1023	70	22
YbAl ₃ -C	PECS	60	1073	60	12.7
YbAl ₃ -D	PECS	10	1073	60	12.7
YbAl ₃ -E	PECS	10	873	60	12.7

Although each of the YbAl_3 specimens were fabricated as discs, prior to microstructural characterization and mechanical property measurement, selected specimens were cut to form rectangular bars and crescent- shaped specimens from the periphery of the bar. The crescent- shaped specimens were used in the microstructural examination and hardness testing while the RUS measurements were made on both the uncut disks and the as-cut bar-shaped specimens. Initially the specimens were cut using an electrical discharge machine, but due to difficulties in cutting the specimens, all subsequent cutting was done using a surface grinder. Prior to hardness and fracture toughness testing, the specimens were polished using diamond paste with a series of grit sizes ranging from 90 microns to 1 micron.

3.2.2 Microstructural characterization

A scanning electron microscope (SEM, JEOL-6400, JEOL Ltd., Japan) with an accelerating voltage of 15 kV and a working distance of 15 mm was used to examine the size and morphology of the grains and pores for both the fractured surfaces and polished surfaces of the YbAl_3 specimens. The electrical conductivity of the specimens was sufficiently high that no conductive surface coatings were required prior to SEM examination.

A mean grain size was calculated using the linear intercept technique from SEM micrographs of the fractured surfaces of specimens. The volume fraction porosity was calculated from the specimen mass and dimensions. The mass of each specimen was measured by an electronic balance with a vendor-specified accuracy of ± 0.0003 g. The specimen dimensions were measured by a digital micrometer.

3.2.3 Hardness testing

For the polished specimens, Vickers indentation was performed at loads from 2.94 N to 19.6 N (Shimadzu Model HMV-2000 indenter). The centers of each indentation impression were located at least 1 mm from the specimen edge, with the indentation impression centers spaced approximately 0.5 mm apart. The hardness, H , was calculated from [Wachtman 2009]

$$H = \frac{1.8544L}{2a^2} \quad (1)$$

where L is the applied load and $2a$ is the average diagonal length of the indentation impression. The average hardness was calculated from the mean of at least 10 indentations on a given specimen. A steel calibration block with a hardness, H , of 7.75 GPa (761-048, Yamamoto Scientific Tools Laboratory, LTD, Japan) was used to calibrate the Vickers indenter.

3.2.4 Elastic modulus measurements

The elastic moduli were measured using a commercial resonant ultrasound spectroscopy apparatus (RUSpec, Magnaflux Quasar, Albuquerque, NM), where the moduli were determined from the mechanical resonance frequencies, the mass, dimensions and geometry of the specimens [Migliori 1997, Ren 2008, Ren 2009].

Two specimen geometries were employed in this study, a disk and a rectangular bar. Since the governing equations for these two geometries differ, the moduli for the disk and bar-shaped specimens were calculated with different commercial software packages, namely CylModel (Magnaflux Quasar, Albuquerque, NM) for the disk

geometry and RModel (Magnaflux Quasar, Albuquerque, NM) for the rectangular bar geometry.

Two different transducer stages were used during the modulus measurements (Fig. 3.1a and b). For the tripod transducer stage (Fig. 3.1a), either a disk or bar-shaped specimen was set onto the three transducers, where one driver transducer induced the mechanical vibrations in the specimens and the remaining two transducers detected the specimen resonances (Fig. 3.1a). In the second type of transducer configuration, namely the two-transducer or bipod transducer stage, a bar-shaped specimen was placed along its face diagonal between a pair of opposing transducers, one driver transducer and one pick-up transducer (Fig. 3.1b). For both the tripod and bipod transducer stages, the sinusoidal driving frequency was swept from 100 kHz to 600 kHz. The use of the two different specimen geometries and the two different transducer stages allowed independent measurements on a single specimen with a fixed modulus value, as will be discussed further in Section 3.3.3.

3.2.5 Fracture toughness measurements

The fracture toughness, K_C , was determined from the length of the Vickers indentation induced radial crack lengths using the relationship [Wachtman 2009]

$$K_C = \frac{\xi(E/H)^{1/2} L}{c^{3/2}} \quad (3)$$

where ξ is a dimensionless calibration constant (0.0016) [Anstis 1981], L is the applied indentation load, and c is half of the radial crack length. In Eq. 3, H is the specimen's hardness determined by Vickers indentation and E is the specimen's Young's modulus

determined by RUS. The mean and standard deviation of the fracture toughness were determined from at least 10 Vickers indentations per specimen.

3.3 Results and Discussion

3.3.1 Microstructural characterization

The five YbAl₃ specimens fabricated in this study had volume fraction porosity, P, ranging from 0.030 to 0.233 (Table 3.2). For each YbAl₃ specimen in this study, the mean grain size ranged from about 0.5 to 1.4 μm (Table 3.3), thus there were no significant differences between the average grain sizes obtained by hot pressing and by PECS.

However, SEM micrographs of fracture surfaces of each of the five specimens indicate that the size and spatial distribution of the HP and the PECS specimens differed from one another (Fig. 3.2). The microstructures of both hot pressed specimens YbAl₃-A (Fig. 3.2a) and specimen YbAl₃-B (Fig. 3.2b) consisted of (1) relatively dense “islands” with roughly micron grain sizes surrounded by (2) a more porous region with submicron average grain size. Two of the PECS specimens were relatively dense with small, uniformly distributed pores (Fig. 3.2c and d), while a PECS specimen intentionally processed to have higher porosity ($P \approx 0.23$) than the other two PECS specimens again showed dense regions adjacent to more porous areas (Fig. 3.2e). The less dense regions in specimens YbAl₃-A, YbAl₃-B and YbAl₃-E are marked by the ovals in Fig. 3.2a, b and e respectively.

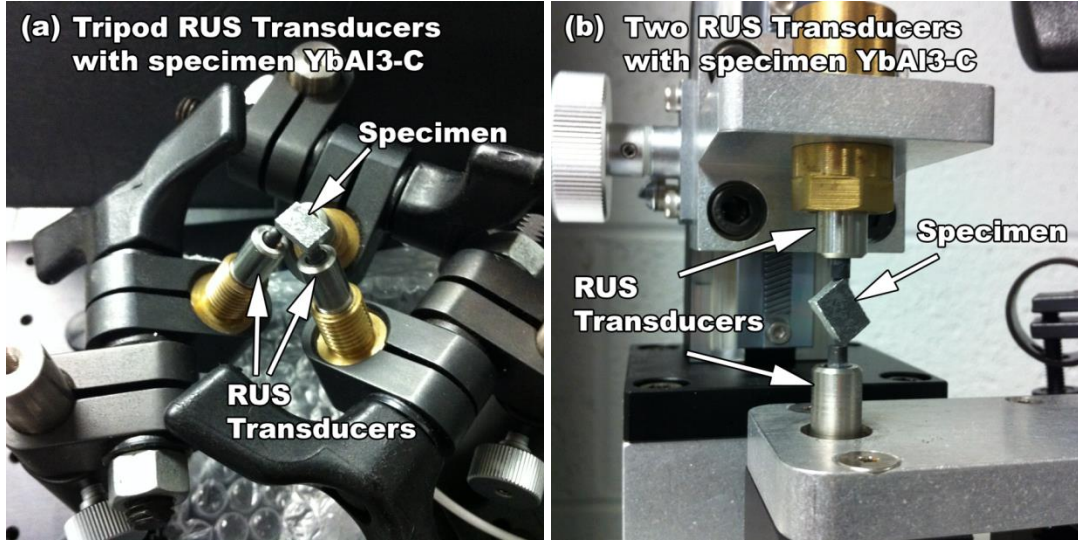


Figure 3.1. Photographs of tripod and bipod transducer stages for the RUS measurements of elastic modulus performed in this study.

Table 3.2. Specimen label, densification method (hot pressed, HP, or pulsed electric current sintering, PECS), mass, dimensions and mass density of each of the YbAl₃ specimens included in this study.

Specimen label	Densification method	Mass (g)	Dimensions (cm)	Mass Density (g/cm ³)	P
YbAl ₃ -A (bar)	HP	1.0276	0.874 × 0.808 × 0.292	4.98	0.125
YbAl ₃ -B (disc)	HP	5.3646	Ø 2.213 × 0.320	4.36	0.233
YbAl ₃ -B (bar)	HP	0.9581	1.091 × 0.320 × 0.617	4.45	0.217
YbAl ₃ -C (disc)	PECS	1.8983	Ø 1.256 × 0.287	5.34	0.060
YbAl ₃ -C (bar)	PECS	0.8125	0.869 × 0.607 × 0.286	5.38	0.054
YbAl ₃ -D (bar)	PECS	0.8675	0.922 × 0.656 × 0.260	5.52	0.030
YbAl ₃ -E (bar)	PECS	1.2582	0.973 × 0.719 × 0.409	4.39	0.227

Table 3.3. The number of indentations, indentation load and mean hardness, <H>, of the YbAl₃ specimens and porosity, *P*. In each case, the loading time was 10 s. The porosity reported is the average as measured from the disc and bar specimen geometries.

Specimen label	Number of indentations	Load (N)	<H> (GPa)	Average volume fraction porosity	GS
YbAl ₃ -A	10	0.98	4.81 ± 0.73	0.125	0.7
	20	2.94	4.86 ± 0.74	0.125	
	10	19.61	4.89 ± 0.39	0.125	
YbAl ₃ -B	10	0.98	2.80 ± 0.49	0.225	0.7
YbAl ₃ -C	10	0.98	5.81 ± 0.15	0.057	1.4
YbAl ₃ -D	10	0.98	6.81 ± 0.30	0.030	0.5
YbAl ₃ -E	10	0.98	2.76 ± 0.66	0.227	1.2

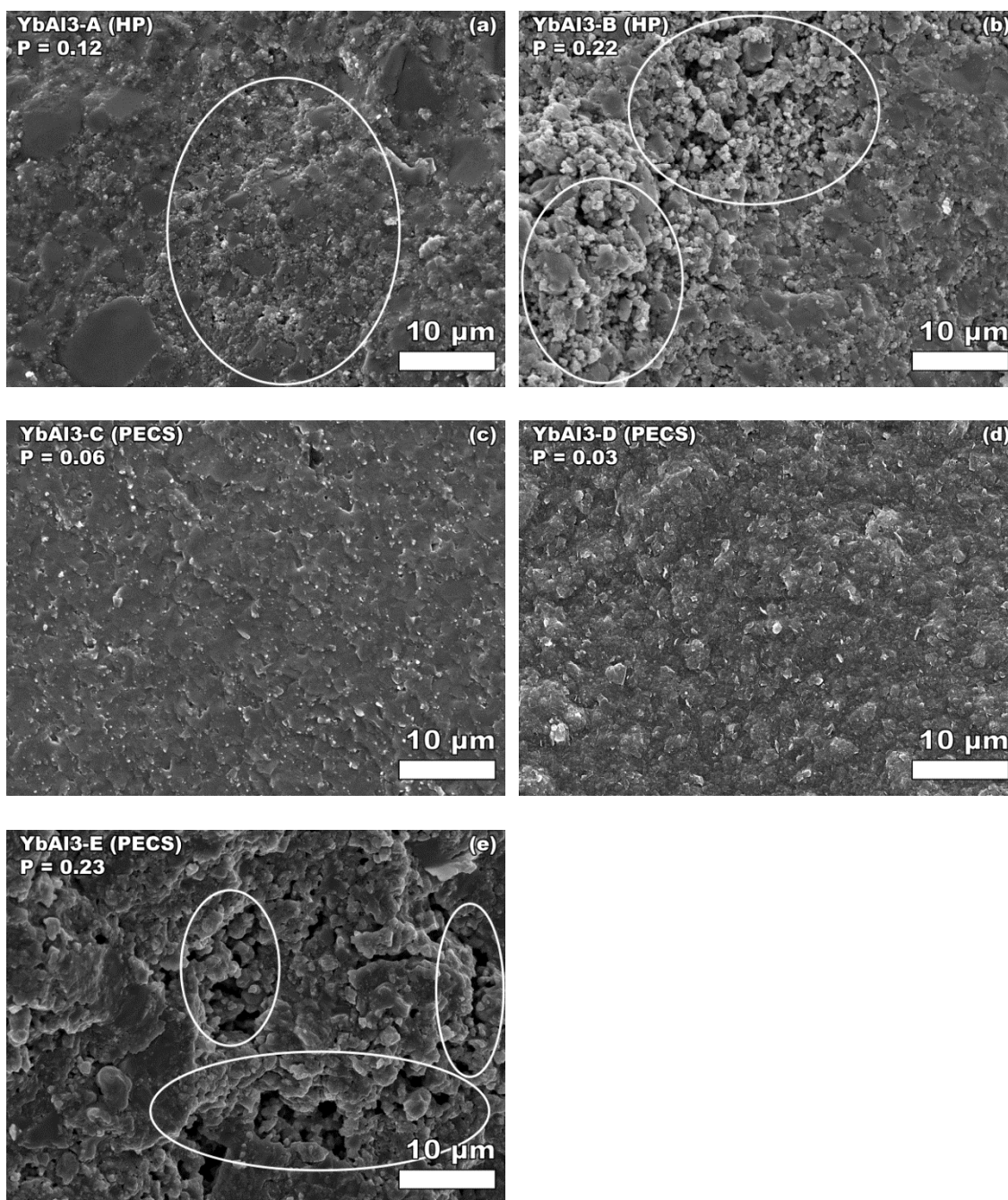


Figure 3.2. SEM micrographs of fracture surfaces and polished surfaces of YbAl₃ specimens included in this study. The ovals indicate more porous regions neighboring more dense areas that occur in the two HP specimens (Fig. 3.2a and b) as well as the PECS specimen intentionally processed to give high porosity (Fig. 3.2e).

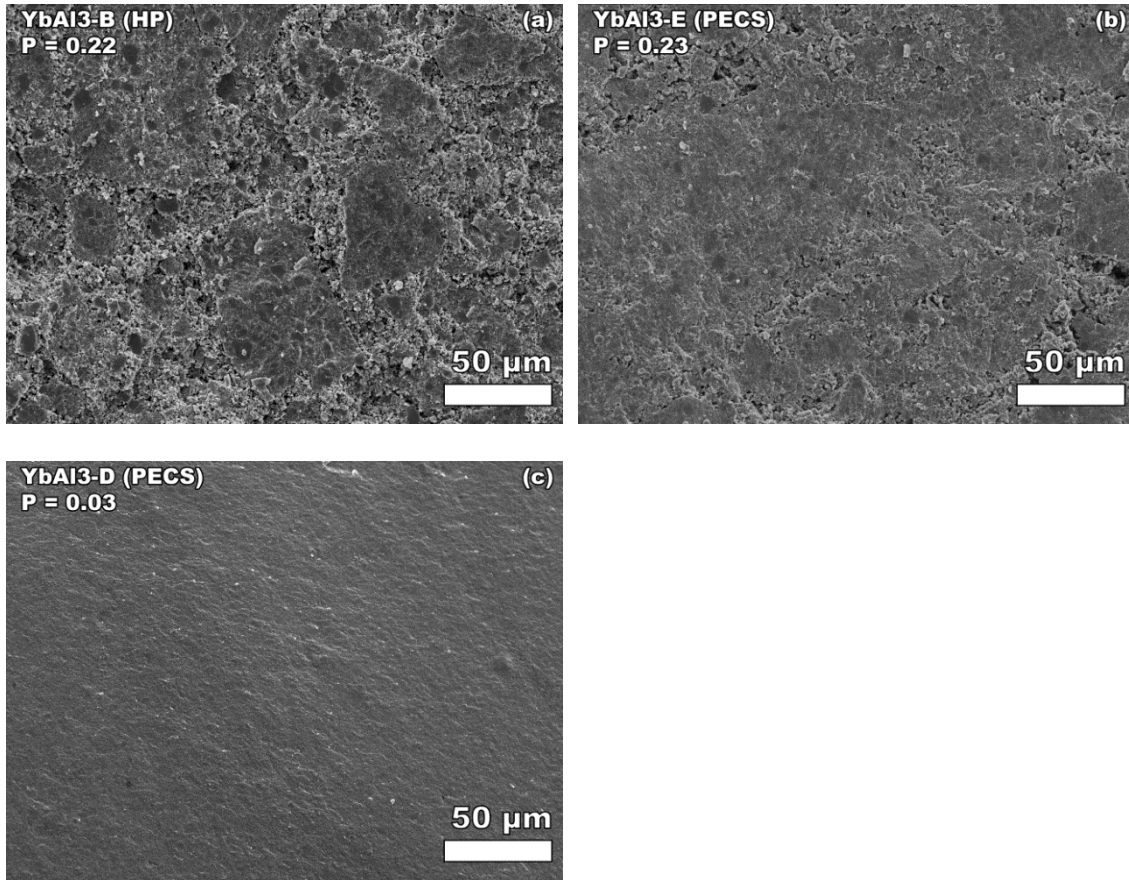


Figure 3.3. The fractured surfaces of specimens YbAl₃-B and YbAl₃-E exhibited lower porosity regions surrounded by channels of higher porosity in (a) and (b), both with similar porosity but each sintered by a different method. In contrast, specimen YbAl₃-D, shown in (c), exhibited a uniform density throughout.

The micrographs included in Fig. 3.3 were taken at a lower magnification than those in Fig. 3.2 in order to better illustrate differences in the spatial distribution of pores among the YbAl_3 specimens included in this study. The fractured surfaces of hot pressed specimen $\text{YbAl}_3\text{-B}$ ($P = 0.22$) and PECS-processed specimen $\text{YbAl}_3\text{-E}$ ($P = 0.23$) exhibited relatively dense regions surrounded by porous regions, where the pores were either quasi-spherical or lenticular in shape with a wide size distribution from roughly sub-micron to $10\text{ }\mu\text{m}$ dimensions (Fig. 3.3a and b). Although the total volume fraction porosity, P , is very similar for specimens $\text{YbAl}_3\text{-B}$ and $\text{YbAl}_3\text{-E}$, both the spatial distribution of pores and the densification technique were different for the two specimens. Note that for the hot pressed specimen $\text{YbAl}_3\text{-B}$, the porous regions appear as bands roughly $100\text{ }\mu\text{m}$ or more across, while in the PECS processed specimen $\text{YbAl}_3\text{-E}$, the bands of porosity are roughly $20\text{ }\mu\text{m}$ across with a maximum pore size that is somewhat smaller than in $\text{YbAl}_3\text{-B}$.

Densifying by HP yielded specimens with volume fraction porosities of 0.125 ($\text{YbAl}_3\text{-A}$) and 0.22 ($\text{YbAl}_3\text{-B}$). In contrast, PECS processing yielded specimens with volume fraction porosities of 0.057 ($\text{YbAl}_3\text{-C}$) and 0.030 ($\text{YbAl}_3\text{-D}$). In order to produce an YbAl_3 specimen with porosity comparable to the HP specimens, the PECS-processed specimen E was fabricated at a sintering temperature of 873 K for only 10 minutes rather than 1073 K for 60 minutes (Table 3.1).

The differences in the processing techniques and the resulting microstructures for the HP and the PECS-processed specimens is quite significant in terms of the observed P dependence of the mechanical properties. As will be discussed in Sections 3.3.2 and 3.3.4, despite these processing/microstructural differences, the porosity dependencies of

the hardness and the elastic moduli are functions of the total volume porosity, P , only, rather than showing property differences based on the size or spatial distribution of porosity in individual specimens.

3.3.2 Hardness

The decrease in H with increasing volume fraction porosity, P , is often expressed in terms of the empirical relationship

$$H = H_0 \exp(-b_H P) \quad (4a)$$

where b_H is a measure of the rate of decrease in H with increasing porosity P and H_0 is the value of hardness corresponding to a fully dense specimen [Rice 1998]. As reviewed by Rice [Rice 1998], for a number of oxides, non-oxides (including Si_3N_4 , TiC , B_4C , and glassy carbon) and the metals Cu and Fe , the decrease in H with increasing P can be described well by Eq. (4a) with b_H values ranging from roughly 2 to 6. Furthermore, for specimens with low to intermediate values of P (such as the YbAl_3 specimens included in this study), a Taylor series expansion of Eq. (4a) leads to the linear approximation

$$H = H_0 (1 - b_H P) \quad (4b)$$

In this study, the linear form of the P versus H relationship (Eq. (4b)) describes the YbAl_3 data well, as indicated by a least-squares fit of the hardness-porosity data to Eq. (4b) which yields a coefficient of determination, r^2 , of 0.965, a b_H value of 2.65 ± 0.18 and $H_0 = 6.99 \pm 0.15$ GPa (Fig. 3.4). Thus despite the differences in processing and microstructure observed for the specimens in this study (Section 3.3.1, Figs. 3.2 and 3.3), the porosity dependence of H can be described well by a function of the total volume fracture porosity (Eq. (4b)), without regard to the details of the differing sizes or spatial distribution of pores. In addition, although no studies of the H versus P behavior of rare-

earth or transition metal trialuminides are available in the open literature, the b_H value for YbAl_3 found in this study falls within the range of the values typically reported in the literature for a broad range of solid materials.

In addition to the lack of data on the H versus P behavior of trialuminides, no room temperature hardness data are available in the literature for a rare-earth or transition metal L1_2 trialuminide material. However, a room temperature Vickers indentation hardness value, H , of 5.0 ± 0.5 GPa was measured by Milman et al. [Milman 2001] for cast ingots of TiAl_3 (tetragonal D0_{22} phase) using a 2.34 N load which is roughly comparable to the H value obtained in this study for PECS processed YbAl_3 (cubic L1_2 , Au_3Cu form) of 6.81 ± 0.30 GPa at an indentation load of 0.98 N (Table 3.3).

The load dependence of H for YbAl_3 was also explored since in some cases H is a function of the applied indentation load [Nix 1998, Weaver 2003, Sangwal 2000, Milman 2011, Rice 1998], where with increasing indentation load the measured H can either increase (indentation size effect, ISE [Nix 1998, Weaver 2003, Milman 2011]) or decrease (reverse indentation size effect, RISE [Sangwal 2000]). The ISE can be especially pronounced in nanoindentation studies [Milman 2011]. In this study, the H value of YbAl_3 is essentially independent of the indentation load over the range from 0.98 to 19.6 N (Table 3.3). Over load ranges similar to that used in this study, the measured hardness also has been reported to be relatively insensitive to the applied Vickers indentation load for other brittle thermoelectric materials including Mg_2Si [Schmidt 2012], PbTe-PbS [Ni 2010] and LAST [Ren 2009].

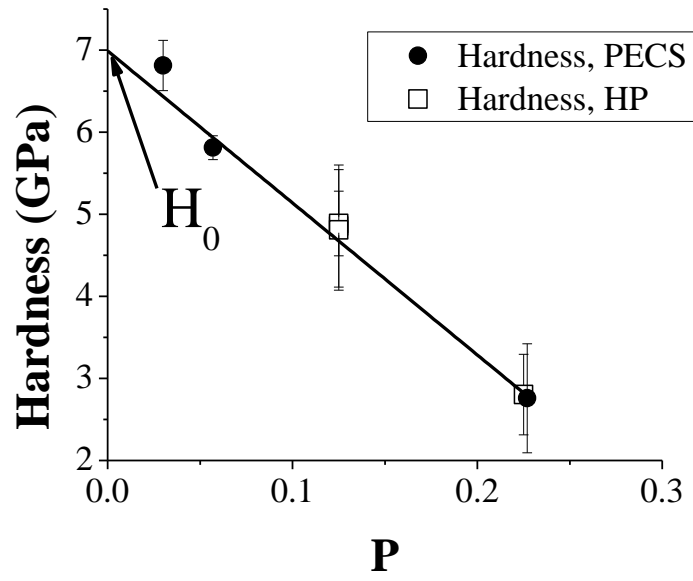


Figure 3.4. The hardness, H , versus volume fraction porosity, P , for the YbAl_3 specimens included in this study. The solid line represents a least-squares fit to Eq. (4b).

3.3.3 Fracture Toughness

For the specimens examined in this study, the fracture toughness, K_C , by Vickers indentation of YbAl_3 was between $1.13 \text{ MPa m}^{1/2}$ and $1.69 \text{ MPa m}^{1/2}$ (Table 3.4). No K_C values for rare earth trialuminides are available in the literature. However there are the following fracture toughness data for the following single phase L1_2 transition metal trialuminides: (1) $(\text{Al} + 12.5 \text{ at.} \% \text{ Mn})_3\text{Zr}$, where K_C increased from $1.86 \text{ MPa m}^{1/2}$ to $2.16 \text{ MPa m}^{1/2}$ during annealing at 800°C to 1000°C [Lee 2006], (2) $(\text{Al} + x \text{ at.} \% \text{ Mn})_3\text{Ti}$, $x = 3$ to 12 , with K_C ranging from $1.1 \text{ MPa m}^{1/2}$ to $1.54 \text{ MPa m}^{1/2}$ as a function of x [Jang 2004], (3) $(\text{Al} + 8 \text{ at.} \% \text{ Mn})_3\text{Ti}$, with a K_C value of $1.54 \text{ MPa m}^{1/2}$ which increased to $4.12 \text{ MPa m}^{1/2}$ when annealed to 1100°C [Jang 2004], and (4) $\text{Al}_3\text{Ti(9Mn)}$, with $K_C \approx 2 \text{ MPa m}^{0.5}$ for Vickers indentation loads from 200 g to 2000 g and a range of porosity from 0.005 to 0.12 [Varin 2001]. Thus, while the heat treatment and alloying of these transition metal trialuminides from the literature was primarily aimed at optimizing the mechanical properties, especially K_C [Lee 2006; Jang 2004; Varin 2001], it is interesting that the K_C values for the thermoelectric YbAl_3 specimens in this study is roughly comparable to the K_C measured for the transition metal trialuminides.

Table 3.4. For YbAl₃ specimens included in this study, the fracture toughness, K_C , measured by Vickers indentation, including the applied load, specimen grain size and volume fraction porosity, P . The K_C was obtained from the mean of 10 indentations per specimen.

Specimen	K_C (MPa m ^{1/2})	Indentation load (N)	Grain size (μm)	P
YbAl ₃ -A	1.69 ± 0.20	19.61	0.65	0.125
YbAl ₃ -D	1.13 ± 0.07	0.98	0.54	0.030

3.3.4 Elastic modulus

As is the case for hardness, the P dependence of the elastic moduli is often expressed empirically in terms of an exponential decrease in moduli with increasing P which can be approximated by the linear functions

$$E = E_0(1 - b_E P) \quad (5a)$$

$$G = G_0(1 - b_G P) \quad (5b)$$

$$B = B_0(1 - b_B P) \quad (5c)$$

where E is Young's modulus, G is the shear modulus and B is the bulk modulus and E_0 , G_0 and B_0 are the $P = 0$ intercepts of the E , G , and B data, respectively (Table 3.5, Fig. 3.5a). The material dependent values of b_E , b_G and b_B are measures of the decrease in the respective moduli as a function of increasing P .

Rice [Rice 1998] also reviewed the P dependence of the elastic moduli E , G and B . The values of the coefficients b_E , b_G and b_B (Eqs. (5a) – (5c)) typically range from about 2 to 6 for metals (Fe, Co, Ni, Cu, Be, Cu-Sn), polymer-based materials (epoxy and polyester) in addition to a number of oxide, carbide and nitride materials. For this study of the elasticity- P behavior of YbAl_3 , a least-squares fit of the modulus-porosity data to Eqs. (5a) – (5c), respectively (Fig. 3.5a), resulted in b_E , b_G and b_B values that ranged from 2.21 ± 0.17 (b_B) to 2.38 ± 0.05 (b_G) (Table 3.5). Note that the b_E , b_G and b_B coefficients obtained for YbAl_3 in this study fall within the range of b_E , b_G and b_B values reported by Rice [Rice 1998]. Thus, as was the case for the P dependence of H , the P dependence of the Young's, shear and bulk moduli of YbAl_3 is consistent with elasticity versus P relationships reported for a number of ceramic, polymer and metallic materials in the literature [Rice 1998]. Also in accord with the observed P dependence of H , the P

dependence of the elastic moduli are described well by functions of the total volume fraction porosity, P (Eqs. (5a) – (5c)), without taking into account the specimen to specimen differences in the size and spatial distribution of pores (Section 3.3.1, Figs. 3.2 and 3) that are likely related to the two difference processing techniques used in this study (HP and PECS).

No experimental or theoretical studies in the open literature treat the porosity dependence of the elastic moduli of YbAl_3 or any other trialuminide. Also, no experimental values of the elastic moduli for YbAl_3 are available in the literature for any value of P . However, since E_0 , G_0 and B_0 (Eqs. (5a) – (5c)) represent estimates of the elastic moduli for $P = 0$, they can be compared directly to the theoretically calculated values of the elastic moduli (Table 3.6).

The YbAl_3 elastic modulus values determined experimentally in this study are presented in Table 3.6, along with a summary of calculated elastic modulus results for YbAl_3 [Sa 2011; Zhou 2010; Tao 2008]. In addition, Table 3.6 includes calculated and experimental elastic modulus results for the additional rare earth trialuminide ScAl_3 [Tao 2008; Hyland 1991; Fu 1990; Xu 1990; Jahnatek 2007] and TmAl_3 [Tao 2008; Sa 2011; Zhou 2010]. Also, Table 3.6 includes a calculated bulk modulus value of a transition metal trialuminide, ZrAl_3 [Xu 1990]. The three rare-earth and transition metal trialuminides have roughly similar elastic moduli, with E for the theoretical values ranging between 124.19 GPa and 165.36 GPa and the experimental YbAl_3 value from this study 174.0 GPa.

Table 3.5. The fitting parameters obtained from the least-squares fit of the appropriate elastic modulus to Eqs. (5a) – (5c). The coefficient of determination, R^2 , is given for each of the fitted equations.

Property	P=0 Intercept (GPa)	b (unitless)	R^2
Young's Modulus	$173.8 \pm 2.3 (E_0)$	$2.35 \pm 0.06 (b_E)$	0.994
Shear Modulus	$73.5 \pm 0.9 (G_0)$	$2.38 \pm 0.05 (b_G)$	0.995
Bulk Modulus	$91.6 \pm 3.4 (B_0)$	$2.21 \pm 0.17 (b_B)$	0.947

Table 3.6. A comparison of this study's experimentally determined values of elastic moduli (E, Young's modulus, G, shear modulus, B, bulk modulus and ν , Poisson's ratio) for YbAl₃ with calculated and experimental values of other trialuminide materials, R-Al₃, from the literature for R = Yb, Sc, Tm, or Zr [Sa 2011, Zhou 2010, Tao 2008, Hyland 1991, Fu 1990, Xu 1990, Jahnatek 2007].

Material	E (GPa)	G (GPa)	B (GPa)	ν	Method	Reference
YbAl ₃	174.0 ± 2.5	73.6 ± 0.9	91.3 ± 2.9	0.182 ± 0.003	Exp (RUS)	This study
YbAl ₃	N.A.	66.0	N.A	N.A	Calculated	[Sa 2011]
YbAl ₃	N.A.	N.A.	67	N.A	Calculated	[Zhou 2010]
YbAl ₃	124.19	54.17	58.51	0.146	Calculated	[Tao 2008]
ScAl ₃	165.36	69.62	88.24	0.188	Calculated	[Tao 2008]
ScAl ₃	164.2 ± 1.9	68.4 ± 0.8	91.5 ± 1.1	0.201 ± 0.001	Exp (Pulse echo)	[Hyland 1991]
ScAl ₃	166	69	92	0.20	Calculated	[Fu 1990]
ScAl ₃	N.A.	N.A.	93	N.A.	Calculated	[Xu 1990]
ScAl ₃	174	78	87	N.A.	Calculated	[Jahnatek 2007]
TmAl ₃	146.19	61.48	78.3	0.189	Calculated	[Tao 2008]
TmAl ₃	N.A.	60.3	N.A	N.A	Calculated	[Sa 2011]
TmAl ₃	N.A.	N.A.	80	N.A	Calculated	[Zhou 2010]
ZrAl ₃	N.A.	N.A.	100	N.A.	Calculated	[Xu 1990]

N.A. = Not available

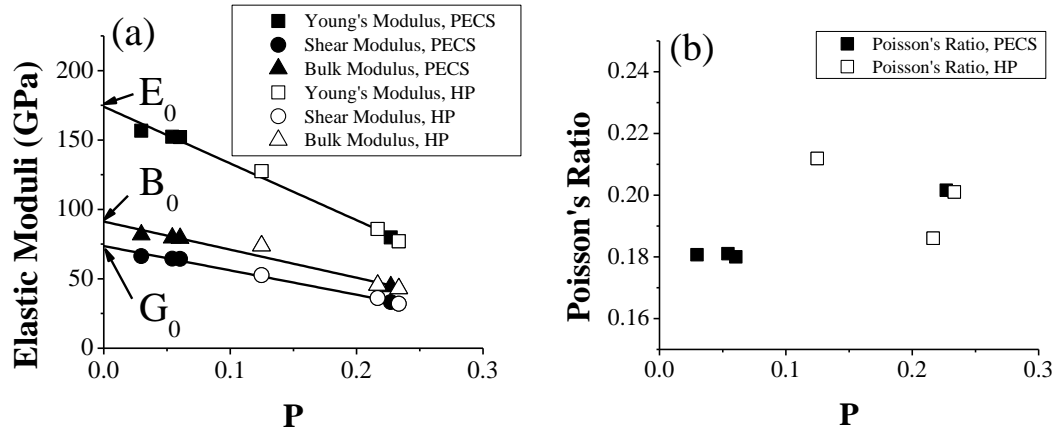


Figure 3.5. For the YbAl₃ specimens included in this study, the RUS measurement results for (a) the Young's modulus, E , shear modulus, G , bulk modulus, B as a function of P and (b) Poisson's ratio as a function of P . The solid lines in Fig. 3.5a represent least-squares fits to Eqs. (5a), (5b) and (5c) for the Young's modulus, shear modulus and bulk modulus, respectively.

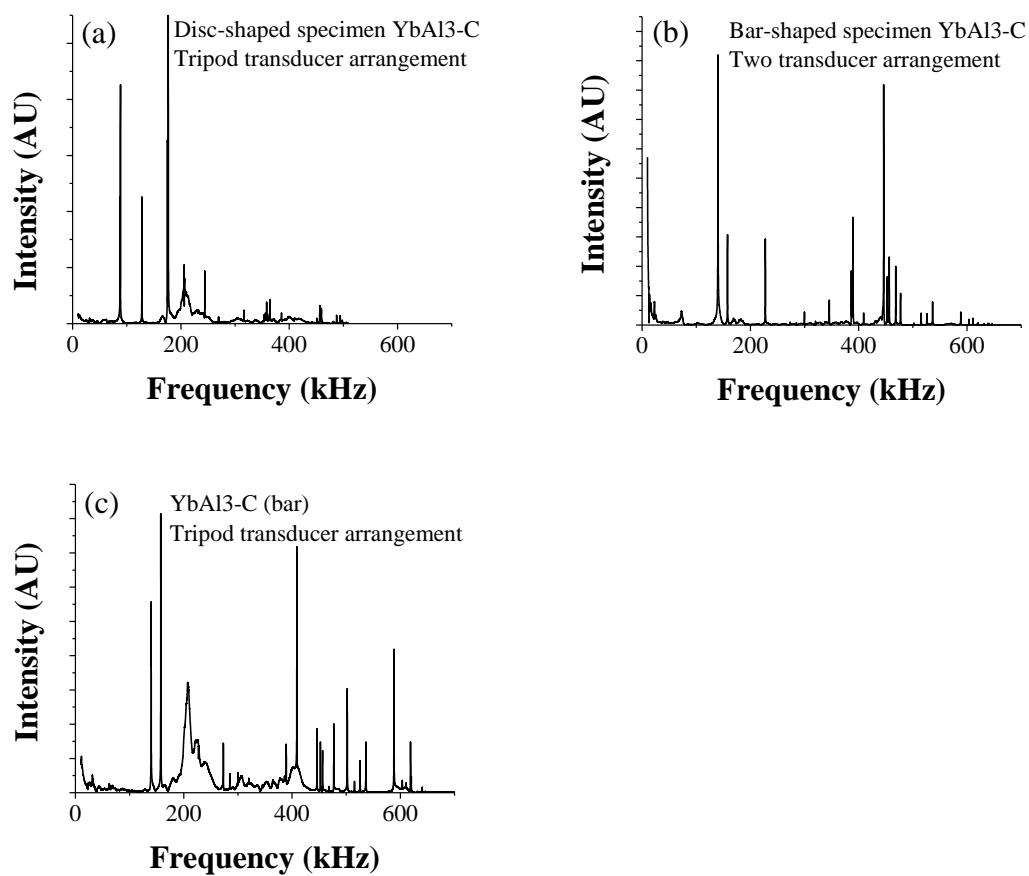


Figure 3.6. The RUS mechanical vibration spectra for the two-transducer stage and tripod specimen stage.

The values of the elastic moduli for YbAl_3 theoretically predicted from DFT theory are considerably lower than the experimental modulus values obtained from this study. For example, the E_0 , G_0 and B_0 values of moduli theoretically predicted by Tao [Tao 2008] are approximately 29%, 21% and 36% lower, respectively, than the experimental modulus values obtained from this study (Table 3.6). Also the G_0 value for YbAl_3 calculated by Sa [Sa 2011] is about 10% lower than this study's experimental value of G_0 (Table 3.6) and Zhou's calculated value for B_0 [Zhou 2010] was about 27% lower than this study's experimentally value of YbAl_3 (Table 3.6).

However, it is also critical to note that there are also significant disagreements among the theoretical elastic moduli obtained for YbAl_3 (Table 3.6). In particular, the G_0 values calculated by Tao [Tao 2008] and Sa [Sa 2011] differ by about 18% (Table 3.6). Also, the B_0 values calculated by Zhou [Zhou 2010] and Tao [Tao 2008] differ by approximately 13% (Table 3.6). Thus, although each of these three theoretical studies are relatively recent (2008, 2010 and 2011) for the Tao et al. [Tao 2008], Zhou et al. [Zhou 2010] and Sao [Sao 2011] studies, respectively, the differences among these theoretical studies of the elastic moduli YbAl_3 indicate a difficulty in obtaining consistent theoretical predictions. In contrast to the lack of agreement among the theoretical studies/experimental studies for the elastic moduli of YbAl_3 , the situation appears to be different for another rare earth trialuminide, namely ScAl_3 where theoretical values for B_0 for four theoretical studies [Tao 2008; Fu 1990; Xu 1990; Jahnateck 2007] are each within about 6 - 10% of one another (Table 3.6). (B_0 is used here as a basis of comparison for the theoretical studies, as shown in Table 3.6, since B_0 is the only elastic modulus that is common to the four theoretical studies as well as the experimental study). The

experimentally determined moduli E_0 , G_0 and B_0 [Hyland 1991] for ScAl_3 all lie within the range defined by the maximum and the minimum of the theoretical estimates [Tao 2008, Fu 1990, Xu 1990, Jahnateck 2007] (Table 3.6). In addition, although the agreement may be fortuitous, it is interesting to note that each of the E_0 , G_0 and B_0 values calculated by Jahnateck et al. [Jahnateck 2007] for ScAl_3 agree relatively well with the experimental values obtained for YbAl_3 in this study (Table 3.6).

Furthermore, for yet another rare earth trialuminide, TmAl_3 , the B_0 and G_0 values calculated among the theoretical studies differ by roughly 2% (Table 3.6) [Tao 2008, Sa 2011, Zhou 2011]. However, the experimental values for the elastic moduli of TmAl_3 are not available in the literature to allow comparison among the various theoretical predictions and experimental data.

Thus, among the three rare earth trialuminides, YbAl_3 , ScAl_3 and TmAl_3 , the elasticity results summarized in Table 3.6 indicate that the difficulty in obtaining consistent results for the elastic moduli is much more pronounced for YbAl_3 than for ScAl_3 and TmAl_3 . The apparent difficulty in calculating the elastic moduli for YbAl_3 in particular may be related to complexities in modeling and theoretically understanding the intermediate valent nature of the Yb ion in these compounds [4] and its effect on the elastic properties.

As an internal check on the RUS data included in our study, the elastic moduli for selected YbAl_3 disc-shaped specimens were measured on the tripod transducer stage for the RUS (Fig. 3.1a). The specimen was then cut into a bar shaped specimen and measured using the two-transducer stage (Fig. 3.1b). The significance of these measurements with the differing specimen geometries (disk and bar) and differing modes of excitation (tripod

and two-transducer or bipod stages) is that mechanical resonant mode patterns are sensitive on specimen geometry [Rossing 1982, Ogi 2002] although the mechanical resonances excited in the two-transducer stage should be similar except for the relative intensities.

The differences in the resulting RUS resonant spectra are directly demonstrated in Fig. 3.6, which shows differing resonance frequencies and relative intensities for the bar specimen YAl₃-C on the tripod transducer stage (Fig. 3.6a), the disc geometry on the transducer tripod (Fig. 3.6b) and the bar specimen on the two transducer stage. Specimen YAl₃-C specimen was first measured as a disc on the tripod transducer stage, then it was cut into a bar and measured on the both the tripod and two transducer stages. Although the RUS measurements for the specimen YAl₃-C was thus determined in three separate experiments, the E and G values measured for the various transducer stages/specimen geometries (Fig. 3.5) differ by less than 1 percent (Table 3.7), indicating a great deal of internal consistency in the measurements.

As an example of modulus-porosity study for a thermoelectric material other than YbAl₃, for 12 specimens of the thermoelectric LAST (lead-antimony-silver-tellurium) with the compositions Ag_{0.43}Pb₁₈Sb_{1.2}Te₂₀ and Ag_{0.86}Pb₁₉Sb_{1.0}Te₂₀ having volume fraction porosities, P , ranging from 0.01 to 0.14, the Young's modulus and shear modulus versus P behavior was described well by Eqs. (5a) and (5b) respectively [Ni 2009]. In particular, for the Young's modulus versus P data for LAST, a least-squares fit to Eq. (5a) yielded $E_0 = 58.3 \pm 0.3$ GPa, $b_E = 3.6 \pm 0.1$ with a correlation coefficient, $r^2 = 0.994$ [Ni 2009]. Thus, Eq. (5a) describes the Young's modulus versus porosity behavior relatively well for both LAST and YbAl₃.

Table 3.7. For the seven YbAl₃ specimens included in this study, N , the number of RUS resonant peaks measured, the RMS error in RUS, the Young's modulus, E , shear modulus, G , Poisson's ratio, ν , longitudinal and shear velocity, V_L and V_S , acoustic Debye temperature, θ_D , and porosity, P , were measured. The RUS analysis on each specimen was performed on the tripod configuration (Fig. 3.1a).

Specimen Label	N	RMS Error	E (GPa)	G (GPa)	ν	V_L (m/s)	V_S (m/s)	θ_D (K)	P
YbAl ₃ -A (bar)	20	0.19%	126.2 \pm 0.3	51.65 \pm 0.05	0.222 \pm 0.001	5390	3220	384	0.125
YbAl ₃ -B (disc)	39	0.41%	77.1 \pm 0.2	32.08 \pm 0.05	0.201 \pm 0.001	4440	2710	308	0.233
YbAl ₃ -B (bar)	24	0.27%	85.8 \pm 0.3	36.19 \pm 0.05	0.186 \pm 0.002	4590	2850	326	0.217
YbAl ₃ -C (disc)	28	0.21%	152.1 \pm 0.2	64.42 \pm 0.05	0.180 \pm 0.001	5560	3470	421	0.060
YbAl ₃ -C (bar, tripod)	17	0.25%	152.3 \pm 0.4	64.51 \pm 0.08	0.181 \pm 0.002	5550	3460	421	0.054
YbAl ₃ -C (bar, two transducer)	19	0.33%	152.9 \pm 0.5	64.89 \pm 0.10	0.178 \pm 0.002	5550	3470	422	0.054
YbAl ₃ -D (bar)	25	0.28%	156.7 \pm 0.5	66.37 \pm 0.08	0.181 \pm 0.002	5560	3470	426	0.030
YbAl ₃ -E (bar)	22	0.21%	79.7 \pm 0.2	33.2 \pm 0.04	0.202 \pm 0.002	4490	2750	313	0.227

Over the range from $P = 0.030$ to 0.060 , the Poisson's ratio, ν , of YbAl_3 is relatively constant at $\nu = 0.18$ (Fig. 3.5b). For $P = 0.125$ the Poisson's ratio increases 0.21 , then as P increases further ν ranges from about 0.19 to 0.20 (Fig. 3.5b). In the literature for oxide materials, Boccaccini found empirically that, although there was considerable scatter in the ν versus P data, the increase or decrease in ν with increasing P seemed to be correlated with the value of ν_0 (ν at $P = 0$), that is, where ν increased with increasing P for $\nu_0 > 0.25$ and ν decreased with increasing P for $\nu_0 < 0.25$ [Boccaccini 1994]. In this study, the apparent scatter in ν between values of about 0.18 to 0.21 makes it difficult to discern a trend in the P dependence of ν for YbAl_3 (Fig. 3.5b).

3.3.5. Acoustic wave speeds and the Debye temperature

The longitudinal acoustic wave speed, V_L and the shear acoustic wave speed, V_S , are also obtained from the RUS analysis. For specimens with low to intermediate values of P , the acoustic velocities can be approximated as a linear function of P [Aliev 2011, Solunke 2007] such that

$$V_L = V_{L0}(1 - c_L P) \quad (6a)$$

$$V_S = V_{S0}(1 - c_S P) \quad (6b)$$

where V_{L0} and V_{S0} are the acoustic wave speeds corresponding to a theoretically dense material and c_L and c_S are material-dependent constants. For the YbAl_3 specimens included in this study, Eqs. (6a) and (6b) describe relatively well the P dependence of the acoustic wave speeds (Table 3.8, Fig. 3.7a).

Table 3.8. The fitting parameters obtained from the least-squares fit of the V_L and V_S versus P data to Eqs. (6a) and (6b), respectively, with the coefficient of determination, R^2 .

Property	Equation	$P = 0$ Intercept (mm/ μ s)	c (unitless)	R^2
Longitudinal Velocity	(6a)	5.88 ± 0.09 (v_{l0})	1.00 ± 0.09	0.958
Shear Velocity	(6b)	3.67 ± 0.04 (v_{s0})	1.07 ± 0.06	0.986

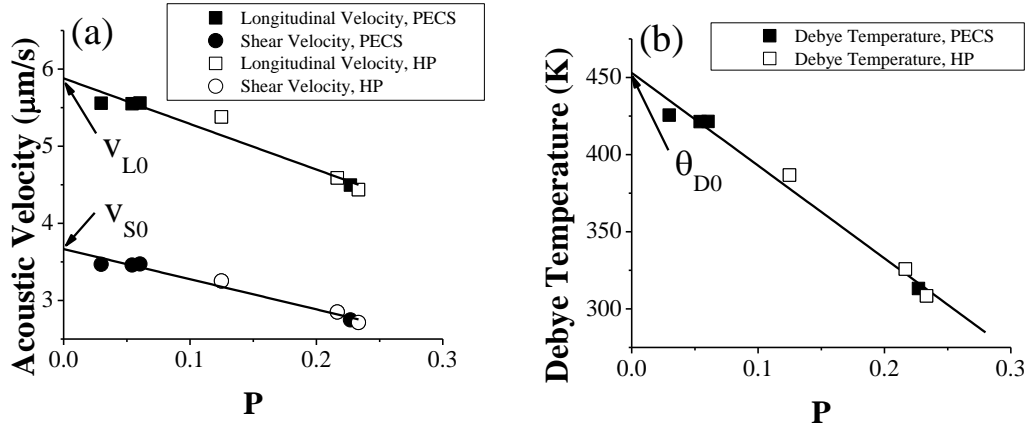


Figure 3.7. From the RUS measurements of the YbAl_3 specimens included in this study, (a) shear and longitudinal wave speeds as a function of P , where the solid lines in represent least-squares fits to Eq. (6a) and (6b) for the longitudinal and shear velocities, respectively. (b) the effective Debye temperature as a function of P , where the solid line represents a least-squares fit to Eq. (9).

The Anderson approximation [Anderson 1963] was used to calculate θ_D , the acoustic Debye temperature

$$\theta_D = \frac{h}{k_B} \left[\frac{3q}{4\pi} \frac{N_A \rho}{M} \right]^{1/3} V_m \quad (7)$$

where h is Planck's constant, k_B is Boltzmann's constant, N_A is Avogadro's number, ρ is density, M is molecular weight, and q is the number of atoms per molecule. The average acoustic velocity, V_M , was calculated from V_L and V_S using the relationship [Anderson 1963]

$$V_M = \left(\frac{1}{3} \left[\frac{2}{V_S^3} + \frac{1}{V_L^3} \right] \right)^{-1/3} \quad (8)$$

The linear decrease in the effective Debye temperature with increasing porosity (Fig. 3.7b) and can be described by

$$\theta_D = \theta_{D0} (1 - b_\theta P) \quad (9)$$

where a least-squares fit of the θ_D versus P data gives fitting parameters $\theta_{D0} = 453 \pm K$, $b_\theta = 1.32 \pm 0.06$ with a coefficient of determination of 0.99.

3.3.6 Mechanical properties as a function of processing technique

In this study, the YbAl_3 specimens were densified either by HP or PECS processing (Table 3.2). Although some researchers have reported that differing processing techniques can result in differing mechanical properties [Rice 1998], the Vickers indentation hardness measurements (Fig. 3.4) and the RUS elasticity measurements for the Young's, shear and bulk moduli (Fig. 3.5a) as well as the acoustic velocity (Fig. 3.7a) and the Debye temperature (Fig. 3.7b) show no significant differences

in the magnitudes of H , E , G , B , V_L , V_S or θ_D as a function of two processing techniques (HP or PECS).

Thus, although the HP and PECS processing parameters (sintering temperature and sintering time) yield differing sizes and spatial distribution of pores (Figs. 3.2 and 3.3 and Section 3.3.1), the physical properties measured for the YbAl_3 specimens included in this study were functions of the volume fraction porosity P and not the processing details. The practical significance of this is that for the two most common techniques of densifying thermoelectric materials, namely HP and PECS, the property-porosity relationships found in this study for YbAl_3 do not appear to be functions of the processing technique.

3.4 Summary and Conclusions

For the low temperature thermoelectric material YbAl_3 , the room temperature hardness, Young's modulus, shear modulus, bulk modulus and Poisson's ratio were measured using RUS for polycrystalline specimens with volume fraction porosities, P , over the interval $0.030 < P < 0.233$. The rates of linear decrease in hardness with increasing P (Fig. 3.4, Eq. (4b)) and the elastic moduli (Fig. 5, Eqs. (5a) – (5c)) are consistent with the literature.

Although no fracture toughness literature is available for rare earth trialumindes, the YbAl_3 values of approximately 1.1 to $1.6 \text{ MPa m}^{1/2}$ that were found in this study are comparable to lower ranges of K_C measured for transition metal trialumindes, for which significant efforts have been directed toward enhancing K_C for structural materials applications. Therefore, it appears that the K_C of YbAl_3 may be sufficiently high so as not

to hinder its development as a low temperature thermoelectric material. Also, the hardness value 6.81 GPa for YbAl_3 ($P = 0.030$) is comparable to the literature hardness value of the transition metal trialuminide TiAl_3 , thus the hardness of YbAl_3 is likely sufficient to impart reasonable in-service scratch and abrasion resistance. However, once again, the lack of hardness data in the rare earth trialuminide literature limits the hardness comparisons that can be made.

For this study, extrapolation of the elastic moduli versus porosity results to zero porosity gives intercepts E_0 , G_0 and B_0 for YbAl_3 (Eqs. (5a) – (5c), Fig. 3.6). These zero porosity values are roughly 10 - 36% higher than the E_0 , G_0 and B_0 values predicted from density functional theory (Table 3.6). However, the E_0 , G_0 and B_0 values predicted theoretically for YbAl_3 are also significantly different from one another (Table 3.6). In contrast, the theoretical and experimental moduli for ScAl_3 are relatively successful. The apparent difficulty in calculating the elastic moduli for YbAl_3 may be related to complexities in modeling and understanding the nature of the intermediate valence nature of the Yb ion in YbAl_3 .

ACKNOWLEDGEMENTS

GJL and DTM. acknowledge support by the Air Force Office of Scientific Research under the MURI program “Cryogenic Peltier Cooling,” Contract #FA9550-10-1-0533. In addition, R.D.S. and E.D.C. acknowledge the financial support of the Department of Energy, “Revolutionary Materials for Solid State Energy Conversion Center,” an Energy Frontiers Research Center funded by the U.S. Department of Energy, Office of Science, Office of Basic energy Sciences under award number DE-SC0001054.

REFERENCES

REFERENCES

- [Aliev 2011] G. N. Aliev, B. Goller, and P. A. Snow, Elastic properties of porous silicon studied by acoustic transmission spectroscopy, *J. Appl. Phys.* 110, (2011).043534
- [Anstis 1981] GR Anstis, P Chantikul, BR Lawn, DB Marshall, A Critical Evaluation of Indentation Techniques for Measuring Fracture Toughness: I, Direct Crack Measurements *Journal of the American Ceramic Society*, 64 (1981) 533 – 538.
- [Biswas 2011] K. Biswas, J. He, Q. Zhang, G. Wang, C. Uher, V. P. Dravid, and M. G. Kanatzidis, “Strained endotaxial nanostructures with high thermoelectric figure of merit, *Nature Chemistry* 3 (2011) 160
- [Boccaccini 1994] A.R. Boccaccini, *J. Am. Ceram. Soc.* 77 (1994) 2779.
- [Canfield 1992] P.C. Canfield, Z. Fisk, Growth of single crystals from metallic fluxes, *Philosophical Magazine B* 65, 1117 (1992).
- [Fu 1990] C. L. Fu, Electronic, elastic, and fracture properties of trialuminide alloys: Al_3Sc and Al_3Ti , *J. Mater. Res.* 5 (1990)971 – 979.
- [Havinga 1973] E.E. Havinga, K.H.J. Buschow and H.J. van Daal, The ambivalence of Yb in YbAl_2 and YbAl_3 , *Solid State Communications* 13 (1973) 621.
- [Hu 2011] C. Hu, Y. Sakka1, Toshiyuki Nishimura, S. Guo, S. Grasso. H, Tanaka, Physical and mechanical properties of highly textured polycrystalline Nb_4AlC_3 ceramic, *Sci. Technol. Adv. Mater.* 12 (2011) 044603.
- [Hyland 1991] R. W. Hyland, R. C. Stiffler, Determination of the elastic constants of polycrystalline of Al_3Sc , *Scripta Metallurgica* 25 (1991) 473 – 477.
- [Jahnatek 2007] M. Jahnatek , M. Krajcí , J. Hafner, Interatomic bonds and the tensile anisotropy of trialuminides in the elastic limit: a density functional study for $\text{Al}_3(\text{Sc}, \text{Ti}, \text{V}, \text{Cr})$, *Philosophical Magazine* 87 (2007) 1769 – 1794.
- [Jang 2004] H.S. Jang, C.W. Kang, Y. Kim, K.T. Hong, S.-J. Kim, Effects of Mn additions on microstructure and mechanical properties of $(\text{Al} + x \text{ at. \% Mn})_3\text{Ti}$ intermetallic compounds prepared by mechanical alloying and spark plasma sintering, *Intermetallics* 12 (2004) 477 – 485.
- [Lee 2006] S.H. Lee, K.I. Moon, K.S. Lee, Enhancement of the fracture toughness of bulk L1_2 -based $(\text{Al} + 12.5 \text{ at. \% M})_3\text{Zr}$ ($\text{M} = \text{Cu}, \text{Mn}$) intermetallics synthesized by mechanical alloying, *Intermetallics* 14 (2006) 1 – 8.

- [Mahan 1998] G.D. Mahan, in H. Ehrenreich and F. Spaepen, editors, “Good Thermoelectrics,” in *Solid State Physics: Advances in Research and Applications*, Academic Press, San Diego, CA, volume 51, 1998 page 137.
- [Massalski 1987] T.B. Massalski editor, *Binary Alloy Phase Diagrams*, ASM International, Materials Park, OH, volume 1, 1987 page 238.
- [Migliori 1997] A Migliori, JL Sarrao, *Resonant ultrasound spectroscopy applications to physics, materials measurements and nondestructive evaluation*, Wiley-Interscience, Hoboken, NJ, USA, 1997.
- [Milman 2001] Y. V. Milman, D.B. Miracle, S.I. Chugunova, I.V. Voskoboinik, N.P. Korzhova, T.N. Legkaya, Y.N. Podrezov, Mechanical behaviour of Al_3Ti intermetallics , *Intermetallics* 9 (2001) 839–845
- [Milman 2011] Y.V. Milman, A.A. Golubenko, S.N. Dub, Indentation size effect in nanohardness, *Acta Materialia* 59 (2011) 7480–7487
- [Ni 2009] J. E. Ni, F. Ren, E. D. Case, E. J. Timm, Porosity dependence of elastic moduli in LAST (Lead-antimony-silver-tellurium) thermoelectric materials, *Materials Chemistry and Physics* 118[2-3] (2009) 459 – 466.
- [Ni 2010] J. E. Ni, E. D. Case, K. Khabir, C.-I Wu, T. P. Hogan, E. J. Timm, S. Girard, M. G. Kanatzidis, Room temperature Young’s modulus, shear modulus, Poisson’s ratio and hardness of PbTe-PbS thermoelectric materials, *Materials Science and Engineering B* 170 (2010) 58 – 66.
- [Ni 2012] J. E. Ni, E. D. Case, R. Stewart, C.-I Wu, T. Hogan, M. G. Kanatzidis, , Bloating in $(\text{Pb}_{0.95}\text{Sn}_{0.05}\text{Te})_{0.92}(\text{PbS})_{0.08-0.055\% \text{ PbI}_2}$ specimens as a result of processing conditions, *Journal of Electronic Materials*, 41 (2012) 1153 – 1158.
- [Nix 1998] W.D. Nix, H. Gao, *J. Mech. Phys. Solids* 46 (1998) 411 – 425.
- [Ogi 2002] H. Ogi, K. Sato, T. Asada , M Hirao Complete mode identification for resonance ultrasound spectroscopy, *J. Acoust. Soc. Am.* 112 (2002) 2553 – 2557.
- [Ran 2010a] S. Ran, L. Zhang, O. Van der Biest, J. Vleugels, Pulsed electric current, in situ synthesis and sintering of textured TiB_2 ceramics, *Journal of the European Ceramic Society* 30 (2010) 1043 – 1047.
- [Ran 2010b] S. Ran, O. Van der Biest, J. Vleugels, ZrB_2 – SiC composites prepared by reactive pulsed electric current sintering, *Journal of the European Ceramic Society* 30 (2010) 2633 – 2642.

- [Ren 2008] F. Ren, E. D. Case, J. R. Sootsman and M. G. Kanatzidis, H. Kong, C. Uher E. Lara-Curzio and R. M. Trejo, C. Uher, The high temperature elastic moduli of polycrystalline PbTe measured by resonant ultrasound spectroscopy, *Acta Materialia* 56 (2008) 5954 – 5963.
- [Ren 2009a] F. Ren, E. D. Case, J. E. Ni, E. J. Timm, E. Lara-Curzio, R. M. Trejo, C.-H. Lin, M. G. Kanatzidis, 2009, Temperature-dependent elastic moduli of lead-telluride based thermoelectric materials, *Philosophical Magazine*, 89 (2009) 143 – 167.
- [Rice 1998] R. W. Rice, *Porosity of Ceramics*, Marcel-Dekker, Inc., New York. 1998.
- [Rossing 1982] T.D. Rossing, Chladni's law for vibrating plates, *Am. J. Phys.* 50 (1982) 271 – 274.
- [Rowe 2002] D.M. Rowe, V.L. Kuznetsov, L.A. Kuznetsova, and G. Min, Electrical and thermal transport properties of intermediate-valent YbAl₃, *J. Phys. D: Applied Physics* 35 (2002) 2183.
- [Sa 2011] B. Sa, J. Zhou, Z. Sun, Electronic mechanism of shear modulus enhancement in rare earth intermetallics Yb_{1-x}Tm_xAl₃, *Intermetallics* 19 (2011) 1020 – 1023.
- [Sangwal 2000] K. Sangwal, *Mater. Chem. Phys.* 63 (2000) 145 – 152.
- [Schmidt 2012] R. D. Schmidt, E. Case, J.E. Ni, J. Giles III, T. P. Hogan, Room-temperature mechanical properties and slow crack growth behavior of Mg₂Si thermoelectric materials, *Journal of Electronic Materials*, 41 (2012) 1210 – 1216.
- [Shi 2011] X. Shi, J. Yang, J. R. Salvador, M. Chi, J. Y. Cho, H. Wang, S. Bai, J. Yang, W. Zhang, and L. Chen, "Multiple-filled skutterudites: high thermoelectric figure of merit through separately optimizing electrical and thermal transports," *Journal of the American Chemical Society* 133,7837 (2011).
- [Solunke 2007] M.B. Solunke, P.U. Sharma, V.K. Lakhani, M.P. Pandya, K.B. Modi, P.V. Reddy, S.S. Shah, Elastic properties of gallium substituted Bi (Pb)-2212 superconducting system at 300 K, *Ceramics International* 33 (2007) 21 – 26.
- [Tao 2008] X. Tao, Y. Ouyang, H. Liu, Y. Feng, Y. DU, Z. Jin, First Principles Calculations of the Thermodynamic and elastic properties of the L12-based Al₃RE (RE = Sc, Y, La – Lu), *International Journal of Materials Research*, 99 (2008) 582 – 588.
- [Van Daal 1974] H.J. Van Daal, P.B. Van Aken, and K.H.J Buschow, The Seebeck coefficient of YbAl₂ and YbAl₃, *Physics Letters* 49A (1974) 246.

- [Varin 2001] R.A. Varin, L. Zbronic, T. Czujko, Y.-K. Song, Fracture toughness of intermetallic compacts consolidated from nanocrystalline powders, *Mater. Sci. Eng A300* (2001) 1 – 11.
- [Wachtman 2009] JB Wachtman, WR Cannon, Matthewson MJ, *Mechanical Properties of Ceramics, Second Edition*, John Wiley & Sons, Inc., New York, 2009.
- [Weaver 2003] M.L. Weaver, M.E. Stevenson, R.C. Bradt, *Mater. Sci. Eng. A345* (2003) 113 – 117.
- [Xu 1990] J.-H. Xu, A.J. Freeman, Phase stability and electronic structure of ScAl_3 and ZrAl_3 and of Sc-stabilized cubic ZrAl_3 precipitates, *Phys. Rev. B* 41 (1990) 12553 – 12561.
- [Zhou 2010] J Zhou, BS Sa, ZM Sun., First-principles investigations on phase stability and electronic structures of $\text{Yb}_{(1-x)}\text{M}_{(x)}\text{Al}_{(3)}$ ($\text{M} = \text{Ho}, \text{Er}$ and Tm) alloys, *Intermetallics* 18 (2010) 2394 – 2399.

4 Room-Temperature Mechanical Properties and Slow Crack Growth Behavior of Mg₂Si Thermoelectric Materials

Robert D. Schmidt¹, Eldon D. Case¹, Jesse Giles III¹, Jennifer E. Ni¹, Timothy P. Hogan²

¹Chemical Engineering and Materials Science Department,
Michigan State University, East Lansing, MI, 48824

²Electrical and Computer Engineering Department,
Michigan State University, East Lansing, MI, 48824

Published in: Journal of Electronic Materials 41 (2012) 1210 – 1216.

Abstract

Mg₂Si is of interest as a thermoelectric (TE) material in part due to its low materials cost, lack of toxic components, and low mass density. However, harvesting of waste heat subjects TE materials to a range of mechanical and thermal stresses. To understand and model the material's response to such stresses, the mechanical properties of the TE material must be known. The Mg₂Si specimens included in this study were powder processed and then sintered via pulsed electrical current sintering. The elastic moduli (Young's modulus, shear modulus, and Poisson's ratio) were measured using resonant ultrasound spectroscopy, while the hardness and fracture toughness were examined using Vickers indentation. Also, the Vickers indentation crack lengths were measured as a function of time in room air to determine the susceptibility of Mg₂Si to slow crack growth.

Keywords: Magnesium silicide, fracture toughness, elastic modulus, hardness, slow crack growth

4.1 Introduction

New thermoelectric (TE) materials based on Mg_2Si are candidates for a wide variety of waste heat recovery applications due to their low mass density [$\sim 2 \text{ g/cm}^3$ for Mg_2Si versus densities of 6 g/cm^3 to 8 g/cm^3 for TE materials such as PbTe, lead-antimony-silver-tellurium (LAST), CoSb_3 , FeSb_3 , and Bi_2Te_3]. Also, Mg_2Si is composed of abundant, inexpensive, and nontoxic elements. Previous studies have determined a ZT as high as 1.0 at 800 K for an Mg_2Si -based material [Mars 2009]. Energy harvesting applications subject TE materials to thermal cycling during the startup and operation of the device, as well as to the thermal gradient required to operate a TE generator. The designer must know the mechanical properties such as the elastic moduli in order to calculate the material's response to imposed thermal and mechanical loads. The room-temperature elastic moduli, hardness, and fracture toughness of Mg_2Si are determined in this study. In addition, since fine powders of Mg_2Si react vigorously with water, [Aesar] a slow crack growth study was performed in which the length of Vickers radial indentation cracks was monitored as a function of time in room air. Slow crack growth involves a concerted chemical reaction [Michalsky 1983] of a polar molecule such as water with the highly strained atomic bonds at a crack tip, with the result that the reaction breaks bonds at the crack tip and the crack slowly advances [Wiederhorn 1968; West 1998; Freiman 2009]. Slow crack growth has been observed in a variety of brittle materials, including ceramics [Freiman 2009] as well as in single crystal silicon [Connally 1992]. If slow crack growth occurs in Mg_2Si , this would imply that the flaws produced by cutting and grinding procedures during module preparation could extend upon exposure to either room air or an aqueous environment.

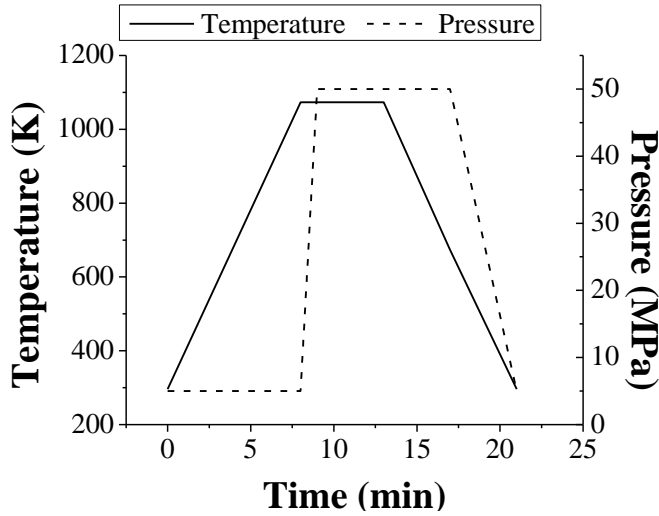


Figure 4.1. The time–temperature and time–pressure profiles used in the PECS processing of each of the Mg_2Si specimens included in this study.

Table 4.1. The Mg_2Si specimens used in this study for Vicker’s hardness, H , fracture toughness, K_{IC} , Young’s modulus, E , shear modulus, G , Poisson’s ratio, ν , and acoustic debye temperature, θ_{D} , measurements. The Mg_2Si pieces were reduced using a (1) mechanical mortar and pestle until all powder passed through a $53\ \mu\text{m}$ sieve and then either densified or further reduced using a (2) planetary mill at 150 rpm for 3 hours. For indentation the specimens were polished to $1\ \mu\text{m}$ diamond grit, further details are available elsewhere [Ni 2010]. Due to reactions with water [Aesar], the specimens were cleaned using ethanol instead of water between polishing grit sizes.

Specimen Name	Powder Processing	Form	Dimensions (mm)	Mass (g)	Density (g/cm^3)	Mechanical properties measured
Mg2Si-01	Planetary mill	Disc	19.55 dia 3.35 ht	2.01	2.01	H , $K_{\text{IC}}^{\text{a, b}}$
Mg2Si-03	Planetary mill	Parallelepiped	9.89 x 13.01 x 3.35	0.90	2.09	E , G , ν , $\theta_{\text{D}}^{\text{c}}$
Mg2Si-05	Mechanical mortar and pestle	Disc	12.54 dia 3.41 ht	0.88	2.08	H , K_{IC}^{a}
Mg2Si-11	Mechanical mortar and pestle	Parallelepiped	11.45 x 14.86 x 3.31	1.18	2.09	E , G , ν , $\theta_{\text{D}}^{\text{c}}$
Mg2Si-12	Mechanical mortar and pestle	Parallelepiped	11.36 x 15.06 x 3.01	1.07	2.07	E , G , ν , $\theta_{\text{D}}^{\text{c}}$

^a Measured using Vicker’s indentations, ^b Slow crack growth monitored using this specimen, ^c Measured using RUS

4.2 Experimental procedure

Mg₂Si (99.99% metals basis purity), purchased from Alfa Aesar (45518, Ward Hill, MA), was reduced in size using a mechanical mortar and pestle and planetary milling (Table 4.1). Further details of the powder processing are presented elsewhere [Ni 2010]. The powders were densified using pulsed electronic sintering (PECS) at 1073 K for 5 min and 50 MPa pressure (Fig. 4.1) in argon.

The grain size was measured using the linear intercept technique with a stereographic projection factor of 1.5 [Underwood 1968; Case 1981]. All of the grain size analysis on the Mg₂Si specimens was performed on micrographs of fractured surfaces taken in the secondary electron mode on a scanning electron microscope (SEM). The elastic moduli (Table 4.1) were calculated using a dynamic method, resonant ultrasound spectroscopy (RUS), and commercially available software. Additional details of the RUS elasticity technique are provided elsewhere [Ni 2010; Ren 2009].

The Vickers hardness, H , and fracture toughness, K_{IC} , were determined using Vickers indentations with loads ranging from 2.94 N to 9.81 N. H was calculated by [Wachtman 2009]

$$H = \frac{1.8544P}{(2a)^2} \quad (1)$$

where P is the indenter load and $2a$ is the length of the indentation diagonal. K_{IC} was estimated from [Wachtman 2009]

$$K_{IC} = \xi \frac{(E/H)^{1/2}P}{c^{3/2}} \quad (2)$$

where E is the Young's modulus calculated using RUS, c is the radial crack length extending from the center of a Vickers indentation, and ξ is a dimensionless constant assumed to be 0.016 [Wachtman 2009].

The Vickers indentation was performed by a Buehler indenter (Buehler Semimacro Indenter, Lake Bluff, IL) and a Shimadzu hardness tester (Shimadzu HMV-2000, Kyoto, Japan). Each indenter was calibrated using a steel calibration block with H of 7.75 GPa (761-048; Yamamoto Scientific Tools Lab, Co LTD, Japan). For both the hardness calibration and for each Vickers indentation performed on the Mg_2Si specimens in this study, a load time of 5 s and a loading speed of 70 $\mu\text{m/s}$ were used. Also, both the calibration block and the Mg_2Si specimens were indented at loads of 2.95 N, 4.90 N, and 9.81 N, with 10 indentations performed for each load on a given specimen. The radial crack length and the diagonal length of the indentation impression were measured optically using the movable filars on the Buehler and Shimadzu indentation machines.

To compare the hardness results obtained from the Buehler and Shimadzu indentation machines, a Mg_2Si specimen was indented 10 times at each load of 2.95 N and 4.90 N by each machine at a load time of 5 s and a loading speed of 70 $\mu\text{m/s}$.

Possible slow crack growth was monitored using radial cracks induced by Vickers indentation at 2.94 N load. The radial cracks were measured at intervals between 1 min and 3 days after indentation. During the slow crack growth study, the room temperature and relative humidity ranged between 23.2°C and 24.3°C and 46% and 51%, respectively.

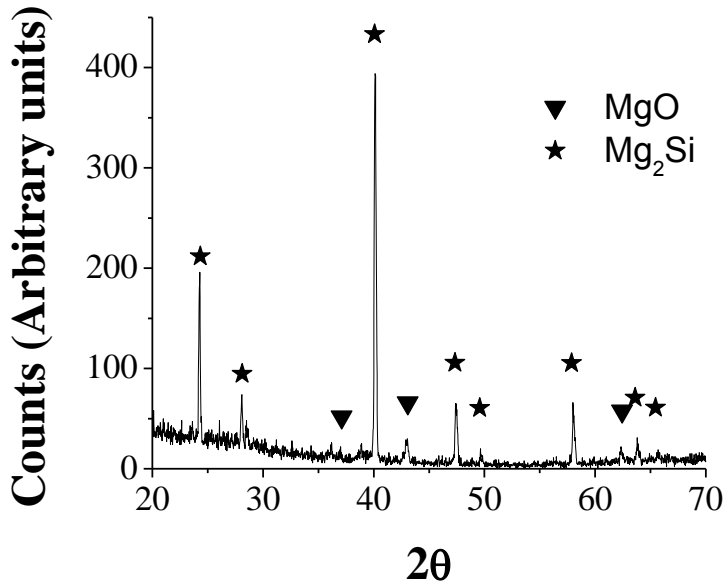


Figure 4.2. X-ray diffraction of planetary-milled Mg_2Si powder with peaks compared with the literature for MgO [Hazen 1976] and Mg_2Si [Owen 1923].

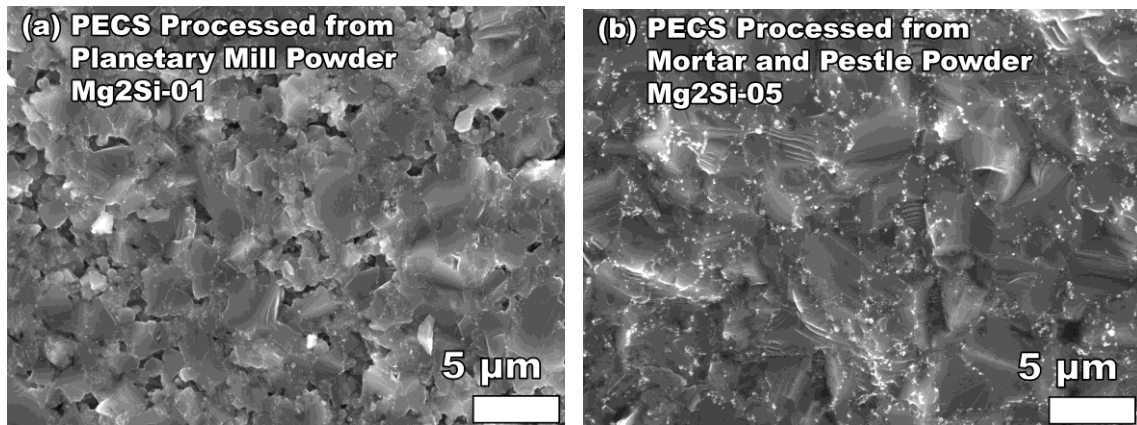


Figure 4.3. Fractured surface of specimens (a) Mg_2Si -01 and (b) Mg_2Si -05, PECS processed from planetary mill and mechanical mortar and pestle Mg_2Si powder, respectively. Cleavage steps show mixed-mode fracture, with both intergranular and transgranular fracture present. Entrapped pores visible at grain boundaries were approximately $1\ \mu\text{m}$ to $3\ \mu\text{m}$ diameter with polygonal shape. The dark areas between grains are porosity within the specimens, typically around $1\ \mu\text{m}$ or less in diameter

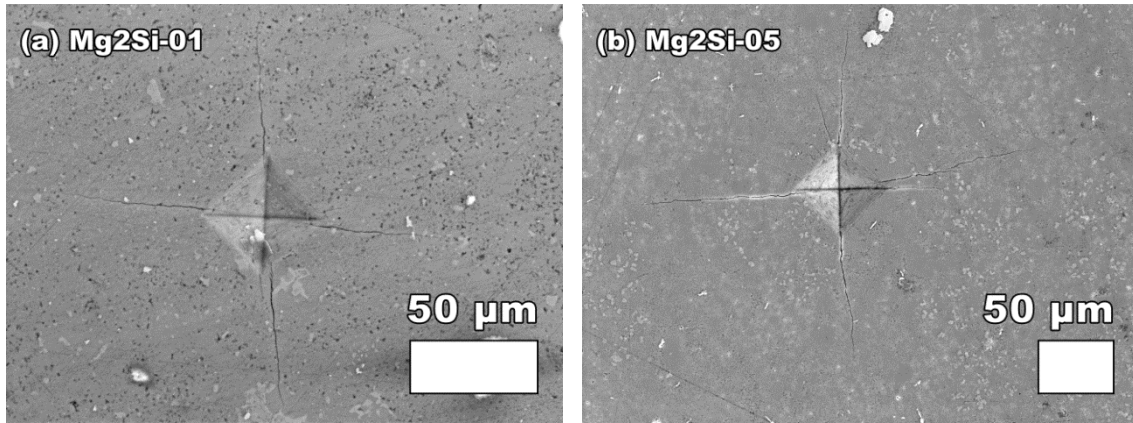


Figure 4.4. Typical Vickers indentation crack systems for specimens Mg₂Si-01 and Mg₂Si-05, which display indentation impressions, little chipping or spalling, and a fully developed radial crack system.

Table 4.2. The density, Young's modulus, E, shear modulus, G, Poisson's ratio, ν , and Debye temperature, θ_D , from this study compared with the literature. The moduli were determined using resonant ultrasound spectroscopy, RUS, first principle calculation, FPC, resonance technique, RT, and compression.

Reference	Density (g/cm ³)	Modulus Measurement Method	E (GPa)	G (GPa)	ν	θ_D (K)
This Study (Mg ₂ Si-03)	2.09	RUS	117.2 ± 0.2	49.53 ± 0.04	0.183 ± 0.001	585 ^a
This Study (Mg ₂ Si-11)	2.09	RUS	117.7 ± 0.2	50.09 ± 0.05	0.175 ± 0.001	588 ^a
This Study (Mg ₂ Si-12)	2.07	RUS	116.9 ± 0.5	48.92 ± 0.13	0.195 ± 0.001	583 ^a
[Zhang 2009]	1.98 ^b	FPC	115.6	49.50	0.17	N/A
[Tani 2008]	2.04 ^b	FPC	113.5	49.2	0.161	432
[Whitten 1965]	2.00	RT	110.9 ^c	47.6 ^c	0.165 ^c	578 _d
[Milekhine 2002]	1.94 ^e	Compression	76 ± 6	N/A	N/A	N/A

N/A Not available, ^a Acoustic Debye temperature, ^b Density calculated from the given lattice parameter, ^c From the average of Hashin and Shtrikman bounds at 300 K [Simmons 1971], ^d Debye temperature at 0 K, ^e Density estimated by 3% porosity and 2.00 g/cc porosity free density

4.3 Results and Discussion

In this study, the Mg₂Si specimens had a mean mass density of 2.07 g/cm³, calculated from the measured mass and dimensions (Table 4.1). Single-crystal Mg₂Si has mass density of 1.98 g/cm³ and 2.00 g/cm³ [Zhang 2009; Whitten 1965]. X-ray diffraction determined that an MgO phase [Hazen 1976] was present in the Mg₂Si powder [Owen 1923] used to fabricate the specimens (Fig. 4.2), which may account for the increase in density for the PECS Mg₂Si specimens in this study. The grain size was 2.4 μm (Fig. 4.3a) and 3.9 μm (Fig. 4.3b) for the specimens fabricated using powder reduced by the planetary mill and mortar and pestle, respectively. Based on SEM micrographs of the specimens (Figs. 4.3, 4.4), we estimate volume fraction porosity to be 0.05 or less, and a resulting approximate volume fraction of 0.89 ± 0.03 Mg₂Si and 0.08 ± 0.03 MgO to account for the measured mass density.

In this study, the mean values of the measured elastic moduli for Mg₂Si were 117.3 GPa for Young's modulus, E , 49.5 GPa for shear modulus, G , and 0.184 for Poisson's ratio, ν . In the literature, E ranged from 110.9 GPa to 115.6 GPa, [Zhang 2009; Whitten 1965; Simmons 1971; Tani 2008] which was comparable to this study's mean E of 117.3 GPa. The exception was Milekhine et al., who reported an E of 76 GPa; however, Milekhine et al. recognized that their Young's modulus value was not consistent with literature [Milekhine 2002] (Table 4.2). For comparison with other TE materials, E values include CoSb₃ at 140.6 GPa [Schmidt 2010] and PbTe-PbS 8% at 53.1 GPa [Ni 2010].

The calibration factors from 10 indentations at each load for the Shimadzu were 0.98, 0.96, and 0.98 at 2.95 N, 4.90 N, and 9.81 N loads, respectively, and for the Buehler

were 1.10, 1.10, and 1.03 at the same loads. The calibration factor was multiplied by the uncorrected H value for the reported H values in this study.

For indentation loads of 2.95 N, 4.90 N, and 9.81 N, the Vickers hardness, H , in this study ranged from 4.8 ± 0.3 GPa to 5.6 ± 0.2 GPa. Over this relatively restricted load range, no load dependence of H was observed. Also, based on the mean and standard deviation of the measured H using the Shimadzu and Buehler indenters, there was no statistically significant difference in the H values measured, although the measured H was different from literature values [Milekhine 2002; Li 1993] (Table 4.3). The average hardness of 5.1 GPa for the PECS-processed specimens in this study was higher than the range of 3.96 GPa to 4.38 GPa for cast specimens in the literature [Milekhine 2002; Li 1993] (Table 4.3).

In general, hardness increases with decreasing grain size [Ni 2010; Lawn 1993; Barsoum 2003]. The grain sizes of the cast specimens included in their studies were not given by Milekhine et al. [Milekhine 2002] and Li et al. [Li 1993]. However, grain sizes for cast specimens are often greater than 500 μm [Ni 2010; Ren 2008], which is significantly larger than the roughly 33 μm or smaller Vickers impression dimensions reported by Milekhine et al. [Milekhine 2002]. The likely grain size for the cast specimens is also much larger than the average grain sizes of 2.4 μm for the Mg_2Si -01 and 3.9 μm for the Mg_2Si -05 specimen included in this study. The narrow range of grain sizes (2.4 μm to 3.9 μm) makes it extremely unlikely that an H dependence on grain size would be observed for the specimens included in this study. However, the H value of 5.1 GPa for this study is expected to be higher than the H values of 3.96 GPa to 4.38 GPa measured for cast specimens [Milekhine 2002; Li 1993], since the cast specimens likely

Table 4.3. A comparisons of Vickers hardness, H , and fracture toughness, K_{IC} , from this study to the literature. For the PECS processed specimens in this study, the H and K_{IC} was determined using at least 10 indentations per load with one standard deviation reported as error. For cast specimens in literature, Milekhine et al. measured at least 10 indentations per load [Milekhine 2002] and Li et al. measured 5 indentations [Li 1993].

Reference	Grain Size (μm)	Mechanical Property	Load			
			0.981 N	2.94 N	4.90 N	9.81 N
This Study (Mg2Si-01)	2.4	H (GPa)	N/A	5.4 ± 0.2^a 5.0 ± 0.3^b	5.6 ± 0.2^a 5.0 ± 0.1^b	5.4 ± 0.2^a
		K_{IC} ($\text{MPa}\cdot\text{m}^{1/2}$)		1.2 ± 0.2^b	1.3 ± 0.3^b	1.3 ± 0.5^b
This Study (Mg2Si-05)	3.9	H (GPa)	N/A	4.8 ± 0.2^b	4.8 ± 0.2^b	5.0 ± 0.2^a
		K_{IC} ($\text{MPa}\cdot\text{m}^{1/2}$)		0.7 ± 0.2^b	1.1 ± 0.2^b	0.9 ± 0.1^b
[Milekhine 2002]	N/A	H (GPa)	N/A	3.96	4.05	4.20
		K_{IC} ($\text{MPa}\cdot\text{m}^{1/2}$)		0.88	0.81	0.74
[Li 1993]	N/A	H (GPa)	4.38 ± 0.07	N/A	N/A	N/A
		K_{IC} ($\text{MPa}\cdot\text{m}^{1/2}$)	N/A			

^aUsing a Buehler indenter

^bUsing a Shimadzu indenter

N/A = not available

have much larger grain sizes. For other TE materials, the Vickers hardness is 1.10 GPa to 1.28 GPa for PbTe-PbS8% when powder processed [Ni 2010], 0.51 GPa to 1.2 GPa for lead-antimony- silver-tellurium (LAST) [Ren 2008], and 5.7 GPa for $\text{MM}_{0.7}\text{Fe}_3\text{CoSb}_{12}$ (where MM denotes mischmetal) [Zhang 2010].

Fracture toughness, K_{IC} , by Vickers indentation (Fig. 4.4) was $0.7 \pm 0.2 \text{ MPa m}^{1/2}$ to $1.3 \pm 0.5 \text{ MPa m}^{1/2}$ for indentation loads from 2.94 N to 9.81 N (Table 4.3). Milekhine et al. reported K_{IC} values ranging from $0.81 \text{ MPa m}^{1/2}$ to $0.97 \text{ MPa m}^{1/2}$ measured by indentation fracture [Milekhine 2002]. However, Milekhine et al. used their measured E and H values (Tables 4.2 and 4.3) to calculate K_{IC} , and their E and H values are lower than the E and H values found in this study and in the literature (Tables 4.2 and 4.3). Using the crack length, c , reported by Milekhine et al. and the E and H values from this study (117 GPa and 5.1 GPa, respectively), the recalculated values for Milekhine et al.'s K_{IC} values would be $0.8 \text{ MPa m}^{1/2}$, $0.9 \text{ MPa m}^{1/2}$, and $1.1 \text{ MPa m}^{1/2}$ using Eq. 2, which are in better agreement with the data from this study (Table 4.3). The K_{IC} values of other thermoelectric materials include $1.12 \text{ MPa m}^{1/2}$ to $1.35 \text{ MPa m}^{1/2}$ for Bi_2Te_3 [Zhao 2008], $0.35 \text{ MPa m}^{1/2}$ for PbTe-PbS 8% [Ni 2010], and $0.34 \text{ MPa m}^{1/2}$ for LAST [Ren 2008].

The radial crack length was measured on six indentations of specimen Mg2Si-01. Slow crack growth was not observed when examining the average length of the two radial cracks per indentation (Fig. 4.4) as a function of time for six indentations for a period of days (Fig. 4.5). Two indentations had a crack pop-in within the first 5 min after indentation, which was not considered slow crack growth. The mean and standard deviation of the radial crack length measurement versus time are shown in Fig. 4.5 and Table 4.4, indicating that there was no statistically significant slow crack growth that

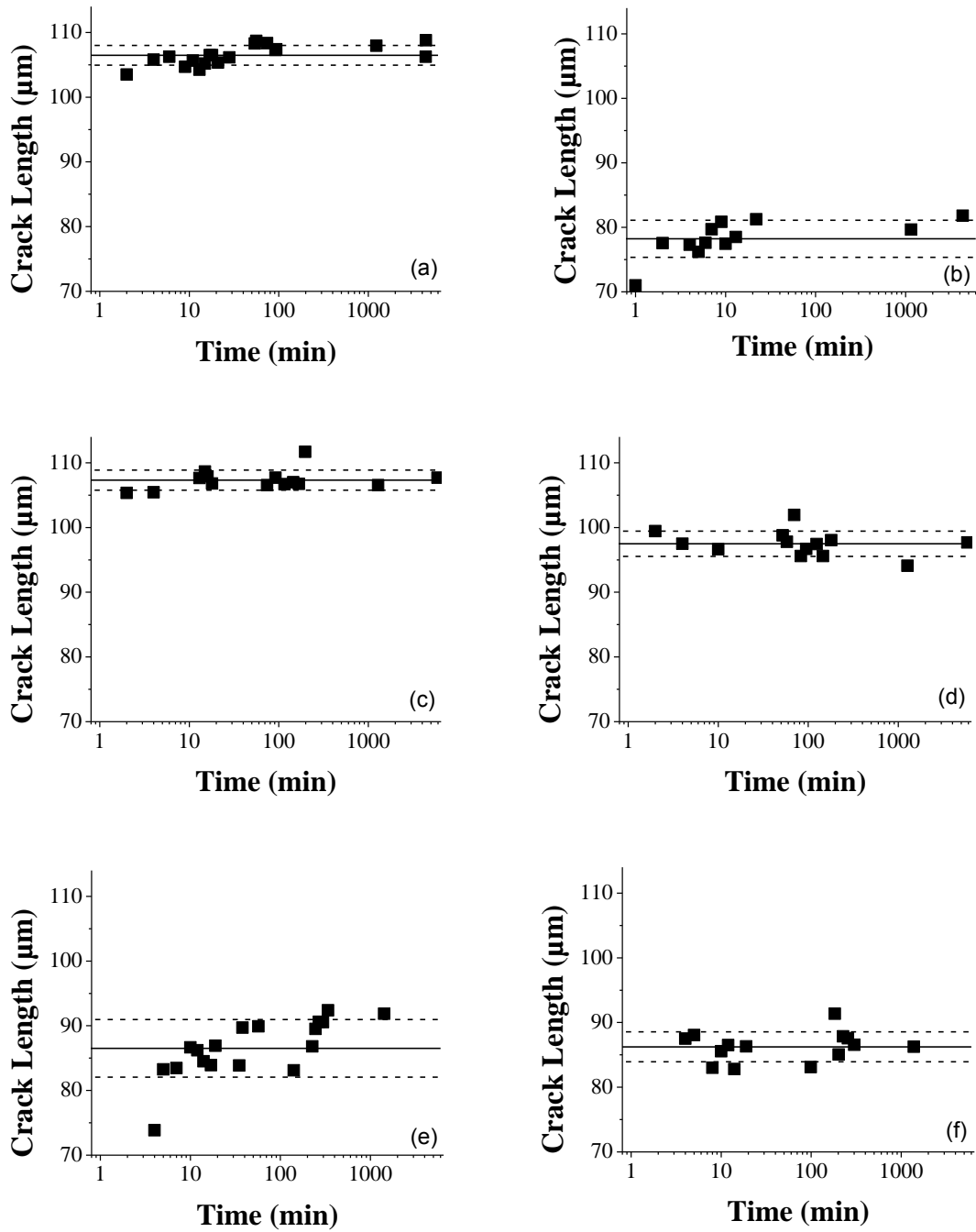


Figure 4.5. For specimen Mg2Si-01, plots of radial crack length versus time for six Vickers indentation crack systems loaded at 2.94 N. In figures (b) and (e), a radial crack popped in within 1 min to 5 min following the initial indentation event. The average crack length and one standard deviation variation is indicated by solid and dashed lines, respectively, for each indentation crack. The crack length may vary significantly between indentations, resulting in the uncertainties in the reported K_{IC} values in Table 4.3.

Table 4.4. No significant slow crack growth occurred for the six Vickers indentation cracks listed below for specimen Mg₂Si-01, where the radial crack lengths were monitored for up to 3 days (Fig. 4.5). For the radial crack length measurements performed over the entire time range, the measured crack lengths did not depart significantly from the mean length of each crack, as indicated by the coefficient of variation (CV, standard deviation/mean), where CV ranges from about 1.4% to 5%.

Indent identification	Mean crack length (μm)	Standard deviation (μm)	Coefficient of variation (CV)
Mg ₂ Si-01 (a)	106.5	1.5	0.014
Mg ₂ Si-01 (b)	78.2	2.9	0.037
Mg ₂ Si-01 (c)	107.3	1.6	0.014
Mg ₂ Si-01 (d)	97.5	2.0	0.020
Mg ₂ Si-01 (e)	86.5	4.5	0.051
Mg ₂ Si-01 (f)	86.2	2.3	0.027

occurred for Mg₂Si for times up to 3 days (Fig. 4.5). There was no pattern of crack length growth with time outside of one standard deviation (Fig. 4.5). Differences in crack length between Figs. 4.5a–f are based on the individual indentations. With no pattern of crack length change with time, any variation in length measurements (Table 4.4) for an indentation may be attributed to the error of the optical measurement technique.

4.4 Conclusions

The elastic moduli, hardness, fracture toughness, and slow crack growth were measured on powder-processed and PECS-sintered specimens of Mg₂Si. The average E of 117.3 GPa, H of 5.3 GPa, and K_{IC} of 1.3 MPa m^{1/2} obtained in this study agree well with the literature (Tables 4.2 and 4.3).

No examination of the susceptibility of Mg₂Si to slow crack growth has appeared in the literature prior to this study. In spite of a known reaction with water [Aesar], this reaction did not drive slow crack growth for the radial cracks observed in this study. The lack of significant slow crack growth is beneficial to the development and fabrication of Mg₂Si, as microcracks induced by cutting or grinding during fabrication would not be expected to grow under normal atmospheric conditions.

Mg₂Si has several advantages as a potential thermoelectric material. It has low mass density and contains only nontoxic, inexpensive, and readily available elements. Thus, Mg₂Si is a very viable candidate for widespread application as a thermoelectric material.

ACKNOWLEDGEMENTS

The authors acknowledge the financial support of the Department of Energy, “Revolutionary Materials for Solid State Energy Conversion Center,” an Energy

Frontiers Research Center funded by the US Department of Energy, Office of Basic Energy Sciences under Award Number DE-SC0001054. Jennifer Ni (under the Office of Naval Research Grant N00014-08-1-0613) assisted with the scanning electron microscopy of the specimen surfaces and assisted Jesse Giles with the hardness measurements. Financial support for Mr. Giles was provided through the Michigan Louis Stokes Alliance for Minority Participation (MI-LSAMP) Summer Undergraduate Research Academy (SURA), which was hosted in collaboration with the Michigan State University Summer Research Opportunity Program (MSU SROP).

REFERENCES

REFERENCES

- [Aesar] Aesar, A. Material Safety Data Sheet, Magnesium Silicide.
<http://www.alfa.com/content/msds/USA/45518.pdf>.
- [Barsoum 2003] Barsoum, M.W. *Fundamentals of Ceramics*. Taylor & Francis Group, New York, 2003.
- [Case, Smyth, Hunter 1981] Case, E.D., Smyth, J.R., Hunter, O. Microcracking in Large-grain Al₂O₃. *51* (1981) 175–179.
- [Connally, Brown 1992] Connally, J.A., Brown, S.B. Slow crack growth in single-crystal silicon. *Science* 256 (1992) 1537–9.
- [Freiman, Wiederhorn, Mecholsky 2009] Freiman, S.W., Wiederhorn, S.M., Mecholsky, J.J. Environmentally Enhanced Fracture of Glass: A Historical Perspective. *Journal of the American Ceramic Society* 92 (2009) 1371–1382.
- [Hazen 1976] Hazen, R. Effects of temperature and pressure on the cell dimension and X-ray temperature factors of periclase. *American Mineralogist* 61 (1976) 266–271.
- [Lawn 1993] Lawn, B.R. *Fracture of Brittle Solids*. Cambridge University Press, New York, 1993.
- [Li, Gill, Varin 1993] Li, G., Gill, H., Varin, R. Magnesium silicide intermetallic alloys. *Metallurgical transactions A* 24 (1993) 2383–2391.
- [Mars, Ihou-Mouko, Pont, Tobola, Scherrer 2009] Mars, K., Ihou-Mouko, H., Pont, G., Tobola, J., Scherrer, H. Thermoelectric Properties and Electronic Structure of Bi- and Ag-Doped Mg₂Si_{1-x}Ge_x Compounds. *Journal of Electronic Materials* 38 (2009) 1360–1364.
- [Michalsky, Freiman 1983] Michalsky, T.A., Freiman, S.W. A Molecular Mechanism for Stress Corrosion in Vitreous Silica. *Journal of the American Ceramic Society* 66 (1983) 284–288.
- [Milekhine, Onsøyen, Solberg, Skaland 2002] Milekhine, V., Onsøyen, M.I., Solberg, J.K., Skaland, T. Mechanical properties of FeSi (e), FeSi₂ (za) and Mg₂Si. *Intermetallics* 10 (2002) 743–750.
- [Ni, Case, Khabir, Stewart, Wu, Hogan, Timm, Girard, Kanatzidis 2010] Ni, J.E., Case, E.D., Khabir, K.N., Stewart, R.C., Wu, C.-I., Hogan, T.P., Timm, E.J., Girard, S.N., Kanatzidis, M.G. Room temperature Young's modulus, shear modulus, Poisson's

ratio and hardness of PbTe–PbS thermoelectric materials. *Materials Science and Engineering: B* 170 (2010) 58–66.

- [Owen, Preston 1923] Owen, E.A., Preston, G.D. The atomic structure of two intermetallic compounds. *Proceedings of the Physical Society of London* 36 (1923) 341–348.
- [Ren, Case, Ni, Timm, Lara-Curzio, Trejo, Lin, Kanatzidis 2009] Ren, F., Case, E.D., Ni, J.E., Timm, E.J., Lara-Curzio, E., Trejo, R.M., Lin, C.-H., Kanatzidis, M.G. Temperature-dependent elastic moduli of lead telluride-based thermoelectric materials. *Philosophical Magazine* 89 (2009) 143–167.
- [Ren, Hall, Ni, Case, Sootsman, Mercouri 2008] Ren, F., Hall, B.D., Ni, J.E., Case, E.D., Sootsman, J., Mercouri, G. Mechanical Characterization of PbTe-based Thermoelectric Materials. *1044* (2008) .
- [Schmidt, Ni, Case, Sakamoto, Kleinow, Wing, Stewart, Timm 2010] Schmidt, R.D., Ni, J.E., Case, E.D., Sakamoto, J.S., Kleinow, D.C., Wing, B.L., Stewart, R.C., Timm, E.J. Room temperature Young's modulus, shear modulus, and Poisson's ratio of $\text{Ce}_{0.9}\text{Fe}_{3.5}\text{Co}_{0.5}\text{Sb}_{12}$ and $\text{Co}_{0.95}\text{Pd}_{0.05}\text{Te}_{0.05}\text{Sb}_3$ skutterudite materials. *Journal of Alloys and Compounds* 504 (2010) 303–309.
- [Simmons, Wang 1971] Simmons, G., Wang, H. *Single Crystal Elastic Constants and Calculated Aggregate Properties: A Handbook*. The M.I.T. Press, Cambridge, Massachusetts, 1971.
- [Tani, Kido 2008] Tani, J., Kido, H. Lattice dynamics of Mg_2Si and Mg_2Ge compounds from first-principles calculations. *Computational Materials Science* 42 (2008) 531–536.
- [Underwood, Colcord, Waugh 1968] Underwood, E.E., Colcord, A.R., Waugh, R.C. *Ceramic Microstructures*. Wiley, New York, 1968.
- [Wachtman, Cannon, Matthewson 2009] Wachtman, J.B., Cannon, W.R., Matthewson, M.J. *Mechanical Properties of Ceramics*. Wiley-Vch, Hoboken, N.J., 2009.
- [West, Hench 1998] West, J.K., Hench, L.L. The effect of environment on silica fracture: Vacuum, carbon monoxide, water and nitrogen. *Philosophical Magazine A* 77 (1998) 85–113.
- [Whitten, Chung, Danielson 1965] Whitten, W., Chung, P., Danielson, G. Elastic constants and lattice vibration frequencies of Mg_2Si . *Journal of Physics and Chemistry of Solids* 26 (1965) 49–56.

- [Wiederhorn 1968] Wiederhorn, S. Moisture assisted crack growth in ceramics. *International Journal of Fracture Mechanics* 4 (1968) 171–177.
- [Zhang, Han, Yan, Wang, Xia, Xu 2009] Zhang, C., Han, P., Yan, X., Wang, C., Xia, L., Xu, B. First-principles study of typical precipitates in creep resistant magnesium alloys. *Journal of Physics D: Applied Physics* 42 (2009) 125403.
- [Zhang, Rogl, Grytsiv, Puchegger, Koppensteiner, Spieckermann, Kabelka, Reinecker, Rogl, Schranz, Zehetbauer, Carpenter 2010] Zhang, L., Rogl, G., Grytsiv, A., Puchegger, S., Koppensteiner, J., Spieckermann, F., Kabelka, H., Reinecker, M., Rogl, P., Schranz, W., Zehetbauer, M., Carpenter, M.A. Mechanical properties of filled antimonide skutterudites. *Materials Science and Engineering: B* 170 (2010) 26–31.
- [Zhao, Zhang, Li, Zhou, Liu, Liu 2008] Zhao, L.-D., Zhang, B.-P., Li, J.-F., Zhou, M., Liu, W.-S., Liu, J. Thermoelectric and mechanical properties of nano-SiC-dispersed Bi₂Te₃ fabricated by mechanical alloying and spark plasma sintering. *Journal of Alloys and Compounds* 455 (2008) 259–264.

5 Mechanical properties of Mg₂Si thermoelectric materials with the addition of 0 to 4 volume percent silicon carbide nanoparticles (SiC_{NP})

Robert D. Schmidt, Xiaofeng Fan, Eldon D. Case,

Chemical Engineering and Materials Science Department,
Michigan State University, East Lansing, MI, 48824

To be submitted to: Journal of Materials Science

Abstract

For thermoelectric generators, the individual thermoelectric elements are subjected to a significant stresses under in-service conditions, due to thermal cycles, transients and gradients, as well as thermal expansion mismatch and externally applied mechanical stresses. Most thermoelectric (TE) materials are brittle and with low fracture toughness, typically no more than $1.5 \text{ MPa m}^{1/2}$ and often less than $0.5 \text{ MPa m}^{1/2}$. The combination of the stresses encountered in the device application environment and the materials' low fracture toughness constitute a severe challenge to the viability of thermoelectric generators. The addition of silicon carbide nanoparticles (SiC_{NP}) may provide a route to improving the fracture toughness for a wide range of thermoelectric materials. This study examines the mechanical properties, including elastic modulus, hardness and fracture toughness for 0 to 4 vol.% SiC_{NP} incorporated into Mg₂Si thermoelectric matrices.

5.1 Background

Thermoelectric (TE) materials for solid state energy conversion have been extensively investigated in recent years, with the potential to recapture energy from waste

heat sources. Typically, the efficiency of a material is measured by use of the dimensionless figure of merit, ZT ,

$$ZT = \frac{S^2 \sigma}{\kappa} T \quad (1)$$

where S is the Seebeck coefficient, σ is the electrical conductivity, κ is the thermal conductivity, and T is temperature.

Thermoelectric generators, particularly when used in waste heat applications, are subjected to multiple sources of stress, including stresses due to thermal gradients, thermal shock, thermal expansion mismatch between materials, and externally applied stresses. Waste heat applications typically involve a heat source, such as exhaust from an engine. Automotive engines are typically run with several accelerations or decelerations, and the waste heat produced will likewise involve several thermal cycles during operation. The waste heat source therefore is a source with thermal transients, thermal shock, and thermal gradients, which produce stresses in the TE material. These stresses require a detailed knowledge of the mechanical properties of the material to understand the material response to the stress, particularly the elastic properties and the fracture toughness. The elastic moduli are necessary to understanding the mechanical response to stresses, including stresses that cause fracture and the calculation of fracture toughness.

In addition, stresses and flaws resulting from the manufacturing processes, such as scratches and surface microcracks during cutting or grinding, may result in fracture. A typical TE module has tens to hundreds of legs, all thermally in parallel, but electrically in series, creating a condition where each leg is subjected to the full thermal cycle, but the failure in any one leg of the TE material electrically breaks the circuit and renders an

entire module of a generator inoperable. Therefore, an understanding and control of the mechanical response and failure of the TE materials is critical to the reliable operation of a TE generator.

The fracture toughness, K_C , of thermoelectric materials is typically very low, less than $1.5 \text{ MPa m}^{1/2}$, and often less than $0.5 \text{ MPa m}^{1/2}$ [Schmidt 2012; Eilertsen 2013; Ren 2008; Ni 2010]. For comparison, window glass has a fracture toughness of about $0.75 \text{ MPa m}^{1/2}$ [Wiederhorn 1969]. Adding particles such as silicon carbide nanoparticles (SiC_{NP}) may improve the fracture toughness for a wide range of TE materials.

Fracture toughness may be increased by the incorporation of second phases, additions such as particles or whiskers, microstructural changes or other mechanisms. For the purposes of this study, these may be grouped into intrinsic or extrinsic toughening mechanisms [Launey 2009]. Intrinsic mechanisms (such as crack blunting or crack deflection) change the fracture toughness by acting on the area ahead of the crack tip, by distributing the load, changing the interface properties, or other methods to “increase the microstructural resistance” of the material [Launey 2009]. Extrinsic mechanisms (such as fiber or grain bridging) work on the area behind the crack tip, redistributing the force to reduce the force acting at the crack tip [Launey 2009]. These differences have important implications in the potential for improving the fracture toughness overall, and specific implications for materials under fatigue conditions such as thermal cycling.

Extrinsic mechanisms may, for a few cycles, significantly improve fracture toughness. For example, in alumina the addition of 20% SiC whiskers increased K_C by a multiple of 3 [Becher 1991], and additions of 20% and 40% tetragonal zirconia increased

K_C by a multiple of 3 and 5, respectively [Becher 1991]. Similar increases were observed in glass and mullite [Becher 1991].

These extrinsic toughening methods, however, are not desirable in a fatigue condition [Ritchie 1999; Launey 2009; Case 2012a; Case 2012b] and can be destructive to the material [Lathabai 1991; Bhowmick 2007; Bhowmick 2009]. Bridging, for example, has been observed to be defeated by fatigue and can even be destructive in alumina [Knehans 1982; Lathabai 1991] and silicon [Bhowmick 2009]. When a bridge is defeated, the debris may fall into the crack and act as a wedge and extend the crack.

Intrinsic toughening mechanisms, including crack deflection, crack blunting, crack branching or bowing, are not defeated by thermal fatigue [Launey 2009]. Therefore, intrinsic toughening mechanisms acting ahead of the crack tip are the desired type of toughening in fatigue [Launey 2009; Case 2012a; Case 2012b] as would be the case for a TE device in waste heat recovery that is subjected to multiple thermal cycles.

The addition of nanoparticles can lead to intrinsic toughening. However, compared to large increases in K_C that are possible with extrinsic toughening, intrinsic toughening offers smaller but significant increases in K_C (Table 5.1). In alumina, additions of 5-20% SiC nanoparticles increases the relative K_C by a factor of 1.16 [Perez-Rigueiro 1998; Parchovianský 2013]. In Bi_2Te_3 , a TE material, additions of 0.1 to 0.5 vol% SiC nanoparticles increased relative K_C by a factor of 1.18 [Zhao 2008].

Mg_2Si may be used to examine several toughening mechanisms. Literature values of ZT show Mg_2Si to be a good TE material (Table 5.2), with ZT of 0.86 at 862 K for ($\text{Mg}_2\text{Si}:\text{Bi} = 1:0.02$) [Tani 2005] and 0.97 at 873 K for 0.5 at.% Sb doped $\text{Mg}_2\text{Si} + 5$ wt.% Ni [Hayatsu 2012]. With values of ZT from 0.23 to 0.97 when doped with 2% or less

Table 5.1. The fracture toughness, K_{IC} , has been improved in brittle materials, including the thermoelectric Bi_2Te_3 , by the addition of SiC nanoparticles.

Matrix material	K_{IC} ($\text{MPa}\cdot\text{m}^{1/2}$)	SiC addition	K_{IC} ($\text{MPa}\cdot\text{m}^{1/2}$)	Relative change	Reference
Bi_2Te_3	1.14	0.1 vol % 0.5 vol % 1.0 vol %	1.35 1.33 1.19	1.18 1.17 1.04	[Zhao 2008]
Al_2O_3	3.7 to 3.8 ^a 3.0 to 3.3 ^b	5 vol. % ^a 20 vol. % ^a 5 vol. % ^b 20 vol. % ^b	3.6 3.4 to 3.6 3.6 3.5 to 3.7	0.96 ^a 0.93 ^a 1.14 ^b 1.14 ^b	[Pérez-Rigueiro 1988]
Al_2O_3	5.0 ± 0.3	5 vol. % 10 vol. % 15 vol. % 20 vol. %	5.4 to 5.6 5.6 to 6.0 5.2 to 5.3 5.1 to 5.3	1.10 1.16 1.05 1.04	[Parchovianský 2013]

^a Specimen tested by single-edged notched beam

^b Specimen tested by Vickers indentation

Table 5.2. Doped Mg_2Si -based thermoelectric materials with ZT near 1 have been reported. These reasonable ZT values for a thermoelectric material support the use of Mg_2Si as a model system.

Composition	Maximum ZT	Temperature for maximum ZT (K)	Reference
$\text{Mg}_2\text{Si}:\text{Bi} = 1:0.02$	0.86	862	[Tani 2005]
$\text{Mg}_2\text{Si}:\text{Sb} = 1:0.005$ + 5 wt.% Ni	0.97	873	[Hayatsu 2012]
$\text{Mg}_2\text{Si}_{0.9}\text{Sn}_{0.1}:\text{Al} = 1:0.02$	0.68	864	[Tani 2008]
$\text{Mg}_2\text{Si}:\text{Y} = 1:0.006$ (2000 ppm of Y)	0.23	600	[Meng 2011]
$\text{Mg}_2\text{Si}:\text{Mg}_2\text{Pb} = 1:0.02$	0.56	873	[Muthiah 2013]
$\text{Mg}_2\text{Si}:\text{Sb} = 1:0.02$	0.56	862	[Tani 2007]

of dopant [Tani 2005; Hayatsu 2012; Tani 2008; Meng 2011; Muthiah 2013; Tani 2007], Mg_2Si may be used as a suitable TE system to test additions of SiC_{NP} .

As reported on the MSDS, Mg_2Si reacts with water [Aesar], which requires handling without water or water-based solutions. However, this reaction is not a problem for crack growth and mechanical integrity when the material is handled in dry air [Schmidt 2012]. Mg_2Si is a suitable material for examination of fracture properties by Vickers indentation [Schmidt 2012].

To understand the mechanical response to the stresses, as well as the potential for fracture, the mechanical properties of the TE material must be not only understood, but optimized to properly withstand the thermal fatigue environment typical of many thermoelectric generator applications.

5.2 Experimental Procedure

In this study, silicon carbide nanoparticles, SiC_{NP} , were added to Mg_2Si powders which were then processed to produce Mg_2Si - SiC_{NP} composites.

5.2.1 Materials and Specimen Preparation

Powder was produced from lump Mg_2Si (45518, 3-12 mm pieces, Alfa Aesar, Ward Hill MA), ground and sieved through a 53 μm sieve, then milled by either (i) a planetary ball mill (PM) using an alumina-lined mill jar with 10 mm diameter alumina grinding media at 150 RPM for 3 h, or (ii) a vibratory mill (VM) with a WC lined jar, two 11.2 mm spheres and four 7.9 mm spheres, and a Viton gasket, sealed in the glove box with an additional layer of electrical tape. The PM processed Mg_2Si powders were milled in an argon-filled glove box and the VM processed powders were milled in a sealed, argon-filled jar.

Specimens were densified by pulsed electric current sintering (SPS Model 10-3, Thermal Technology LLC, Santa Rosa, CA) in a 12.7 mm diameter graphite die. Sintering was performed at 800°C and 50 MPa for 5 min, and with ramp rates of 100°C/min and 45 MPa/min.

5.2.2 Elasticity Measurements

Elastic moduli were measured by resonant ultrasound spectroscopy (RUS). In RUS, the specimen is placed on a tripod of transducers. One transducer was swept through a range of frequencies and the mechanical resonance frequencies are picked up by the other two transducers. The resonances were fit to a model for the geometry, mass and dimensions of the specimen to determine the elastic moduli. Additional details of the RUS procedure are provided elsewhere [Ni 2010; Schmidt 2010; Migliori 1997].

5.2.3 Hardness and toughness measurements

Prior to indentation, each specimen was mounted with thermoplastic (CrystalBond 509, EMS, Hatfield, PA) onto an aluminum stub, then polished with a series of diamond compounds with grit size from 35 μm to 1 μm . Cleaning of the specimen between polishing grit sizes was performed by hand with ethanol rather than water to lessen any surface reaction between the Mg_2Si and water [Aesar].

Hardness and fracture toughness for each of the specimens were measured by Vickers indentation. Vickers hardness, H , is calculated by the equation,

$$H = \zeta \frac{1.8544F}{(2a)^2} \quad (2)$$

where F is the indentation load, $2a$ is the diagonal impression length, and ζ is a correction factor, set at 0.95 to 0.97 based on indentations of a steel standard calibration block (Yamamoto Scientific Tools Lab Co. LTD, Chiba, Japan).

The fracture toughness, K_C , of a material may be estimated by measuring the radial crack length, c , of a Vickers indentation, by the equation,

$$K_C = \frac{\xi(E/H)^{1/2} P}{c^{3/2}} \quad (3)$$

where ξ is a dimensionless constant, set as 0.016, E is the Young's modulus, H is the hardness, and P is the applied load [Wachtman 2009].

5.2.4 Microscopy

The specimens were examined by scanning electron microscope (SEM) at a working distance of either 8 mm or 15 mm, and at an accelerating voltage of 15 kV (JEOL 6610LV or JSM-7500F, JEOL Ltd., Japan). The average grain size (GS) of each of the sintered specimens was determined using the linear intercept procedure (ASTM E112) with a minimum of 200 intercepts per image, and a stereographic projection factor of 1.5 [ASTM-Standard-E112-13 2014]. Surface details were examined with secondary electron imaging (SEI) and elemental contrasts were examined by backscatter electron imaging (BEI).

5.3 Results and Discussion

5.3.1 Microstructural analysis

Prior to sintering, both the PM and the VM powders were examined for size range and morphology. For the PM powder, there was a wide distribution from sub-micron

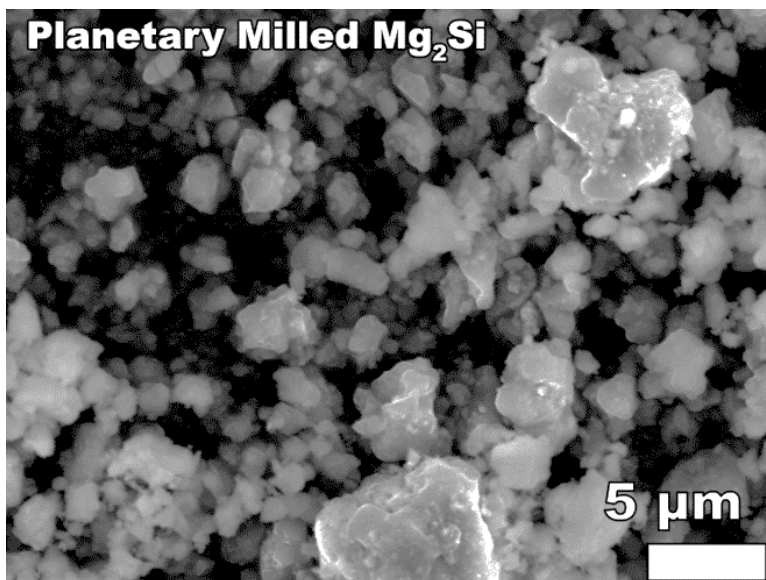


Figure 5.1. Planetary milled Mg_2Si powder exhibited typical particle sizes of sub-micron to 5 μm in SEM. The powder has a surface area of 4.4 m^2/g measured by BET, or approximately 0.7 μm average particle size.

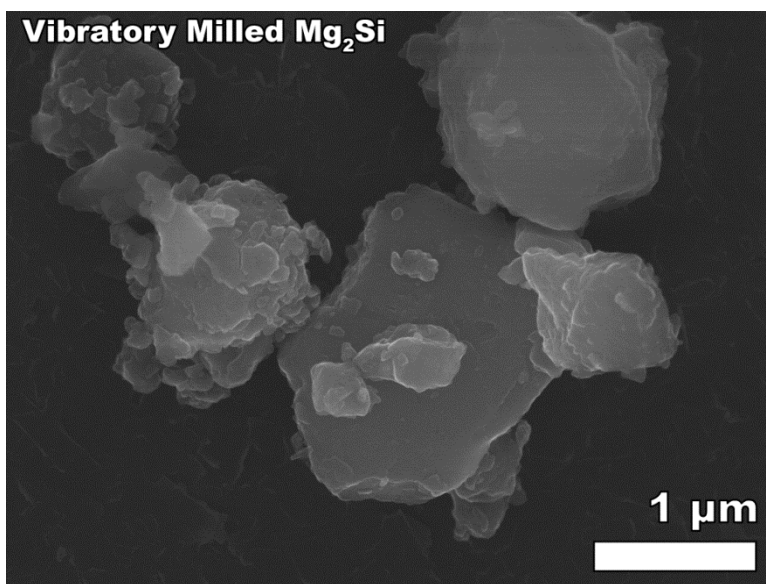


Figure 5.2. Vibratory milled Mg_2Si powder exhibited typical particle sizes of 0.2 μm to 2 μm in SEM.

particles to 5 μm particles or greater, average particle size by BET was 0.7 μm (Figure 5.1).

To incorporate SiC_{NP} with a vendor specified average particle size of 45-55 nm (44646, Lot number E15T018, Alfa Aesar) into the PM powder, the PM milled Mg_2Si and SiC_{NP} were planetary ball milled at 120 RPM for 3 h in an argon-filled glove box with the same mill jar and media used to mill the Mg_2Si powder.

For the VM powder, there was a relatively uniform distribution of powder, 0.2 μm to 2 μm in size (Figure 2). The SiC_{NP} (44646, Lot number E15T018, Alfa Aesar) were incorporated into the VM powder simultaneously with milling the sieved powder.

The original PM powder average particle size of 0.7 μm (Figure 1) was smaller than the average GS of the sintered PM specimens of 2.0 μm to 3.9 μm (Table 5.3), indicating some grain growth during sintering (Figure 3a – c).

No BET particle size measurement was performed on the VM powder to compare to GS, however the average GS of the VM specimens of 0.4 μm to 0.8 μm (Table 5.3) is consistent with only limited grain growth from the original VM powder (Figure 5.2) to the sintered specimens (Figure 5.3d).

5.3.1.1 Starting material density and microstructure

All sintered specimens in this study except one have a density of 2.00 to 2.06 g/cm^3 . The one specimen with a density of 1.93 g/cm^3 , VM-0SiC-02, is mentioned individually, but any averages or trends in mechanical properties excluded VM-0SiC-02 as an outlier.

Most of the sintered specimen densities are higher than theoretical density for Mg_2Si of 2.00 g/cm^3 reported in the literature [Whitten 1965]. The higher density is

Table 5.3. Specimens in this study were either milled by planetary ball mill (PM) or vibratory mill (VM), with up to 4 vol% SiC_{NP} additions, then sintered by pulsed electric current sintering to produce specimens with a density (ρ) of 2.00 g/cm³ or greater for all specimens except VM-0SiC-2. The average grain size (GS) by the lineal intercept method are a function of the milling method, and not a function of SiC_{NP} additions.

Specimen	SiC _{NP} vol% addition	ρ (g/cm ³)	GS (μ m)
PM-0SiC	0.0	2.03	2.4
PM-0.5SiC	0.5	2.02	2.0
PM-1SiC	1.0	2.02	2.0
PM-1.5SiC	1.5	2.01	2.1
PM-2SiC	2.0	2.06	1.3
PM-3SiC	3.0	2.04	3.9
PM-4SiC	4.0	2.02	3.6
VM-0SiC-1	0.0	2.00	0.6
VM-0SiC-2	0.0	1.93	0.4
VM-0.5SiC	0.5	2.01	0.6
VM-1SiC	1.0	2.03	0.7
VM-1.5SiC	1.5	2.03	0.8
VM-2SiC	2.0	2.03	0.6

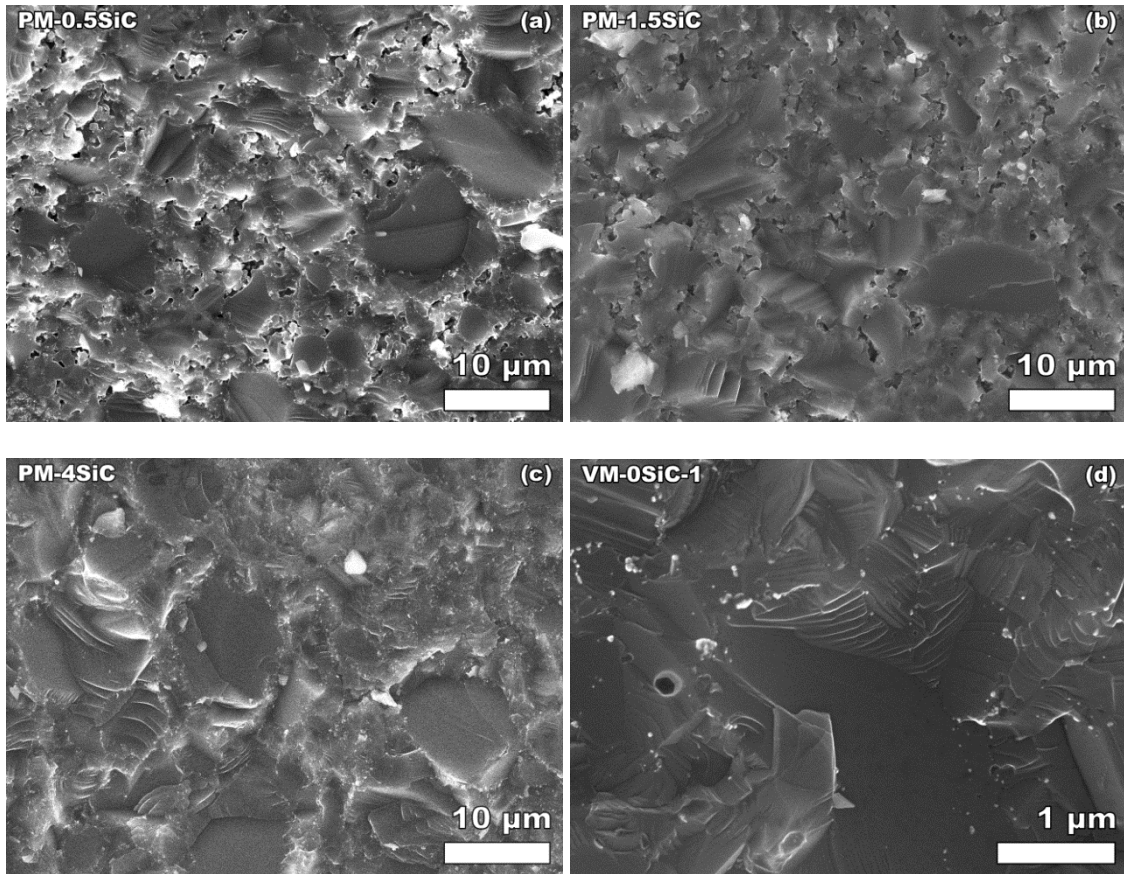


Figure 5.3. For Mg_2Si fracture surfaces, transgranular fracture dominate in all specimens. The PM specimens (a-c) with varying amounts of SiC_{NP} addition did not show any appreciable difference in grain size, although changing to VM processing significantly reduced the grain size (d). Note the difference in scale between the PM images (a-c) and the VM image (d).

because of the presence of MgO within the material. The starting material as received from the vendor has been shown to contain approximately 8 vol% of MgO, and likely to have a composite theoretical density near 2.12 g/cm^3 [Schmidt 2012] (see section 5.3.2).

Previous examination of the SiC_{NP} material has shown that the as-received nanopowder from two vendors (Alfa Aesar and Nanostructured & Amorphous Materials Inc.) consists primarily of particles, approximately 50 nm in diameter, agglomerated into clusters of 100 nm to 20 μm in diameter [Schmidt 2013b]. These agglomerates do not appreciably break apart with milling [Schmidt 2013b]. In this study, the SiC_{NP} material was from one of the two previously examined vendors (Alfa Aesar).

5.3.2 Elasticity results

The elasticity for specimens with SiC_{NP} , excluding the outlier specimen VM-0SiC-02 with density of 1.93 g/cm^3 , is not a function of SiC_{NP} addition up to 4 vol%, nor powder processing methodology (Figure 5.4, Table 5.4). Average Young's modulus, E , for the PM specimens with 0 to 4 vol% SiC_{NP} is $113.3 \pm 4.0 \text{ GPa}$, and $111.1 \pm 2.3 \text{ GPa}$ for VM specimens (Figure 5.4a – b). The small variations in elastic moduli observed are not observed to be a function of the SiC_{NP} addition (Figure 5.4), rather a function of the limited differences in porosity among specimens (Figure 5.5).

5.3.2.1 Elasticity and SiC_{NP} addition

If the SiC_{NP} addition does not react with the Mg_2Si matrix, the elastic modulus of the composite material with addition of up to 4 vol% SiC_{NP} may be modeled as a mixture of two independent materials. In a study of SnTe with 0 vol% to 4 vol% SiC_{NP} addition [Schmidt 2013b], the Hashin model [Hashin 1962; Bedolla 2012; Couturier 1997]

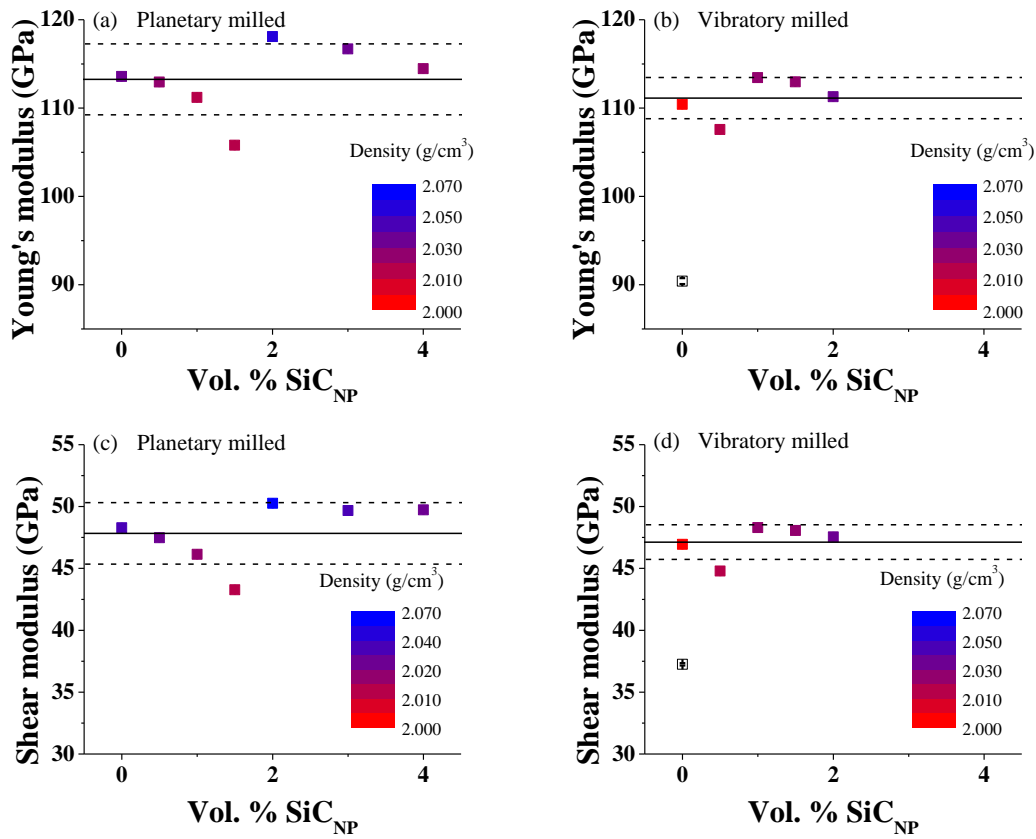


Figure 5.4. The Young's modulus (a, b) and shear modulus (c, d) of Mg₂Si varied primarily due to small variations in density. The variation in vol. % SiC_{NP} did not significantly affect the moduli, regardless of if the specimens were planetary milled (a, c) or vibratory milled (b, d).

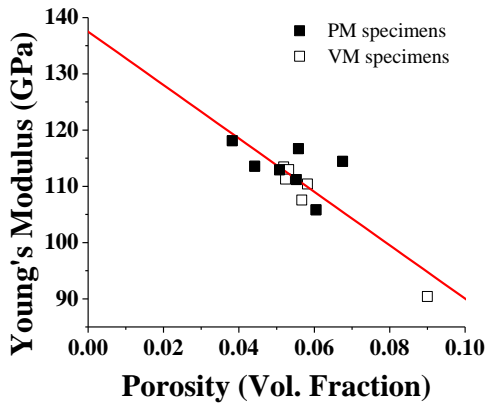


Figure 5.5. The Young's modulus, E , decreases linearly with porosity for the set of 13 specimens in this study.

Table 5.4. The Young's modulus, E , shear modulus, G , and density, ρ , for the specimens in this study, as compared to the range of E , G and ρ in a previous study on three Mg_2Si specimens produced by the same vendor.

Specimen	E (MPa)	G (MPa)	ρ (g/cm³)	Reference
PM-0SiC	113.6 ± 0.3	48.3 ± 0.1	2.03	This study
PM-0.5SiC	112.9 ± 0.3	47.5 ± 0.1	2.02	This study
PM-1SiC	111.2 ± 0.3	46.1 ± 0.1	2.02	This study
PM-1.5SiC	105.8 ± 0.4	43.3 ± 0.1	2.01	This study
PM-2SiC	118.1 ± 0.2	50.3 ± 0.1	2.06	This study
PM-3SiC	116.7 ± 0.2	49.7 ± 0.1	2.04	This study
PM-4SiC	114.5 ± 0.6	49.7 ± 0.2	2.02	This study
VM-0SiC-1	110.4 ± 0.2	46.9 ± 0.1	2.00	This study
VM-0SiC-2	90.4 ± 0.3	37.3 ± 0.1	1.93	This study
VM-0.5SiC	107.6 ± 0.4	44.7 ± 0.1	2.01	This study
VM-1SiC	113.4 ± 0.2	48.3 ± 0.1	2.03	This study
VM-1.5SiC	113.0 ± 0.2	48.1 ± 0.1	2.03	This study
VM-2SiC	111.3 ± 0.3	47.5 ± 0.1	2.03	This study
Mg_2Si	116.9 – 117.7	48.92 – 50.09	2.07 – 2.09	[Schmidt 2012]

described relatively well the resulting change in Young's modulus where the Hashin model can be written as

$$E_C = E_m \left(\frac{E_m V_m + E_r \{V_r + 1\}}{E_r V_m + E_m \{V_r + 1\}} \right) \quad (4)$$

where E_C is the Young's modulus of the composite, E_m is the Young's modulus of the matrix material, E_r is the Young's modulus of the reinforcing phase, and V_m and V_r are the volume fraction of the matrix and the reinforcing phase, respectively. Applying the Hashin model (equation (4)) to the materials in this study, using the Young's modulus of the reinforcing phase SiC_{NP}, E_r , at 450 GPa [Schreiber 1966; Carnahan 1968] and the E_m of 112 GPa the Mg₂Si measured in this study, the E_C for the composite with the maximum 4 vol% SiC_{NP} is 117.5 GPa, which is similar to the measured E of 114.5 ± 0.6 GPa from specimen PM-4SiC (Figure 5.4a).

5.3.2.2 Elasticity and porosity

Small variations in density of the specimens in this study, from 2.00 to 2.06 g/cm³, is likely the dominant source of variation in E measured in this study (Figure 5.4a – b, Figure 5.5). Typically, for small variations in porosity, P , the change in E with porosity may be modeled by the empirical equation,

$$E = E_0 (1 - b_E P) \quad (5)$$

where E_0 is the Young's modulus of a fully dense material and b_E is a material-dependent constant, typically between 2 and 6 for a wide range of materials [Rice 1998]. For TE materials YbAl₃ [Schmidt 2013a] and lead-antimony-silver-tellurium (LAST) [Ni 2009], the experimentally determined values of b_E were 2.34 and 3.5, respectively .

Assuming the matrix material contains 8% MgO [Schmidt 2012] (density 3.58 g/cm³

[Anderson 1966; Bogardus 1965]) and 92% Mg₂Si (density 2.00 g/cm³ [Whitten 1965]), the composite theoretical densities (matrix density, 2.126 g/cm³, SiC_{NP} density, 3.16 g/cm³ [Aesar]) were calculated. The volume fraction porosity, P , was calculated for the composite materials. The E versus P for the full set of 13 composite specimens in this study were fit to equation (5), with the b_E was 3.5 ± 0.5 and the E_0 was 138 ± 5 GPa (Figure 5.5). The linear relationship indicates that the E for the 14 specimens is a function of P . The error on the E_0 and b_E are relatively large because of the restricted range of P for the specimens this study.

A previous study on Mg₂Si from lump material purchased from the same vendor and processed by PM measured E of 116.9 GPa to 117.7 GPa [Schmidt 2012] (Table 5.4). The small (~4%) difference in elastic moduli between this study and the previous study is likely due to the slightly higher density specimens in the previous study, 2.07 g/cm³ to 2.09 g/cm³ (Table 5.4).

5.3.3 Hardness and Toughness Results

Hardness, H , by Vickers indentation for specimens with SiC_{NP}, excluding one outlier, was relatively insensitive to vol% SiC_{NP}, from 0 % to 4 vol% SiC_{NP}, indentation load, from 1.96 N to 4.9 N, or powder processing technique, averaging 4.76 ± 0.37 GPa for the PM specimens (Figure 5.6a) and 4.83 ± 0.15 GPa for the VM specimens (Figure 5.6b). The outlier is specimen VM-0SiC-02 with a density of 1.93 g/cm³, lower than the 2.00 g/cm³ to 2.06 g/cm³ density of the other 12 specimens in this study. The H of the outlier VM-0SiC-02 specimen is indicated by the open symbol in Figure 5.6b.

The fracture toughness, K_C , is dependent on the powder processing conditions. The K_C of the PM composite reached a maximum at 1 vol% SiC_{NP}, an increase of about

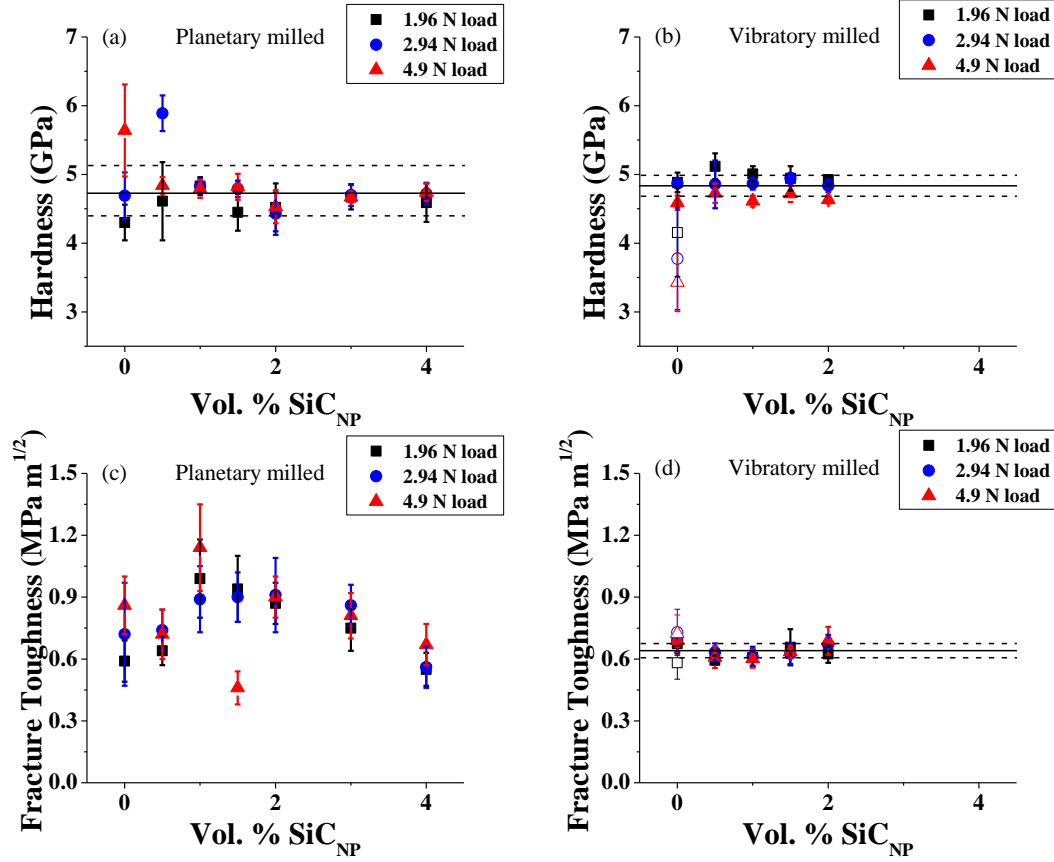


Figure 5.6. The hardness, (a) and (b) is not a function of the milling procedure or the vol% SiC_{NP}, but less scatter was observed in the (b) vibratory milled specimens than the (a) planetary ball milled specimens. The fracture toughness exhibited a maximum at 1 vol% SiC_{NP} for the (c) planetary ball milled specimens, but the fracture toughness is not a function of vol% SiC_{NP} for the (d) vibratory milled specimens. Open symbols in (b) and (d) indicate a specimen with lower density of 1.93 g/cm³, relative to the 2.00 to 2.06 g/cm³ for all other specimens in this study.

33% over the unreinforced PM material, and is relatively insensitive to SiC_{NP} addition between 1 vol% and 2 vol% SiC_{NP} addition (Figure 5.6c). In contrast, the VM composite material was relatively insensitive to any additions of up to 2 vol% SiC_{NP} (Figure 5.6d). The VM material also exhibited a much smaller variation in measured K_C , with the coefficient of variation, CV , averaging 0.08 and ranging from 0.04 to 0.14 (Figure 5.6d). The CV of the PM material averages 0.16 and ranging from 0.11 to 0.34.

The smaller CV observed in the VM specimens relative to the PM specimens may be related to the smaller GS of the VM specimens, leading to a more uniform crack length and possibly more uniform distribution of bridging and stalling. The smaller CV is particularly important when considering the distribution of strength, and the related probability of failure at a given load. The strength of the material that may be used safely in a design depends upon the scatter in strength [Wachtman 2009], and the smaller CV for the strength values in the VM specimens indicates a smaller scatter of strength for VM specimens than PM specimens.

In this study, K_C is not a function of GS for the Mg_2Si with no SiC_{NP} addition (Figure 5.6c – d). This result is expected for cubic materials such as Mg_2Si , because K_C is largely independent of GS [Wachtman 2009], and specifically for Vickers indentation crack length, “there should be a rather weak dependence of crack length on GS” [Wachtman 2009, pg 217].

However, the effect of SiC_{NP} addition on K_C was influenced by the powder processing technique. The difference in size between the added SiC_{NP} particles and the Mg_2Si matrix may play a role in the behavior of K_C . In a study on fracture toughness on TE material specimens sintered from a blend of nanoparticles with microparticles of the

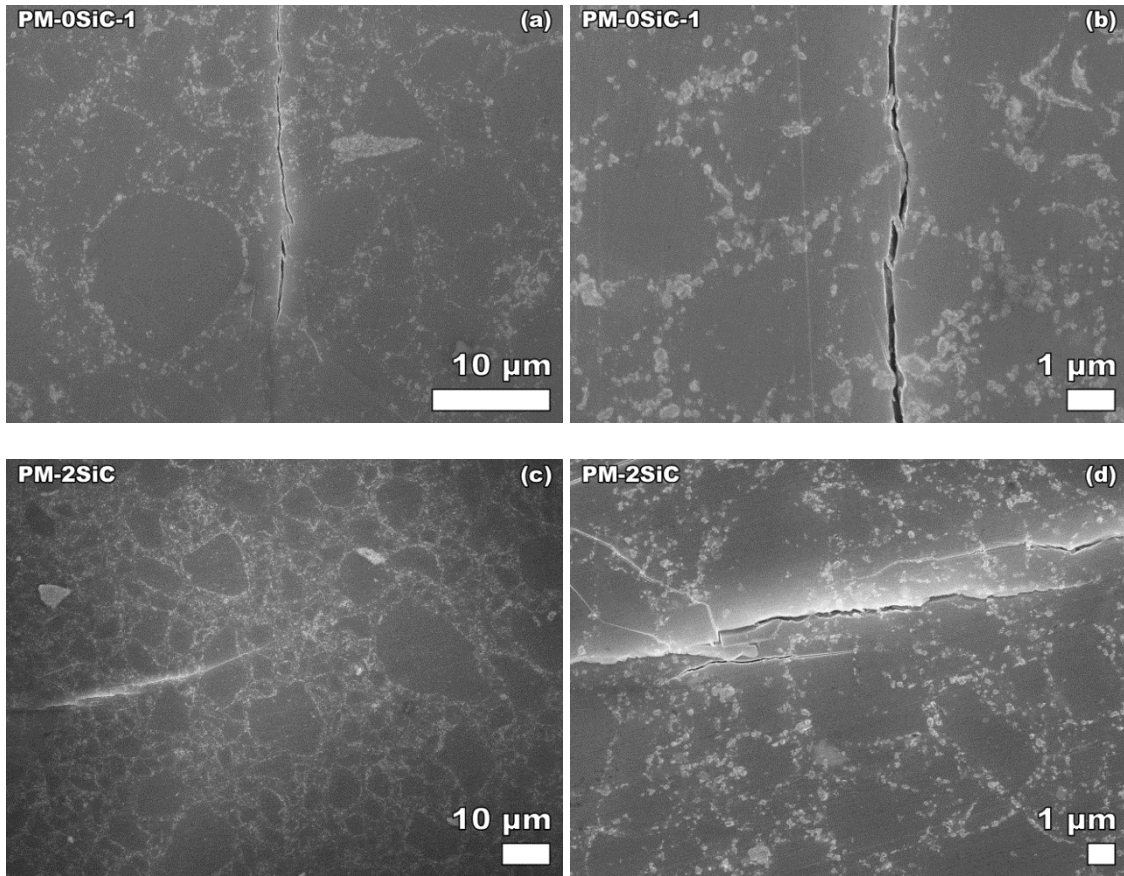


Figure 5.7. Crack bridging, in PM Mg_2Si was commonly observed in radial cracks for all the Mg_2Si specimens in this study.

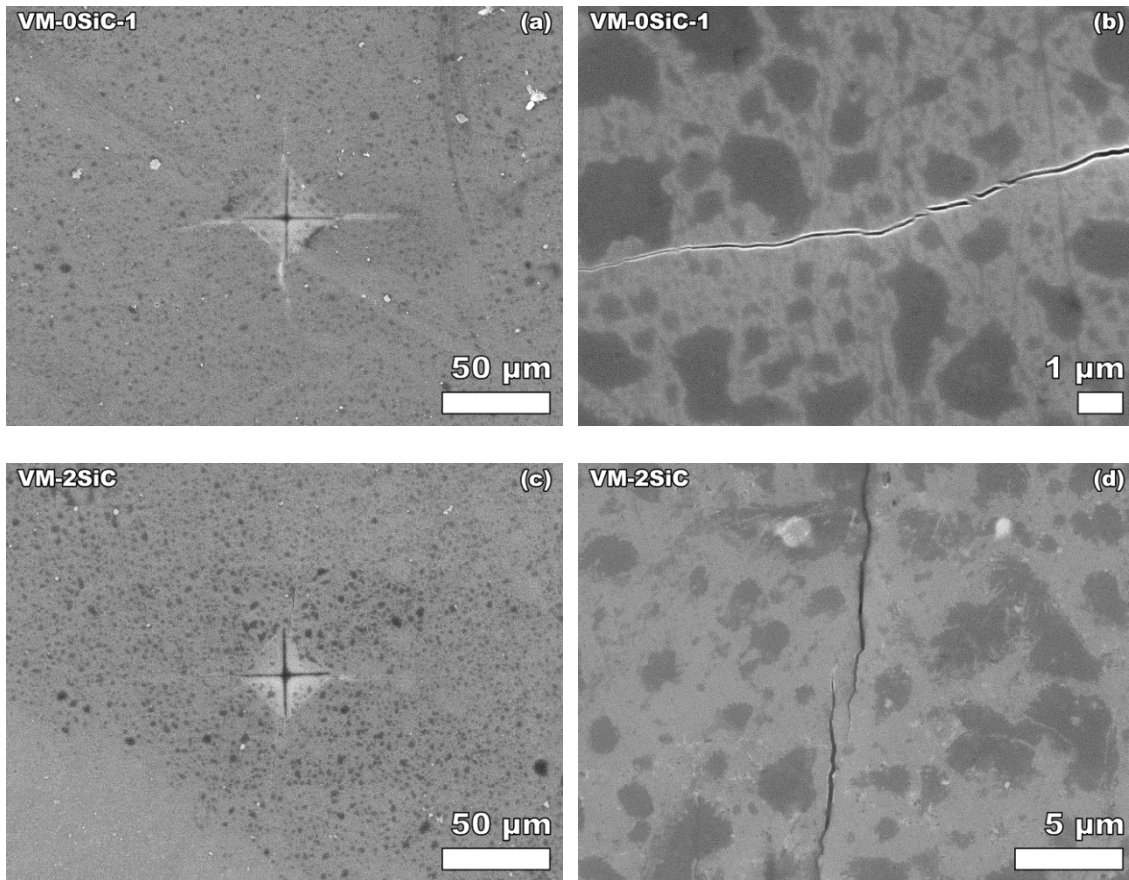


Figure 5.8. Crack bridges were commonly observed in VM specimens regardless of SiC_{NP} addition. Crack bridging in radial cracks was not eliminated by reducing grain size through VM processing. Spotting is from oil residue on the surface of the specimen.

same composition, $\text{Co}_4\text{Sb}_{11.5}\text{Te}_{0.5}$, the K_C increased with additions of nanoparticles [Duan 2014]. Similar to the K_C of $\text{Co}_4\text{Sb}_{11.5}\text{Te}_{0.5}$ [Duan 2014], this study indicates that the toughening due to addition of SiC_{NP} may depend on GS of the matrix Mg_2Si relative to the SiC_{NP} .

5.3.3.1 Crack bridging and toughness

Crack bridging and stalling was observed on all of the different Mg_2Si specimens, both with and without additions and regardless of processing by PM (Figure 5.7) or VM (Figure 5.8). Both bridging and stalling are extrinsic toughening mechanisms, and not beneficial to K_C in a fatigue loading condition such as thermal cycling [Lathabai 1991; Ritchie 1999]. In some cases, these may be controlled for through processing. Bridging in monophase alumina material was eliminated by reducing the GS [Lathabai 1991], although changing the powder processing of the Mg_2Si in this study did not produce a similar result.

5.4 Conclusions

Fracture toughness, K_C , of Mg_2Si increases for PM material by 33% with the addition of 1 – 2 vol% SiC_{NP} , but K_C is independent of SiC_{NP} addition for VM material. As is typical of cubic materials such as Mg_2Si , K_C is independent of GS for specimens with no addition of SiC_{NP} . The coefficient of variation for the K_C of the VM samples was smaller, 0.08, than for the PM samples, 0.16, indicating a likely smaller scatter of specimen strength for VM specimens than the PM specimens.

ACKNOWLEDGEMENTS

The authors acknowledge the financial support of the Department of Energy, Revolutionary Materials for Solid State Energy Conversion Center, an Energy Frontiers

Research Center funded by the U.S. Department of Energy, Office of Science, Office of Basic Energy Sciences under award number DE-SC0001054.

REFERENCES

REFERENCES

- [Aesar] Aesar, A. Material Safety Data Sheet, Magnesium Silicide.
<http://www.alfa.com/content/msds/USA/45518.pdf>.
- [Anderson, Andreatch 1966] Anderson, O.L., Andreatch, P. Pressure Derivatives of Elastic Constants of Single-Crystal MgO at 23° and -195.8°C. *Journal of the American Ceramic Society* 49 (1966) 404–409.
- [ASTM-Standard-E112-13 2014] ASTM-Standard-E112-13. Standard Test Methods for Determining Average Grain Size. In: *ASTM Volume 03.01 Metals Mechanical Testing; Elevated and Low Temperature Tests; Metallography*. ASTM International, West Conshohocken, PA, 2014.
- [Becher 1991] Becher, P.F. Microstructural Design of Toughened Ceramics. *Journal of the American Ceramic Society* 74 (1991) 255–269.
- [Bedolla, Lemus-Ruiz, Contreras 2012] Bedolla, E., Lemus-Ruiz, J., Contreras, A. Synthesis and characterization of Mg-AZ91/AlN composites. *Materials and Design* 38 (2012) 91–98.
- [Bhowmick, Cha, Jung, Lawn 2009] Bhowmick, S., Cha, H., Jung, Y.-G., Lawn, B.R. Fatigue and debris generation at indentation-induced cracks in silicon. *Acta Materialia* 57 (2009) 582–589.
- [Bhowmick, Meléndez-Martínez, Lawn 2007] Bhowmick, S., Meléndez-Martínez, J.J., Lawn, B.R. Bulk silicon is susceptible to fatigue. *Applied Physics Letters* 91 (2007) 201902.
- [Bogardus 1965] Bogardus, E.H. Third-Order Elastic Constants of Ge, MgO, and Fused SiO₂. *Journal of Applied Physics* 36 (1965) 2504.
- [Carnahan 1968] Carnahan, R. Elastic Properties of Silicon Carbide. *Journal of the American Ceramic Society* 51 (1968) 223–224.
- [Case 2012a] Case, E.D. Thermo-mechanical properties of thermoelectric materials. In: D.M. Rowe, ed., *Thermoelectrics and its Energy Harvesting: Modules, Systems and Applications*. CRC Press, Boca Raton, Florida, 2012, 581.
- [Case 2012b] Case, E.D. Thermal Fatigue and Waste Heat Recovery via Thermoelectrics. *Journal of Electronic Materials* 41 (2012) 1811–1819.

- [Couturier, Ducret, Merle, Disson, Joubert 1997] Couturier, R., Ducret, D., Merle, P., Disson, J.P., Joubert, P. Elaboration and characterization of a metal matrix composite: Al/AlN. *Journal of the European Ceramic Society* 17 (1997) 1861–1866.
- [Duan, Zhai, Ding, Xu, Li, Liu, Li, Zhang 2014] Duan, B., Zhai, P., Ding, S., Xu, C., Li, G., Liu, L., Li, P., Zhang, Q. Effects of Nanoparticle Size on the Thermoelectric and Mechanical Properties of Skutterudite Nanocomposites. *Journal of Electronic Materials* 43 (2014) 2115–2120.
- [Eilertsen, Subramanian, Kruzic 2013] Eilertsen, J., Subramanian, M. a., Kruzic, J.J. Fracture toughness of Co₄Sb₁₂ and In_{0.1}Co₄Sb₁₂ thermoelectric skutterudites evaluated by three methods. *Journal of Alloys and Compounds* 552 (2013) 492–498.
- [Hashin 1962] Hashin, Z. The Elastic Moduli of Heterogeneous Materials. *Journal of Applied Mechanics* 29 (1962) 143–150.
- [Hayatsu, Iida, Sakamoto, Kurosaki, Nishio, Kogo, Takanashi 2012] Hayatsu, Y., Iida, T., Sakamoto, T., Kurosaki, S., Nishio, K., Kogo, Y., Takanashi, Y. Fabrication of large sintered pellets of Sb-doped n-type Mg₂Si using a plasma activated sintering method. *Journal of Solid State Chemistry* 193 (2012) 161–165.
- [Knehans, Steinbrech 1982] Knehans, R., Steinbrech, R. Memory effect of crack resistance during slow crack growth in notched Al₂O₃ bend specimens. (1982) 327–329.
- [Lathabai, Rodel, Lawn 1991] Lathabai, S., Rodel, J., Lawn, B.R. Cyclic Fatigue from Frictional Degradation at Bridging Grains in Alumina. *Journal of the American Ceramic Society* 74 (1991) 1340–1348.
- [Launey, Ritchie 2009] Launey, M.E., Ritchie, R.O. On the Fracture Toughness of Advanced Materials. *Advanced Materials* 21 (2009) 2103–2110.
- [Meng, Fan, Chen, Munir 2011] Meng, Q.S., Fan, W.H., Chen, R.X., Munir, Z. a. Thermoelectric properties of Sc- and Y-doped Mg₂Si prepared by field-activated and pressure-assisted reactive sintering. *Journal of Alloys and Compounds* 509 (2011) 7922–7926.
- [Migliori, Sarrao 1997] Migliori, A., Sarrao, J.L. *Resonant Ultrasound Spectroscopy: Applications to Physics, Materials Measurements, and Nondestructive Evaluation*. Wiley-Vch, New York, 1997.
- [Muthiah, Pulikkotil, Srivastava, Kumar, Pathak, Dhar, Budhani 2013] Muthiah, S., Pulikkotil, J., Srivastava, a. K., Kumar, A., Pathak, B.D., Dhar, A., Budhani, R.C. Conducting grain boundaries enhancing thermoelectric performance in doped Mg₂Si. *Applied Physics Letters* 103 (2013) 053901.

- [Ni, Ren, Case, Timm 2009] Ni, J., Ren, F., Case, E., Timm, E. Porosity dependence of elastic moduli in LAST (lead–antimony–silver–tellurium) thermoelectric materials. *Materials Chemistry and Physics*(2009) .
- [Ni, Case, Khabir, Stewart, Wu, Hogan, Timm, Girard, Kanatzidis 2010] Ni, J.E., Case, E.D., Khabir, K.N., Stewart, R.C., Wu, C.-I., Hogan, T.P., Timm, E.J., Girard, S.N., Kanatzidis, M.G. Room temperature Young's modulus, shear modulus, Poisson's ratio and hardness of PbTe–PbS thermoelectric materials. *Materials Science and Engineering: B* 170 (2010) 58–66.
- [Parchovianský, Galusek, Sedláček, Švančárek, Kašiarová, Dusza, Šajgalík 2013] Parchovianský, M., Galusek, D., Sedláček, J., Švančárek, P., Kašiarová, M., Dusza, J., Šajgalík, P. Microstructure and mechanical properties of hot pressed Al₂O₃/SiC nanocomposites. *Journal of the European Ceramic Society* 33 (2013) 2291–2298.
- [Perez-Rigueiro, Pastor, Llorca 1998] Perez-Rigueiro, J., Pastor, J., Llorca, J. Revisiting the mechanical behavior of alumina/silicon carbide nanocomposites. *Acta materialia* 46 (1998) .
- [Ren, Case, Timm, Schock 2008] Ren, F., Case, E.D., Timm, E.J., Schock, H.J. Hardness as a function of composition for n-type LAST thermoelectric material. *Journal of Alloys and Compounds* 455 (2008) 340–345.
- [Rice 1998] Rice, R.W. *Porosity of Ceramics*. Marcel Dekker, New York, 1998.
- [Ritchie 1999] Ritchie, R. Mechanisms of fatigue-crack propagation in ductile and brittle solids. *International Journal of Fracture*(1999) 55–83.
- [Schmidt, Case, Giles, Ni, Hogan 2012] Schmidt, R.D., Case, E.D., Giles, J., Ni, J.E., Hogan, T.P. Room-Temperature Mechanical Properties and Slow Crack Growth Behavior of Mg₂Si Thermoelectric Materials. *Journal of Electronic Materials* 41 (2012) 1210–1216.
- [Schmidt, Case, Lehr, Morelli 2013a] Schmidt, R.D., Case, E.D., Lehr, G.J., Morelli, D.T. Room temperature mechanical properties of polycrystalline YbAl₃, a promising low temperature thermoelectric material. *Intermetallics* 35 (2013) 15–24.
- [Schmidt, Case, Ni, Trejo, Lara-Curzio, Korkosz, Kanatzidis 2013b] Schmidt, R.D., Case, E.D., Ni, J.E., Trejo, R.M., Lara-Curzio, E., Korkosz, R.J., Kanatzidis, M.G. High-temperature elastic moduli of thermoelectric SnTe_{1±x} – y SiC nanoparticulate composites. *Journal of Materials Science* 48 (2013) 8244–8258.
- [Schmidt, Ni, Case, Sakamoto, Kleinow, Wing, Stewart, Timm 2010] Schmidt, R.D., Ni, J.E., Case, E.D., Sakamoto, J.S., Kleinow, D.C., Wing, B.L., Stewart, R.C., Timm, E.J. Room temperature Young's modulus, shear modulus, and Poisson's ratio of

Ce_{0.9}Fe_{3.5}Co_{0.5}Sb₁₂ and Co_{0.95}Pd_{0.05}Te_{0.05}Sb₃ skutterudite materials. *Journal of Alloys and Compounds* 504 (2010) 303–309.

[Schreiber, Soga 1966] Schreiber, E., Soga, N. Elastic Constants of Silicon Carbide. *Journal of the American Ceramic Society* 49 (1966) 342.

[Tani, Kido 2005] Tani, J., Kido, H. Thermoelectric properties of Bi-doped Mg₂Si semiconductors. *Physica B: Condensed Matter* 364 (2005) 218–224.

[Tani, Kido 2007] Tani, J., Kido, H. Thermoelectric properties of Sb-doped Mg₂Si semiconductors. *Intermetallics* 15 (2007) 1202–1207.

[Tani, Kido 2008] Tani, J., Kido, H. Thermoelectric properties of Al-doped Mg₂Si_{1-x}Sn_x ($x \leq 0.1$). *Journal of Alloys and Compounds* 466 (2008) 335–340.

[Wachtman, Cannon, Matthewson 2009] Wachtman, J.B., Cannon, W.R., Matthewson, M.J. *Mechanical Properties of Ceramics*. Wiley-Vch, Hoboken, N.J., 2009.

[Whitten, Chung, Danielson 1965] Whitten, W., Chung, P., Danielson, G. Elastic constants and lattice vibration frequencies of Mg₂Si. *Journal of Physics and Chemistry of Solids* 26 (1965) 49–56.

[Wiederhorn 1969] Wiederhorn, S. Fracture surface energy of glass. *Journal of the American Ceramic Society* 52 (1969) 99–105.

[Zhao, Zhang, Li, Zhou, Liu, Liu 2008] Zhao, L.-D., Zhang, B.-P., Li, J.-F., Zhou, M., Liu, W.-S., Liu, J. Thermoelectric and mechanical properties of nano-SiC-dispersed Bi₂Te₃ fabricated by mechanical alloying and spark plasma sintering. *Journal of Alloys and Compounds* 455 (2008) 259–264.

6 Influence of silver nanoparticle addition, porosity and processing technique on the mechanical properties of $\text{Ba}_{0.3}\text{Co}_4\text{Sb}_{12}$ skutterudites

Robert D. Schmidt¹, Eldon D. Case¹, Zayra Lobo¹, Travis R. Thompson¹, Jeffrey S. Sakamoto¹, Xiao-Yuan Zhou², Ctirad Uher²

¹Chemical Engineering and Materials Science Department,
Michigan State University, East Lansing, MI, 48824

²Physics Department, University of Michigan, Ann Arbor, MI, 48109

Published in: Journal of Materials Science (2014) DOI:10.1007/s10853-014-8427-5.

Abstract

The thermoelectric skutterudite $\text{Ba}_{0.3}\text{Co}_4\text{Sb}_{12}$ is a promising candidate for waste heat recovery applications. Recently, it was demonstrated that the addition of silver nanoparticles (Ag_{NP}) to $\text{Ba}_{0.3}\text{Co}_4\text{Sb}_{12}$ increases both the thermoelectric figure of merit and electrical conductivity. This study is the first to examine the effect of Ag_{NP} addition on the material's mechanical properties. This study also found that the Young's modulus, E , shear modulus, G , and bulk modulus, B decreased linearly with increasing volume fraction porosity, P . Resonant ultrasound spectroscopy (RUS) was employed to measure the elastic moduli and Vickers indentation was used to determine the hardness, H , and fracture toughness, K_C . Trends in the mechanical properties as a function of grain size, porosity and the Ag_{NP} are discussed in terms of the pertinent literature. While K_C was independent of Ag_{NP} addition, porosity and grain size, both E and H decreased linearly with increasing porosity. In addition, this study is the first to identify (i) the Ag_3Sb phase formed and (ii) the enhanced densification that occurs when the Ag_{NP} is sintered with $\text{Ba}_{0.3}\text{Co}_4\text{Sb}_{12}$ powders, where both effects are consistent with the eutectic and peritectic reactions observed in the binary phase diagram Ag-Sb. These eutectic/peritectic

reactions may also be linked to the enhancement of electrical conductivity previously observed when Ag is added to $\text{Ba}_{0.3}\text{Co}_4\text{Sb}_{12}$. Also, similar beneficial eutectic/peritectic reactions may be available for other systems where conductive particles are added to other antimonides or other thermoelectric systems.

Keywords: thermoelectric; skutterudite, porosity, elastic modulus, peritectic reaction

6.1 Introduction

The conversion of waste heat to electrical energy by thermoelectric (TE) materials is typically characterized by the material's figure of merit, ZT , such that

$$ZT = \frac{S^2 \sigma}{\kappa} T \quad (1)$$

where S is the Seebeck coefficient, σ is the electrical conductivity, κ is the thermal conductivity, and T is temperature [Ioffe 1960]. ZT values of up to 1.7 [Shi 2011] have been reported for bulk skutterudite TE materials.

In-service conditions subject thermoelectric materials to stresses from thermal gradients, thermal transients, thermal expansion mismatch, and applied external stresses. Due to these challenges, the mechanical properties of thermoelectric materials are important, especially in waste heat harvesting applications. The response of a material to imposed stresses requires knowledge of the elastic properties; for example the Young's modulus and Poisson's ratio are needed in order to construct the stiffness matrix for finite element analysis [Segerland 1984; Hutton 2004; Zienkiewicz 2005]. Also, the fracture toughness, K_C , which measures the resistance to crack growth [Wachtman 2009], is

important to the mechanical integrity. In addition, hardness is related to wear characteristics of the material [Ren 2008].

A key motivation for this study is the recent work on $\text{Ba}_{0.3}\text{Co}_4\text{Sb}_{12}$ by Zhou et al. [Zhou 2012] which showed the addition of 0.5 wt% silver nanoparticles (Ag_{NP}) lead to a 30% increase in ZT , which was attributed primarily to an increase in electrical conductivity. Also, while carrier concentrations remain unchanged, a modest increase in the Seebeck coefficient also was observed with the added Ag_{NP} [Zhou 2012].

In general, the nanostructural and microstructural details can be extremely important for the transport properties of thermoelectric materials, and many previous studies have used nanostructures to reduce thermal conductivity by enhancing phonon scattering [Androulakis 2007; Zhao 2012; Zhou 2008; Alleno 2009; Ji 2007; Toprak 2004; Mi 2008], which can lead, in turn, to increases in ZT . Also, reducing the grain size or increasing porosity can enhance phonon scattering and thus increase ZT [Yoon 2013; Tokiai 1997].

Although in this study, an increased porosity leads to decreases in the elastic moduli, an increase in porosity also has the potential to increase the resistance to thermal fatigue damage [Case 2012b; Case 2012a], which is important due to the inevitable thermal cycling that thermoelectrics are subjected to during waste heat harvesting. In addition to affecting mechanical properties, porosity also impacts transport properties. In thermoelectrics such as nanoporous GeSi alloys [Lee 2010], porosity decreases both the electrical and thermal conductivity, although the decrease in electrical conductivity overwhelms the decrease in thermal conductivity, resulting in a net lowering of ZT due to porosity. However, in skutterudites including $\text{La}_{0.75}\text{Fe}_3\text{CoSb}_{12}$ [Yang 2004],

Co_{0.9}Ni_{0.1}Sb₃, Co_{0.8}Ni_{0.2}Sb₃ [He 2008] and a TiN nanoparticles-Co₄Sb_{11.5}Te_{0.5} composite [Wen 2013], enhancements in ZT have been reported for porosity levels between $P = 0.003$ and 0.15 . For example, Wen et al. [Wen 2013] densified a 0.01 volume fraction TiN nanoparticles -Co₄Sb_{11.5}Te_{0.5} skutterudite and subsequent thermal annealing at 773 K for 120 hours in vacuum led to bloating (the formation of internal porosity) and a 10 percent increase in porosity which Wen et al. ascribed to a reaction between the TiN nanoparticles and the Co₄Sb_{11.5}Te_{0.5} matrix phases. Wen et al. noted that “The electrical conductivity and the thermal conductivity of the annealed sample decline simultaneously due to the higher porosity, but the thermal conductivity reduces more remarkably”, leading to a 20 percent increase in ZT compared to the denser specimens (prior to annealing and bloating) [Wen 2013]. Thus, in addition to having the potential to boost thermal fatigue resistance, in some skutterudites porosity can increase ZT making it important to also assess the mechanical properties such as elastic moduli, hardness and toughness for porous thermoelectrics.

In this study, we examine the Young’s modulus, E , shear modulus, G , bulk modulus, B , Poisson’s ratio, ν , hardness, H , and fracture toughness, K_C , of Ba_{0.3}Co₄Sb₁₂ with and without the addition 0.5 wt% Ag_{NP}. We further explore the effects of microstructure/nanostructure and processing pursuing two processing routes: (i) planetary milling (PM), then hot press (HP) sintering and (ii) vibratory milling (VM) followed by pulsed electric current sintering (PECS). In this way, we produced specimens with a range of porosity and grain size while using the two most common milling techniques (planetary milling and vibratory milling) and densification techniques (HP and PECS) used to process thermoelectric materials.

6.2 Experimental procedure

6.2.1 Materials and Specimen Preparation

To fabricate $\text{Ba}_{0.3}\text{Co}_4\text{Sb}_{12}$, elemental Ba (pieces, 99.9% pure), Co (powder 99.5% pure), and Sb (shot 99.999% pure) in stoichiometric ratio were placed inside evacuated carbon coated quartz ampoules, heated to 1100°C and held at that temperature 5 hours, then quenched into a supersaturated salt water solution. The resulting ingots were then annealed at 750°C for 7 days. Finally, the ingots were planetary ball milled.

In this study, two different processing techniques were used to fabricate two sets of specimens with differing microstructures. First, Ag_{NP} powders, which had a vendor specified purity of 99.9% and a size range of from 20 nm to 40 nm (45509, Alfa Aesar, Ward Hill MA), were dispersed into the $\text{Ba}_{0.3}\text{Co}_4\text{Sb}_{12}$ powder by planetary ball milling at 300 rpm for 15 min [Pilchak 2007]. Then specimens approximately 10.5 mm in diameter and 10 mm in height were fabricated by hot pressing $\text{Ba}_{0.3}\text{Co}_4\text{Sb}_{12}$ powders (with and without the added Ag_{NP}) in a graphite die for 20 minutes in an argon atmosphere with 50 MPa pressure at temperatures of 673 K, 773 K or 873 K in order to produce specimens with a range of volume fraction porosity, P , from 0.30 to 0.05 (Table 6.1). The hot pressed specimens were then cut into discs approximately 1.7 mm thick using a slow speed saw (Isomet, Buehler, Lake Bluff IL) with 0.3 mm thick diamond blade (801-137, Leco Corp., St. Joseph, MI).

A second set of specimens was fabricated by reprocessing the specimens hot pressed without Ag_{NP} additions by first grinding the hot pressed specimens without Ag addition in an automated mortar and pestle (PM100, Retch) and then sieving with a 75 μm sieve, where the grinding and sieving steps were performed in an argon-filled glove

box containing less than 10 ppm oxygen. Using Viton gaskets (WC mill jar set 8004, WC media 5004A, Viton gasket 39322, SPEX Sample Prep, Metuchen, NJ) the resulting 7.1 g ground powder batches were sealed in a WC mill jar with a total of six spherical WC milling media (two WC spheres 11.2 mm in diameter and four WC spheres 7.9 mm in diameter). In order to perform vibratory milling outside the glove box, prior to removing the mill jar from the glove box, the mill jar and end cap were wrapped with electrical tape (Super 88, 3m, St. Paul, MN) and Parafilm “M” (PM-996 Pechiney Plastic Packaging, Menasha WI). The powders were milled for 10 minutes in a vibratory mill (8000M SPEX SamplePrep) then the mill jar was returned to the glove box. The reading of the oxygen meter on the glove box did not change when the mill jar was opened in the glove box. The oxygen meter is sensitive to changes within ± 0.1 ppm, implying that the sealing of the mill jar was effective. The vibratory milled powder then was sintered in an argon atmosphere by PECS (SPS Model 10-3, Thermal Technology LLC, Santa Rosa, CA) in a grafoil-lined graphite die at 673 K, 723 K or 773 K for 10 minutes with 50 MPa pressure (Table 6.1), producing disk-shaped specimens approximately 12.6 mm in diameter and 2.6 mm thick.

6.2.2 Elasticity Measurements

Resonant ultrasound spectroscopy (RUS) elasticity measurements were performed using a tripod arrangement of piezoelectric transducers. A driving transducer which was swept through a range of frequency from 35 kHz to 485 kHz excited mechanical resonances in the specimen which were detected via the two pickup transducers. The peaks in the intensity versus frequency output of the pickup transducers (Figure 6.1)

Table 6.1. Specimens of skutterudite $\text{Ba}_{0.3}\text{Co}_4\text{Sb}_{12}$ used in this study varied based on Ag_{NP} addition, sintering procedure and temperature, resulting porosity, and powder processing. Specimens VM-PECS-673, VM-PECS-723 and VM-PECS-773 were reprocessed from specimens PM-HP-673, PM-HP-773 and PM-HP-873 by grinding and powder processing by vibratory milling, and sintering by PECS.

Specimen	Ag_{NP} addition	Powder processing	Sintering procedure	Sintering temperature	Vol. fraction porosity
PM-HP-673	No	PM	HP	673K	0.30
PM-HP-773	No	PM	HP	773K	0.21
PM-HP-873	No	PM	HP	873K	0.16
PM-HP-673-Ag	Yes	PM	HP	673K	0.27
PM-HP-773-Ag	Yes	PM	HP	773K	0.18
PM-HP-873-Ag	Yes	PM	HP	873K	0.05
VM-PECS-673	No	VM	PECS	673K	0.16
VM-PECS-723	No	VM	PECS	723K	0.13
VM-PECS-773	No	VM	PECS	773K	0.09

PM: Planetary milling, VM: Vibratory milling,
HP: Hot pressed, PECS: Pulsed electric current sintering

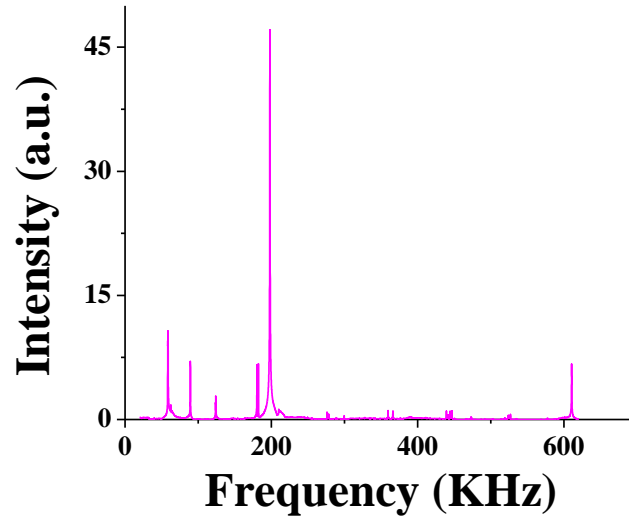


Figure 6.1. RUS spectrum from specimen PM-HP-873-Ag, $P = 0.05$ with Ag_{NP} . The elastic moduli of each of the specimens in this study are calculated from the specimen mass, dimensions, shape, and resonant frequencies. Each peak in the spectrum represents a mechanical resonance at that frequency

represent the mechanical resonance frequencies of the specimen. From the resonant frequencies, specimen mass, dimensions and geometry, the elastic moduli of the disk spaced specimens were calculated using commercial software (RUSpec and CylModel, Quasar International, Inc., Albuquerque, NM). Additional details of the RUS procedure are provided elsewhere [Ren 2009; Ni 2010; Schmidt 2010; Migliori 1997; Schmidt 2013].

6.2.3 Hardness and toughness measurements

Prior to indentation measurements of H and K_C , and prior to energy-dispersive X-ray spectroscopy measurements, the specimens were polished with diamond paste with grit sizes ranging from 30 μm to 1 μm . At least ten indentations per load for loads of 1.96 N, 2.94 N, 4.9 N and 9.8 N were made on the polished surface of each specimen, with a loading time of 5 seconds for each indentation. Prior to the hardness measurements, the Vickers indenter was calibrated using a steel standard calibration block (Yamamoto Scientific Tools Lab Co. LTD, Chiba, Japan). The hardness calibration factor, ζ , ranged from 0.95 to 0.97 for the indentation loads used in this study. The hardness, H , for indentation was calculated from [Lawn 2012]

$$H = \zeta \frac{1.8544F}{(2a)^2} \quad (2)$$

where F is the applied indentation load and a is half of the diagonal length of the indentation impression.

The fracture toughness, K_C , was calculated from

$$K_C = \frac{\xi(E/H)^{0.5} F}{c^{3/2}} \quad (3)$$

where ζ is a dimensionless calibration constant equal to 0.016 [Wachtman 2009], E is the Young's modulus measured by RUS, H is the hardness value and c is half of the radial crack length and F is the applied load [Wachtman 2009] .

6.2.4 Energy-dispersive X-ray spectroscopy and microscopy

Except for specimen PM-HP-673-Ag, each of the sintered specimens was first polished and then examined by energy-dispersive X-ray spectroscopy (EDS). However, polishing was unsuccessful for PM-HP-673-Ag, so the examined surfaces were those cut by a low speed diamond saw.

The microstructure and nanostructure of the powders and sintered specimens was observed by scanning electron microscope (SEM, JEOL 6610LV or JSM-7500F, JEOL Ltd., Japan) at a 15 kV accelerating voltage and either a 15 mm or 8 mm working distance. Using SEM micrographs of the fracture surfaces of sintered specimens, the grain size of sintered specimens was determined using the linear intercept method with at least 200 intercepts per micrograph and a stereographic projection factor of 1.5 [Underwood 1969; Case 1981]. The microstructure of the polished specimen surfaces was observed using the secondary electron image (SEI) mode. Atomic number contrast was observed in the backscattered electron image (BEI) mode. Compositions were determined in the BEI mode using EDS. For SEM observation, all specimens were mounted on aluminum stubs, where the silver nanoparticles were adhered to the stubs using carbon paint (05006-AB, SPI Supplies, West Chester, PA) and the sintered specimens were mounted using carbon tape.

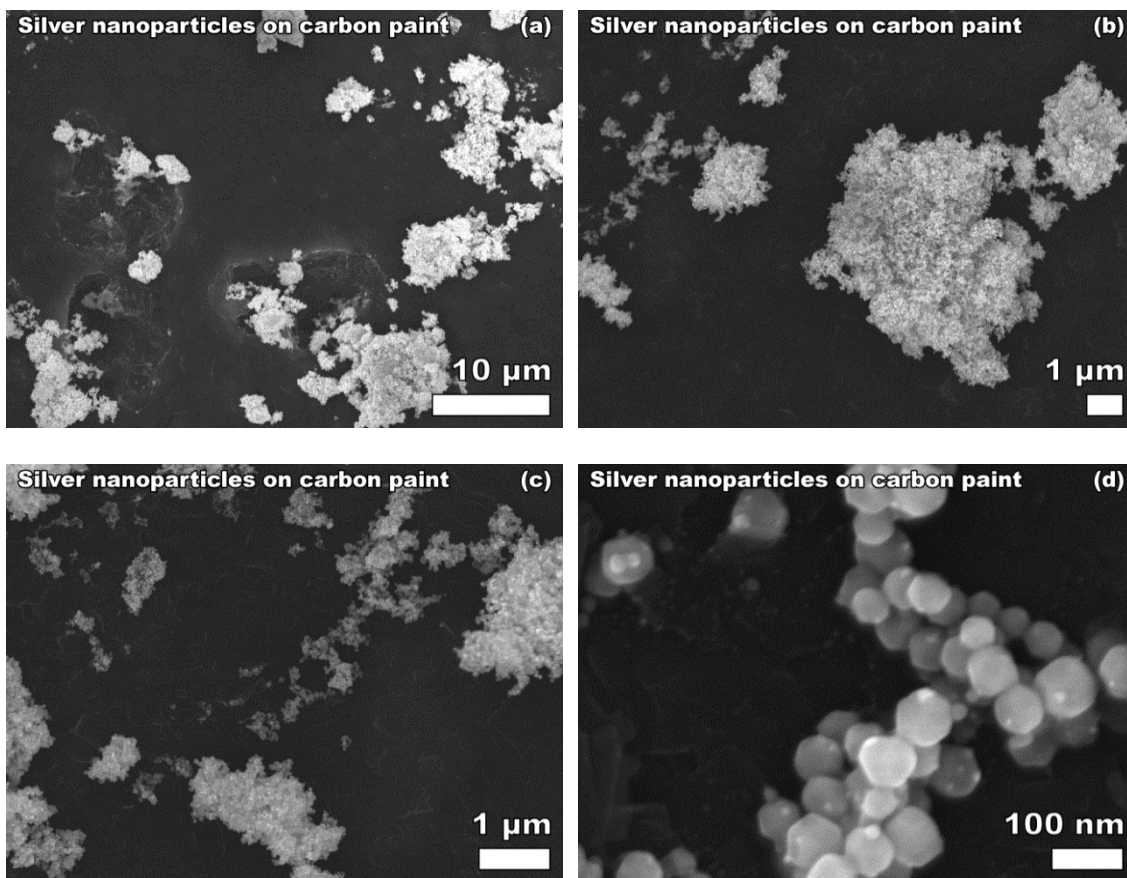


Figure 6.2. Silver nanoparticles exhibited agglomerates of 10 μm or greater (a-c), but consisting of individual grains or particles consistent with the manufacturer claimed average particle size of 20-40 nm (d)

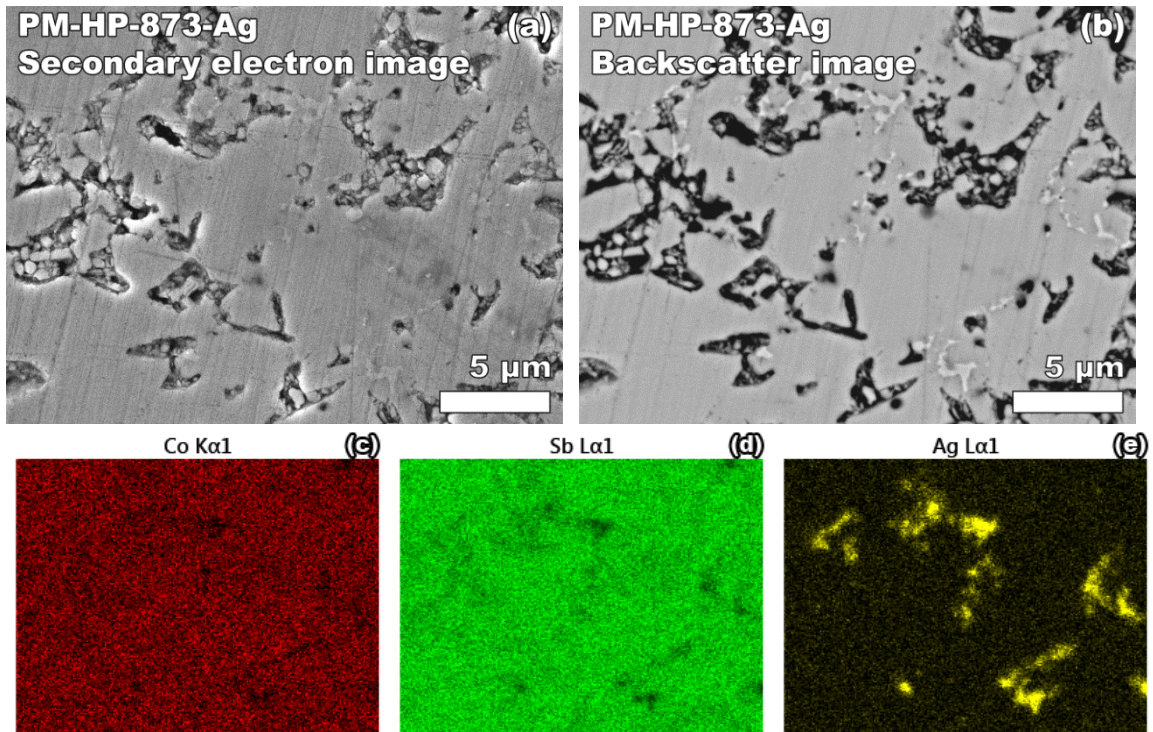


Figure 6.3. Polished surfaces of specimen PM-HP-873-Ag, both in secondary electron images (a) and backscatter images (b). Porosity is observed between larger grains (a and b), but also with areas of Ag visible in backscatter as bright areas (b), due to the higher average atomic weight of the silver rich regions. The abundance of Ag and the relative deficiency of Co or Sb in the bright areas of the backscatter image (b) is confirmed by energy-dispersive x-ray spectroscopy maps (c-e)

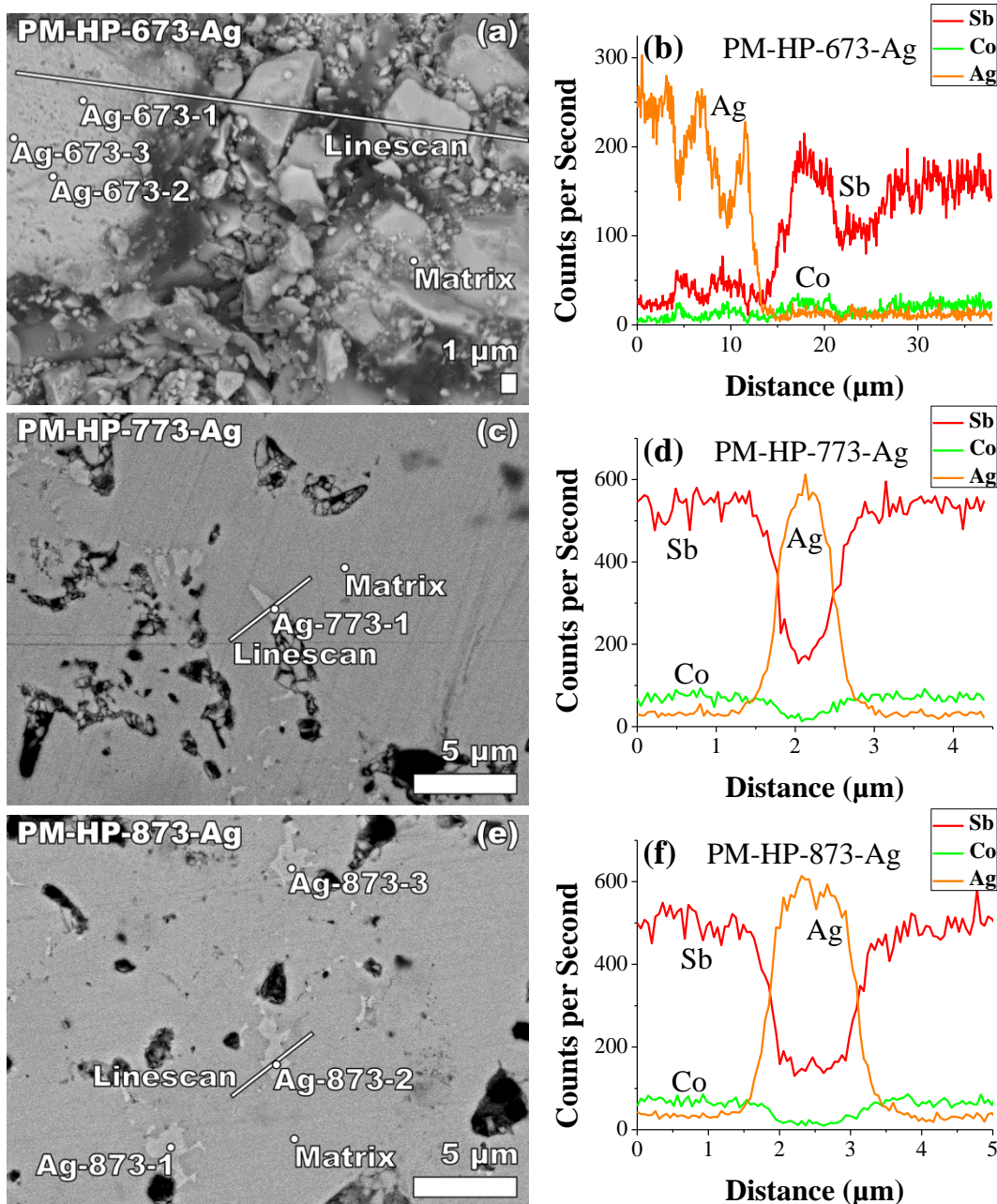


Figure 6.4. For each of the hot pressed specimens with Ag_{NP} additions, an EDS line scan was performed and point ID locations were chosen. For PM-HP-673-Ag, a cut surface was used (a) because the specimen was not successfully polished. For PM-HP-773-Ag and PM-HP-873-Ag, polished surfaces were examined (c and e). The line scan for PM-HP-673-Ag (b) indicated only silver present except for two regions in the silver where antimony and cobalt were present in concentrations consistent with skutterudite particles. In contrast, the line scan for PM-HP-773-Ag (d) and PM-HP-873-Ag (f) indicated the presence of antimony in the silver-rich locations. No silver was observed in the matrix outside of the silver-rich locations

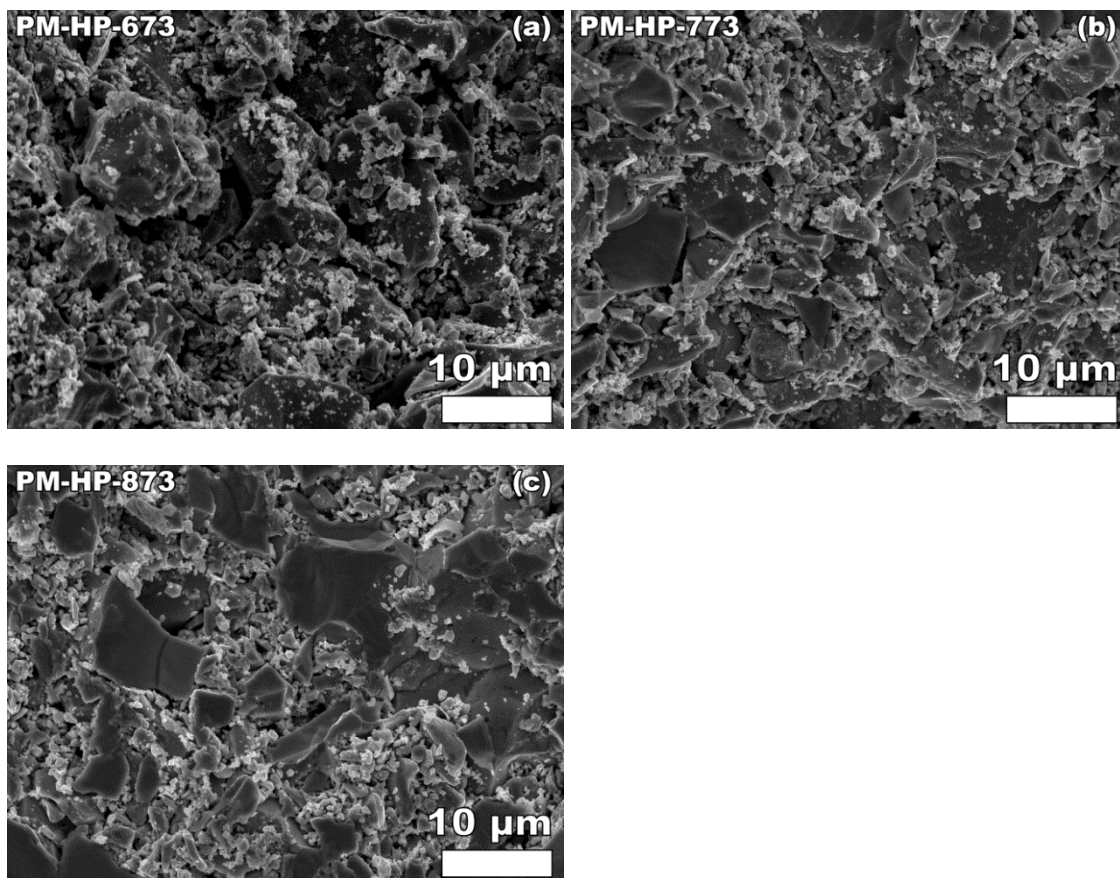


Figure 6.5. The microstructure of $\text{Ba}_{0.3}\text{Co}_4\text{Sb}_{12}$, without Ag addition, changed as a function of sintering temperature. For (a) a sintering temperature of 673 K, microstructure and porosity, P , are consistent with a specimen with little to no observed sintering or densification. After sintering at 773 K (b), only minimal densification and neck formation are observed. Hot pressing at 873 K (c) enhanced both grain growth and densification in the specimen without Ag nanoparticles, however, the microstructure still is observed to be very porous, consistent with measurement of $P = 0.16$

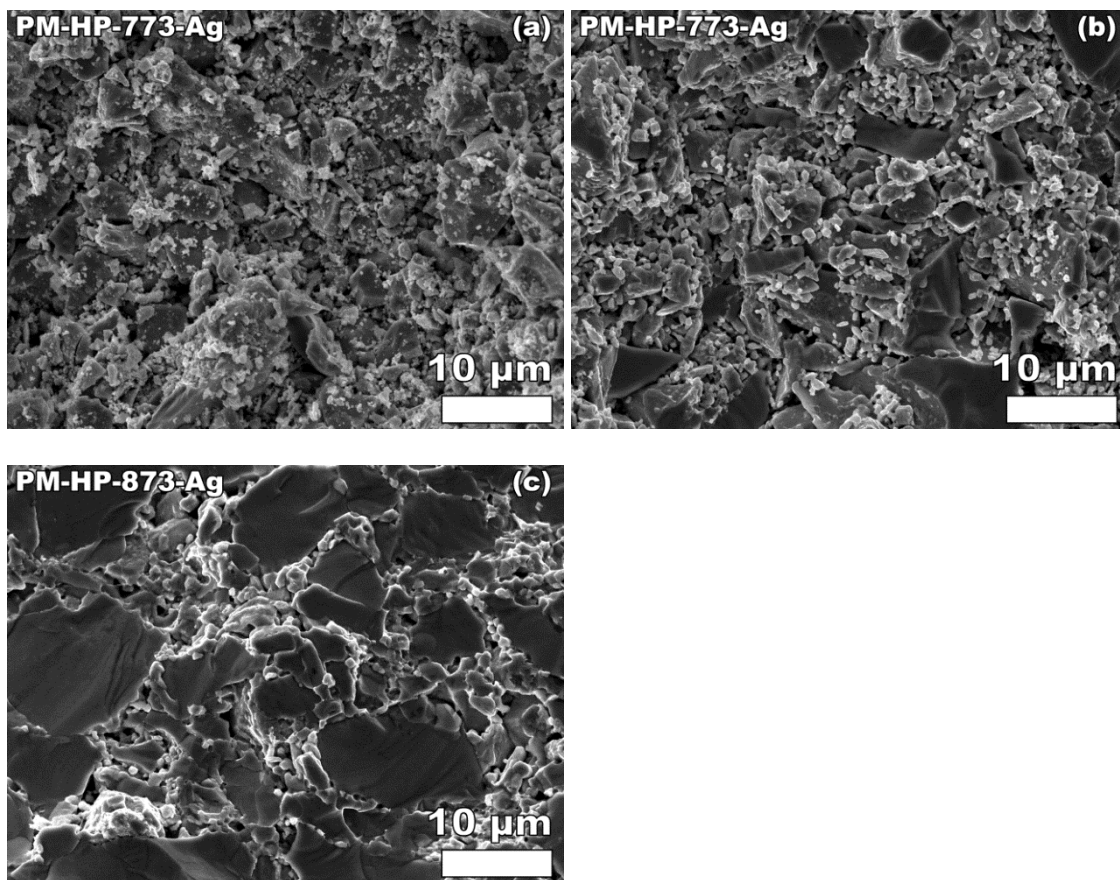


Figure 6.6. The microstructure of $\text{Ba}_{0.3}\text{Co}_4\text{Sb}_{12}$ with 0.5 wt% Ag_{NP} addition changed as a function of sintering temperature. At 673 K (a), little to no sintering is observed in the microstructure. Hot pressing at 773 K (b) resulted in limited grain growth and densification, with necks observed between the grains but significant porosity observed, consistent with early stage sintering. The porosity for the specimen with Ag nanoparticles sintered at 873 K (c) is the lowest ($P = 0.03$) of all the specimens in this study

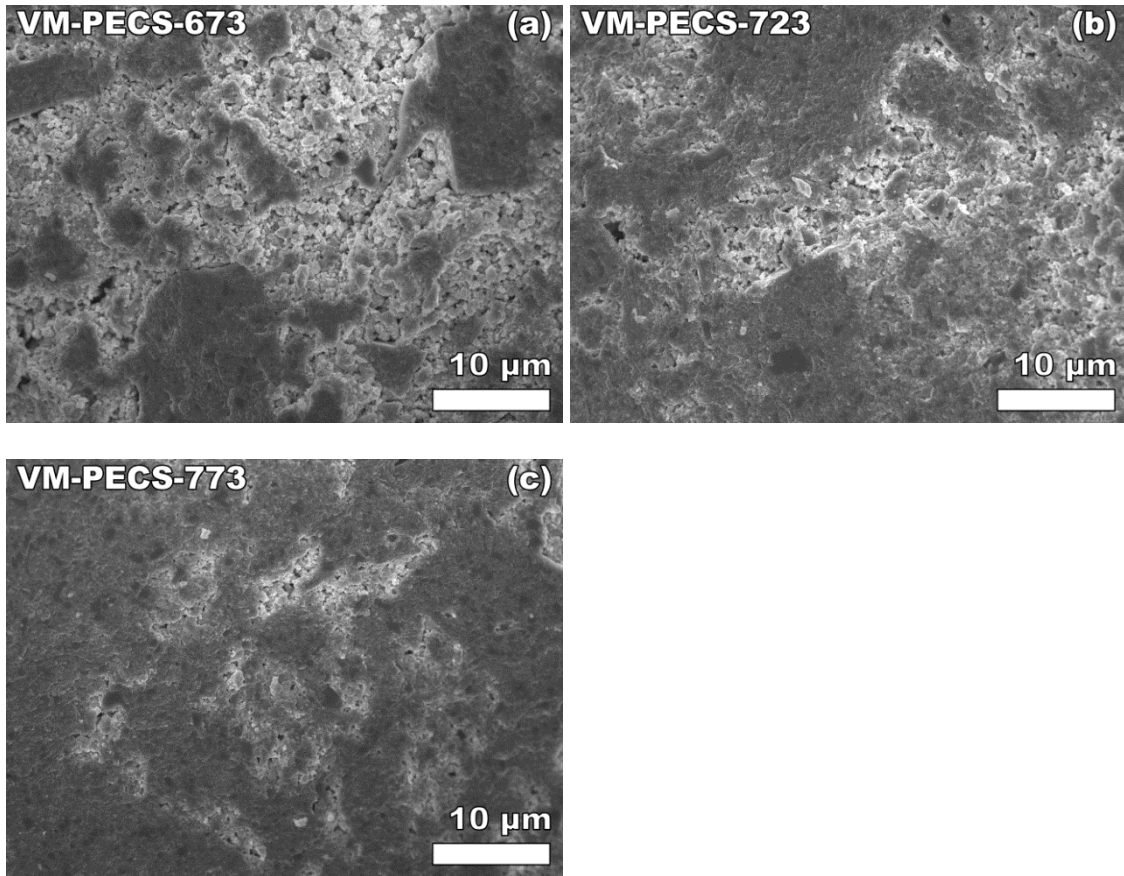


Figure 6.7. Fracture surface images of reprocessed material sintered by PECS exhibit dense regions surrounded by regions of higher porosity. All regions of the specimens exhibit similar grain sizes. The porous areas decrease as the sintering temperature increased from (a) 673 K, to (b) 723 K, to 773 K

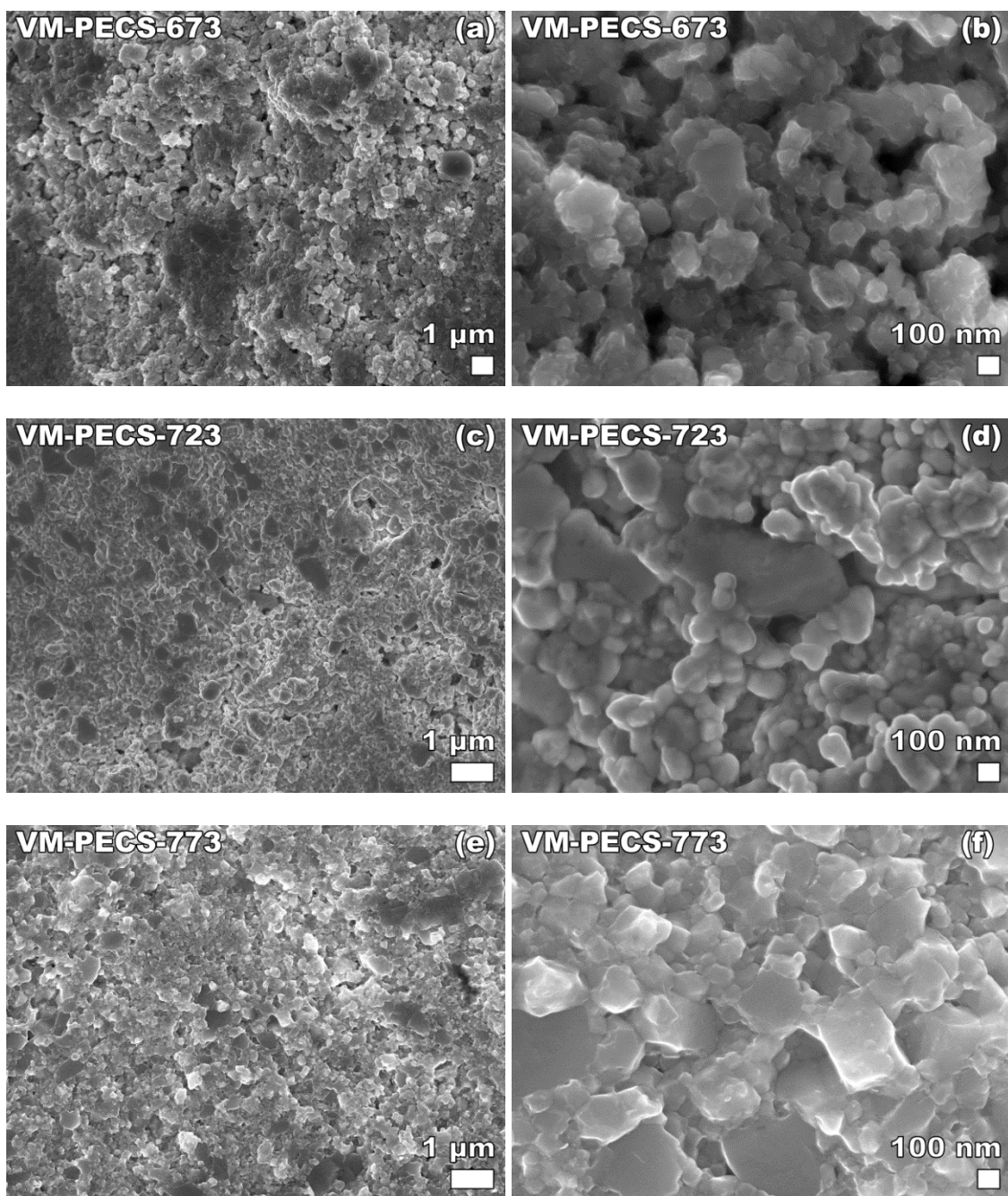


Figure 6.8. After reprocessing by SPEX milling and sintering by PECS, the samples exhibit a unimodal, sub-micron grain size distribution.

6.3 Results and Discussion

6.3.1 Microstructural and chemical analysis

The addition of Ag_{NP} resulted in a greater change in density at the higher sintering temperature than the specimen without Ag_{NP} addition (Table 6.1). When HP sintered at 673 K, the porosity was nearly identical for the specimen without ($P = 0.30$) and with Ag_{NP} ($P = 0.27$), but when sintered at 873 K, the specimen without Ag_{NP} addition ($P = 0.16$) was significantly less dense than the specimen with Ag_{NP} addition ($P = 0.05$). The density difference for specimens sintered at the same temperature requires a close examination of the microstructural features of the Ag_{NP} addition, examined in two parts.

The microstructural and nanostructural features examined in this study included:

- (i) the as-received Ag_{NP} powders (Figure 6.2), and for the sintered Ba_{0.3}Co₄Sb₁₂ specimens the micron-sized Ag inclusions (Figures 6.3 and 6.4) in section 6.3.1.1, and
- (ii) porosity (Figures 6.5 – 6.7) as well as grain size and size distribution (Figure 6.5 – 6.8) in section 6.3.1.2.

6.3.1.1 Microstructure of the Ag_{NP} and Ag agglomerates

The as-received Ag_{NP} powders consisted of (i) large, irregularly-shaped agglomerates up to 30 μm across, with most agglomerates being between 0.5 μm and 10 μm in diameter, (ii) individual spherical nanoparticles with diameters 30 nm (Figure 6.2d) and (iii) small clusters of nanoparticles (Figure 6.2). Similar agglomerates, small clusters and individual Ag_{NP} are visible in micrographs taken by Zhou (Figure 2a of Zhou 2012]) of Ag_{NP} powders received from the same vendor as in this study.

After hot pressing at 673 K, 773 K and 873 K, the consolidated, micron-size Ag particles observed in the Ba_{0.3}Co₄Sb₁₂ specimens with 0.5 wt% Ag_{NP} (Figures 6.3 and

6.4) had roughly the same dimensions as the original Ag_{NP} agglomerates present in the as-received Ag_{NP} powders (Figure 6.2). In the sintered specimens, the typical dimension of Ag particles observed in PM-HP-773-Ag and PM-HP-873-Ag was between 0.3 μm and 10 μm , with a few Ag particles of 20 μm diameter or greater, as observed by backscatter electron images of polished surfaces (Figures 6.3 and 6.4). Thus the Ag_{NP} agglomerates may not have broken up significantly during mixing in the planetary mill prior to hot pressing.

As a rough gauge of how easily the Ag_{NP} agglomerates can be broken apart by milling, 0.0225g of Ag_{NP} was wet milled by hand for 60 sec in a porcelain mortar and pestle (60310 and 60311, CoorsTek, Golden, CO) with 5 mL of ethanol. After milling, the Ag_{NP} agglomerates were still present but some surfaces of the agglomerate surfaces appeared to be deformed by the hand milling and some of the nanoparticles on the deformed surfaces of the agglomerates appeared to be smeared (Figure 6.9). After hand milling, the Ag_{NP} agglomerates typically ranged in diameter from sub-micron to 100 μm (Figure 6.9), similar to or greater than the dimensions of Ag_{NP} agglomerates before milling. Thus, based on both the SEM examination of the Ag_{NP} agglomerates before and after hand milling, the hand milling process did not appear to significantly break up the agglomerates.

While the hand milling conditions are likely different than those encountered during the planetary milling, it is likely that some of the original Ag_{NP} agglomerates in the as-received powders survived (at least partially intact) the mixing process with the Ag_{NP} agglomerates powders to give the micron-sized consolidated Ag particles observed in the as-sintered Ba-skutterudite-Ag_{NP} specimens in this study. This is further

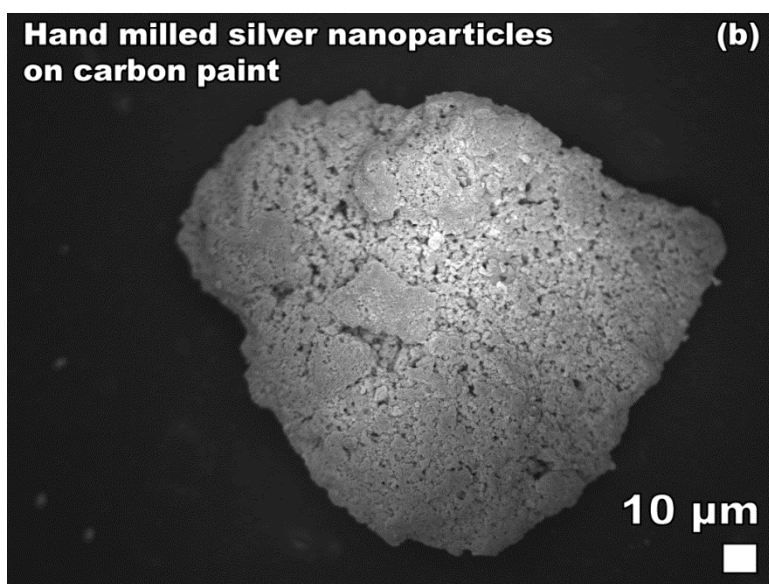
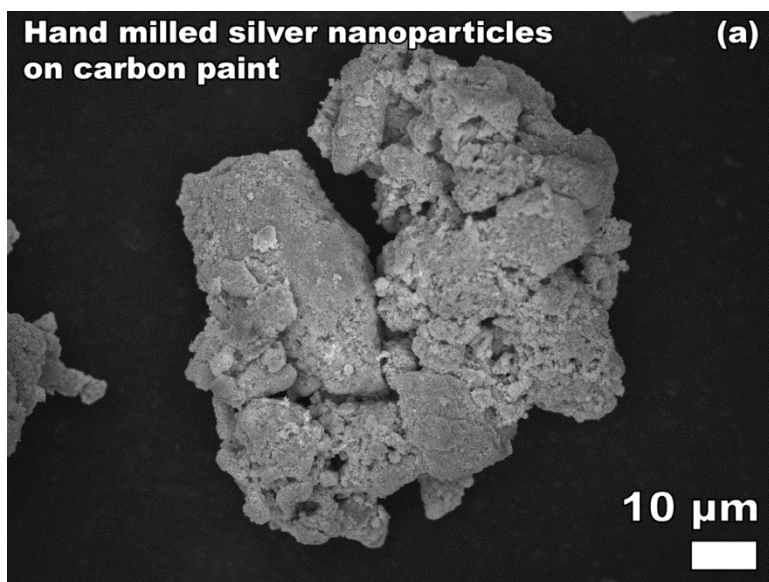


Figure 6.9. Hand milling of Ag_{NP} agglomerates in ethanol were not observed to reduce the size of the nanoparticle agglomerates. After hand milling, silver nanoparticle agglomerates of 10 μm or greater were typically observed, similar to the size of agglomerates for the as received Ag_{NP}. Several faces of the agglomerates appear to be deformed after hand milling

supported by the SEM-based observation that the size of the Ag_{NP} agglomerates in the powders is similar to the size of the Ag particles in the sintered specimens. Thus, it does not seem to be necessary to postulate an accretion of Ag_{NP} during milling to explain the present of micron-sized Ag particles in the sintered specimens.

6.3.1.2 Porosity and grain size and relationship to the processing technique

The six hot pressed specimens included this study (Table 6.1) showed a bimodal grain size distribution (Figures 6.5 and 6.6) consisting of a polycrystalline matrix with grain sizes ranging from approximately 0.3 μm to 3 μm , with an average grain size (*GS*) of roughly 1 μm . Also, grains approximately 5 μm to 20 μm across were observed in each HP specimen, both without Ag_{NP} (Figure 6.5) and with Ag_{NP} (Figure 6.6) additions. Pores with diameters of submicron to a few microns across were distributed through the matrix, consisting of open, interconnected porosity when sintered at 673 K, and consisting of partially to fully isolated porosity at 773 K and 873 K (Figures 6.5 and 6.6). The observed pore morphologies for the specimens sintered at 673 K, 773 K and 873 K agrees with the pore evolution in sintered powders [Barsoum 2003].

Each of the three reprocessed specimens (vibratory milled and then sintered via PECS at 773 K, 723 K and 673 K) had a much different microstructure than those obtained by planetary milling and hot pressing. Namely, the VM-PECS specimens a unimodal *GS* distribution (Figure 6.8) with a significantly smaller average *GS* of 0.17 μm , 0.14 μm , and 0.15 μm , respectively, than the specimens that were planetary milled and hot pressed. The reprocessed specimen VM-PECS-773 had a volume fraction porosity of only 0.09, which included dense regions with clusters of pores (Figure 6.7c). However, specimen VM-PECS-673 included clusters of pores with islands of denser

material (Table 6.1, Figures 6.7a). The microstructure of specimen VM-PECS-723 was intermediate in between specimens VM-PECS-773 and VM-PECS-673 (Table 6.1, Figures 6.7b).

The addition of Ag_{NP} results in an increased density of hot pressed specimens at a sintering temperature of 873 K, where the specimen without Ag_{NP} had a *P* value of 0.16 while the specimen sintered with 0.5 wt% Ag_{NP} had *P* = 0.05 (Table 6.1). At a hot press sintering temperature of 773 K, the porosities of the specimens with and without 0.5 wt% Ag_{NP} were 0.18 and 0.21, respectively (Table 6.1). Also, for a sintering temperature of 673 K, the porosities of the specimens with and without 0.5 wt% Ag_{NP} were 0.27 and 0.30, respectively (Table 6.1). Thus, hot press sintering at 773 K and 673 K resulted in similar porosities for specimens with and without 0.5 wt% Ag_{NP} additions. However, the Ag_{NP} addition resulted in considerably enhanced densification for hot press sintering at 873 K. The enhanced sintering is likely related to a reaction between the 0.5 wt% Ag_{NP} addition and the Ba_{0.3}Co₄Sb₁₂ matrix, as discussed in section 6.3.2.

6.3.2 Chemical analysis

6.3.2.1 Chemistry of the Ag_{NP} and Ag agglomerates

EDS analysis showed the as-received Ag_{NP} powder to be 99.5 at% Ag, with oxygen and Al impurities (Table 6.2). The Al in the EDS analysis likely originated from the aluminum stub on which the specimens were mounted.

Polished surfaces of specimens PM-HP-873-Ag and PM-HP-773-Ag were examined by EDS, with matrix region and Ag-rich regions in each specimen examined separately at the points indicated in Figures 6.4c and 6.4e, and line scans extending

Table 6.2 Results of EDS scan using Point ID mode on two as-received Ag_{NP} agglomerates.

Location label	Ag	Al	O	Ag:Al
AgNP-1	85.15	0.60	14.25	99.3:0.7
AgNP-2	99.5	0.5	Not Detected	99.5:0.5

Table 6.3 Results of EDS scan using Point ID mode on specimen PM-HP-873-Ag. Spacing between spots is approximately 5 to 10 μm (Figure 6.4e). Ag areas examined are 1-3 μm in diameter.

Location label	Ba	Co	Ag	Sb	O
Matrix	1.69	21.54	Not Detected	76.78	Not Detected
Ag-873-1	Not Detected	1.28	73.96	24.76	Not Detected
Ag-873-2	Not Detected	Not Detected	76.78	23.22	Not Detected
Ag-873-3	Not Detected	1.37	71.82	22.54	6.78

Table 6.4 Results of EDS scan using Point ID mode on specimen PM-HP-773-Ag. Spacing between spots is approximately 4 μm (Figure 6.4c). Ag area examined approximately 1-3 μm in diameter.

Location label	Ba	Co	Ag	Sb	O
Matrix	2.14	23.96	Not Detected	73.89	Not Detected
Ag-773-1	Not Detected	2.49	70.01	27.50	Not Detected

Table 6.5 Results of EDS scan using Point ID mode on specimen PM-HP-673-Ag. Spacing between spots is approximately 5 to 10 μm (Figure 6.4a). Ag area examined is approximately 20 μm in diameter.

Location label	Ba	Co	Ag	Sb	O
Matrix	1.44	21.01	Not Detected	77.56	Not Detected
Ag-673-1	Not Detected	6.80	72.21	20.99	Not Detected
Ag-673-2	Not Detected	Not Detected	92.99	7.01	Not Detected
Ag-673-3	Not Detected	Not Detected	94.21	5.79	Not Detected

across both matrix material and Ag-rich regions (Figure 6.4c – 6.4f). As determined by EDS, the elemental composition of the matrix region is consistent with $\text{Ba}_{0.3}\text{Co}_4\text{Sb}_{12}$ (Tables 6.3 and 6.4, Figure 6.4c – 6.4f). In the Ag-rich regions, the composition is consistent with primarily Ag_3Sb phase material. In specimen PM-HP-873-Ag, the Ag:Sb ratio was 3.0:1 to 3.3:1 in the silver-rich regions (Table 6.3, Figure 6.4e), and in specimen PM-HP-773-Ag, the ratio was 2.5:1 (Table 6.4, Figure 6.4c). Less than 2 at% Co was detected in each of the silver-rich regions, consistent with little to no skutterudite phase present in the silver-rich regions.

In contrast to the preparation of specimens PM-HP-873-Ag and PM-HP-773-Ag, specimen PM-HP-673-Ag was cut on a low speed diamond saw because the high porosity of the specimen ($P = 0.27$, Table 6.1) made it too friable for polishing. The elemental composition of the matrix region is consistent with $\text{Ba}_{0.3}\text{Co}_4\text{Sb}_{12}$ (Table 6.5, Figure 6.4a and 6.4b). In the Ag-rich regions of PM-HP-673-Ag, the Ag:Sb ratio was highly variable, with ratios of 3.4:1, 13.3:1 and 16.3:1 (Table 6.5), which is more indicative of a mixture than a single phase. In the Ag-rich location with the highest concentration of Sb, Ag-673-1, a significant concentration of Co was also detected, 6.80 at%, and in a Co:Sb ratio of 1:3.1 (Table 6.5), consistent with a particle or particles of $\text{Ba}_{0.3}\text{CoSb}_3$ (matrix material) embedded in otherwise pure Ag. Particles of $\text{Ba}_{0.3}\text{CoSb}_3$ may have become embedded in the Ag-rich region during cutting. The presence of small, discrete skutterudite particles embedded in the silver in specimen PM-HP-673-Ag is further supported by the line scan (Figure 6.4b), in which there are two dips in the counts of silver at distances of 5 μm and 10 μm , with corresponding increases of both Co and Sb counts at each location. The EDS results from the other two Ag-rich locations, Ag-673-2

and Ag-673-3 (Table 6.5), are primarily pure Ag material, with no indication of embedded $\text{Ba}_{0.3}\text{CoSb}_3$ particles.

6.3.2.2 Sintering behavior changes and scavenging of Sb

Although the $\text{Ba}_{0.3}\text{Co}_4\text{Sb}_{12}$ -Ag composition is within a quaternary Ba-Co-Sb-Ag system for which no phase diagram is available, the Ag-Sb binary phase diagram may provide important guidance to understanding the formation of Ag_3Sb particles. In the binary phase diagram for Ag-Sb, there are only two intermediate compounds, Ag_3Sb and Ag_6Sb [Voronin 2013; Cipriani 1996; Feschotte 1992]. Upon cooling, Ag_3Sb forms via a peritectic reaction $\text{Ag}_6\text{Sb} + L \Leftrightarrow \text{Ag}_3\text{Sb}$ at 835 ± 2 K and an initial Sb concentration of 21.2 at% [Feschotte 1992]. Also, the eutectic reaction $L \Leftrightarrow \text{Ag}_3\text{Sb} + \text{Sb}$ occurs at 757 K with a eutectic composition reported as 38 at% Sb [Voronin 2013; Okamoto 2007; Hassam 2001] or 41 at% Sb [Okamoto 1993].

In the present research, the Sb that reacts with the Ag_{NP} may be scavenged from the $\text{Ba}_{0.3}\text{Co}_4\text{Sb}_{12}$ matrix. Scavenging of excess Sb can aid thermal stability in skutterudites. For example, Zhang and Sakamoto found that the Sb deficient specimens of $\text{Fe}_{3.5}\text{Co}_{0.5}\text{Sb}_{12}$ -based skutterudites were more dimensionally stable than specimens with excess Sb [Zhang 2013].

The presence of a transient liquid phase is known to greatly enhance densification during sintering [Barsoum 2003], thus the enhanced densification for the Ba-skutterudite- Ag_{NP} specimens observed in this study (section 3.1, Table 6.1) may be due to a transient liquid phase during sintering associated with the peritectic and eutectic reactions in the Ag-Sb system. Also, if the liquid phase wets the grain boundaries, the electrical conductivity of the grain boundaries could be greatly enhanced, by a surface film rather

than only point contacts due to discrete Ag_{NP} or Ag particles, as was suggested by Zhao et al. [Zhou 2012]. A similar binary and ternary eutectic in lead-free Sn-Ag-Cu solders aids in wetting the surfaces of electrical wires, pins or pads [Bukat 2011; Dharma 2009].

6.3.2.3 Possible significance to other thermoelectric material systems

The proposed reaction of Ag with Sb in Ba-filled skutterudite Ba_{0.3}Co₄Sb₁₂ has important implications for other skutterudites, other antimonides and even other thermoelectric systems. In this study the Ba-filled skutterudite is CoSb₃-based, but more generally unfilled skutterudites have the general composition TX₃, where T is a transition metal element (Co, Fe, Ni) and X is a pnictogen element (Sb, As, and P) [Yoshizawa 2004]. “Filler” atoms, often a rare earth element or mischmetal added to the skutterudite composition, scatter phonons to make them an important class of thermoelectric materials [Slack 1994; Morelli 1995; Nolas 1999; Nolas 2000; Uher 2001]. Many CoSb₃-based and FeSb₃-based compositions have been studied in the literature [Zhang 2010], so in addition to the particular Ba-filled skutterudite included in this study, adding Ag_{NP} to other antimonide skutterudites may well lead to the same type of Ag-Sb reaction and thus liquid phase sintering, the formation of Ag₃Sb, enhanced densification and improvements in the *ZT* and electrical conductivity. Also, for an antimonide thermoelectric that is not a skutterudite, a recent study by [Xiong 2013] shows that Ag added to ZnSb leads to the formation of Ag₃Sb particles and a higher electrical conductivity.

This type of reaction may not be limited to Ag and antimonides. In fact, there may be other conductive metal-thermoelectric material combinations in which similar peritectic/eutectic reactions occur, accompanied by similar beneficial effects. One guide to searching for such systems would be appropriate binary or ternary phase diagrams.

6.3.3 Elasticity results

The measured elastic moduli are essentially independent of the Ag_{NP} addition and the processing/grain size, but are strong functions of porosity (Figure 6.10a-c).

6.3.3.1 Elasticity as a function of Ag_{NP} addition

In order to determine whether or not the elastic moduli are functions of the Ag_{NP} addition, for the set of specimens (with and without Ag_{NP} addition) included in this study, we examined the porosity dependence of Young's modulus, shear modulus and bulk modulus (Table 6.1, Figure 6.10). There are no significant differences between the slope and intercept for the least squares fit to the data (i) with and (ii) without Ag_{NP} additions, with coefficient of determination, R^2 , values of 0.955 to 0.998 for E and G , and R^2 of 0.857 and 0.947 for B (Figure 6.10).

To put the elasticity dependence on Ag_{NP} addition into context, the literature shows that the elastic modulus as a function of the overall composition depends on the physical nature of the material system itself, where compositional changes can occur when one has (i) a composite system in which discrete particles are added to a matrix of differing composition or (ii) a solid solution system or (iii) a solid solution system that includes micro- or nano scale particles. Changes in elastic moduli of a particulate composite as a function of the addition of a given volume percent of particulate phase has been modeled by a number of researchers [Hashin 1962; Halpin 1992; Bedolla 2012; Couturier 1997] (Appendix A). The four composite models given in Appendix A predict a decrease in the elastic modulus of the composite, E_C of about 0.39% with the 0.5 wt% Ag_{NP} addition to the Ba-skutterudite in this study.

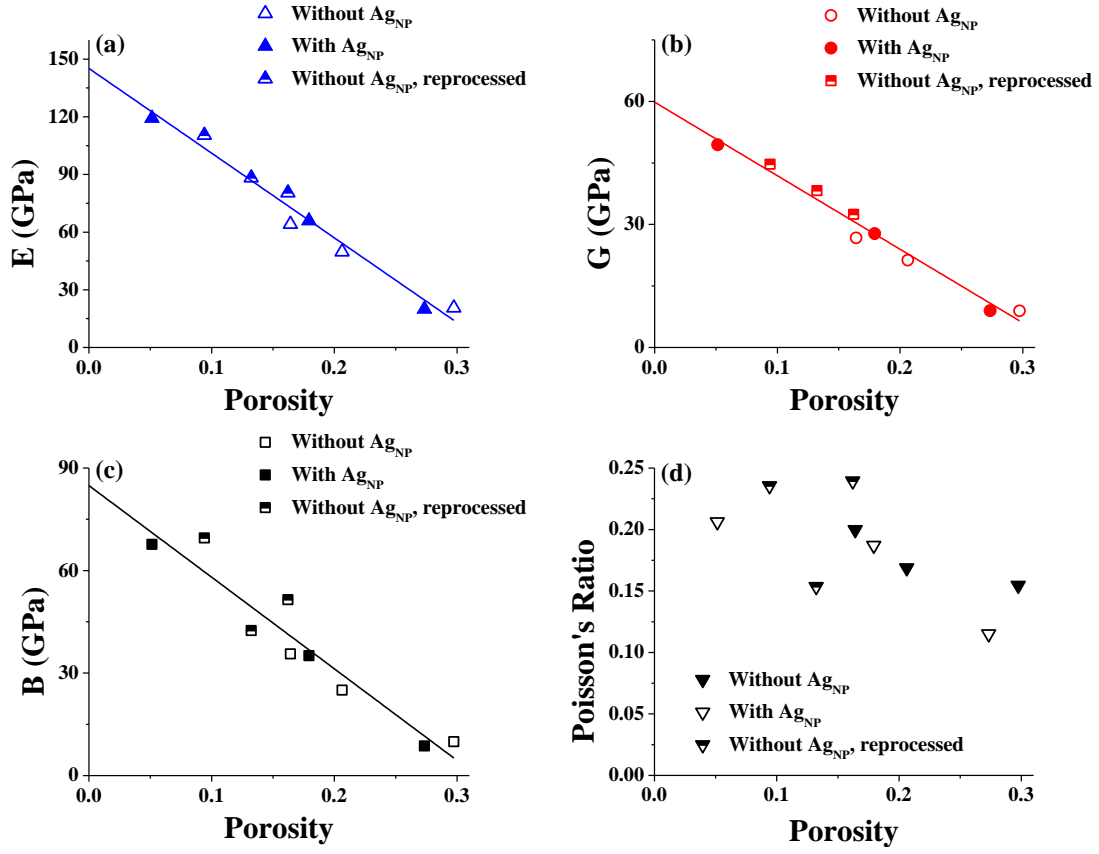


Figure 6.10. The (a) Young's modulus, E , (b) shear modulus, G , and (c) bulk modulus, B , are each a function of porosity. In each figure, the solid lines represent a least-squares fit to equation (5b). The Poisson's ratio (d) is observed to be a weak function of porosity. The elastic moduli were not observed to be a function of the addition of 0.5 wt% Ag_{NP} or of reprocessing

Table 6.6. The linear decrease in elastic moduli, E, G, and B, according to equation (5b), for this study of $\text{Ba}_{0.3}\text{Co}_4\text{Sb}_{12}$ is consistent with the limited information available in the literature for porosity dependence of elastic moduli for thermoelectric materials [Schmidt 2013; Ni 2009].

Material	A_0 (GPa)	b	N	P_{range}	R^2	Reference
$\text{Ba}_{0.3}\text{Co}_4\text{Sb}_{12} + 0.5$ wt% Ag_{NP} , E	143 ± 4 (E_0)	3.11 ± 0.08	3	0.05-0.27	0.998	This study
$\text{Ba}_{0.3}\text{Co}_4\text{Sb}_{12}$, E	146 ± 9 (E_0)	3.00 ± 0.16	6	0.09-0.30	0.955	This study
YbAl_3 , E	174.0 ± 2.5 (E_0)	2.34 ± 0.06	7	0.03-0.23	0.994	[Schmidt 2013]
LAST, E	58.3 ± 0.3 (E_0)	3.6 ± 0.1	12	0.01-0.14	0.994	[Ni 2009]
$\text{Ba}_{0.3}\text{Co}_4\text{Sb}_{12} + 0.5$ wt% Ag_{NP} , G	59 ± 2 (G_0)	3.07 ± 0.08	3	0.05-0.27	0.998	This study
$\text{Ba}_{0.3}\text{Co}_4\text{Sb}_{12}$, G	60 ± 3 (G_0)	2.96 ± 0.15	6	0.09-0.30	0.962	This study
YbAl_3 , G	73.6 ± 0.9 (G_0)	2.38 ± 0.06	7	0.03-0.23	0.995	[Schmidt 2013]
LAST, G	22.9 ± 0.1 (G_0)	3.5 ± 0.1	12	0.01-0.14	0.991	[Ni 2009]
$\text{Ba}_{0.3}\text{Co}_4\text{Sb}_{12} + 0.5$ wt% Ag_{NP} , B	82 ± 2 (B_0)	3.25 ± 0.05	3	0.05-0.27	0.999	This study
$\text{Ba}_{0.3}\text{Co}_4\text{Sb}_{12}$, B	87 ± 10 (B_0)	3.14 ± 0.31	6	0.09-0.30	0.857	This study
YbAl_3 , B	91.3 ± 2.9 (B_0)	2.22 ± 0.14	7	0.03-0.23	0.947	[Schmidt 2013]

6.3.3.2 Elastic moduli and porosity

The elastic moduli of the skutterudite $\text{Ba}_{0.3}\text{Co}_4\text{Sb}_{12}$ in this study are linear functions of porosity over the range of volume fraction porosity included in this study (between 0.05 and 0.30, Table 6.6, Figure 6.10). In addition, the elastic modulus versus porosity data is independent of either the presence or absence of the 0.5 wt% Ag_{NP} (Table 6.6, Figure 6.10). Also, the powder processing technique (planetary milling or vibratory milling) and the densification method (hot pressing or PECS (Table 6.1)) does not affect the elastic modulus versus porosity behavior (Table 6.6, Figure 6.10).

The elastic moduli of TE materials are porosity dependent [Schmidt 2013; Ni 2009]. An empirical expression frequently used to describe the porosity dependence of Young's modulus, E , shear modulus, G , and bulk modulus, B [Schmidt 2013; Ni 2009] of brittle materials [Rice 1998], including TE materials [Schmidt 2013; Ni 2009]

$$A = A_0(\exp(-b_AP)) \quad (5a)$$

where A represents the property E , G , or B [Rice 1998] and b_A is a unitless, material-dependent parameter that measures the rate of decrease in property A with increase P . If b_AP is small, the equation may be linearized by using the first two terms of the Taylor series expansion of equation (5a) [Schmidt 2013].

$$A = A_0(1 - b_AP) \quad (5b)$$

For the nine $\text{Ba}_{0.3}\text{Co}_4\text{Sb}_{12}$ specimens in this study (with and without Ag_{NP} addition), a least-squares fit of the modulus data to equation (5b) yielded $P = 0$ intercept values of $E_0 = 145.1 \pm 5.2$ GPa, $G_0 = 59.8 \pm 2.0$ GPa, and $B_0 = 84.9 \pm 5.9$ GPa with coefficients of determination, R^2 , of at least 0.90 for E , G , and B . There is no significant difference between the $P = 0$ intercept for the three specimens with 0.5 wt% Ag_{NP} as

compared to the six specimens without Ag_{NP} addition (Table 6.6). Also, the rate of decrease in modulus with porosity (given by b_A in equation (5b)) was between 3.0 and 3.2 for the Ba_{0.3}Co₄Sb₁₂ (Table 6.6), which is consistent with values of 2 to 6 for a wide range of solid materials [Rice 1998].

Although the data for the porosity dependence of elastic moduli of thermoelectric materials is relatively limited, modulus versus P data is available for YbAl₃ [Schmidt 2013], LAST [Ni 2009] (Table 6.6) and several for Co₄Sb₁₂-based skutterudites other than the Ba-filled skutterudite included in this study (Figure 6.11) [Zhang 2010]. The b_A values for the Ba-filled skutterudite for E , G , and B in this study are bracketed by the b_A values for YbAl₃ and LAST for the corresponding moduli (Table 6.6). Also, the elastic modulus-porosity behavior for Ba_{0.3}Co₄Sb₁₂ in this study is quite similar to that reported by Zhang [Zhang 2010] for other Co₄Sb₁₂-based skutterudites (Figure 6.11).

In this study, Poisson's ratio is insensitive to P for porosities $P < \text{approximately } 0.20$, but there is considerable scatter in the data (Figure 6.10d). For two previous studies of TE materials, the Poisson's ratio for LAST [Ni 2009] and YbAl₃ [Schmidt 2013] was essentially constant or weakly decreasing with increasing P , for P less than 0.15 or 0.12.

In this study, the scatter in Poisson's ratio (Figure 6.10d) is typical of observations for porous ceramics [Ramakrishnan 1993; Boccaccini 1994], and the observed relative decrease in Poisson's ratio at P greater than about 0.20 may be reasonably expected. Ramakrishnan and Arunachalam developed a model using 2-dimensional finite element simulation showing Poisson's ratio approaches 0.25 as porosity increases [Ramakrishnan 1993]. However, the model does not agree with the

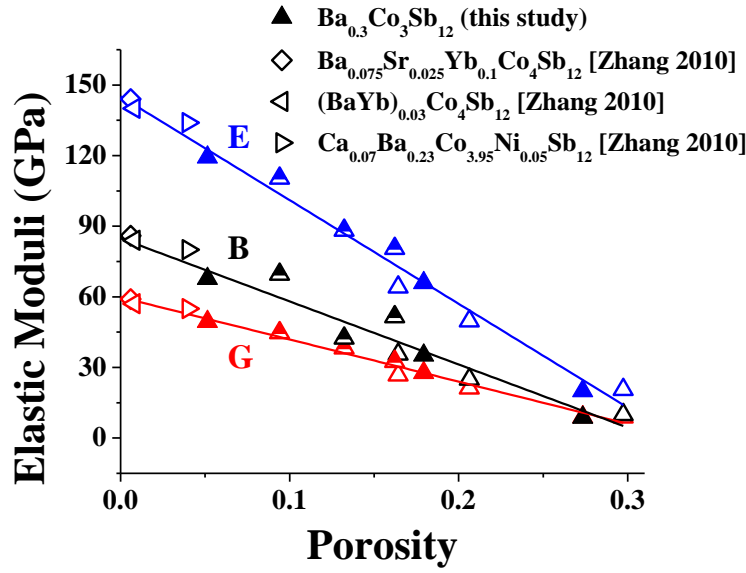


Figure 6.11. The elastic moduli for the exact composition of skutterudite in this study are not recorded in literature, however the moduli for specimens of similar composition [Zhang 2010] are consistent with the porosity dependent elastic moduli relationships observed in this study. Filled symbols indicate specimens with 0.5 wt% Ag_{NP} , unfilled for specimens without any Ag_{NP} , and half-filled symbols for reprocessed specimens without any Ag_{NP} . The solid lines represent a least squares fit to equation (5b) of the data in this study

available data on porous ceramics [Boccaccini 1994], and may be limited by the nature of the model, ignoring the heterogeneity of porosity [Rice 1995]. Furthermore, Rice argues that any model should converge to 0 for $P = 1$, and argues that Poisson's ratio should generally decrease when approaching higher values of P [Rice 1995]. In an examination of both pore shape and P , Dunn and Ledbetter determine that Poisson's ratio may increase, decrease or remain unchanged, depending on pore shape and distribution [Dunn 2011]. Thus for a Poisson's ratio in the range of about 0.20 to 0.25 (for the pore-free material), the experimental observations [Ramakrishnan 1993; Boccaccini 1994; Rice 1995] and theoretical predictions [Ramakrishnan 1993; Dunn 2011] agree that Poisson's ratio is nearly independent of P (for spherical pores) over the interval from approximately $0 < P < 0.20$, which agrees with behavior observed for the Ba-skutterudites in this study (Figure 6.10d).

6.3.3.3 Elastic moduli and grain size/processing effects

There was no observed difference between porosity dependent modulus behavior of the reprocessed specimens and the HP specimens (Figure 6.10). The elastic moduli of the skutterudite $\text{Ba}_{0.3}\text{Co}_4\text{Sb}_{12}$ in this study (Figure 6.10) are not functions of grain size (Figures 6.5-6.8, Table 6.7) or processing (Table 6.1). Grain size varied from bimodal with grains up to approximately 20 μm across (Figures 6.5 and 6.6, Table 6.7) to less than 0.2 μm (Figures 6.7 and 6.8, Table 6.7), based on processing by PM and HP, or reprocessed by VM and PECS (Table 6.1).

The bimodal grain size distribution is not expected to influence the elastic moduli of the material, as the elastic moduli of materials with grain sizes greater than approximately 20 nm are typically not a function of grain size [Kim 1999].

Table 6.7. For CoSb₃-based thermoelectric materials, a comparison of the K_C results from this study with the literature, including the porosity, P , the grain size, GS , of the specimens and the K_C measurement technique [Ravi 2009; Eilertsen 2013; Rogl 2011].

Material	K_C (MPam ^{0.5})	P	GS (μm)	K_C measurement method	Reference
Ba _{0.3} Co ₄ Sb ₁₂	0.8 - 1.3	0.09 - 0.20	Bimodal ^a , 0.14-0.17	Vickers indentation	This study
Ba _{0.3} Co ₄ Sb ₁₂ - 0.5 wt% Ag	1.0 - 1.3	0.05 - 0.18	Bimodal ^a	Vickers indentation	This study
CoSb ₃	1.7	< 0.01	NA	Chevron notch bend	[Ravi 2009]
CeFe ₃ - xRu _x Sb ₁₂	1.1 - 2.8	< 0.01	NA	Chevron notch bend	[Ravi 2009]
CoSb ₃	0.82 \pm 0.11	Nearly dense	1-2 μm , 15 μm	Vickers indentation	[Eilertsen 2013]
CoSb ₃	0.52 \pm 0.04	Nearly dense	1-2 μm , 15 μm	Crack opening displacement	[Eilertsen 2013]
CoSb ₃	0.51 \pm 0.06	Nearly dense	15 μm	Single-edge vee- notch bend	[Eilertsen 2013]
0.1In CoSb ₃	0.46 \pm 0.13	Nearly dense	15-40 μm	Vickers indentation	[Eilertsen 2013]
0.1In CoSb ₃	0.49 \pm 0.03	Nearly dense	15-40 μm	Crack opening displacement	[Eilertsen 2013]
0.1In CoSb ₃	0.57 \pm 0.06	Nearly dense	15 μm	Single-edge vee- notch bend	[Eilertsen 2013]
Fe ₄ Sb ₁₂ - and Fe ₃ CoSb ₁₂ - based ^b	1.5 to 2.2	Typically < 0.02 ^b	NA	Vickers indentation	[Rogl 2011]

NA: Information not available

^a Bimodal specimens had matrix grain sizes of 0.3 μm to 3 μm , with larger grains approximately 5 μm to 20 μm across

^b DD_{0.88}Fe₄Sb₁₂, $P = 0.014$; Ca_{0.41}DD_{0.41}Fe₄Sb₁₂, $P = 0.015$; Ba_{0.44}DD_{0.42}Fe₄Sb₁₂, $P = 0.018$; Ca_{0.20}Sr_{0.12}DD_{0.39}Fe₃CoSb₁₂, $P = 0.011$; Ca_{0.20}Ba_{0.14}DD_{0.38}Fe₃CoSb₁₂, P not given; Sr_{0.12}Ba_{0.18}DD_{0.39}Fe₃CoSb₁₂, $P = 0.010$; Sr_{0.066}Ba_{0.066}Yb_{0.066}Co₄Sb₁₂, P not given; Mm_{0.78}Fe₃CoSb₁₂, P not given

The distribution of porosity may be influenced by the microstructure, with associated influences on elastic moduli, however previous studies of TE materials showed only a relation based on the volume fraction porosity and no pore distribution or shape factor required to describe the modulus-porosity relationship [Schmidt 2013; Ni 2009].

6.3.4 Hardness and fracture toughness results

Specimens PM-HP-673 and PM-HP-673-Ag, both hot pressed at 673 K, were too fragile to polish, limiting the hardness and fracture toughness measurements for the HP specimens to the two sintered at 773 K and the two sintered at 873 K. However, H and K_C measurements were made on each of the three reprocessed PECS specimens since all of those specimens had sufficient mechanical integrity so that polishing and indentation was not a problem. Also, for the toughness measurements, radial cracks were not present at a Vickers indentation load of 1.96 N for any of the specimens except VM-PECS-673 and VM-PECS-773, nor at 2.94 N for specimen PM-HP-673, so no K_C data is reported for the 1.96 N indentations for any specimen, nor at 2.94 N for specimen PM-HP-673 (Figure 6.12).

6.3.4.1 Hardness and toughness as a function of Ag addition

As was the case for the elastic moduli, the hardness and fracture toughness of the Ba-skutterudite in this study were not sensitive to the Ag_{NP} addition (Figure 6.12, Table 6.7). For H , much of the literature on micro-sized and nanosized metallic particles added to brittle matrices has focused on higher volume percentages. For example, H of alumina decreased from 18 GPa to 9.5 GPa with the addition of 0.20 volume fraction aluminum

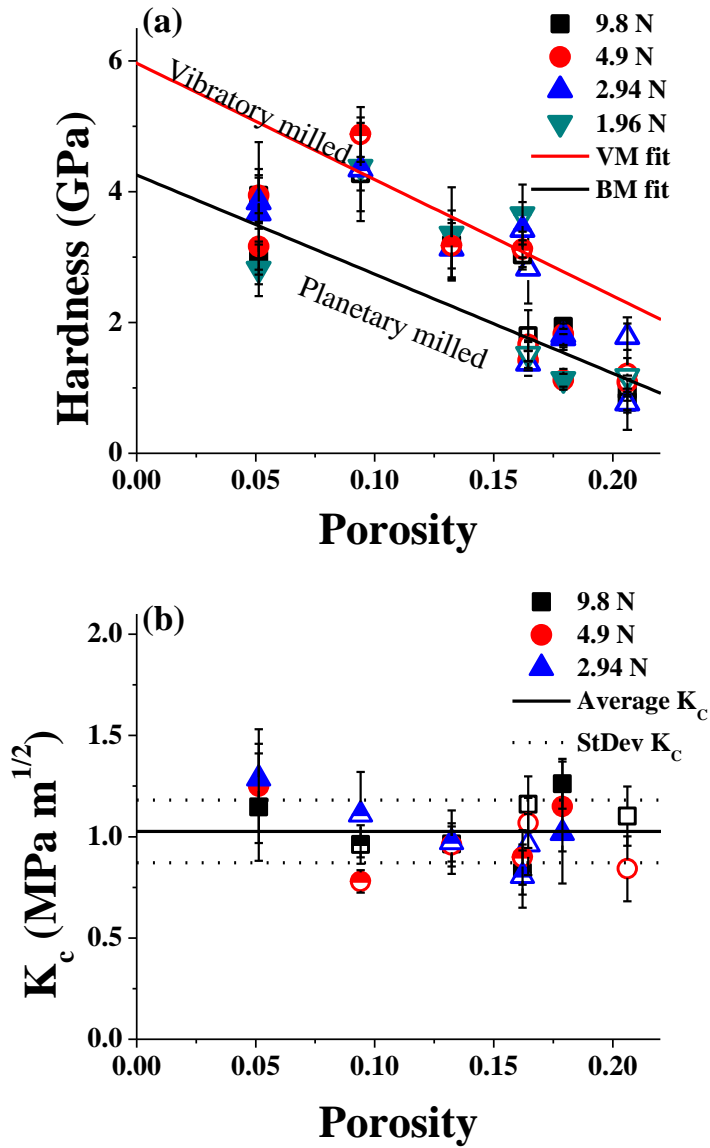


Figure 6.12. The (a) hardness and (b) fracture toughness for the hot pressed specimens with Ag_{NP} , filled symbols, the hot pressed specimens without Ag_{NP} , open symbols, and the reprocessed PECS specimens without Ag_{NP} , half-filled symbols, from Vickers indentation at four loads, 9.8 N, 4.9 N, 2.94 N, and 1.96 N. Full radial cracks were not observed on the specimens at 1.96 N load and therefore no fracture toughness values are available at 1.96 N load. The hot pressed specimens sintered at 673 K were not able to be polished and were not tested. The solid lines in the figure (a) represent hardness for the reprocessed specimens were fit to equation (6) separately from the hot pressed specimens because hardness is a function of grain size. Fracture toughness, figure (b), was not observed to be a function of either porosity or load, as plotted by the average (solid) and standard deviation (dotted) lines, with an average K_c for all 7 specimens of $1.0 \pm 0.2 \text{ MPa-m}^{1/2}$

particles (average XRD crystallite size of 25 nm, TEM grain size 26 ± 3 nm) [Zawrah 2012], and from 8.2 GPa to 7.3 GPa in hydroxyapatite with the addition of 5 wt% irregularly-shaped 67%Ti-33%Fe particles which were less than 200 μm across [Chang 2010].

However, the choice of Pt_{NP} or Ag_{NP} additions strongly effected the observed change in the hardness and fracture toughness of porcelain. The H and K_C were 4.94 ± 0.33 GPa and 1.36 ± 0.03 $\text{MPa}\cdot\text{m}^{1/2}$, respectively, for the porcelain matrix itself. The addition of Ag_{NP} raised the H and K_C to 6.10 ± 0.14 GPa and 1.54 ± 0.05 $\text{MPa}\cdot\text{m}^{1/2}$, 23% and 13% greater, respectively, than the H and K_C of the matrix. In contrast, after the addition of 26 wt% Pt_{NP} the hardness and fracture toughness were essentially unchanged from that of the dental porcelain matrix with $H = 5.05 \pm 0.15$ GPa and $K_C = 1.42 \pm 0.02$ $\text{MPa}\cdot\text{m}^{1/2}$. Thus, while the addition of Pt_{NP} left both the H and K_C values essentially intact, the addition of an equivalent weight % of Ag_{NP} to the same porcelain matrix material resulted in large changes in both H and K_C [Fujieda 2012]. For dilute concentrations of nanoparticles, changes in the elastic modulus are typically on the order of a few percent or less.

6.3.4.2 Hardness and fracture toughness as function of porosity

6.3.4.2.1 Hardness as function of porosity

In this study, the hardness, H , of $\text{Ba}_{0.3}\text{Co}_4\text{Sb}_{12}$ and $\text{Ba}_{0.3}\text{Co}_4\text{Sb}_{12}\text{-Ag}_{\text{NP}}$ decreased linearly with increasing porosity (Figure 6.12a). In general, hardness is a function of porosity for ceramics or brittle semiconductors [Fan 2013; Ramadass 1983; Mangalaraja 2009]. A least-squares fit of the H versus volume fraction porosity, P , data was done to the relationship

$$H = H_0(1 - b_HP) \quad (6)$$

where H_0 = the value of hardness at $P = 0$ and b_H is a unitless constant that describes the rate of decrease in H with increasing P . For the four HP specimens, a least-squares fit of the hardness-porosity data to equation (6) yielded $H_0 = 4.3 \pm 0.2$ GPa and $b_H = 3.6 \pm 0.2$ with the coefficient of determination $R^2 = 0.84$ (Figure 6.12a). For the three reprocessed specimens, $H_0 = 6.0 \pm 0.5$ GPa and $b_H = 3.0 \pm 0.4$, with $R^2 = 0.67$ (Figure 6.12a). The low R^2 is likely due to the small data set (three reprocessed specimens) and scatter in the data.

6.3.4.2.2 Fracture toughness as function of porosity

The fracture toughness of the specimens in this study is independent of porosity, averaging 1.0 ± 0.2 MPa-m^{1/2} over the entire range of porosity for which K_C was measured in this study, namely from $P = 0.05$ to 0.21 (Figure 6.12b, Table 6.1). Note that fracture toughness was not measured for specimens PM-HP-673 ($P = 0.30$) or PM-HP-673-Ag ($P = 0.27$) since these specimens were too fragile to be polished. In the literature, it has been noted that K_C can increase, decrease, or remain unchanged with increasing P [Rice 1995; Shao 2013].

In a comprehensive review of the effects of porosity on the mechanical properties of brittle materials [Rice 1995], Rice noted, especially for the intermediate porosity range from roughly $P = 0.1$ to $P = 0.15$, there are a number of examples of materials in the literature (including Al_2O_3 , B_4C , Si_3N_4) showing “that K_{IC} values for some of these porous bodies were clearly at least as high or higher than bodies with little or no porosity”. Proposed mechanisms for an increasing or constant K_C with increasing

porosity include crack-pore interactions, where pores can blunt or deflect a growing crack [Case 2012b; Case 2012a].

6.3.4.3 Hardness and fracture toughness as a function of load

Over the indentation load range of 1.96 N to 9.8 N that is included in this study, both H and K_C were independent of the load for Ba-skutterudite (Figure 6.12). The H , while independent of load, varied between specimens, but the K_C was essentially constant for all seven specimens examined. The average K_C of the seven specimens in this study is $1.0 \pm 0.2 \text{ MPa-m}^{1/2}$, which is comparable to the K_C range of $0.46 \text{ MPa-m}^{1/2}$ to $1.7 \text{ MPa-m}^{1/2}$ measured for similar skutterudites (Table 6.7) [Ravi 2008; Eilertsen 2013; Rogl 2011].

For K_C , the fracture toughness should ideally be independent of load. In order to test this load independence, the $c^{3/2}$ (where c = radial crack length) versus indentation load, F , behavior was examined for each of the Ba-skutterudite specimens included in this study. A plot of $c^{3/2}$ versus F yielded a straight line plot with $R^2 > 0.98$ in each case, as demonstrated by plots from specimens VM-PECS-673 and PM-HP-873-Ag (Figure 6.13). Thus, the radial crack length versus indentation load behavior is consistent with equation (3) for each specimen in this study, where equation (3) can be rewritten as

$$c^{3/2} = \frac{\xi(E/H)^{0.5} F}{K_C} \quad (7)$$

For a given specimen, we assume the ξ , E , H and K_C are constant, thus equation (7) is a straight line. The high value of R^2 for the least-squares fit to equation (7) supports the use of equation (3) to calculate K_C .

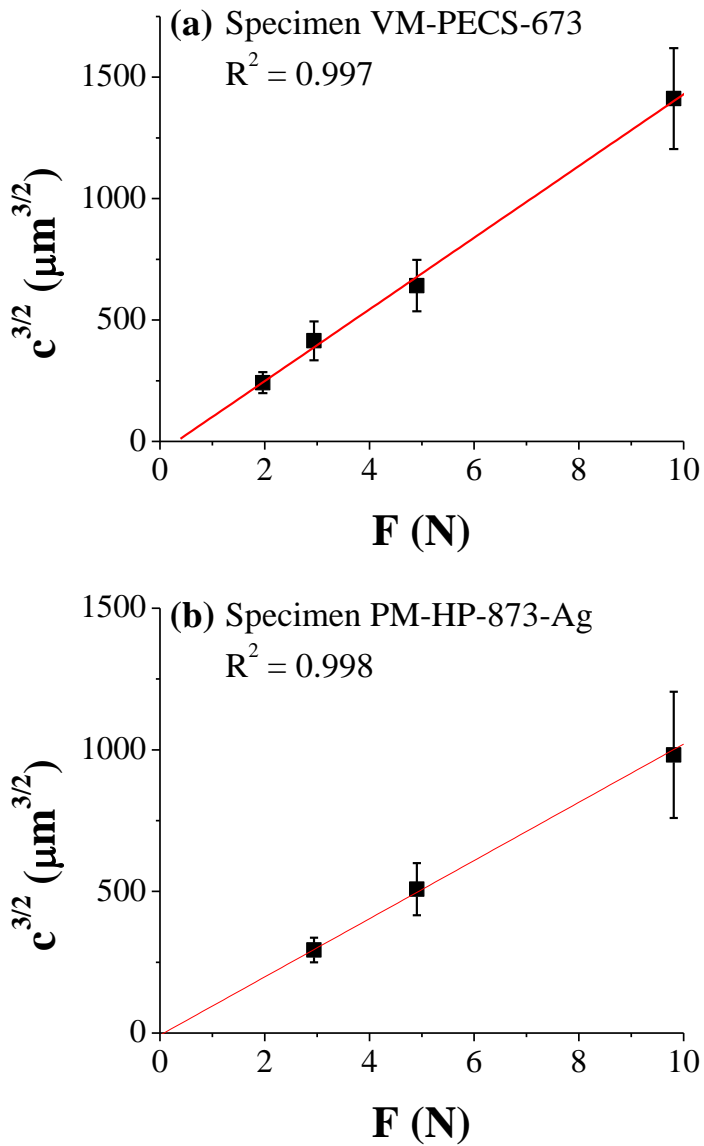


Figure 6.13. For each of the specimens, a plot of $c^{3/2}$ versus load, F , was used to determine the suitability of the fracture toughness by Vickers indentation. For 5 of 7 specimens, the coefficient of determination, R^2 , for a linear regression to equation (7) through the data points is 0.99 or greater, with an R^2 of 0.98 for specimen VM-PECS-773, and 0.84 for specimen PM-HP-773. Note specimen PM-HP-773 also has a low fracture toughness measurement at 2.94 N load. All specimens were measured at three loads, except VM-PECS-673 and VM-PECS-773 with a fourth measurement at a Vickers indentation load of 1.96 N

In contrast to K_C , hardness is frequently observed to be a function of the applied load. From the literature, for both metals [Pharr 2010; Nix 1998] and brittle solids [Bull 1989; Sangwal 2009], the measured hardness can be a function of the applied indentation load. The indentation size effect (ISE) [Nix 1998], where H decreases as the applied load increases, has been ascribed to elastic recovery and working hardening during indentation [Bull 1989; Sangwal 2009] while an observed reverse indentation size effect (RISE) [Sangwal 2000], where H decreases with decreasing load has been attributed to stress relaxation during unloading [Sangwal 2000].

6.3.4.4 Hardness and fracture toughness results as a function of grain size

The hardness varied as a function of grain size, as observed by the fit to equation (6) in Figure 6.12a, while the fracture toughness is independent of grain size, averaging $1.0 \pm 0.2 \text{ MPa-m}^{1/2}$ (Table 6.7). For the bimodal grain size HP specimens (matrix grain sizes of $0.3 \text{ }\mu\text{m}$ to $3 \text{ }\mu\text{m}$, with larger grains approximately $5 \text{ }\mu\text{m}$ to $20 \text{ }\mu\text{m}$ across), the H_0 is $4.3 \pm 0.2 \text{ GPa}$, while for the reprocessed specimens with average grain sizes of $0.17 \text{ }\mu\text{m}$, $0.16 \text{ }\mu\text{m}$ and $0.14 \text{ }\mu\text{m}$, the H_0 is $6.0 \pm 0.5 \text{ GPa}$ (Figure 6.12a).

6.3.4.4.1 Hardness results as a function of grain size

The difference in H_0 between planetary milled and HP specimens and the vibratory milled and PECS processed specimens likely is related to the grain size dependence of H . A Hall-Petch type relationship between H and grain size, GS , available in the literature is [Rice 2000]

$$H = H_0 + kGS^{-1/2} \quad (8)$$

where H_0 is considered as the H value in the single crystal limit and k is called the Petch parameter. While Hall-Petch behavior is very common in metals [Lawn 1993], the nature of the H versus GS dependence is uncertain for many ceramics [Rice 2000; Armstrong 2011]. Hall-Petch behavior is common for relatively soft ceramics such as alkaline halides, but there is a great deal of scatter in the H versus GS data for most hard ceramics [Rice 2000; Armstrong 2011]. Furthermore, the H_0 obtained from H versus GS data is not always a good predictor for the H of single crystals (as is typically assumed for equation (8)) [Rice 2000]. In addition, for some ceramics, such as ZrO_2 and $AlMg_2O_4$, H is independent of grain size [Rice 2000]. Also, minima in H versus GS data are often observed for intermediate grain sizes (GS on the order of several μm) such that the Petch parameter k can take on both negative and positive values (with unequal magnitudes) for a given data set [Rice 2000; Armstrong 2011]. Nevertheless, a well-accepted alternative to equation (8) is not available in the literature and thus, in general, the H versus GS behavior for brittle materials is not clear from the standpoint of the available data or the available functional relationship (equation (8)).

6.3.4.4.2 Fracture toughness results as a function of grain size

In this study, fracture toughness, K_C , is essentially independent of grain size, GS , averaging $1.0 \pm 0.2 \text{ MPa}\cdot\text{m}^{1/2}$ (Figure 6.12b).

This result may be counterintuitive, since fracture strength is typically a function of grain size [Barsoum 2003]. However, fracture strength is based on the stress required for failure of a specimen and is typically dependent on the largest flaw, and the intrinsic flaw size typically scales with GS [Barsoum 2003]. In contrast, K_C is based on the work

necessary to extend a crack [Barsoum 2003], which may or may not be related to grain size.

Thus, grain size engineering alone will not likely improve fracture toughness either for Ba-skutterudite or other cubic thermoelectric materials. Although no studies are currently available in the literature for the grain size dependence of K_C for thermoelectric materials, K_C has been observed to be essentially independent of grain size for various cubic materials, tested using a variety of test methods, including Y_2O_3 (notched beam test [Monroe 1978] and double cantilever beam technique [Rhoades 1986]), MgO (Chevron notch method [Yasuda 1990]), NiZn ferrite (notched beam [Veldkamp 1979]), and $MgAl_2O_4$ (double cantilever beam and Vickers indentation [Rice 1996]). In addition, for noncubic materials with small grain size, K_C can be independent of grain size as was the case in a study by Yao et al. who found that K_C was independent of grain size for PECS-processed, fully dense polycrystalline alumina with grain sizes ranging from 0.3 μm to 3.3 μm for K_C measured by the surface crack in flexure technique [Yao 2011].

In contrast to cubic materials, for noncubic materials with intermediate grain sizes (roughly on the order of 10 to 100 μm), a maximum in K_C has been observed as a function of grain size [Wachtman 2009]. Lawn and co-workers ascribed the observed increase in K_C with increasing grain size to grain bridging [Vekinis 1990; Swanson 1987; Foulk III 2007], with the principle mechanism responsible for grain bridging being the clamping forces generated by thermal expansion anisotropy [Bennison 1989]. After the maximum in K_C , $K_{C_{MAX}}$, is reached, the subsequent decrease in K_C with further increases in grain size has been linked to thermal expansion anisotropy-induced microcracking in

noncubic materials, where the grain size at $K_{C_{MAX}}$ coincides roughly with the critical grain size for microcracking [Rice 1998]. Thus, while for noncubic materials, a grain-size dependent maximum in K_C has been observed, the insensitivity of K_C to grain size for the cubic Ba-skutterudite in this study is consistent with the literature. In addition to the grain size and porosity trends, the value of K_C for the Ba-skutterudite measured in this study is comparable to K_C values in the literature for other CoSb_3 systems [Ravi 2008; Eilertsen 2013; Rogl 2011] (Table 6.7).

6.4 Summary and conclusions

In this study, the elastic moduli (Figure 6.10), hardness (Figure 6.12a), and fracture toughness (Figure 6.12b) of $\text{Ba}_{0.3}\text{Co}_4\text{Sb}_{12}$ were insensitive to the addition of 0.5 wt% Ag_{NP} . Both the elastic moduli and hardness were functions of porosity (Figures 6.10, 6.12a), which agrees with previous literature results for elasticity (Figure 6.11) [Zhang 2010] and hardness [Ramadass 1983; Mangalaraja 2009; Shao 2013]. Fracture toughness (Figure 6.12b) was not a function of porosity (Figure 6.12b), which may indicate an interaction between the pores and the growing cracks.

The study by Zhou [Zhou 2012] demonstrated that Ag addition results in important changes in thermoelectric properties (increasing electrical conduction) for Ba-skutterudite. However, this study indicates that the addition of silver also affects the densification process which in turn can affect changes in mechanical properties. At a sintering temperature of 873 K, the specimen without Ag_{NP} had a P value of 0.16 while the specimen sintered with 0.5 wt% Ag_{NP} had $P = 0.05$. The increased densification with the addition of Ag was likely due to a liquid phase sintering from the peritectic reaction that formed the Ag_3Sb phase observed in the specimen.

Based on the results of this study, a similar peritectic reaction may explain the formation of Ag_3Sb and an enhanced ZT when Ag was added to ZnSb [Xiong 2013]. Similar peritectic or eutectic reactions may take place in other antimonide thermoelectric systems when Ag or another conductive material is added to enhance electrical conductivity. More generally, this type of eutectic or peritectic reaction to enhance densification and improve electrical conductivity may operate in a number of thermoelectric systems in addition to antimonides. Although a set of ternary or quaternary phase diagrams may not be available for many thermoelectric systems, a search of binary phase diagrams (such as the Ag-Sb phase diagrams used in this study) may act as a guide to discover potential beneficial peritectic or eutectic reactions.

ACKNOWLEDGEMENTS

The authors acknowledge the financial support of the Department of Energy, Revolutionary Materials for Solid State Energy Conversion Center, an Energy Frontiers Research Center funded by the U.S. Department of Energy, Office of Science, Office of Basic Energy Sciences under award number DE-SC0001054.

REFERENCES

REFERENCES

- [Alleno, Chen, Chubilleau, Lenoir, Rouleau, Trichet, Villeroy 2009] Alleno, E., Chen, L., Chubilleau, C., Lenoir, B., Rouleau, O., Trichet, M.F., Villeroy, B. Thermal Conductivity Reduction in CoSb₃–CeO₂ Nanocomposites. *Journal of Electronic Materials* 39 (2009) 1966–1970.
- [Androulakis, Lin, Kong, Uher, Wu, Hogan, Cook, Caillat, Paraskevopoulos, Kanatzidis 2007] Androulakis, J., Lin, C.-H., Kong, H.-J., Uher, C., Wu, C.-I., Hogan, T., Cook, B.A., Caillat, T., Paraskevopoulos, K.M., Kanatzidis, M.G. Spinodal decomposition and nucleation and growth as a means to bulk nanostructured thermoelectrics: enhanced performance in Pb(1-x)Sn(x)Te-PbS. *Journal of the American Chemical Society* 129 (2007) 9780–8.
- [Armstrong 2011] Armstrong, R.W. The Hardness and Strength Properties of WC-Co Composites. *Materials* 4 (2011) 1287–1308.
- [Barsoum 2003] Barsoum, M.W. *Fundamentals of Ceramics*. Taylor & Francis Group, New York, 2003.
- [Bedolla, Lemus-Ruiz, Contreras 2012] Bedolla, E., Lemus-Ruiz, J., Contreras, A. Synthesis and characterization of Mg-AZ91/AlN composites. *Materials and Design* 38 (2012) 91–98.
- [Bennison, Lawn 1989] Bennison, S.J., Lawn, B.R. Role of interfacial grain-bridging sliding friction in the crack-resistance and strength properties of nontransforming ceramics. *Acta Metallurgica* 37 (1989) 2659–2671.
- [Boccaccini 1994] Boccaccini, A. Comment on “Effective elastic moduli of porous ceramic materials.” *Journal of the American Ceramic Society* (1994) 2779–2781.
- [Bukat, Koscielski, Sitek, Jakubowska, Mlozniak 2011] Bukat, K., Koscielski, M., Sitek, J., Jakubowska, M., Mlozniak, A. Silver nanoparticles effect on the wettability of Sn-Ag-Cu solder pastes and solder joints microstructure on copper. *Soldering & Surface Mount Technology* 23 (2011) 150–160.
- [Bull, Page, Yoffe 1989] Bull, S.J., Page, T.F., Yoffe, E.H. An explanation of the indentation size effect in ceramics. *Philosophical Magazine Letters* 59 (1989) 281–288.
- [Case 2012a] Case, E.D. Thermo-mechanical properties of thermoelectric materials. In: D.M. Rowe, ed., *Thermoelectrics and its Energy Harvesting: Modules, Systems and Applications*. CRC Press, Boca Raton, Florida, 2012, 581.

- [Case 2012b] Case, E.D. Thermal Fatigue and Waste Heat Recovery via Thermoelectrics. *Journal of Electronic Materials* 41 (2012) 1811–1819.
- [Case, Smyth, Monthei 1981] Case, E.D., Smyth, J.R., Monthei, V. Grain-Size Determinations. *Journal of the American Ceramic Society* 64 (1981) C–24–C–25.
- [Chang, Chen, Ru, Yue, Yu, Zhang 2010] Chang, Q., Chen, D.L., Ru, H.Q., Yue, X.Y., Yu, L., Zhang, C.P. Toughening mechanisms in iron-containing hydroxyapatite/titanium composites. *Biomaterials* 31 (2010) 1493–501.
- [Cipriani, Corazza, Mazzetti 1996] Cipriani, C., Corazza, M., Mazzetti, G. Reinvestigation of natural silver antimonides. *European Journal of Mineralogy* 8 (1996) 1347–1350.
- [Couturier, Ducret, Merle, Disson, Joubert 1997] Couturier, R., Ducret, D., Merle, P., Disson, J.P., Joubert, P. Elaboration and characterization of a metal matrix composite: Al/AlN. *Journal of the European Ceramic Society* 17 (1997) 1861–1866.
- [Dharma, Shukor, Ariga 2009] Dharma, I.G.B.B., Shukor, M.H.A., Ariga, T. Wettability of Low Silver Content Lead-Free Solder Alloy. *Materials Transactions* 50 (2009) 1135–1138.
- [Dunn, Ledbetter 2011] Dunn, M.L., Ledbetter, H. Poisson's ratio of porous and microcracked solids: Theory and application to oxide superconductors. *Journal of Materials Research* 10 (2011) 2715–2722.
- [Eilertsen, Subramanian, Kruzic 2013] Eilertsen, J., Subramanian, M. a., Kruzic, J.J. Fracture toughness of Co₄Sb₁₂ and In_{0.1}Co₄Sb₁₂ thermoelectric skutterudites evaluated by three methods. *Journal of Alloys and Compounds* 552 (2013) 492–498.
- [Fan, Case, Yang, Nicholas 2013] Fan, X., Case, E.D., Yang, Q., Nicholas, J.D. Room temperature hardness of gadolinia-doped ceria as a function of porosity. *Journal of Materials Science* 48 (2013) 6977–6985.
- [Feschotte, Monachon, Durussel 1992] Feschotte, P., Monachon, F., Durussel, P. The binary system Sb-Ag: a revision of the Ag₃Sb phase boundaries. *Journal of Alloys and Compounds* 186 (1992) L17–L18.
- [Foulk III, Cannon, Johnson, Klein, Ritchie 2007] Foulk III, J.W., Cannon, R.M., Johnson, G.C., Klein, P. a., Ritchie, R.O. A micromechanical basis for partitioning the evolution of grain bridging in brittle materials. *Journal of the Mechanics and Physics of Solids* 55 (2007) 719–743.
- [Fujieda, Uno, Ishigami, Kurachi, Wakamatsu, Doi 2012] Fujieda, T., Uno, M., Ishigami, H., Kurachi, M., Wakamatsu, N., Doi, Y. Addition of platinum and silver

- nanoparticles to toughen dental porcelain. *Dental Materials Journal* 31 (2012) 711–716.
- [Halpin 1992] Halpin, J.C. *Primer on composite materials analysis*. Technomic Publishing Company, Inc., Lancaster, Pennsylvania, 1992.
- [Hashin 1962] Hashin, Z. The Elastic Moduli of Heterogeneous Materials. *Journal of Applied Mechanics* 29 (1962) 143–150.
- [Hassam, Bahari, Legendre 2001] Hassam, S., Bahari, Z., Legendre, B. Phase diagram of the Ag–Bi–Sb ternary system. *Journal of Alloys and Compounds* 315 (2001) 211–217.
- [He, Hu, Tang, Lan, Yang, Wang, Ren, Hao, Chen 2008] He, Q., Hu, S., Tang, X., Lan, Y., Yang, J., Wang, X., Ren, Z., Hao, Q., Chen, G. The great improvement effect of pores on ZT in $\text{Co}_{1-x}\text{Ni}_x\text{Sb}_3$ system. *Applied Physics Letters* 93 (2008) 042108.
- [Hutton 2004] Hutton, D. V. *Fundamentals of finite element analysis*. McGraw-Hill, New York, 2004.
- [Ioffe 1960] Ioffe, A. *Physics of Semiconductors*. Infosearch Limited, London, 1960.
- [Ji, He, Alboni, Su, Gothard, Zhang, Tritt, Kolis 2007] Ji, X., He, J., Alboni, P., Su, Z., Gothard, N., Zhang, B., Tritt, T.M., Kolis, J.W. Thermal conductivity of CoSb_3 nano-composites grown via a novel solvothermal nano-plating technique. *physica status solidi RRL – Rapid Research Letters* 1 (2007) 229–231.
- [Kim, Bush 1999] Kim, H.S., Bush, M.B. The effects of grain size and porosity on the elastic modulus of nanocrystalline materials. *Nanostructured Materials* 11 (1999) 361–367.
- [Lawn 1993] Lawn, B.R. *Fracture of Brittle Solids*. Cambridge University Press, New York, 1993.
- [Lawn, Cook 2012] Lawn, B.R., Cook, R.F. Probing material properties with sharp indenters: a retrospective. *Journal of Materials Science* 47 (2012) 1–22.
- [Lee, Vashaee, Wang, Dresselhaus, Ren, Chen 2010] Lee, H., Vashaee, D., Wang, D.Z., Dresselhaus, M.S., Ren, Z.F., Chen, G. Effects of nanoscale porosity on thermoelectric properties of SiGe. *Journal of Applied Physics* 107 (2010) 094308.
- [Mangalaraja, Ananthakumar, Uma, Jiménez, López, Camurri 2009] Mangalaraja, R.V., Ananthakumar, S., Uma, K., Jiménez, R.M., López, M., Camurri, C.P.

- Microhardness and fracture toughness of Ce_{0.9}Gd_{0.1}O_{1.95} for manufacturing solid oxide electrolytes. *Materials Science and Engineering: A* 517 (2009) 91–96.
- [Mi, Zhao, Zhu, Tu 2008] Mi, J.L., Zhao, X.B., Zhu, T.J., Tu, J.P. Thermoelectric properties of Yb_{0.15}Co_{0.4}Sb₁₂ based nanocomposites with CoSb₃ nano-inclusion. *Journal of Physics D: Applied Physics* 41 (2008) 205403.
- [Migliori, Sarrao 1997] Migliori, A., Sarrao, J.L. *Resonant Ultrasound Spectroscopy: Applications to Physics, Materials Measurements, and Nondestructive Evaluation*. Wiley-Vch, New York, 1997.
- [Monroe, Smyth 1978] Monroe, L.D., Smyth, J.R. Grain Size Dependence of Fracture Energy of Y₂O₃. *Journal of the American Ceramic Society* 61 (1978) 538–539.
- [Morelli, Meisner 1995] Morelli, D.T., Meisner, G.P. Low temperature properties of the filled skutterudite CeFe₄Sb₁₂. *Journal of Applied Physics* 77 (1995) 3777.
- [Ni, Ren, Case, Timm 2009] Ni, J., Ren, F., Case, E., Timm, E. Porosity dependence of elastic moduli in LAST (lead–antimony–silver–tellurium) thermoelectric materials. *Materials Chemistry and Physics*(2009) .
- [Ni, Case, Khabir, Stewart, Wu, Hogan, Timm, Girard, Kanatzidis 2010] Ni, J.E., Case, E.D., Khabir, K.N., Stewart, R.C., Wu, C.-I., Hogan, T.P., Timm, E.J., Girard, S.N., Kanatzidis, M.G. Room temperature Young's modulus, shear modulus, Poisson's ratio and hardness of PbTe–PbS thermoelectric materials. *Materials Science and Engineering: B* 170 (2010) 58–66.
- [Nix, Gao 1998] Nix, W.D., Gao, H. Indentation size effects in crystalline materials: A law for strain gradient plasticity. *Journal of the Mechanics and Physics of Solids* 46 (1998) 411–425.
- [Nolas, Kaeser, Littleton, Tritt 2000] Nolas, G.S., Kaeser, M., Littleton, R.T., Tritt, T.M. High figure of merit in partially filled ytterbium skutterudite materials. *Applied Physics Letters* 77 (2000) 1855.
- [Nolas, Morelli, Tritt 1999] Nolas, G.S., Morelli, D.T., Tritt, T.M. SKUTTERUDITES: A Phonon-Glass-Electron Crystal Approach to Advanced Thermoelectric Energy Conversion Applications. *Annual Review of Materials Science* 29 (1999) 89–116.
- [Okamoto 1993] Okamoto, H. Ag-Sb (Silver-Antimony). *Journal of Phase Equilibria* 14 (1993) 531–532.
- [Okamoto 2007] Okamoto, H. Ag-Sb (Silver-Antimony). *Journal of Phase Equilibria and Diffusion* 28 (2007) 403–403.

- [Pharr, Herbert, Gao 2010] Pharr, G.M., Herbert, E.G., Gao, Y. The Indentation Size Effect: A Critical Examination of Experimental Observations and Mechanistic Interpretations. *Annual Review of Materials Research* 40 (2010) 271–292.
- [Pilchak, Ren, Case, Timm, Schock, Wu, Hogan 2007] Pilchak, A.L., Ren, F., Case, E.D., Timm, E.J., Schock, H.J., Wu, C.-I., Hogan, T.P. Characterization of dry milled powders of LAST (lead–antimony–silver–tellurium) thermoelectric material. *Philosophical Magazine* 87 (2007) 4567–4591.
- [Ramadass, Mohan, Reddy 1983] Ramadass, N., Mohan, S., Reddy, S.R. Studies on the metastable phase retention and hardness in zirconia ceramics. *Materials Science and Engineering* 60 (1983) 65–72.
- [Ramakrishnan, Arunachalam 1993] Ramakrishnan, N., Arunachalam, V.S. Effective Elastic Moduli of Porous Ceramic Materials. *Journal of the American Ceramic Society* 76 (1993) 2745–2752.
- [Ravi, Firdosy, Caillat, Brandon, Walde, Maricic, Sayir 2009] Ravi, V., Firdosy, S., Caillat, T., Brandon, E., Walde, K., Maricic, L., Sayir, A. Thermal Expansion Studies of Selected High-Temperature Thermoelectric Materials. *Journal of Electronic Materials* 38 (2009) 1433–1442.
- [Ravi, Firdosy, Caillat, Lerch, Calamino, Pawlik, Nathal, Sechrist, Buchhalter, Nutt 2008] Ravi, V., Firdosy, S., Caillat, T., Lerch, B., Calamino, A., Pawlik, R., Nathal, M., Sechrist, A., Buchhalter, J., Nutt, S. Mechanical Properties of Thermoelectric Skutterudites. *Space Technology and Applications International Forum—STAIF 2008*(2008) 656–662.
- [Ren, Case, Ni, Timm, Lara-Curzio, Trejo, Lin, Kanatzidis 2009] Ren, F., Case, E.D., Ni, J.E., Timm, E.J., Lara-Curzio, E., Trejo, R.M., Lin, C.-H., Kanatzidis, M.G. Temperature-dependent elastic moduli of lead telluride-based thermoelectric materials. *Philosophical Magazine* 89 (2009) 143–167.
- [Ren, Case, Timm, Schock 2008] Ren, F., Case, E.D., Timm, E.J., Schock, H.J. Hardness as a function of composition for n-type LAST thermoelectric material. *Journal of Alloys and Compounds* 455 (2008) 340–345.
- [Rhoades, Baldoni, Wei 1986] Rhoades, W., Baldoni, J., Wei, G. Final report for ORN contract N00014-82-C-0452. *GTE Laboratory*(1986) .
- [Rice 1995] Rice, R.W. Comment on “Effective elastic moduli of porous ceramic materials.” *Journal of the American Ceramic Society* 78 (1995) 1711.
- [Rice 1996] Rice, R.W. Grain size and porosity dependence of ceramic fracture energy and toughness at 22°C. *Journal of Materials Science* 31 (1996) 1969–1983.

- [Rice 1998] Rice, R.W. *Porosity of Ceramics*. Marcel Dekker, New York, 1998.
- [Rice 2000] Rice, R.W. *Mechanical Properties of Ceramics and Composites: Grain And Particle Effects*. Marcel Dekker, New York, 2000.
- [Rogl, Rogl 2011] Rogl, G., Rogl, P. Mechanical Properties of Skutterudites. *Science of Advanced Materials* 3 (2011) 517–538.
- [Sangwal 2000] Sangwal, K. On the reverse indentation size effect and microhardness measurement of solids. *Materials Chemistry and Physics* 63 (2000) 145–152.
- [Sangwal 2009] Sangwal, K. Review: Indentation size effect, indentation cracks and microhardness measurement of brittle crystalline solids - some basic concepts and trends. *Crystal Research and Technology* 44 (2009) 1019–1037.
- [Schmidt, Case, Lehr, Morelli 2013] Schmidt, R.D., Case, E.D., Lehr, G.J., Morelli, D.T. Room temperature mechanical properties of polycrystalline YbAl₃, a promising low temperature thermoelectric material. *Intermetallics* 35 (2013) 15–24.
- [Schmidt, Ni, Case, Sakamoto, Kleinow, Wing, Stewart, Timm 2010] Schmidt, R.D., Ni, J.E., Case, E.D., Sakamoto, J.S., Kleinow, D.C., Wing, B.L., Stewart, R.C., Timm, E.J. Room temperature Young's modulus, shear modulus, and Poisson's ratio of Ce_{0.9}Fe_{3.5}Co_{0.5}Sb₁₂ and Co_{0.95}Pd_{0.05}Te_{0.05}Sb₃ skutterudite materials. *Journal of Alloys and Compounds* 504 (2010) 303–309.
- [Segerland 1984] Segerland, L. *Applied finite element analysis*. Wiley, New York, 1984.
- [Shao, Du, Wu, Song, Xu, Jiang 2013] Shao, Y., Du, R., Wu, X., Song, F., Xu, X., Jiang, C. Effect of porosity on the crack pattern and residual strength of ceramics after quenching. *Journal of Materials Science* 48 (2013) 6431–6436.
- [Shi, Yang, Salvador, Chi, Cho, Wang, Bai, Yang, Zhang, Chen 2011] Shi, X., Yang, J., Salvador, J.R., Chi, M., Cho, J.Y., Wang, H., Bai, S., Yang, J., Zhang, W., Chen, L. Multiple-filled skutterudites: high thermoelectric figure of merit through separately optimizing electrical and thermal transports. *Journal of the American Chemical Society* 133 (2011) 7837–46.
- [Slack, Tsoukala 1994] Slack, G. a., Tsoukala, V.G. Some properties of semiconducting IrSb₃. *Journal of Applied Physics* 76 (1994) 1665–1671.
- [Swanson, Fairbanks, Lawn, Mai, Hockey 1987] Swanson, P.L., Fairbanks, C.J., Lawn, B.R., Mai, Y.-W., Hockey, B.J. Crack-Interface Grain Bridging as a Fracture Resistance I, Mechanism in Ceramics: I, Experimental Study on Alumina. *Journal of the American Ceramic Society* 70 (1987) 279–289.

- [Tokiai, Uesugi, Nosaka, Hirayama, Ito, Koumoto 1997] Tokiai, T., Uesugi, T., Nosaka, M., Hirayama, A., Ito, K., Koumoto, K. Thermoelectric properties of Mn-doped iron disilicide ceramics fabricated from radio-frequency plasma-treated fine powders. *Journal of materials Science* 32 (1997) 3007–3011.
- [Toprak, Stiewe, Platzek, Williams, Bertini, Muller, Gatti, Zhang, Rowe, Muhammed 2004] Toprak, M.S., Stiewe, C., Platzek, D., Williams, S., Bertini, L., Muller, E., Gatti, C., Zhang, Y., Rowe, M., Muhammed, M. The Impact of Nanostructuring on the Thermal Conductivity of Thermoelectric CoSb₃. *Advanced Functional Materials* 14 (2004) 1189–1196.
- [Uher 2001] Uher, C. Skutterudites: Prospective Novel Thermoelectrics. In: T.M. Tritt, ed., *Semiconductors and Semimetals*, Vol. 69. Academic Press, San Diego, 2001, 139–253.
- [Underwood 1969] Underwood, E.E. Stereology, or the quantitative evaluation of microstructures. *Journal of Microscopy* 89 (1969) 161–180.
- [Vekinis, Ashby, Beaumont 1990] Vekinis, G., Ashby, M.F., Beaumont, P.W.R. R-curve behaviour of Al₂O₃ ceramics. *Acta Metallurgica et Materialia* 38 (1990) 1151–1162.
- [Veldkamp, Hattu 1979] Veldkamp, J., Hattu, N. On the fracture toughness of brittle materials. *Philips Journal Research* 34 (1979) 1–25.
- [Voronin, Osadchii 2013] Voronin, M. V., Osadchii, E.G. Standard thermodynamic properties of Ag₃Sb and Ag₆Sb evaluated by EMF measurements. *Inorganic Materials* 49 (2013) 550–554.
- [Wachtman, Cannon, Matthewson 2009] Wachtman, J.B., Cannon, W.R., Matthewson, M.J. *Mechanical Properties of Ceramics*. Wiley-Vch, Hoboken, N.J., 2009.
- [Wen, Duan, Zhai, Li, Zhang 2013] Wen, P., Duan, B., Zhai, P., Li, P., Zhang, Q. Effect of thermal annealing on the microstructure and thermoelectric properties of nano-TiN/Co₄Sb_{11.5}Te_{0.5} composites. *Journal of Materials Science: Materials in Electronics* 24 (2013) 5155–5161.
- [Xiong, Okamoto, Inui 2013] Xiong, D.-B., Okamoto, N.L., Inui, H. Enhanced thermoelectric figure of merit in p-type Ag-doped ZnSb nanostructured with Ag₃Sb. *Scripta Materialia* 69 (2013) 397–400.
- [Yang, Wu, Zhang 2004] Yang, L., Wu, J.S., Zhang, L.T. Synthesis of filled skutterudite compound La_{0.75}Fe₃CoSb₁₂ by spark plasma sintering and effect of porosity on thermoelectric properties. *Journal of Alloys and Compounds* 364 (2004) 83–88.

- [Yao, Liu, Holland, Huang, Xiong, Schoenung, Mukherjee 2011] Yao, W., Liu, J., Holland, T.B., Huang, L., Xiong, Y., Schoenung, J.M., Mukherjee, A.K. Grain size dependence of fracture toughness for fine grained alumina. *Scripta Materialia* 65 (2011) 143–146.
- [Yasuda, SD, Kanemichi, Matsuo, Kimura 1990] Yasuda, K., SD, K., Kanemichi, Y., Matsuo, Y., Kimura, S. Influence of Grain Size and Temperature on Fracture Toughness of MgO Sintered Body. *Journal of the Ceramic Society of Japan* 98 (1990) 1103–1108.
- [Yoon, Kwon, Ahn, Kim, Koo, Bae, Cho, Kim, Park 2013] Yoon, S., Kwon, O.-J., Ahn, S., Kim, J.-Y., Koo, H., Bae, S.-H., Cho, J.-Y., Kim, J.-S., Park, C. The Effect of Grain Size and Density on the Thermoelectric Properties of Bi₂Te₃-PbTe Compounds. *Journal of Electronic Materials* 42 (2013) 3390–3396.
- [Yoshizawa, Nakanishi, Kumagai, Oikawa, Sekine, Shirotani 2004] Yoshizawa, M., Nakanishi, Y., Kumagai, T., Oikawa, M., Sekine, C., Shirotani, I. Elastic Anomalies of Polycrystalline SmRu₄P₁₂ Associated with Metal–Insulator Transition. *Journal of the Physical Society of Japan* 73 (2004) 315–318.
- [Zawrah, Abdel-kader, Elbaly 2012] Zawrah, M.F., Abdel-kader, H., Elbaly, N.E. Fabrication of Al₂O₃–20vol.% Al nanocomposite powders using high energy milling and their sinterability. *Materials Research Bulletin* 47 (2012) 655–661.
- [Zhang, Rogl, Grytsiv, Puchegger, Koppensteiner, Spieckermann, Kabelka, Reinecker, Rogl, Schranz, Zehetbauer, Carpenter 2010] Zhang, L., Rogl, G., Grytsiv, A., Puchegger, S., Koppensteiner, J., Spieckermann, F., Kabelka, H., Reinecker, M., Rogl, P., Schranz, W., Zehetbauer, M., Carpenter, M.A. Mechanical properties of filled antimonide skutterudites. *Materials Science and Engineering: B* 170 (2010) 26–31.
- [Zhang, Sakamoto 2013] Zhang, L., Sakamoto, J. The microstructural stability and thermoelectric properties of Mm_{0.9}Fe_{3.5}Co_{0.5}Sb₁₂-based skutterudites. *Materials Chemistry and Physics* 138 (2013) 601–607.
- [Zhao, He, Hao, Wu, Hogan, Wolverton, Dravid, Kanatzidis 2012] Zhao, L.-D., He, J., Hao, S., Wu, C.-I., Hogan, T.P., Wolverton, C., Dravid, V.P., Kanatzidis, M.G. Raising the thermoelectric performance of p-type PbS with endotaxial nanostructuring and valence-band offset engineering using CdS and ZnS. *Journal of the American Chemical Society* 134 (2012) 16327–36.
- [Zhou, Li, Kita 2008] Zhou, M., Li, J.-F., Kita, T. Nanostructured AgPb(m)SbTe(m+2) system bulk materials with enhanced thermoelectric performance. *Journal of the American Chemical Society* 130 (2008) 4527–32.

[Zhou, Wang, Zhang, Chi, Su, Sakamoto, Uher 2012] Zhou, X., Wang, G., Zhang, L., Chi, H., Su, X., Sakamoto, J., Uher, C. Enhanced thermoelectric properties of Ba-filled skutterudites by grain size reduction and Ag nanoparticle inclusion. *Journal of Materials Chemistry* 22 (2012) 2958.

[Zienkiewicz, Taylor 2005] Zienkiewicz, O.C., Taylor, R.L. *The Finite Element Method for Solid and Structural Mechanics*. Butterworth-Heinemann, Boston, 2005.

7 High temperature elastic moduli of thermoelectric SnTe_{1+x} -y SiC

nanoparticulate composites

Robert D. Schmidt¹, Eldon D. Case¹, Jennifer E. Ni¹, Rosa M. Trejo², Edgar Lara-Curzio², Rachel J. Korkosz³, Mercouri G. Kanatzidis³

¹ Chemical Engineering and Materials Science Department,
Michigan State University, East Lansing, MI, 48824

² High Temperature Materials Laboratory,
Oak Ridge National Laboratory, Oak Ridge, TN 37831

³ Department of Chemistry,
Northwestern University, Evanston, IL, 60208

Published in: Journal of Materials Science 48 (2013) 8244 – 8258.

Abstract

In waste heat recovery applications, thermoelectric (TE) generators are subjected to thermal gradients and thermal transients, creating mechanical stresses in the thermoelectric legs. Such stresses are functions of the elastic moduli of the TE material. For SnTe_{1+x} matrices (where $x = 0.0$ or 0.016) composite specimens with 0 to 4 vol.% SiC nanoparticle (SiC_{NP}) additions, the elastic moduli (Young's modulus, shear modulus, bulk modulus and Poisson's ratio) were measured by resonant ultrasound spectroscopy (RUS) from room temperature to 663 K. The effects of matrix composition and the SiC_{NP} additions on the room temperature intercepts and the slopes of the elastic modulus as a function of temperature are also discussed.

Keywords: thermoelectrics; elastic modulus; SnTe ; SiC nanoparticles

7.1 Introduction

A number of thermoelectric (TE) materials, including SnTe are candidates for harvesting waste heat from a variety of sources, including incinerators and automotive or truck exhaust. The energy conversion efficiency, η , of a thermoelectric device can be written as [Bux 2010]

$$\eta = \left(\frac{T_H - T_C}{T_H} \right) \left(\frac{\sqrt{1 + ZT} - 1}{\sqrt{1 + ZT} + \left(\frac{T_C}{T_H} \right)} \right) \quad (1)$$

where T_H and T_C are, respectively, the hot and cold side temperatures of the thermoelectric device and T is the average device temperature. ZT is the dimensionless figure of merit which is given by

$$ZT = \frac{S^2 \sigma_e T}{\kappa} \quad (2)$$

where S = the Seebeck coefficient, σ_e = the electrical conductivity, $S^2 \sigma_e$ = the power factor and κ = the thermal conductivity. As shown by equation (1), as ZT increases the conversion efficiency increases.

However, in addition to the thermal and electrical transport properties, the mechanical properties of the thermoelectric material are also important. Especially in the context of harvesting waste energy, as the heat source (say an automobile engine or an industrial furnace) is cycled on and off, the TE elements that are in place to capture waste heat will also experience thermal transients. The maximum surface thermal stress, Λ_{max} , induced by a thermal transient on a flat plate of uniform thickness is a function of the

temperature-dependent elastic modulus, $E(T)$, and Poisson's ratio, $\nu(T)$, and thermal expansion coefficient, $\alpha(T)$ such that [Lu 1998; Zhao 2000; Manson 1966]

$$\Delta_{max} = \frac{E(T)}{1 - \nu(T)} \alpha(T) \cdot \Delta T \cdot f(Bi) \quad (3)$$

The function $f(Bi)$ increases monotonically with increasing Biot modulus Bi , where $Bi = ah/\kappa$ [Kreith 1973] and a is the characteristic dimension of the specimen, h is the surface heat transfer coefficient and κ is the thermal conductivity of the specimen. In the thermal transient case, ΔT is the difference between the initial and final temperature during the temperature excursion and the function $f(Bi)$ depends on the dimensionless parameter Bi . Also, $\Delta T = (T_i - T_\infty)$ is the quench temperature difference, where T_i is the initial temperature of the specimen and T_∞ is the temperature of the ambient medium.

In addition to stresses induced by thermal transients (equation 3), there are thermal gradients imposed between the hot and cold plates of a thermoelectric device that are essential for current to flow [D'Angelo 2011]. Also, the thermoelectric elements will be subjected to stresses due to thermal expansion mismatch within the thermoelectric module as well as to various external, mechanical stresses. Regardless of the mechanism that generates the stress, calculations via both finite element [Martin 1973; Kaliakin 2002] and analytical techniques [Manson 1966] require knowledge of the elastic modulus and Poisson's ratio in order to analyze the stress-strain response of the material. Also, if microcracks are induced by either mechanical or thermal loading, then the microcrack-induced changes in elastic moduli provide a means of monitoring the extent of microcrack damage [Fan 2012; Case 1993; Chotard 2008].

In this study, the Young's modulus, shear modulus, Poisson's ratio, acoustic wavespeed and Debye temperature were measured over the temperature range from 298 K to 663 K for six bulk SnTe_{1+x} -SiC nanoparticle composites specimens with the SiC nanoparticle (SiC_{NP}) loading from 0 to 4 volume percent. Also, the effects of an off-stoichiometric SnTe composition on the elastic moduli are discussed.

7.2 Experimental procedure

7.2.1 Specimen Preparation

To fabricate each SnTe_{1+x} ingot, high purity powders of Sn (Plasmaterials, purity 99.999%) and Te (5N Plus Inc., purity 99.999%) with no added dopants were flame sealed in a quartz tube under vacuum. For ingot $\text{SnTe}(x=0)$, stoichiometric amounts of each powder were placed into quartz tubes (21.2499 g of Sn and 22.8462 g of Te in first batch, 21.2478 g of Sn and 22.8486 g of Te in second batch). The sealed tubes were heated to 1273 K in 10 hours, held at 1273 K for 10 hours then air quenched to room temperature (RT).

For ingot $\text{SnTe}(x=0.016)$, a non-stoichiometric amount of powder was added (44.9274 g of Sn and 49.0715 g of Te) to a quartz tube to produce $\text{SnTe}_{1.016}$. The sealed tube was heated to 1148 K in 12 hours, held for 12-13 hours at temperature, then quenched into water.

The resulting ingot was crushed and ground in a WC-lined mechanical mortar and pestle. The ground powder was passed through a 53 μm sieve on a shaker table for 5 to 15 minutes. Powder that did not pass through the sieve was reground and re-sieved. Additional details on the crush-grind-sieve-regrind (CGSR) procedure are provided elsewhere [Pilchak 2007].

Table 7.1. For each of the six SnTe-SiC_{NP} specimens included in this study, the volume fraction SiC_{NP} addition, specimen mass, dimensions, mass density, porosity, P, and mean grain size. Specimens were prepared from one of two starting ingots, designated A or B in the specimen label.

Specimen label	SiC Nanoparticle Volume Fraction	Mass (g)	Dimensions (cm)	Mass Density (g/cm ³)	P	Mean Grain Size (μm)
SnTe(x=0)V0	0.00	7.7749	Ø 1.984 × 0.401	6.27	0.028	N.A. ^a
SnTe(x=0)V0.01	0.01	7.4952	Ø 1.973 × 0.403	6.09	0.051	2.7
SnTe(x=0)V0.02	0.02	7.3529	Ø 1.989 × 0.31	6.21	0.026	1.0
SnTe(x=0)V0.03	0.03	3.4264	1.162 × 1.249 × 0.385	6.13	0.034	1.0
SnTe(x=0)V0.04	0.04	7.6725	Ø 1.968 × 0.416	6.07	0.039	1.2
SnTe(x=0.016)V0	0.00	7.5693	Ø 1.987 × 0.387	6.30	0.022	1.8

^a Not available

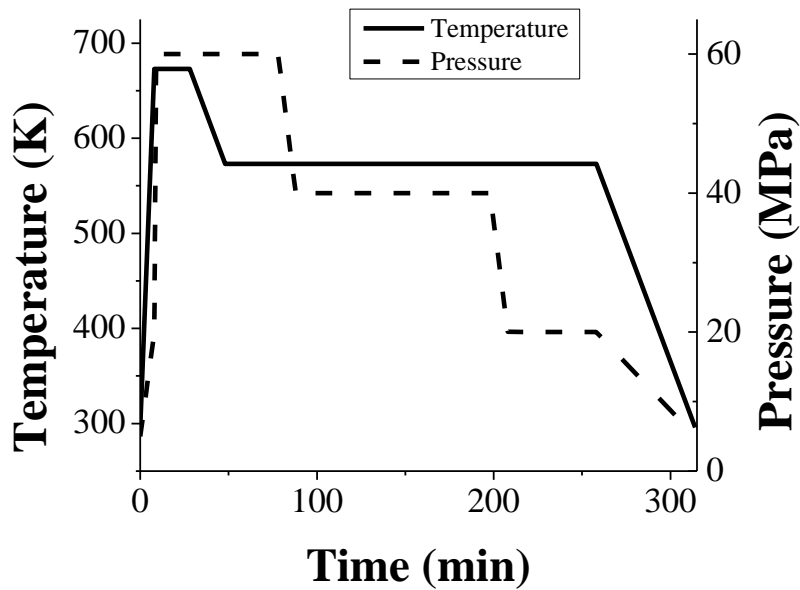


Figure 7.1. Processing parameters (temperature and die pressure) as a function of time for the PECS densification of the SnTe-SiC_{NP} specimens included in this study.

After grinding, the CGSR powder was milled in a planetary ball mill in 20 g to 30 g batches with 100 g of 10 mm diameter spherical alumina media at 150 RPM for 3 h (PM100, Retsch GmbH, Haan, Germany). For specimens with SiC nanoparticle (SiC_{NP}) additions, 95% purity silicon SiC_{NP} with a vendor –specified particle size of 50-60 nm (SiC_{NP} , 4621HW, Lot #4621-110209, Nanostructured & Amorphous Materials Inc., Houston, TX) was added to an 8 g batch of milled SnTe_{1+x} powder and mixed at 110 RPM for 6 h with 100 g of 10 diameter mm alumina media. From 0 to 4 vol% SiC_{NP} was added to the SnTe_{1+x} powders (Table 7.1).

Sintering of the milled powder was performed by pulsed electric current sintering (PECS) in a 20 mm diameter graphite die lined with two layers of grafoil (SPS Model 10-3, Thermal Technology LLC, Santa Rosa, CA). For each specimen included in this study, the PECS sintering was performed using an argon-filled chamber at 673 K and at a die pressure of 60 MPa for 20 minutes, followed by 210 minutes at 573 K. Details of the time-temperature and pressure-temperature profiles are given in Figure 7.1. The resulting disk-shaped specimens were from about 3 to 4 mm thick, although one specimen (A-04-3) was cut into a rectangular parallelepiped prior to testing (Table 7.1).

7.2.2 Specimen characterization

The microstructure of the specimens was examined using the following scanning electron microscopes (JEOL 6400, JEOL 6610LV or JSM-7500F, JEOL Ltd., Japan). All SEM images taken with the JEOL 6400, JEOL 6610LV used 15 mm working distance with a 15 kV accelerating voltage. For the JSM-7500F (high resolution SEM) a 4.5 mm working distance and 2 kV accelerating voltage was used when imaging powder, 4.5 mm working distance and 5 kV when imaging bulk specimens by secondary electron only,

and 8 mm working distance and 15 kV accelerating voltage on specimens imaged by backscatter electron and for energy-dispersive X-ray spectroscopy (EDS).

The JSM-7500F was used to image fractured and polished surfaces of the SnTe_{1+x} bulk specimens along with the as-received and as-ground SiC_{NP} . The fractured surfaces of the specimens were not coated prior to SEM observation. However, the polished surfaces and the SiC_{NP} powders themselves were sputter coated with osmium since without coating the specimens exhibited localized charging.

In order to attempt to break up extensive clumping in the as-received SiC_{NP} , a 5 gram batch of the as-received SiC_{NP} powders was mixed with 5 ml of ethanol and then hand ground for 5 minutes with an alumina mortar and pestle. While the grinding process in the mortar and pestle is certainly not identical to the grinding process experienced during planetary milling of the SiC_{NP} and SnTe_{1+x} powder mixture that was subsequently sintered, the hand grinding gives a rough gauge of the how easy it is to break-up the agglomerates.

The milled powder was examined by XRD (Miniflex II, Cu K_α radiation, Rigaku, Tokyo, Japan) to verify the phase composition and lattice parameter of the SnTe_{1+x} material.

7.2.3 High temperature Resonant Ultrasound Spectroscopy measurements

The elastic moduli were measured by Resonant Ultrasound Spectroscopy (RUS) in a furnace with a flowing Ar-4% H atmosphere. The elastic moduli were measured at RT before turning on the furnace. The specimen was heated to 333 K for the first measurement at higher temperature, then the furnace temperature was increased in 30 K increments to 663 K. The specimen was then cooled in 30 K increments from 663 K to

333 K. After the furnace was turned off and the specimen cooled to RT, the specimen was measured one final time by RUS. Dimensional changes during heating were calculated using a coefficient of thermal expansion of $22.2 \times 10^{-6} \text{ K}^{-1}$ (Schmidt et al., unpublished data). Additional details of the HT-RUS procedures are provided elsewhere [Ren 2008; Ren 2009b; Ren 2009a].

7.3 Results and Discussion

7.3.1 Microstructural analysis

Both fracture surfaces (Figure 7.2a) and polished surfaces (Figure 7.2b) of the SnTe_{1+x} - SiC_{NP} composite specimens were examined. No surface-breaking cracks were observed for either the fractured surfaces (Figure 7.2a) or the polished surfaces (Figure 7.2b) of the specimens. The polished surfaces of the SnTe_{1+x} specimens showed occasional isolated, quasi-spherical pores with submicron diameters (Figure 7.2b). In addition, the grains were relatively equiaxed with a mean grain size of roughly $1 - 3 \mu\text{m}$ (Figure 7.2a, Table 7.1), as evaluated by the linear intercept technique on SEM micrographs of fractured surfaces [Case 1981b]. Also, the fractures were predominantly intergranular with transgranular fracture observed for some of the larger grains (Figure 7.2a). The mass, mass density, grain size and volume fraction porosity for each specimen included in this study is listed in Table 7.1.

Room temperature X-ray diffraction showed that only the SnTe cubic phase was present in the specimens from both ingots $\text{SnTe}(x=0)$ and $\text{SnTe}(x=0.016)$ (Table 7.1), however there was a systematic shift in the XRD patterns that was likely due to compositional differences in SnTe_{1+x} solid solution. The lattice parameter was $a_0 = 6.3130 \pm 0.0056 \text{ \AA}$ for the planetary-milled powders used to fabricate specimens each of

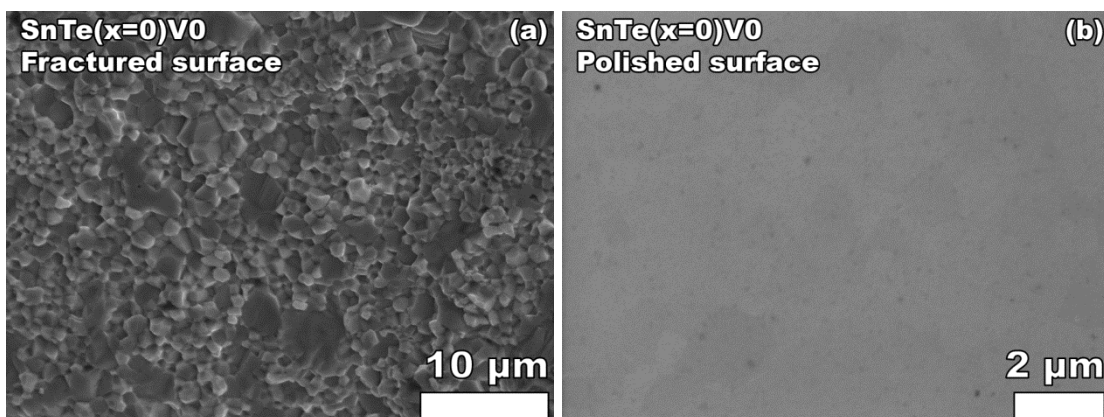


Figure 7.2. For SnTe specimen A-06 (0 vol% SiC_{NP}), (a) fractured specimen surface and (b) polished specimen surface.

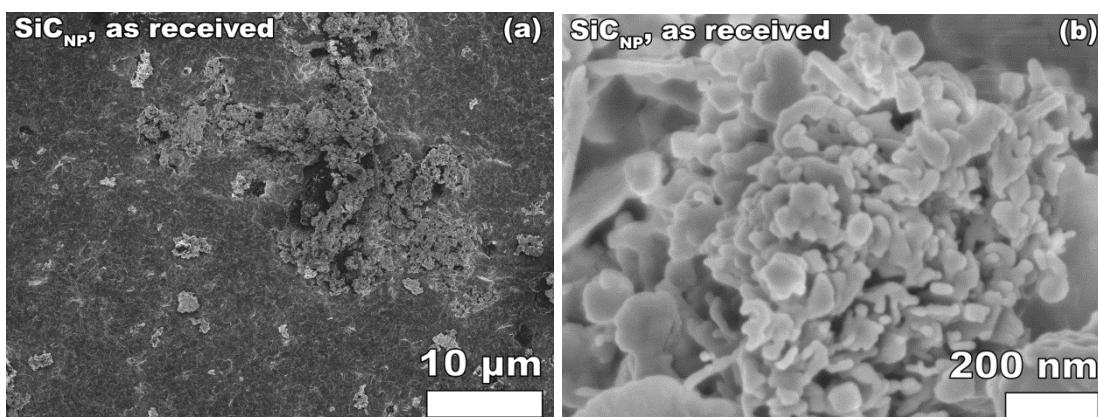


Figure 7.3. The as-received SiC_{NP} consisted of particles roughly 50 nm across agglomerated into clusters ranging in size from approximately 100 nm to 20 μm.

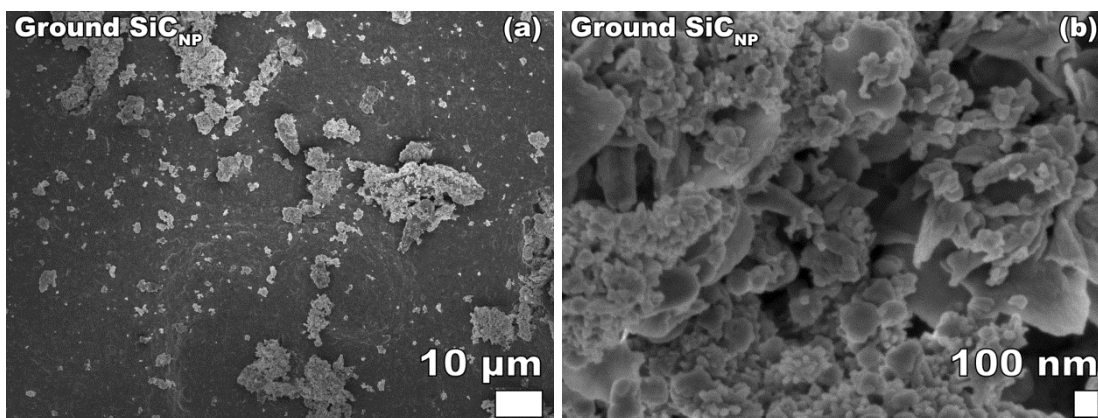


Figure 7.4. (a) After grinding in an alumina mortar and pestle for 5 min in ethanol, the SiC_{NP} exhibited agglomerations of particles ranging from sub-micron to ~10 μm diameter. (b) The agglomerations consisted primarily of nanoparticles with diameter less than 100 nm, but with an occasional micron-scale particle. The size distribution of the agglomerates after manual grinding was similar to that observed prior to manual grinding (Figure 7.3).

the “SnTe($x=0.0$)” specimens, of nominal composition SnTe. For the planetary-milled powders used to fabricate the “SnTe($x=0.016$)” specimen, of composition SnTe_{1.016}, the lattice parameter was 6.3014 ± 0.0056 Angstroms. The literature value for lattice parameter of SnTe given by is 6.313 Angstroms [Wyckoff 1963]. As Te is added to the SnTe structure, Sn vacancies are created in the rock salt lattice, so that the shift in stoichiometry results from the creation of cation vacancies [Rogacheva 1991].

The compositional difference between ingots SnTe($x=0$) and SnTe($x=0.016$) has important implications for mechanical properties of the SnTe_{1+x} specimens since in general the elastic moduli are known to be sensitive to changes in composition within solid solution systems [Ravinder 2001; Srinivas Rao 2003; Ren 2007] including thermoelectric solid solutions [Ren 2007]. The composition-related changes in elastic moduli are discussed further in following section.

The as-received SiCNP powders were not discrete nanoparticles but instead consisted of clumps with diameters from roughly 100 nm to 20 μm across (Figure 7.3), with individual particles roughly 100 nm across (Figure 7.3). Manual grinding in a mortar and pestle did not noticeably reduce the clump size from the original several hundred nm diameter (Figure 7.4). The manual grinding only provides a rough gauge of the ease of breaking up the SiC_{NP} powder agglomerates and does not approximate the grinding action of the planetary mill used to process the bulk specimens in this study.

Fracture surfaces of specimens SnTe($x=0$)V0, SnTe($x=0$)V0.01, SnTe($x=0$)V0.02, SnTe($x=0$)V0.03 and SnTe($x=0$)V0.04 were examined (Figure 7.5a – 7.5e). Each specimen with SiC_{NP} addition showed fine-grained clusters on the fracture surface that likely represented SiC_{NP} clumps on the surface that ranged from about

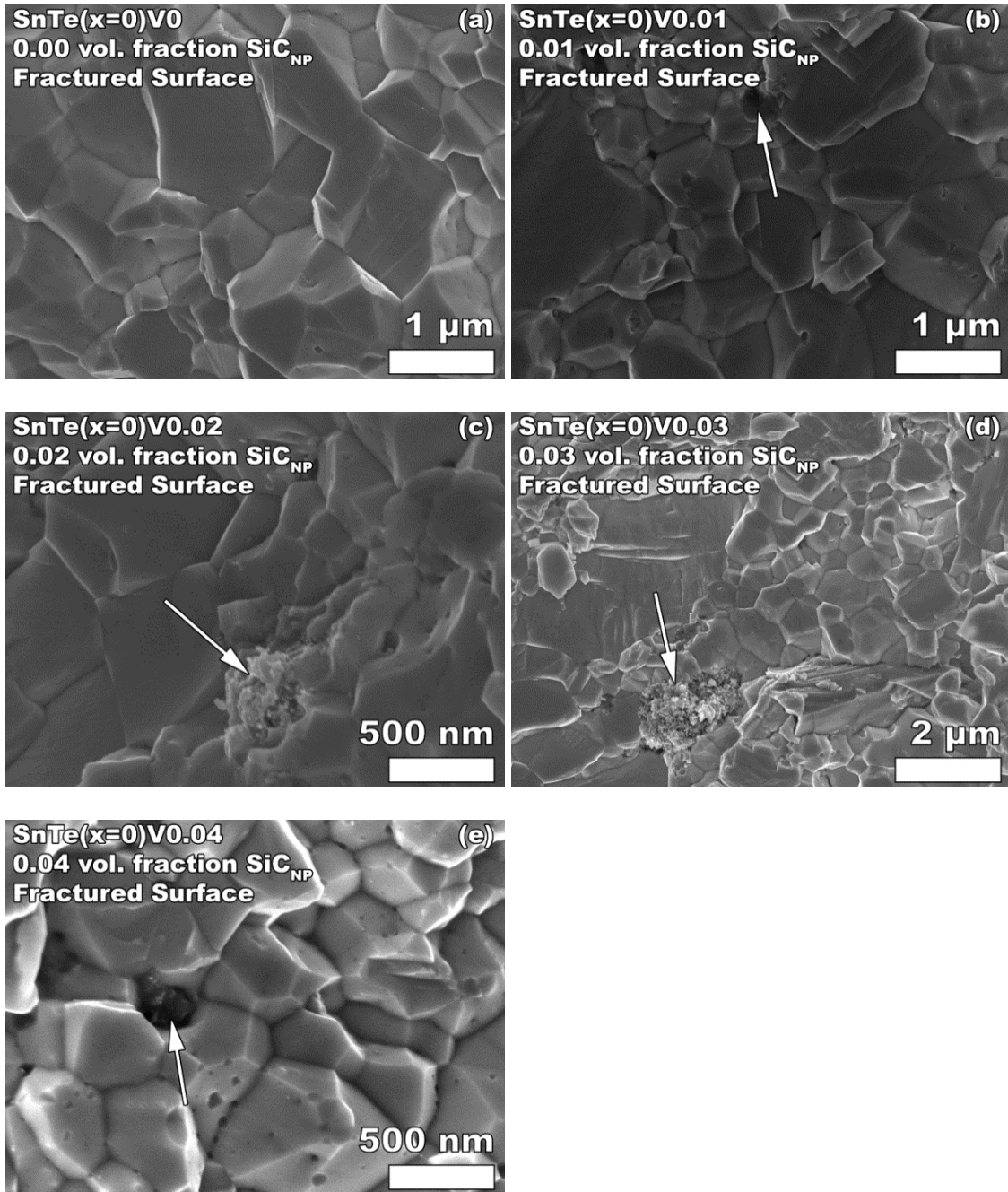


Figure 7.5. Fractured specimen surface images for (a) specimen SnTe ($x = 0$)V₀ with no SiC_{NP} added, and for (b) SnTe ($x = 0$)V_{0.01}, (c) SnTe($x = 0$)V_{0.02}, (d) SnTe($x = 0$)V_{0.03}, and (e) SnTe($x = 0$)V_{0.04}. In (b) – (e), the location of SiC_{NP} clusters is indicated by arrows.

200 nm to 2000 nm in across (Figure 7.5b – 7.5e). The SiC_{NP} clumps are indicated by arrows in Figures 7.5b – 7.5e. The fracture surface of the $\text{SnTe}(x=0)\text{V}0$ was free of such clusters.

In order to determine whether or not the clusters observed on the specimen fracture surfaces of the composites were composed of SiC_{NP} , pairs of secondary electron and backscattered images were taken at high resolution (Figures 7.6a – 7.6d). For specimen $\text{SnTe}(x=0)\text{V}0$, with no SiC_{NP} addition, the secondary electron image (Figure 7.6a) and the backscattered image (Figure 7.6b) were similar in appearance. However, for $\text{SnTe}(x=0)\text{V}0.04$ (with 0.04 volume fraction of SiC_{NP}), the backscattered image of the specimen exhibited dark regions that indicate a lower atomic mass, which is consistent with the presence of SiC_{NP} at or just below the surface of the specimen in the dark regions (Figure 7.6d). However, for the secondary electron image (Figure 7.6d), there was much less atomic number contrast in the image. From measurements on SEM micrographs taken at two different magnifications, the area fraction of SiC_{NP} clusters was estimated as roughly 2.1–2.5 % (Table 7.2).

EDS measurements on specimen $\text{SnTe}(x = 0)\text{V}0.04$ indicated a silicon content of about 13 at% within dark region (the box-labeled “Spectrum 2” in Figure 7.7). In contrast, a Si content of <1 at% was indicated by EDS in the light region marked by the box-labeled “Spectrum 1” in Figure 7.7. Thus, there is a very strong indication that SiC_{NP} clusters ranging from roughly 100 to 1000 nm are distributed within specimen $\text{SnTe}(x = 0)\text{V}0.04$.

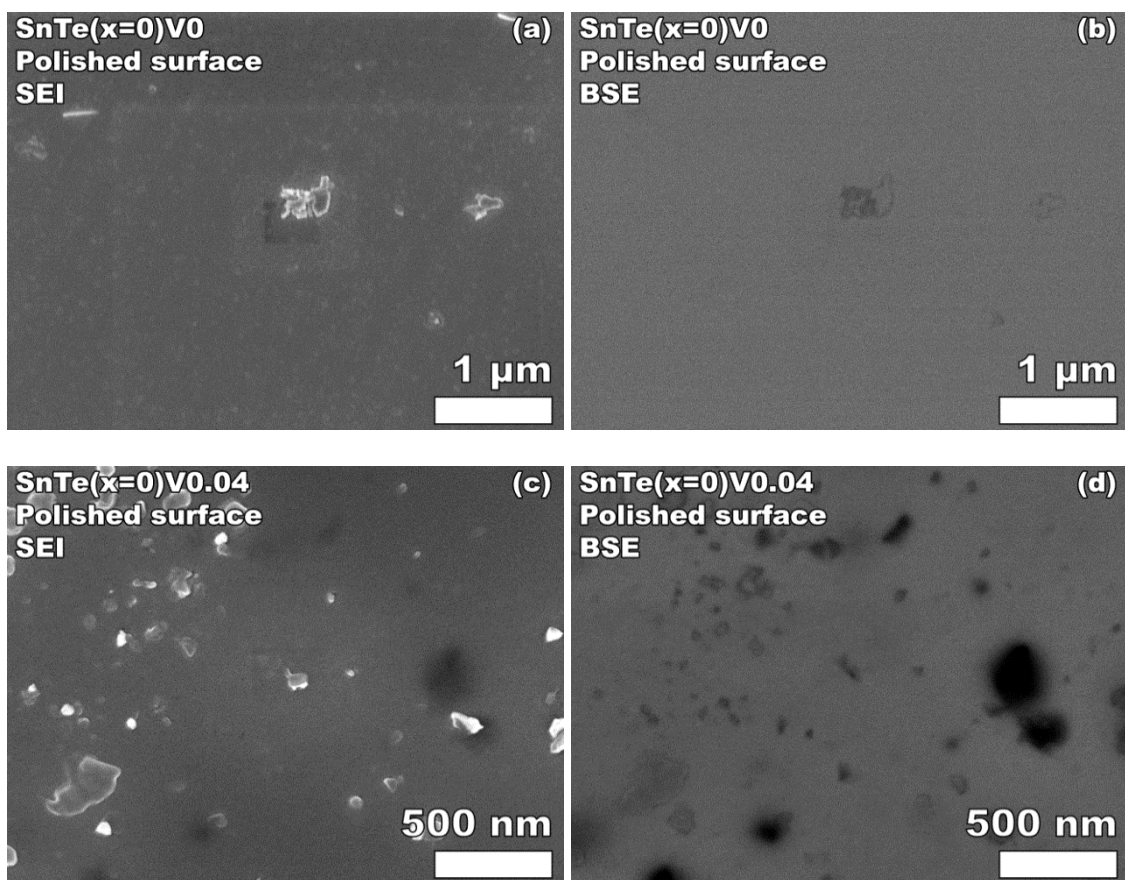


Figure 7.6. Specimen SnTe($x = 0$)V0, with no added SiC_{NP}, shows no surface features other than surface debris in both (a) a secondary electron image (SEI) and in (b) a backscattered electron image. Specimen SnTe($x = 0$)V0.04 with 0.04 vol fraction SiC_{NP} addition shows a difference between the (c) secondary electron image and (d) the backscattered electron image, with the image in the backscattered electron mode showing dark regions indicating likely SiC_{NP} clusters at or near the specimen surface.

Table 7.2. For SiC_{NP} clusters identified by electron backscatter images for specimen SnTe(x = 0)V0.04 (Fig. 6), the SEM magnification, the area of the field of view of the micrograph, along with the number, number density, and size range of the SiC_{NP} clusters

Magnification	Area (μm ²)	Number of SiC spots	Areal number density (#/μm ²)	Average diameter (nm)	Range (nm)	Area fraction SiC
X 25000	17.0	12	0.71	160	54 – 560	0.025
X 50000	4.2	16	3.8	68	21 – 120	0.021

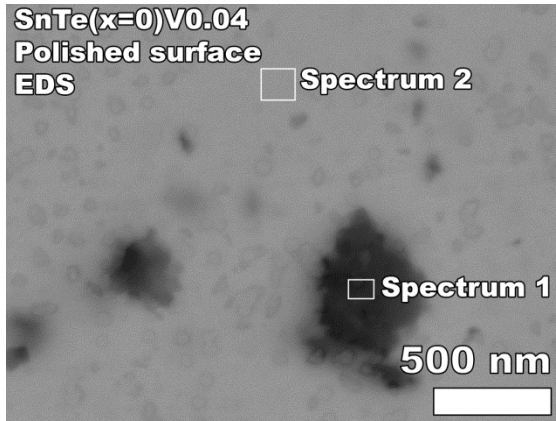


Figure 7.7. A backscattered electron image of a polished surface of specimen SnTe(x = 0)V0.04 indicates darker regions with a lower average atomic weight, likely composed primarily of the SiC_{NP}. Using EDS, silicon was detected at the location of spectrum one, at approximately 13 at%, but not at spectrum two, with <1 at%, confirming that the dark regions contain a high concentration of the SiC_{NP}. The specimen was osmium coated prior to imaging to reduce localized charging.

7.3.2 Elastic modulus as a function of temperature, matrix composition and SiC_{NP} volume fraction

For the six SnTe_{1+x}-ySiC_{NP} ($0 < y < 4$ vol %) composite specimens included in this study, the Young's modulus (Figure 7.8) and shear modulus (not shown) decreased approximately linearly with increasing temperature over the entire temperature range from room temperature to 663 K. Equations (4a) and (4b) were fitted to the high temperature Young's modulus, E , and shear modulus, G , data, respectively, for temperature T

$$E = E_{RT} (1 - b_{TE}(T - T_{RT})) \quad (4a)$$

$$G = G_{RT} (1 - b_{TG}(T - T_{RT})) \quad (4b)$$

where E_{RT} and G_{RT} are the RT intercepts, b_{TE} and b_{TG} are measures of the changes in E and G , respectively, with temperature, T , and RT T_{RT} (295 K). The values of the least-squares parameters E_{RT} , G_{RT} , b_{TE} and b_{TG} are listed in Table 7.3 for each SnTe_{1+x}-SiC_{NP} specimen included in this study.

The near- superposition of the heating and cooling curves for the elastic moduli (Figure 7.8) indicates the absence of either (1) significant microcracking or (2) bloating. Microcracking, if present, can reduce the elastic modulus of a material [Fan 2012; Case 1993; Chotard 2008]. Moreover, for materials that are microcracked at room temperature, heating to a homologous temperature of about 0.6 can induce microcrack healing, which in turn leads to a hysteresis in the modulus versus temperature curve [Chotard 2008; Case 1981a]. Bloating, which refers to the generation of porosity during heating, is often associated with solid phase decomposition reactions within a specimen [Ni 2011].

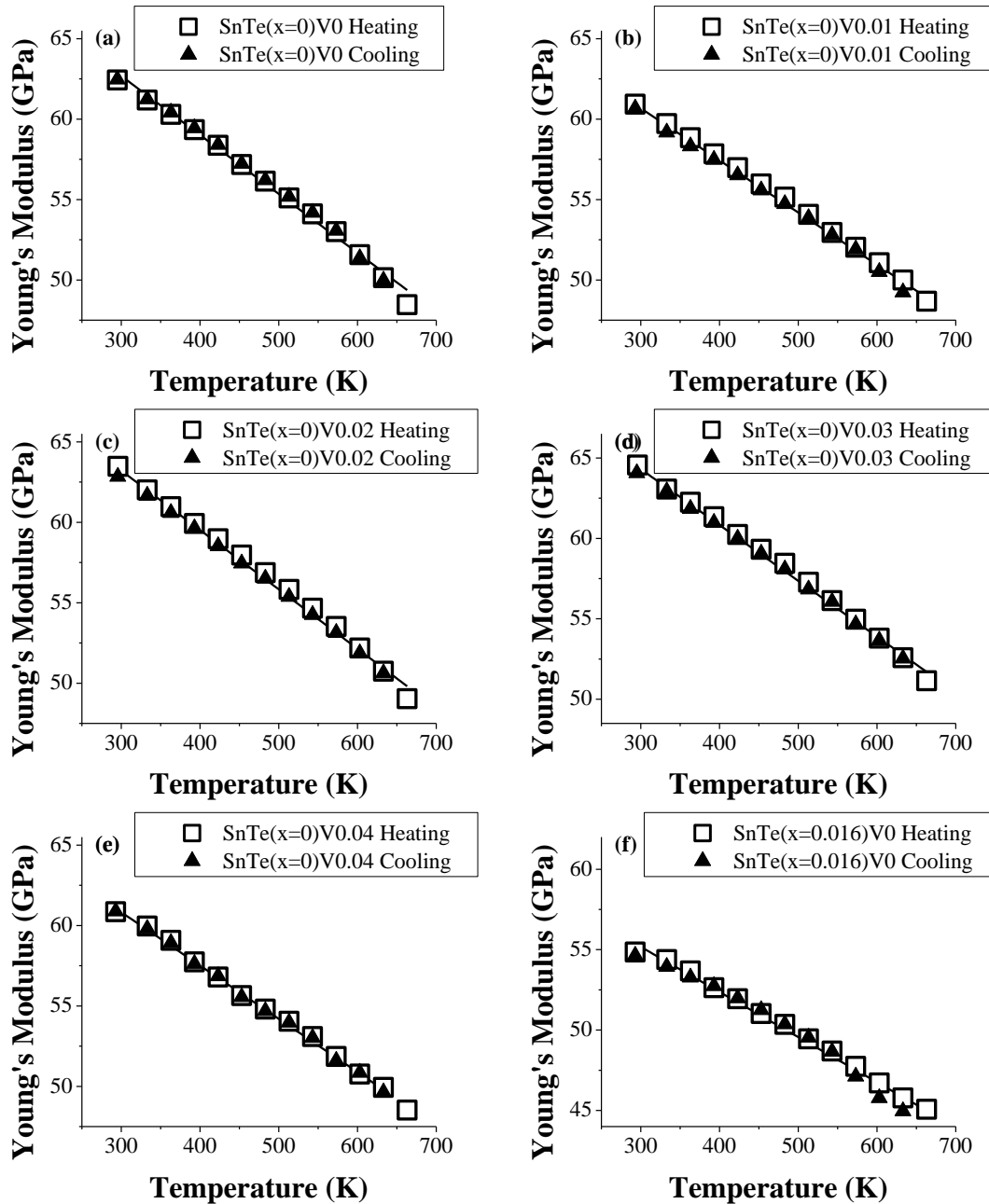


Figure 7.8. The Young's modulus versus temperature for the six SnTe-SiC_{NP} specimens included in this study. For each specimen, there is no observable hysteresis between the heating and cooling curves indicating the lack of significant microcracking or bloating over the test temperature range (room temperature to 663 K). The error bars are smaller than the plotting symbols for each modulus value in (a-f).

Table 7.3. For the six SnTe-SiC_{NP} specimens included in this study, results of a least squares fit to equation (4a) for the Young's modulus, E , versus temperature, T , data and to equation (4b) for the shear modulus, G , versus T , data. The coefficients of determination for the fit of the E versus T and the G versus T data are given by R_E^2 and R_G^2 , respectively.

Specimen	Vol. fraction SiC	E_{RT}	$b_{TE} (K^{-1}) \times 10^{-4}$	R^2	G_{RT}	$b_{TG} (K^{-1})$	R^2
SnTe(x=0)V0	0.00	62.87 ± 0.13	5.83 ± 0.09	0.993	25.27 ± 0.05	6.14 ± 0.09	0.994
SnTe(x=0)V0.01	0.01	60.84 ± 0.10	5.33 ± 0.07	0.995	24.54 ± 0.05	5.62 ± 0.09	0.992
SnTe(x=0)V0.02	0.02	63.40 ± 0.12	5.82 ± 0.08	0.994	25.33 ± 0.05	6.20 ± 0.08	0.995
SnTe(x=0)V0.03	0.03	64.48 ± 0.09	5.38 ± 0.06	0.996	25.42 ± 0.05	5.72 ± 0.08	0.994
SnTe(x=0)V0.04	0.04	61.04 ± 0.07	5.44 ± 0.05	0.998	24.41 ± 0.03	5.37 ± 0.05	0.998
SnTe(x=0.016)V0	0.00	55.31 ± 0.15	5.07 ± 0.12	0.995	21.70 ± 0.07	5.29 ± 0.14	0.980

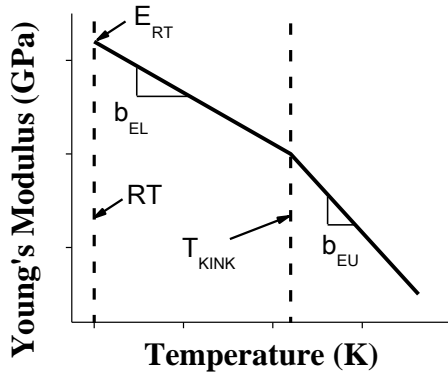


Figure 7.9. Schematic representation of the bilinear Young's modulus, E , versus temperature, T , behavior showing T_{KINK} and the associated slope change in the E versus T curve.

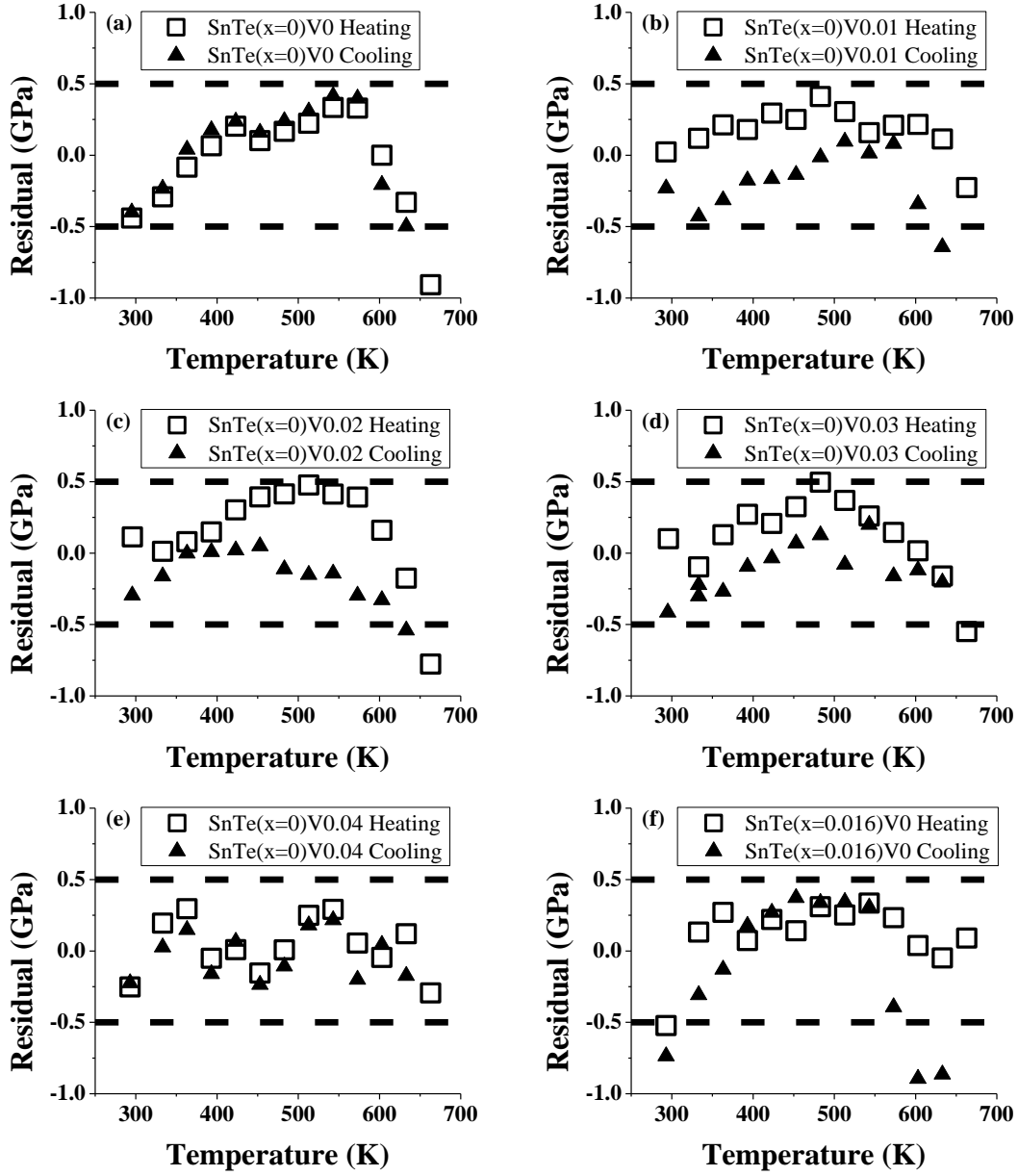


Figure 7.10. The residuals (equation 5) representing the difference between the experimental Young's modulus data and the modulus values predicted from the least-squares fit of the E versus T data to equation (4). The dashed lines at 0.05 GPa are a guide, representing roughly $\pm 0.01 E_{RT}$, where E_{RT} is defined as the room temperature intercept of the modulus–porosity relationship given by equation (4a). A change in the E versus T slope occurs at approximately 543 K (T_{KINK}).

7.3.2.1 Bilinear model of elastic modulus versus temperature

Although in this study the decrease in Young's modulus for SnTe_{1+x} is approximately linear with increasing T , we will consider (1) a bilinear model of the elastic modulus versus temperature behavior and (2) composition-dependent differences and subsequent elastic modulus differences between ingots $\text{SnTe}(x=0)$ and $\text{SnTe}(x=0.016)$ in this study. A schematic of the bilinear model for the E versus T behavior is shown in Figure 7.9.

The motivation for the bilinear model comes from examining the residuals obtained from the least-squares fit of the linear model (equation (4a)) to the SnTe_{1+x} E versus T data. For a given Young's modulus, temperature data pair (E_j, T_j) the j th residual, resid_j is defined as

$$\text{resid}_j = (E_j - E_{\text{pred}}) \quad (5)$$

where E_{pred} = the E value predicted by the least-squares fit to equation (4a) for $T = T_j$. Thus, for a given data set including a total of N data pairs (E_j, T_j) , the least-squares procedure yields N residuals, which measure the differences between the data and the curve obtained by the least-squares fit. Using the E_{pred} values obtained from the linear model, the residuals for each of the six specimens (Figures 7.10a – 7.10f) show maxima in the vicinity of 543 K.

In contrast to the linear model, for the bilinear model for the E versus T behavior, equation 4a is applied separately for the two contiguous temperature segments: (i) $T \leq T_{\text{KINK}}$ and (ii) $T \geq T_{\text{KINK}}$ (Tables 7.4 and 7.5, Figure 7.9). At the temperature $T = T_{\text{KINK}}$, the E versus T slope change is characterized by Δb , such that

Table 7.4. For two separate temperature ranges, RT – 543 K, and 543 K – 663 K, the E versus T was fit to equation (4a).

Specimen	Temperature range (K)	Fitted parameters		R^2
		E_{RT}	$b_{TE} (\times 10^{-4} \text{ K}^{-1})$	
SnTe(x=0)V0	RT to 543	62.6 ± 0.1	5.4 ± 0.1	0.999
	543 to 663	66.0 ± 0.3	7.1 ± 0.2	0.995
SnTe(x=0)V0.01	RT to 543	60.7 ± 0.1	5.1 ± 0.1	0.993
	543 to 663	61.9 ± 0.7	5.8 ± 0.3	0.972
SnTe(x=0)V0.02	RT to 543	63.2 ± 0.1	5.5 ± 0.1	0.993
	543 to 663	65.5 ± 0.6	6.7 ± 0.2	0.987
SnTe(x=0)V0.03	RT to 543	64.3 ± 0.1	5.1 ± 0.1	0.995
	543 to 663	66.0 ± 0.3	6.1 ± 0.1	0.996
SnTe(x=0)V0.04	RT to 543	61.0 ± 0.1	5.3 ± 0.1	0.996
	543 to 663	62.0 ± 0.1	5.9 ± 0.1	0.991
SnTe(x=0.016)V0	RT to 543	55.0 ± 0.1	4.5 ± 0.1	0.991
	543 to 663	56.6 ± 1.2	5.8 ± 0.6	0.907

Table 7.5. Comparison of Δb , equation (6), for this study and LAST [Ren 2010].

Specimen	Material Type	T_{KINK}	Δb	Reference
SnTe(x=0)V0	SnTe	543 K	-0.31	This study
SnTe(x=0)V0.01	SnTe – 1 vol% SiC _{NP}	543 K	-0.14	This study
SnTe(x=0)V0.02	SnTe – 2 vol% SiC _{NP}	543 K	-0.22	This study
SnTe(x=0)V0.03	SnTe – 3 vol% SiC _{NP}	543 K	-0.20	This study
SnTe(x=0)V0.04	SnTe – 4 vol% SiC _{NP}	543 K	-0.11	This study
SnTe(x=0.016)V0	SnTe _{1.016}	543 K	-0.27	This study
155A (5K/min)	Ag _{0.86} Pb ₁₉ Sb _{1.0} Te ₂₀	523 K	+0.47	[Ren 2010]
155B (5K/min)	Ag _{0.86} Pb ₁₉ Sb _{1.0} Te ₂₀	523 K	+0.51	[Ren 2010]
155B (2K/min)	Ag _{0.86} Pb ₁₉ Sb _{1.0} Te ₂₀	523 K	+0.47	[Ren 2010]

$$\Delta b = \frac{b_{EL} - b_{EU}}{b_{EL}} \quad (6)$$

where b_{EL} is the slope of the lower temperature region, $T < T_{KINK}$ and b_{EU} is the slope of the region upper temperature segment, $T > T_{KINK}$ (Table 7.5 and Figure 7.9). If, as suggested above, we let $T_{KINK} = 543$ K and apply equation 4a in a bilinear (piecewise) manner from T_{RT} to T_{KINK} and from T_{KINK} to T_{MAX} then the residuals for the bilinear model are reduced in magnitude (Figure 7.11) compared to the linear model and the maximum near $T = 543$ K largely disappears (Figure 7.10). This result indicates that the bilinear model is useful and that 543 K is a reasonable estimate for T_{KINK} .

Based on a work by Hoang et al. [Hoang 2005], Ren et al. [Ren 2010] derived a model for the similar bilinear E versus T behavior observed for a lead-antimony-silver-tellurium thermoelectric material (LAST, $\text{Ag}_{0.86}\text{Pb}_{19}\text{Sb}_{1.0}\text{Te}_{20}$), where a change in the slope of E , versus was attributed to an order-disorder transition. The change in slope, Δb with increasing temperature (equation (6)) was positive in the Ren et al. study [Ren 2010] while in this study Δb is negative (Table 7.5). However, the values of T_{KINK} are similar for the two studies, namely 523 K for LAST [Ren 2010] and 543 K for this study.

In terms of the possible mechanism for the bilinear behavior of SnTe in this study, it is important to note that the LAST materials studied by Ren *et al.* [Ren 2010] are essentially silver and tin-doped PbTe and that PbTe is quite similar to SnTe in many respects. For example, both SnTe and PbTe are IV-VI tellurides that crystallize in the rocksalt structure [Lawson 1951; Noda 1987; Beattie 1969]. Other physical properties for SnTe and PbTe that also are similar include the lattice constants, a_0 (SnTe $a_0 = 0.6304$ nm, PbTe $a_0 = 0.6454$ nm) [Noda 1987; Mariano 1967; Seddon 1976], hardness, H (SnTe

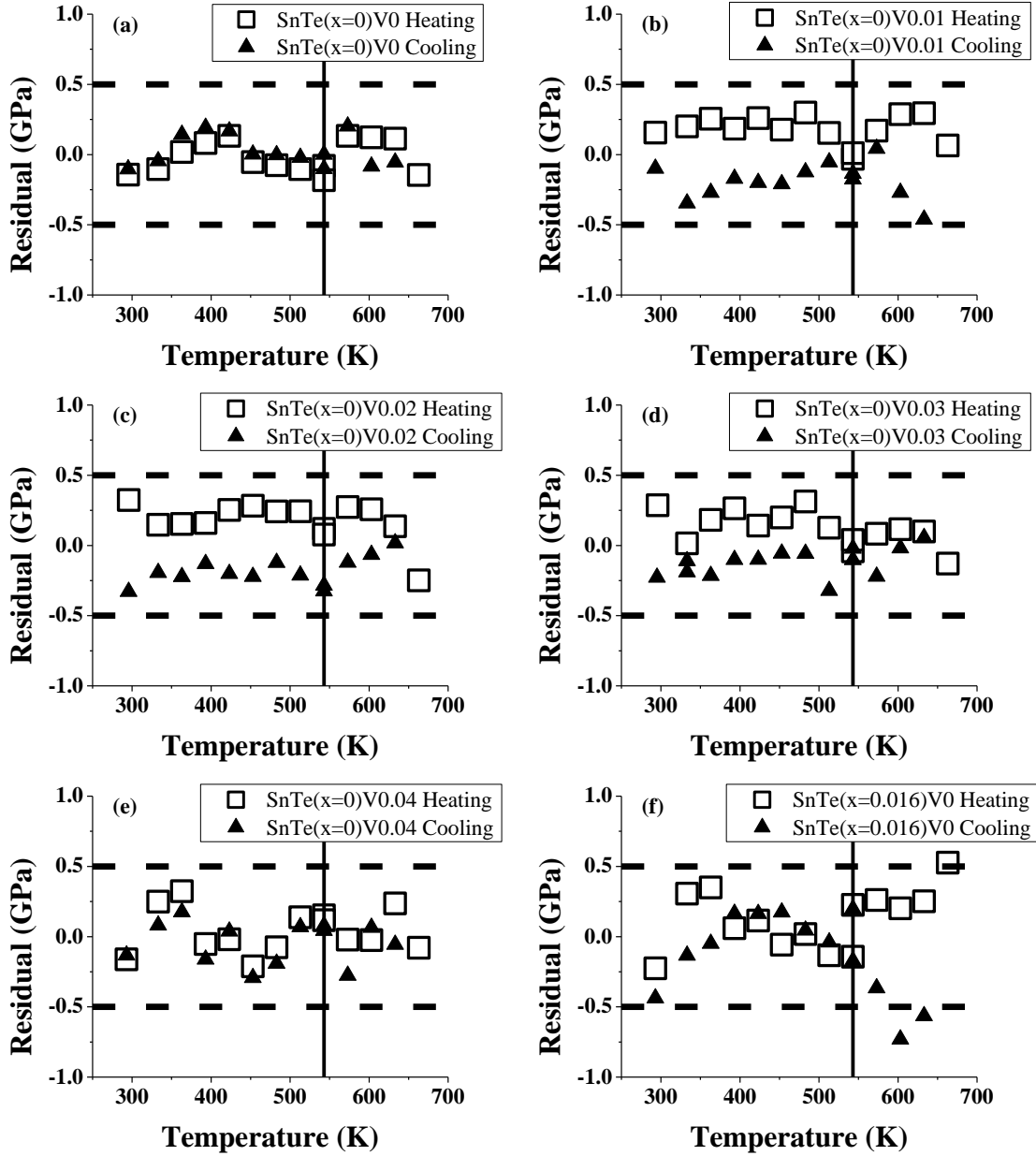


Figure 7.11. Unlike Figure 7.10, the residuals represent the difference between the experimental data and the least-squares fit performed to equation (4) in a piecewise manner, that is least-squares fits were performed separately for the two temperature intervals (i) T_{RT} to T_{KINK} and (ii) T_{KINK} to the maximum test temperature. As in Figure 7.10, the dashed lines at 0.05 GPa represent roughly $\pm 0.01 E_{RT}$, where E_{RT} is defined as the room temperature intercept of the modulus-porosity relationship given by equation (4a). In (a) – (f), the vertical line at 543 K represents T_{KINK} , the temperature at which the change in the E versus T slope occurs.

$H = 0.78$ GPa, PbTe $H = 0.76$ GPa) [Cui 2003], thermal expansion coefficient, α (PbTe $\alpha = 20.4 \times 10^{-6} \text{ K}^{-1}$, SnTe $\alpha = 21.3 \times 10^{-6} \text{ K}^{-1}$) [Houston 1968; Belson 1970] and melting points, T_{MP} (PbTe $T_{\text{MP}} = 1197$ K, SnTe $T_{\text{MP}} = 1079$ K) [Liu 2009]. In addition, the elastic moduli of cubic materials such as SnTe and PbTe can be compared using the mean of the Hashin-Strikman (H-S) bounds. (The H-S bounds, which are computed from the single crystal elastic constants, can be used to estimate the elastic moduli of dense polycrystalline materials without crystallographic texture). For SnTe, the mean of the H-S bounds for the Young's modulus, E , and shear modulus, G , is 55.6 and 21.7 GPa, respectively [Beattie 1969; Simmons 1971]. For PbTe, the mean of the H-S bounds Young's moduli and shear moduli is 58.1 and 23.0 GPa, respectively [Houston 1968]. Thus, both the E and G values of SnTe and PbTe are similar.

Thus, given both the similarity between SnTe and PbTe (and LAST) and the tendency of SnTe to crystallize with an off-stoichiometric composition (as will be discussed in the following section), the order-disorder mechanism proposed by Ren *et al.* [Ren 2010] may also apply to SnTe. However, it must be noted that in LAST, the Ag precipitates as nanoparticles of Ag_2Te [Pei 2011; Cook 2009], but the order-disorder mechanism related to the modulus-temperature kink in LAST [Ren 2010] may be more closely associated with the matrix rather than the Ag_2Te nanoparticles. SnTe does not have a similar nanostructure. Thus, further research is needed to explore the kink behavior in the E versus T behavior of SnTe.

7.3.2.2 Effects of chemical composition and porosity on elastic moduli of the SnTe_{1+x} matrix

In addition to the E versus T slope discussed in the previous section, we shall also consider the nature of changes in elastic modulus both as (i) a function of the chemical composition and (ii) as a function of residual porosity in the specimens. We shall first consider the possible effects on the elastic modulus due to compositional differences.

In this study, the composition of matrix may be written as SnTe_{1+x}, where for ingot SnTe($x=0$), $x = 0$ and for ingot SnTe($x=0.016$), $x = 0.016$. For specimens without SiC_{NP} addition, the room temperature Young's modulus of specimen SnTe($x=0$)V0 from ingot SnTe($x=0$) is 62.9 GPa (Table 7.2 and Figure 7.8) and the Young's modulus of specimen SnTe($x=0.016$)V0 from ingot SnTe($x=0.016$) is 55.3 GPa.

These differences in the elastic moduli between ingots SnTe($x=0$) and SnTe($x=0.016$) may be related to differences in the chemical composition between the two ingots since significant changes in Young's modulus and bulk modulus have been observed to accompany shifts in the chemical composition of solid solution systems [Ren 2007]. As an example, for 14 solid solution systems from the literature, Ren *et al.* [Ren 2007] characterized composition-induced changes in Young's modulus, E , and bulk modulus, K , in terms of E_{max}/E_{min} and K_{max}/K_{min} , where the subscripts "max" and "min" refer to the maximum value in E or K , respectively, over the entire compositional range of the solid solution. As reviewed by Ren *et al.*, E_{max}/E_{min} and K_{max}/K_{min} values as large as 3 have been observed in the literature [Ren 2007].

To further examine the numerical values of composition-related changes in mechanical properties, Table 7.6 compares the observed changes in E with composition

Table 7.6. Fractional changes in Young's modulus, E , shear modulus, G , and hardness H as a function of changes in composition from n_1 to n_2 [this study, [Kawaharada 2004; Ravinder 2001; Schenk 1998].

Material	Property	Property at composition $x = n_1$	Property at composition $x = n_2$	Fractional change in property	References
SnTe_{1+x}	E	$x = 0$ 62.9 GPa	$x = 0.016$ 55.3 GPa	-0.12	This study
$\text{NiZrSn}_{1-x}\text{Sb}_x$	E	$x = 0.01$ 111 GPa	$x = 0.02$ 89.2 GPa	-0.20	[Kawaharada 2004]
$\text{NiZrSn}_{1-x}\text{Sb}_x$	E	$x = 0.01$ 111 GPa	$x = 0.05$ 71.8 GPa	-0.35	[Kawaharada 2004]
$\text{Mn}_{1-x}\text{Cd}_x\text{Fe}_2\text{O}_4$	E	$x = 0$ 352 GPa	$x = 0.2$ 256 GPa	-0.27	[Ravinder 2001]
$\text{Mn}_{1-x}\text{Cd}_x\text{Fe}_2\text{O}_4$	G	$x = 0$ 140 GPa	$x = 0.2$ 108 GPa	-0.23	[Ravinder 2001]
$\text{Zn}_{1-x}\text{Cd}_x\text{Te}$	H	$x = 0$ 700 MPa	$x = 0.04$ 930 MPa	+0.33	[Schenk 1998]

for SnTe_{1+x} in this study, with additional literature data on compositionally-related changes in Young's modulus, E , shear modulus, G , and hardness H for several tellurides, antimonides and oxides [Ravinder 2001; Kosuga 2005; Kawaharada 2004; Schenk 1998]. In Table 7.6, the compositional change in SnTe_{1+x} comes about from the creation of Sn vacancies in the lattice [Rogacheva 1991] (Section 7.3.1) and each of the other examples in Table 7.6 is substitutional systems. From Table 7.6 and the Ren *et al.* study [Ren 2010], it appears to be feasible that the 10% difference in the elastic moduli observed between ingots $\text{SnTe}(x=0)$ and $\text{SnTe}(x=0.016)$ (Table 7.3) in this study might be attributed to compositional differences. The lattice parameter measurements for ingots $\text{SnTe}(x=0)$ and $\text{SnTe}(x=0.016)$ (Section 7.3.1) also are consistent with compositional differences between ingots $\text{SnTe}(x=0)$ and $\text{SnTe}(x=0.016)$.

In addition to composition differences between the ingots $\text{SnTe}(x=0)$ and $\text{SnTe}(x=0.016)$, differences in the volume fraction porosity, P , among the specimens can also affect the elastic moduli of the specimens. In general, frequently used relationship between the Young's modulus, E , shear modulus, G , and P are given by [Rice 1998]

$$E = E_0 \exp(-b_{PE}P) \quad (7a)$$

$$G = G_0 \exp(-b_{PG}P) \quad (7b)$$

where E_0 and G_0 are the Young's modulus or shear modulus at zero volume fraction porosity, P . The mean of the H-S bounds (section 7.3.2.1) can be used to estimate E_0 and G_0 . The parameters b_{PE} and b_{PG} are material dependent constants [Rice 1998] that characterize the rate of decrease in the elastic moduli with increasing P . The values of b_{PE} and b_{PG} for SnTe_{1+x} are not available in the literature and in fact modulus versus

porosity data is very limited in the TEs literature. The only two studies in the literature for which the porosity dependence of E and G for TE materials are Ni et al. [Ni 2009] study of LAST and Schmidt et al. [Schmidt 2013] study of YbAl_3 . For LAST, $b_{PE} = 3.5 \pm 0.2$ and $b_{PG} = 3.5 \pm 0.2$, and for YbAl_3 , $b_{PE} = 2.34 \pm 0.06$ and $b_{PG} = 2.38 \pm 0.06$.

In order to compare the single crystal of E_0 and G_0 from the literature for SnTe [Beattie 1969; Simmons 1971] to the E and G of the polycrystalline specimens in this study, we must account for the effect of porosity in the polycrystalline specimens (Equations (7a), (7b)), since the single crystal data represent materials for which $P = 0$. Beattie's single crystal moduli [Beattie 1969] were corrected for the P for the specimens without SiC_{NP} additions ($\text{SnTe}(x = 0)\text{V0}$ and $\text{SnTe}(x = 0.016)\text{V0}$) using

$$E_{\text{CORR}}(P) = E_0 \exp(-b_{PE}^* P) \quad (7c)$$

$$G_{\text{CORR}}(P) = G_0 \exp(-b_{PG}^* P) \quad (7d)$$

where E_{CORR} and G_{CORR} are the porosity-corrected values of E_0 and G_0 . Also, for b_{PE}^* and b_{PG}^* we use the range of values obtained from the LAST and YbAl_3 studies [Ni 2009; Schmidt 2013]. The experimentally measured RT values of E_{exp} and G_{exp} are compared to the corrected single crystal values, E_{CORR} and G_{CORR} , in Table 7.7. Although the measured E_{exp} and G_{exp} are consistently higher than these calculated values from Beattie's single crystal data [Beattie 1969; Simmons 1971], the E_{exp} and G_{exp} values for the tellurium-rich specimen, $\text{SnTe}(x = 0.016)\text{V0}$, are in significantly better agreement (3–8 % higher) with the porosity-corrected Beattie data than the E_{exp} and G_{exp} values for the stoichiometric specimen, $\text{SnTe}(x = 0)\text{V0}$ (which are 21–26 % higher).

A key question is “Were Beattie's [Beattie 1969] single crystal SnTe specimens also Te rich?” According to Baughman [Baughman 1969], Beattie's SnTe single crystal

Table 7.7. In order to compare the room temperature experimental values of Young's modulus, E_{exp} , and shear modulus, G_{exp} , for this study's specimens without SiC_{NP} additions to the single crystal values of E_0 and G_0 values from SnTe from the literature [Beattie 1969; Simmons 1971], equations (7c) and (7d) were used to calculate porosity corrected values for the single crystal data using the modulus-porosity slope data for two thermoelectric materials, namely YbAl₃ ($b_{PE} = 2.34$, $b_{PG} = 2.38$) and LAST ($b_{PE} = 3.5$, $b_{PG} = 3.5$) [Schmidt 2013; Ni 2009]. This study's experimental E_{exp} and G_{exp} values for the tellurium rich specimen, SnTe(x=0.016)V0, are in the best agreement with the range of porosity corrected values E_{CORR} and G_{CORR} .

Specimen	P	E_{exp} (GPa)	E_{CORR} ($b_{PE}=2.34$) (GPa)	E_{CORR} ($b_{PE}=3.5$) (GPa)	G_{exp} (GPa)	E_{CORR-} ($b_{PE}=2.38$) (GPa)	E_{CORR-} ($b_{PE}=3.5$) (GPa)
SnTe (x=0)V0	0.028	62.87 ± 0.13	52.03	50.36	25.27 ± 0.05	20.68	20.04
SnTe (x=0.016)V0	0.022	55.31 ± 0.15	52.76	51.43	21.70 ± 0.07	20.97	20.46

specimens were likely Te-rich. Beattie's specimens were grown by the Czochralski technique, "from a stoichiometric mixture of the components" [Baughman 1969], however, the resulting SnTe crystals had "an indication that the original crucible charge was not exactly stoichiometric ..." giving a tellurium-rich phase, as supported by Baughman's observation [Baughman 1969] that "The termination of the tin telluride crystal ... is a typical example of this occurrence" [Baughman 1969]. Thus, the SnTe composition is likely off stoichiometry for the available single crystal elasticity literature [Beattie 1969], so that in turn the polycrystalline aggregate values [Simmons 1971] calculated from the Beattie single crystal data in turn also represents the elastic moduli for non-stoichiometric SnTe. Unfortunately, the precise chemical composition of Beattie's SnTe specimens is not given by either Beattie [Beattie 1969] or Baughman [Baughman 1969]. Thus this study is the first study in the literature to show the apparent sensitivity of the elastic moduli of SnTe_{1+x} to small changes in x , although in the literature [Ren 2007] the elastic moduli of other compounds have a documented sensitivity to small changes in composition.

7.3.2.3 Comparison of the Young's modulus versus elasticity behavior of polycrystalline SnTe_{1+x} to the literature

The values of E_{RT} and b_{TE} found in this study for SnTe_{1+x} are comparable to those measured for PbTe and LAST [Ren 2010; Houston 1968], which are also chalcogenides and have the same crystal structure as SnTe (Table 7.8). If we compare the E_{RT} and b_{TE} values SnTe_{1+x} -SiC_{NP} more broadly with other thermoelectric materials, namely with data for selected skutterudites (Table 7.8) we find generally smaller values of b_{TE} , namely

Table 7.8. Comparison of the Young's modulus, E , versus temperature behavior for a variety of brittle materials, SnTe [this study], PbTe [Houston 1968; Simmons 1971; Ren 2010], and selected skutterudite TE materials [Schmidt 2012; Ravi 2008]. The parameters E_{RT} and b_{TE} were obtained via a least-squares fit of each of the data sets to equation (4a). The coefficient of determination, R^2 , was equal to or greater than 0.98 for each data set, indicating that equation (4a) describes the E versus temperature behavior well.

Material	Data points	Temp Range (K)	E_{RT} (GPa)	b_{TE} ($\times 10^{-4} \text{ K}^{-1}$)	R^2_E	Tech-nique	References
SnTe _{1+x} (PC) ^{a,b}	25 ^b	RT – 663	55.3 – 64.5	5.07 – 5.83	0.993 – 0.998	RUS ^c	This study
PbTe (SC) ^a	5	100 – 303	58.4	5.7	0.99	IE ^d	[Houston 1968; Simmons 1971] ^e
Ag _{0.86} Pb ₁₉ Sb _{1.0} Te ₂₀ (PC) ^a	12 ^f	RT – 523	61 – 64	5.9 – 6.6	0.98	RUS ^c	[Ren 2010]
Co _{0.95} Pd _{0.05} Te _{0.05} Sb ₃ doped with 0.1 at.% Ce (PC) ^a	13	295 – 573	140.4	1.9	0.99	RUS ^c	[Schmidt 2012]
Co _{0.95} Pd _{0.05} Te _{0.05} Sb ₃ (PC) ^a	13 ^g	295 – 573	128.2 – 138.7	1.6 to 1.8	0.99	RUS ^c	[Schmidt 2012]
Ce _{0.9} Fe _{3.5} Co _{0.5} Sb ₁₂ (PC) ^a	13	295 – 573	127.7	2.5	0.99	RUS ^c	[Schmidt 2012]
CoSb ₃ – doped (PC) ^a	60 – 64 ^h	293 – 597	137.3 – 140.8	2.1 – 2.2	0.99	IE ^d	[Ravi 2008] ⁱ
CeFe ₃ RuSb ₁₂ (PC) ^a	62 – 63 ^j	293 – 597	132.1 – 138.1	2.2 – 2.3	0.99	IE ^d	[Ravi 2008] ⁱ

^a Single crystal denoted by SC, polycrystalline denoted by PC

^b Includes each of the six specimens included in this study (Table 7.1), measured with 25 data points per specimen

^c Resonant ultrasound spectroscopy

^d Impulse excitation

^e The Young's modulus from Houston was obtained as the average of the Hashin and Shtrikman bounds as calculated by Simmons and Wang [Simmons 1971]

^f Each of 3 specimens were measured, 12 data points per specimen

^g Each of 2 specimens were measured, 13 data points per specimen

^h Each of 4 specimens were measured, 60 to 64 data points per specimen

ⁱ E_{RT} and b_{TE} from calculation in [Schmidt 2012]

^j Each of 4 specimens were measured, 62 to 63 data points per specimen

between 1.6 and 2.3 K⁻¹ [Schmidt 2012; Ravi 2008] (Table 7.8) although the E_{RT} values for the skutterudites are higher than those for SnTe and PbTe.

7.3.2.4 Effect of volume fraction of SiC_{NP} on the elastic moduli of the SnTe_{1+X} -SiC_{NP} composites

Since the maximum surface thermal stress, Λ_{max} , produced by a thermal transient is function of the Young's modulus (equation 3), in order to be able to estimate the in-service Λ_{max} for TE composite, one must determine how the added changes in the make-up of the composite (such as adding SiC_{NP}) change the Young's modulus of the material.

To model the effect of the SiC_{NP} on the Young's modulus, E_C , of the SnTe_{1+X} - SiC_{NP} composites included in this study, where in this case E_r is the elastic modulus of the SiC_{NP} reinforcement, E_m is the Young's modulus of the matrix phase, V_m is the volume fraction of the SnTe_{1+X} matrix and V_r is the volume fraction of the SiC_{NP} reinforcement, we will use the following four composite models (equations 8 – 12), namely: the rule of mixtures (ROM) model

$$E_C = V_m E_m + V_r E_r \quad (8)$$

the Reuss constant strain model [Hashin 1962],

$$\frac{1}{E_C} = \frac{V_m}{E_m} + \frac{V_r}{E_r} \quad (9)$$

the Hashin particulate composite model [Hashin 1962; Bedolla 2012; Couturier 1997],

$$E_C = E_m \left(\frac{E_m V_m + E_r \{V_r + 1\}}{E_r V_m + E_m \{V_r + 1\}} \right) \quad (10)$$

and the Halpin-Tsai composite model [Halpin 1992]

$$E_C = E_m \left(\frac{1 + 2(a/b)qV_r}{E_r V_m + E_m \{V_r + 1\}} \right) \quad (11)$$

where E_C is a function of the boundary condition parameter, q ,

$$q = \frac{\left(\frac{E_r}{E_m} \right) - 1}{\left(\frac{E_r}{E_m} \right) + 2 \left(\frac{a}{b} \right)} \quad (12)$$

and a/b is the length/thickness ratio of the reinforcing phase.

Note that each of the composite models above (equations (8)–(12)) is a function of V_r , the volume fraction of the reinforcing phase. The particle size of the reinforcing phase is not explicitly included in any of the models, although it is assumed that the dimensions of the reinforcing particles are much smaller than the specimen dimensions.

For the calculations of E_C from equations (8) – (12), the volume fractions of SiC_{NP} , V_r , in this study were 0.0, 0.01, 0.02, 0.03 and 0.04. Since the SiC_{NP} are approximately equiaxed, the particle aspect ratio, a/b , in the Halpin-Tsai equation was set to unity. The value of the Young's modulus for SnTe_{1+x} matrix, E_m , was set at 67.1 GPa, which is the RT E value measured on specimen $\text{SnTe}(x=0)\text{V0}$ (without SiC_{NP} addition) and then corrected to zero porosity (Section 7.3.2.2). The Young's modulus of SiC_{NP} , the reinforcing phase, E_r , was set to 450 GPa, which is the Young's modulus for bulk SiC [51 52]. Figure 7.12 includes the experimental values of the Young's modulus of the SnTe_{1+x} - SiC_{NP} , the experimental values corrected to zero porosity and the predictions of the four composite models (equations (8) – (12)).

The porosity, P , of the specimens included in this study ranged over a relatively narrow range, from 0.022 to 0.051 (Table 7.1). However, each composite specimen had a

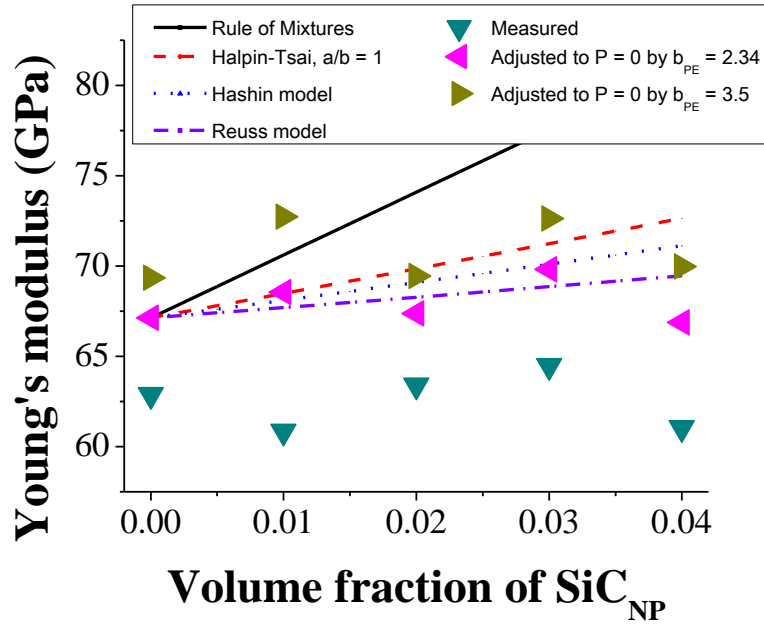


Figure 7.12. Comparison of the experimental Young's modulus, E , results for the composites $\text{SnTe}_{1+x} - y\text{SiC}$ ($y = 0.0$ to 0.04) with the four composite models given by equations (8) – (12). Also plotted are the values of E corrected to zero porosity using equation (7a).

porosity that was different than the other specimens (Table 7.1), thus in order to compare the experimental data with the four elasticity models, the Young's modulus was corrected to correspond to zero porosity. Figure 7.12 shows both (i) the experimental Young's modulus data and (ii) the data corrected to zero P (using equation 7a). The Reuss model (equation (9)) and the Hashin model (equation (10)) correspond best with the experimental data.

7.5 Summary and conclusions

The linear decrease in Young's modulus, E , (Figure 7.8 and Table 7.3) and shear modulus, G , (Table 7.3) with increasing temperature is relatively described well by equations 4(a) and 4(b), respectively. The lack of significant hysteresis between the heating and cooling curves for E and G indicates that no significant microcracking or bloating occurred over the test temperature range (RT to 663 K).

However, there appears to be a bilinear behavior for the elastic modulus versus temperature behavior (Figure 7.9), with a change in the modulus versus temperature behavior at about 543 K. This behavior might be explained by an order–disorder mechanism similar to that proposed by Ren *et al.* [Ren 2010].

The addition of up to 4 vol% SiC_{NP} to the $\text{SnTe}_{1+\text{X}}$ matrix lead to relatively modest changes in (1) the observed modulus versus temperature slope and (2) the RT elastic moduli, E_{RT} . Changes in E_{RT} can be described relatively well by either the Reuss [Hashin 1962] or the Hashin [Hashin 1962] composite models (Figure 7.12). In the study, the elastic modulus changes due to (i) the possible order–disorder transition in off-stoichiometric SnTe and (ii) the addition of up to 4 vol% SiC_{NP} was small. However compositional shifts in the SnTe matrix seem to represent a much larger source of

perturbation on the elastic moduli of the $\text{SnTe}_{1+x} - \text{SiC}_{\text{NP}}$ composite materials than either the SiC_{NP} additions or the bilinear E versus T behavior.

For the SnTe_{1+x} matrix, in the absence of SiC_{NP} addition, the compositional differences between $\text{SnTe}(x = 0)$ and $\text{SnTe}(x = 0.016)$ may be responsible for the differences in the measured elastic moduli between the two ingots. Similar significant changes in elastic moduli with composition of solid solution systems have been reported in the literature for other materials (Table 7.6), but this study is the first to report the sensitivity of the elastic moduli to compositional changes in SnTe . Future studies should explore functional relationship of the elastic moduli of SnTe_{1+x} and the Te composition, especially since there are some questions about the stoichiometry of the SnTe elasticity data currently available in the literature.

ACKNOWLEDGEMENTS

The authors acknowledge the financial support of the Department of Energy, Revolutionary Materials for Solid State Energy Conversion Center, an Energy Frontiers Research Center funded by the U.S. Department of Energy, Office of Science, Office of Basic Energy Sciences under award number DE-SC0001054. The authors also acknowledge the use of the equipment high-temperature RUS measurements through the Oak Ridge National Laboratory's High Temperature Materials Laboratory User Program, which is sponsored by the U. S. Department of Energy, Office of Energy Efficiency and Renewable Energy, Vehicle Technologies Program.

REFERENCES

REFERENCES

- [Baughman, Lefever 1969] Baughman, R., Lefever, R. Czochralski encapsulation growth of GeTe, SnTe and PbTe single crystals. *Materials Research Bulletin* 4 (1969) 721–726.
- [Beattie 1969] Beattie, A.G. Temperature Dependence of the Elastic Constants of Tin Telluride. *Journal of Applied Physics* 40 (1969) 4818.
- [Bedolla, Lemus-Ruiz, Contreras 2012] Bedolla, E., Lemus-Ruiz, J., Contreras, A. Synthesis and characterization of Mg-AZ91/AlN composites. *Materials and Design* 38 (2012) 91–98.
- [Belson 1970] Belson, H.S. Thermal Expansion of Tin Telluride. *Journal of Applied Physics* 41 (1970) 422.
- [Bux, Fleurial, Kaner 2010] Bux, S.K., Fleurial, J.-P., Kaner, R.B. Nanostructured materials for thermoelectric applications. *Chemical communications (Cambridge, England)* 46 (2010) 8311–24.
- [Case, Kim 1993] Case, E.D., Kim, Y. The effect of surface-limited microcracks on the effective Young's modulus of ceramics. *Journal of Materials Science* 28 (1993) 1885–1900.
- [Case, Smyth, Hunter 1981a] Case, E.D., Smyth, J.R., Hunter, O. Microcracking in Large-grain Al₂O₃. *51* (1981) 175–179.
- [Case, Smyth, Monthei 1981b] Case, E.D., Smyth, J.R., Monthei, V. Grain-Size Determinations. *Journal of the American Ceramic Society* 64 (1981) C–24–C–25.
- [Chotard, Soro, Lemerrier, Huger, Gault 2008] Chotard, T., Soro, J., Lemerrier, H., Huger, M., Gault, C. High temperature characterisation of cordierite–mullite refractory by ultrasonic means. *Journal of the European Ceramic Society* 28 (2008) 2129–2135.
- [Cook, Kramer, Harringa, Han, Chung, Kanatzidis 2009] Cook, B. a., Kramer, M.J., Harringa, J.L., Han, M.-K., Chung, D.-Y., Kanatzidis, M.G. Analysis of Nanostructuring in High Figure-of-Merit Ag_{1-x}Pb_mSbTe_{2+m} Thermoelectric Materials. *Advanced Functional Materials* 19 (2009) 1254–1259.
- [Couturier, Ducret, Merle, Disson, Joubert 1997] Couturier, R., Ducret, D., Merle, P., Disson, J.P., Joubert, P. Elaboration and characterization of a metal matrix composite: Al/AlN. *Journal of the European Ceramic Society* 17 (1997) 1861–1866.

- [Cui, Qian, Zhao 2003] Cui, J., Qian, X., Zhao, X. Mechanical and transport properties of pseudo-binary alloys (PbTe) $1-x$ -(SnTe) x by pressureless sintering. *Journal of alloys and compounds* 358 (2003) 228–234.
- [D'Angelo, Case, Matchanov, Wu, Hogan, Barnard, Cauchy, Hendricks, Kanatzidis 2011] D'Angelo, J., Case, E.D., Matchanov, N., Wu, C.-I., Hogan, T.P., Barnard, J., Cauchy, C., Hendricks, T., Kanatzidis, M.G. Electrical, Thermal, and Mechanical Characterization of Novel Segmented-Leg Thermoelectric Modules. *Journal of Electronic Materials* 40 (2011) 2051–2062.
- [Fan, Case, Baumann 2012] Fan, X., Case, E.D., Baumann, M.J. The effect of indentation-induced microcracks on the elastic modulus of hydroxyapatite. *Journal of Materials Science* 47 (2012) 6333–6345.
- [Halpin 1992] Halpin, J.C. *Primer on composite materials analysis*. Technomic Publishing Company, Inc., Lancaster, Pennsylvania, 1992.
- [Hashin 1962] Hashin, Z. The Elastic Moduli of Heterogeneous Materials. *Journal of Applied Mechanics* 29 (1962) 143–150.
- [Hoang, Desai, Mahanti 2005] Hoang, K., Desai, K., Mahanti, S. Charge ordering and self-assembled nanostructures in a fcc Coulomb lattice gas. *Physical Review B* 72 (2005) 064102.
- [Houston, Strakna, Belson 1968] Houston, B., Strakna, R.E., Belson, H.S. Elastic Constants, Thermal Expansion, and Debye Temperature of Lead Telluride. *Journal of Applied Physics* 39 (1968) 3913.
- [Kaliakin 2002] Kaliakin, V.N. *Introduction to approximate solution techniques, numerical modeling, and finite element methods*. Marcel Dekker, New York, 2002.
- [Kawaharada, Kurosaki, Muta, Uno, Yamanaka 2004] Kawaharada, Y., Kurosaki, K., Muta, H., Uno, M., Yamanaka, S. Thermophysical properties of $\text{NiZrSn}_{1-x}\text{Sbx}$ half-Heusler compounds. *Journal of Alloys and Compounds* 381 (2004) 9–11.
- [Kosuga, Uno, Kurosaki, Yamanaka 2005] Kosuga, A., Uno, M., Kurosaki, K., Yamanaka, S. Thermoelectric properties of $\text{Ag}_{1-x}\text{Pb}_{18}\text{SbTe}_{20}$ ($x = 0, 0.1, 0.3$). *Journal of Alloys and Compounds* 387 (2005) 52–55.
- [Kreith 1973] Kreith, F. *Principles of heat transfer*. Intext Educational Publishers, New York, 1973.
- [Lawson 1951] Lawson, W.D. A Method of Growing Single Crystals of Lead Telluride and Lead Selenide. *Journal of Applied Physics* 22 (1951) 1444.

- [Liu, Liang, Zhang 2009] Liu, Y., Liang, D., Zhang, L. Thermodynamic Descriptions for the Sn-Te and Pb-Sn-Te Systems. *Journal of Electronic Materials* 39 (2009) 246–257.
- [Lu, Fleck 1998] Lu, T.J., Fleck, N. a. The thermal shock resistance of solids. *Acta Materialia* 46 (1998) 4755–4768.
- [Manson 1966] Manson, S.S. *Thermal stress and low cycle fatigue*. McGraw-Hill, New York, 1966.
- [Mariano 1967] Mariano, a. N. Polymorphism in Some Iv-Vi Compounds Induced By High Pressure and Thin-Film Epitaxial Growth. *Applied Physics Letters* 10 (1967) 282.
- [Martin, Carey 1973] Martin, H.C., Carey, G.F. *Introduction to finite element analysis*. McGraw-Hill, New York, 1973.
- [Ni, Ren, Case, Timm 2009] Ni, J., Ren, F., Case, E., Timm, E. Porosity dependence of elastic moduli in LAST (lead–antimony–silver–tellurium) thermoelectric materials. *Materials Chemistry and Physics*(2009) .
- [Ni, Case, Stewart, Wu, Hogan, Kanatzidis 2011] Ni, J.E., Case, E.D., Stewart, R., Wu, C.-I., Hogan, T.P., Kanatzidis, M.G. Bloating in (Pb_{0.95}Sn_{0.05}Te)_{0.92}(PbS)_{0.08-0.055%PbI₂} Thermoelectric Specimens as a Result of Processing Conditions. *Journal of Electronic Materials* 41 (2011) 1153–1158.
- [Noda, Masumoto, Ohba, Saito, Toriumi, Iwata, Shibuya 1987] Noda, Y., Masumoto, K., Ohba, S., Saito, Y., Toriumi, K., Iwata, Y., Shibuya, I. Temperature Dependence of Atomic Thermal Parameters of Lead Chalcogenides, PbS, PbSe and PbTe. *Acta Crystallographica C* 43 (1987) 1443–1445.
- [Pei, Lensch-falk, Toberer, Medlin, Snyder 2011] Pei, Y., Lensch-falk, J., Toberer, E.S., Medlin, D.L., Snyder, G.J. High Thermoelectric Performance in PbTe Due to Large Nanoscale Ag₂Te Precipitates and La Doping. (2011) 241–249.
- [Pilchak, Ren, Case, Timm, Schock, Wu, Hogan 2007] Pilchak, A.L., Ren, F., Case, E.D., Timm, E.J., Schock, H.J., Wu, C.-I., Hogan, T.P. Characterization of dry milled powders of LAST (lead–antimony–silver–tellurium) thermoelectric material. *Philosophical Magazine* 87 (2007) 4567–4591.
- [Ravi, Firdosy, Caillat, Lerch, Calamino, Pawlik, Nathal, Sechrist, Buchhalte, Nutt 2008] Ravi, V., Firdosy, S., Caillat, T., Lerch, B., Calamino, A., Pawlik, R., Nathal, M., Sechrist, A., Buchhalte, J., Nutt, S. Mechanical Properties of Thermoelectric Skutterudites. *Space Technology and Applications International Forum—STAIF 2008*(2008) 656–662.

- [Ravinder, Alivelumanga 2001] Ravinder, D., Alivelumanga, T. Room temperature elastic behaviour of cadmium substituted manganese ferrites. *Materials Letters*(2001) 1–6.
- [Ren, Case, Morrison, Tafesse, Baumann 2009a] Ren, F., Case, E.D., Morrison, A., Tafesse, M., Baumann, M.J. Resonant ultrasound spectroscopy measurement of Young's modulus, shear modulus and Poisson's ratio as a function of porosity for alumina and hydroxyapatite. *Philosophical Magazine* 89 (2009) 1163–1182.
- [Ren, Case, Ni, Timm, Lara-Curzio, Trejo, Lin, Kanatzidis 2009b] Ren, F., Case, E.D., Ni, J.E., Timm, E.J., Lara-Curzio, E., Trejo, R.M., Lin, C.-H., Kanatzidis, M.G. Temperature-dependent elastic moduli of lead telluride-based thermoelectric materials. *Philosophical Magazine* 89 (2009) 143–167.
- [Ren, Case, Sootsman, Kanatzidis, Kong, Uher, Lara-Curzio, Trejo 2008] Ren, F., Case, E.D., Sootsman, J.R., Kanatzidis, M.G., Kong, H., Uher, C., Lara-Curzio, E., Trejo, R.M. The high-temperature elastic moduli of polycrystalline PbTe measured by resonant ultrasound spectroscopy. *Acta Materialia* 56 (2008) 5954–5963.
- [Ren, Case, Timm, Lara-Curzio, Trejo 2010] Ren, F., Case, E.D., Timm, E.J., Lara-Curzio, E., Trejo, R.M. Anomalous temperature-dependent Young's modulus of a cast LAST (Pb–Sb–Ag–Te) thermoelectric material. *Acta Materialia* 58 (2010) 31–38.
- [Ren, Case, Timm, Schock 2007] Ren, F., Case, E.D., Timm, E.J., Schock, H.J. Young's modulus as a function of composition for an n-type lead–antimony–silver–telluride (LAST) thermoelectric material. *Philosophical Magazine* 87 (2007) 4907–4934.
- [Rice 1998] Rice, R.W. *Porosity of Ceramics*. Marcel Dekker, New York, 1998.
- [Rogacheva, Gorne, Zhigareva, Ivanova 1991] Rogacheva, E.I., Gorne, G. V, Zhigareva, N.K., Ivanova, A.B. HOMOGENEITY REGION OF TIN MONOTELLURIDE. *INORGANIC MATERIALS* 27 (1991) 194–197.
- [Schenk, Dunog 1998] Schenk, M., Dunog, L.T.H. Solid-solution hardening of Cd $1 - x$ Zn x Te bulk crystals. *Semiconductor Science and Technology* 16 (1998) 335–339.
- [Schmidt, Case, Lehr, Morelli 2013] Schmidt, R.D., Case, E.D., Lehr, G.J., Morelli, D.T. Room temperature mechanical properties of polycrystalline YbAl₃, a promising low temperature thermoelectric material. *Intermetallics* 35 (2013) 15–24.
- [Schmidt, Case, Ni, Sakamoto, Trejo, Lara-Curzio, Payzant, Kirkham, Peascoe-Meisner 2012] Schmidt, R.D., Case, E.D., Ni, J.E., Sakamoto, J.S., Trejo, R.M., Lara-Curzio, E., Payzant, E.A., Kirkham, M.J., Peascoe-Meisner, R.A. The temperature dependence of thermal expansion for p-type Ce_{0.9}Fe_{3.5}Co_{0.5}Sb₁₂ and n-type

Co_{0.95} Pd_{0.05} Te_{0.05} Sb₃ skutterudite thermoelectric materials. *Philosophical Magazine* 92 (2012) 1261–1286.

[Seddon, Gupta, Isci, Saunders 1976] Seddon, T., Gupta, S.C., Isci, C., Saunders, G.A. The elastic constants of IV-VI compound alloys. *Journal of Materials Science* 11 (1976) 1756–1759.

[Simmons, Wang 1971] Simmons, G., Wang, H. *Single Crystal Elastic Constants and Calculated Aggregate Properties: A Handbook*. The M.I.T. Press, Cambridge, Massachusetts, 1971.

[Srinivas Rao, Ravinder 2003] Srinivas Rao, S., Ravinder, D. Composition dependence of elastic moduli of gadolinium-substituted nickel–zinc ferrites. *Materials Letters* 57 (2003) 3802–3804.

[Wyckoff 1963] Wyckoff, R. *Rocksalt crystal structures*. Interscience, New York, 1963.

[Zhao, Lu, Fleck 2000] Zhao, L.G., Lu, T.J., Fleck, N. a. Crack channelling and spalling in a plate due to thermal shock loading. *Journal of the Mechanics and Physics of Solids* 48 (2000) 867–897.

8 Mechanical properties of lower-cost, earth-abundant chalcogenide thermoelectric materials, PbSe and PbS, with additions of 0 to 4% CdS or ZnS

Robert D. Schmidt ¹, Eldon D. Case ¹, Li-Dong Zhao ², Mercouri G. Kanatzidis ²

¹ Chemical Engineering and Materials Science Department,
Michigan State University, East Lansing, MI, 48824

² Department of Chemistry, Northwestern University, Evanston, IL, 60208

To be submitted to: Journal of Materials Science

Abstract

The thermoelectric (TE) properties of PbTe-based materials have been optimized to the extent that the maximum figure of merit, ZT , achieved is greater than 2. However, the tellurium content limits the application potential due to both availability and cost. Replacing the tellurium with selenium or sulfur produces an analogous thermoelectric material using strategies learned from PbTe-based materials to achieve ZT values of 1.3 to 1.6. In order to effectively incorporate these new materials into TE devices, it is important to understand materials' response to thermally and mechanically imposed loads, which in turn requires knowledge of the mechanical properties. In this study, the hardness was determined by Vickers indentation and elastic modulus and Poisson's ratio were measured using resonant ultrasound spectroscopy (RUS) on PbSe- and PbS-based thermoelectric specimens as a function the addition of 0-4 at% of CdS or ZnS. The hardness and moduli of PbSe-based or PbS-based TE materials are not strong functions of the addition of CdS or ZnS. With 2.0 at% or 2.5 at% Na doping, the hardness of PbSe-based or PbS-based TE materials increased by about 30% and the elastic moduli decreased by 5-10%. In addition, PbS may be effectively sintered at 723 K when doped with 2.5 at% Na, but requires a higher sintering temperature when undoped.

Keywords: thermoelectric; hardness; elastic modulus

8.1 Introduction

The figure of merit, ZT , of bulk thermoelectric (TE) materials is defined as [Tritt 2011]

$$ZT = \frac{S^2 \sigma}{\kappa} T \quad (1)$$

where S is Seebeck coefficient, σ is the electrical conductivity, T is temperature, and κ is thermal conductivity. The ZT has been increased using a variety of techniques, including atomic scale doping or substitution [Gelbstein 2008; Zhu 2009; Zhao 2012b], creation of nanostructured bulk materials [Toprak 2004; Mi 2008; Hsu 2004; Zhu 2009], incorporation of nanoparticles [Androulakis 2007; Zhao 2012a; Zhou 2008; Alleno 2009; Ji 2007], or a combination of atomic, nanostructural, and microstructural length scale modifications [Biswas 2012].

The application of these techniques has been particularly successful with lead telluride-based thermoelectrics, with ZT values near or greater than 2 reported [Zhao 2013; Biswas 2012; Heremans 2008]. A limitation on the application of these materials is the use of tellurium, due to the relative scarcity of the element [Haxel 2002], but sulfur or selenium may be substituted for tellurium to produce analogous compounds [Zhao 2011; Zhao 2012a; Zhao 2012b; Zhao 2013]. The thermoelectric properties of lead sulfide and lead selenide have been optimized with the same techniques as the lead telluride-based compounds, such that a ZT value of 1.6 has been achieved for lead selenide [Zhao 2013] and 1.3 for lead sulfide [Zhao 2012a; Zhao 2012b]. Changing the chemistry of the thermoelectric however, can dramatically alter the mechanical properties

of the material, as has been observed in lead telluride-based materials [Ren 2007; Ren 2008].

The elastic properties of the TE materials are required as well to determine the material response to stresses, just as the transport properties are required to determine the ZT of the material. In waste heat harvesting applications, the stresses that the TE material must survive are not trivial, as TE materials are intended for an environment with thermal gradients, thermal shocks, attached to materials with thermal expansion mismatches, and subjected to external loads. In addition, a TE module is typically composed of tens or hundreds of legs of TE material electrically connected in series and thermally in parallel. This arrangement subjects each leg individually to the full thermal gradient and associated stresses, but the failure of just one leg results in the electrical failure of an entire TE module.

The mechanical properties of many undoped TE materials have been published, including PbTe [Houston 1968], Mg_2Si [Whitten 1965; Milekhine 2002], SnTe [Beattie 1969] and CdSe [Cline 1967], but the mechanical properties may be significantly changed when the TE material is optimized for improved ZT . The hardness and/or elastic moduli of a material have been shown to change by the addition of nanoparticles [Zhao 2008; Kvetková 2013], creation of nanoprecipitates in the bulk material [Ni 2010], doping [Gelbstein 2008], or alloying [Gelbstein 2008; Darrow 1969]. Therefore, to understand the mechanical response of a TE material that may be incorporated into a device, the mechanical properties need to be measured on a TE material with the addition of dopants, with nanoparticle or nanoprecipitates.

8.2 Experimental procedure

8.2.1 Materials and Specimen Preparation

Two tellurium-free thermoelectric materials with analogous crystal structure to PbTe-based TE materials were included in this study, using methods similar to those employed to optimize the PbTe-based TE materials [Zhao 2012b; Zhao 2013]. Ingots were fabricated from elemental materials (99.99+% purity) with nominal compositions of PbS or PbSe with x% CdS/ZnS, where the at fraction $x = 1, 2, 3$ and 4. For PbS, 2.5 at% Na dopant was added, and for PbSe, 2.0 at% Na dopant was added [Zhao 2012b; Zhao 2013]. In addition, ingots of PbS and PbSe without Na dopant, and an ingot of PbSe with 2.0 at% Na dopant were made. Carbon-coated fused silica tubes with the elemental material were evacuated to approximately 10^{-4} torr before being flame-sealed [Zhao 2012b; Zhao 2013]. The tubes were heated to 723 K in 12 h, then to 1423 K in 7 h, thermally soaked for 6 h at 1423 K and then water quenched to room temperature [Zhao 2012b; Zhao 2013]. The ingots produced were crushed into powders, sieved through a 53 μm sieve, then densified by Pulsed Electric Current Sintering (PECS, Thermal Technology SPS-10-4 or SPS-DR 2050) at 723 K (PbS), 873 K (undoped PbS) or 823 K (PbSe) for 10 min in a 20 mm diameter graphite die under 60 MPa axial pressure in an argon atmosphere [Zhao 2012b; Zhao 2013]. Except for the undoped PbS sintered at 723 K, this produced highly dense disk-shaped billets 20 mm in diameter and 9 mm thick, with volume fraction porosity less than 0.05. Using a low speed diamond saw, the billets were cut into bars, $\sim 2 \text{ mm} \times 3 \text{ mm}$ in cross section and approximately 9-18 mm long [Zhao 2012b; Zhao 2013].

8.2.2 Elasticity Measurements

In this study, the elastic moduli were determined by a standing acoustic wave technique, resonant ultrasound spectroscopy (RUS). The elastic moduli of each specimen are a function of the specimen geometry, dimensions, density and resonant frequencies. Each of the specimens in this study was of rectangular bar geometry. The dimensions of each specimen were measured by micrometers (293-832, Mitutoyo, Japan), and the mass by electronic balance (Adventurer AR2140, OHAUS, Pine Brook IL). The resonant frequencies were measured by RUS (RUSpec, Quasar International, Albuquerque, NM), in which the specimen was placed so that the corners of the specimen contacted two transducers along the specimen's body diagonal. One transducer was swept across a range of frequencies from 10 kHz to 760 kHz in 29,999 steps and the mechanical response to the frequency was recorded in the second transducer. Each sharp peak in second transducer's response to the driving signal (Figure 8.1) represents a mechanical resonance frequency of the specimen. The set of recorded resonant frequencies were fit to a model by commercial software (RPModel version 2.68b, Quasar International) to determine the elastic moduli. Details of the RUS procedure may be found elsewhere [Ren 2009; Ni 2010; Schmidt 2010; Migliori 1997; Schmidt 2013a].

The elastic moduli of other thermoelectric materials have been measured by RUS, including PbTe-based compounds [Ni 2013; Ni 2009a; Ren 2009; Ni 2011; Ren 2010; Morrison 2012], SnTe [Schmidt 2013b], tetrahedrite [Fan 2013], YbAl₃ [Schmidt 2013a], Mg₂Si [Schmidt 2012a], skutterudite [Rog1 2011; Zhang 2010; Schmidt 2012b; Schmidt 2010; Salvador 2009; Möchel 2011] and Zn₄Sb₃ [Bhattacharya 2006].

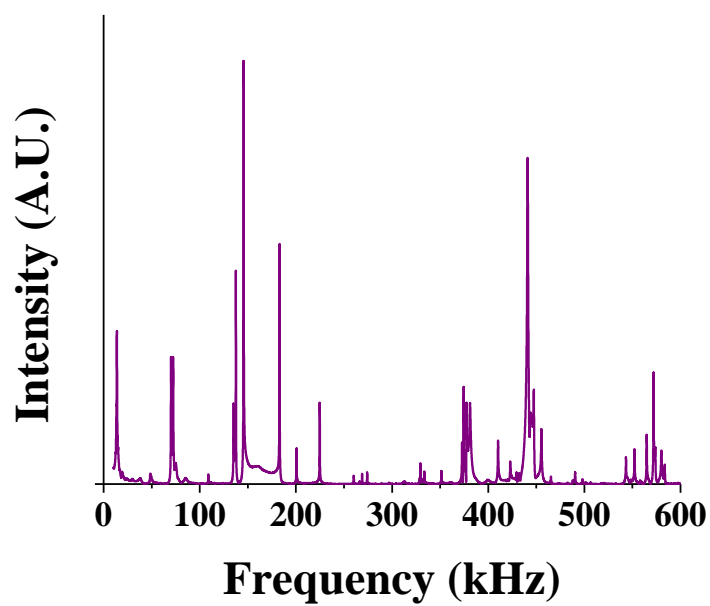


Figure 8.1. RUS scan of PbSe specimen

8.2.3 Hardness and toughness measurements

Hardness was measured by Vickers indentation at 1.98 N load on a microindenter (HMV-2000, Shimadzu, Okinawa, Japan), using the equation

$$H = \beta \frac{1.8544P}{(2a)^2} \quad (2)$$

where P is the indentation load and $2a$ is the length of the indentation diagonal [Wachtman 2009]. The Vickers hardness values from indentation of a standard block (Yamamoto Scientific Tools Lab Co. LTD, Chiba, Japan) were used to determine a calibration constant, β , of 0.95.

8.2.4 Microscopy and X-ray diffraction

The PbS and PbSe specimens were examined by scanning electron microscope (SEM) on both polished and fractured specimen surfaces at 15 kV accelerating voltage and 15 mm working distance (6610LV SEM, JEOL, Tokyo, Japan). Polished surfaces were examined by secondary electron images and backscatter images to examine indentation impressions and the morphology of secondary phases with different average atomic weight. Grain size analysis was performed by the lineal intercept method on secondary electron images of fractured specimen surfaces, with a minimum of 200 intercepts per image and a stereographic projection factor of 1.5. Energy dispersive x-ray spectroscopy (Oxford EDS) was performed in the SEM at 15 kV accelerating voltage and 10 mm working distance for elemental analysis.

Fracture surfaces of each specimen were examined for mode mixity, M , defined here as

$$M = A_{TRANS}/A_{TOTAL} \quad (3)$$

where A_{TRANS} is the area of transgranular fracture, and A_{TOTAL} is the overall area of a fractured surface.

X-ray diffraction (XRD) was performed at the Michigan State University Center for Crystallographic Research with Cu K α radiation and a step size of 0.008° 2 θ (Bruker Davinci Diffractometer) from 25° to 75° 2 θ on a rotary stage. Two XRD scans were performed on the sintered PbS material, (i) on the bulk densified specimen, and (ii) on powder ground by hand from the bulk specimen in a mortar and pestle.

8.3 Results and Discussion

8.3.1 Microstructural analysis

Only isolated spherical porosity was observed which is consistent with dense specimens. Except for 1 at% ZnS in PbSe (with precipitates up to 4 μm), the addition of ZnS in PbS or PbSe resulted in ZnS precipitates with diameters up to 10 to 15 μm (Tables 8.1 and 8.2), observed primarily at the grain boundaries (Figures 8.2 – 8.4). The addition of 1 at% to 4 at% CdS in PbS or PbSe resulted in precipitates with diameters of up to 1 μm to 4 μm (Tables 8.1 and 8.2), observed primarily embedded in the matrix material (Figures 8.2 – 8.4). In backscatter SEM imaging, both the CdS and ZnS precipitates were uniformly distributed through the specimen matrix, with up to 15 μm ZnS precipitates observed in both the PbSe and PbS (Figure 8.4, Tables 8.1 and 8.2). No precipitates were observed in the samples of either PbS or PbSe without CdS or ZnS additions. All the precipitates observed in this study were faceted (Figures 8.4 and 8.5). In particular, the precipitate morphology was rod or plate-like for the CdS additions in both PbS and PbSe

Table 8.1. Composition, theoretical density, ρ_{theo} , measured density, ρ_{meas} , volume fraction porosity, P , average grain size, $\langle GS \rangle$, typical observed inclusion size range, $Incl$, and mode mixity, M (equation 3) for the PbS-based specimens included in this study.

Composition	ρ_{theo}^a	ρ_{meas}	P	$\langle GS \rangle$ (μm)	$Incl$ (μm)	M
PbS	7.5970	7.535	0.008	5.9 ^b	NA	0.91
Pb _{0.975} Na _{0.025} S	7.5970	7.325	0.036	1.8	NA	0.15
Pb _{0.975} Na _{0.025} S + 1 at% CdS	7.5716	7.278	0.039	3.2	0.2 to 1	0.94
Pb _{0.975} Na _{0.025} S + 2 at% CdS	7.5462	7.315	0.031	5.4	0.2 to 1.5	0.98
Pb _{0.975} Na _{0.025} S + 3 at% CdS	7.5207	7.148	0.050	4.5	0.2 to 2 ^c	0.92
Pb _{0.975} Na _{0.025} S + 4 at% CdS	7.4952	7.148	0.046	3.6	0.2 to 3 ^c	0.93
Pb _{0.975} Na _{0.025} S + 1 at% ZnS	7.5704	7.231	0.045	2.1	0.2 to 12	0.34
Pb _{0.975} Na _{0.025} S + 2 at% ZnS	7.5437	7.264	0.037	2.2	0.2 to 10 ^d	0.72
Pb _{0.975} Na _{0.025} S + 3 at% ZnS	7.5168	7.241	0.037	2.3	0.2 to 15 ^d	0.91
Pb _{0.975} Na _{0.025} S + 4 at% ZnS	7.4898	7.245	0.033	2.8	0.2 to 10	0.76

NA: Not applicable. No inclusions because no addition of CdS or ZnS

^a The ρ_{theo} values are calculated in Table S1 from [Zhao 2012a]

^b The $\langle GS \rangle$ includes a distribution of several large grains, 5 μm to 30 μm , and smaller grains, 0.2 μm to 2 μm

^c Inclusions were typically rod- or plate-like shape

^d Larger inclusions were typically stacked plate-like shapes

Table 8.2. Composition, theoretical density, ρ_{theo} , measured density, ρ_{meas} , volume fraction porosity, P , average grain size, $\langle GS \rangle$, typical observed inclusion size range, $Incl$, and mode mixity, M (equation 3) for the PbSe-based specimens included in this study.

Composition	ρ_{theo}^a	ρ_{meas}	P	$\langle GS \rangle$ (μm)	$Incl$ (μm)	M
PbSe	8.258	8.125	0.016	9.9	NA	0.07
Pb _{0.98} Na _{0.02} Se	8.258	7.955	0.037	4.0	NA	0.28
Pb _{0.98} Na _{0.02} Se + 1 at% CdS	8.2243	8.112	0.014	3.2	0.2 to 3	0.17
Pb _{0.98} Na _{0.02} Se + 2 at% CdS	8.1906	8.048	0.017	3.6	0.2 to 2	0.92
Pb _{0.98} Na _{0.02} Se + 3 at% CdS	8.157	7.950	0.025	4.0	0.2 to 3 ^b	0.81
Pb _{0.98} Na _{0.02} Se + 4 at% CdS	8.1232	7.966	0.019	18.7	0.2 to 4 ^b	0.98
Pb _{0.98} Na _{0.02} Se + 1 at% ZnS	8.2163	8.074	0.017	3.3	0.2 to 4	0.27
Pb _{0.98} Na _{0.02} Se + 2 at% ZnS	8.1746	8.005	0.021	3.2	0.2 to 10	0.73
Pb _{0.98} Na _{0.02} Se + 3 at% ZnS	8.1329	8.049	0.010	3.2	0.2 to 12	0.83
Pb _{0.98} Na _{0.02} Se + 4 at% ZnS	8.0912	7.880	0.026	7.0	0.2 to 15	0.51

NA: Not applicable. No inclusions because no addition of CdS or ZnS

^a The ρ_{theo} values are calculated in Table S1 from [Zhao 2013]

^b Inclusions were typically rod- or plate-like shape

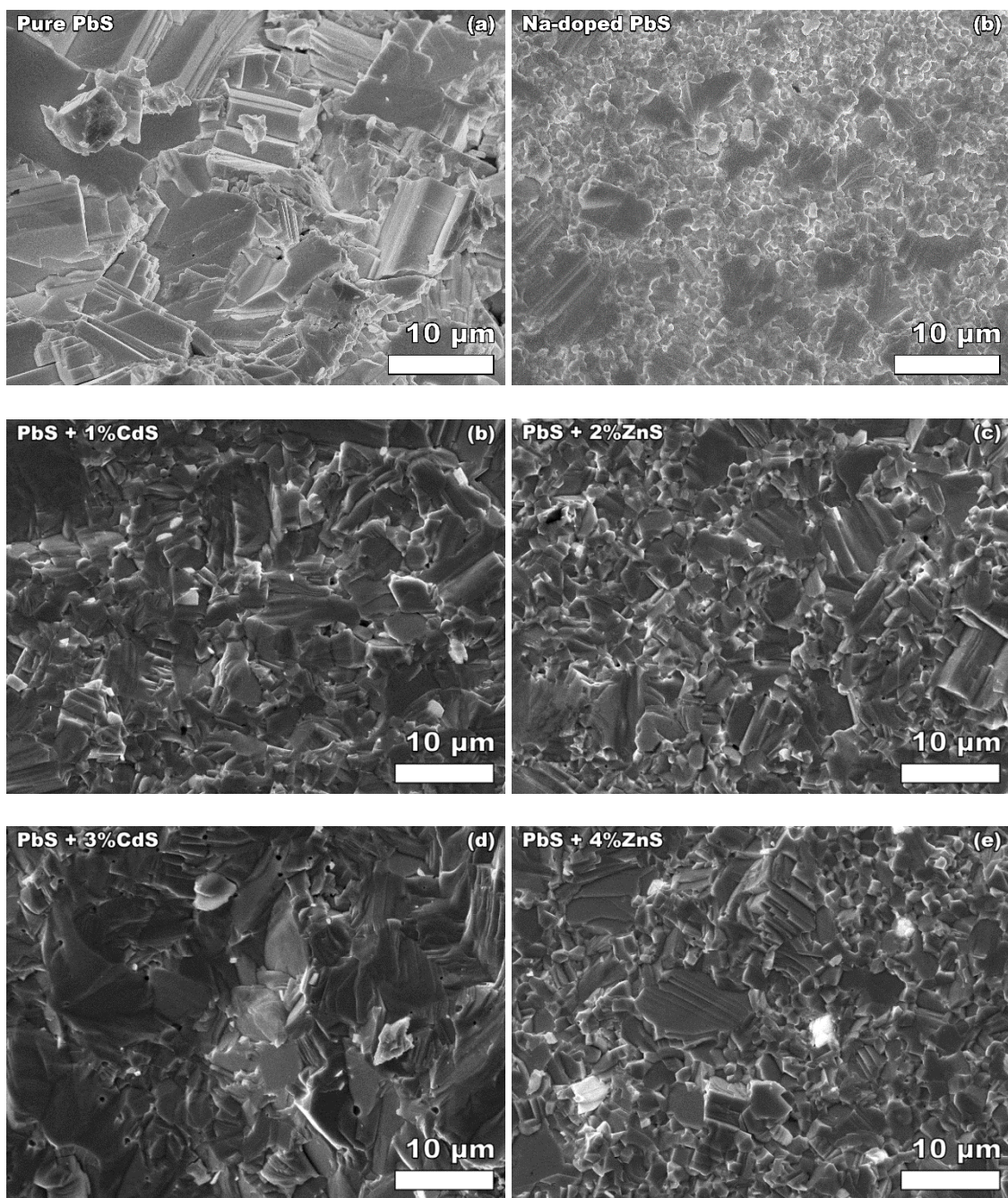


Figure 8.2. Fracture surfaces of PbS specimens indicate primarily transgranular fracture in undoped PbS (a) changing to intergranular fracture for the Na-doped PbS specimen (b). With 1% to 4% addition of CdS, the fracture mode changes to primarily transgranular fracture (b, d), and with 1% to 4% addition of ZnS, the fracture mode changes to mixed, with majority transgranular and minority intergranular (c, e). Note the bright areas in images (c) and (e) are the ZnS precipitates.

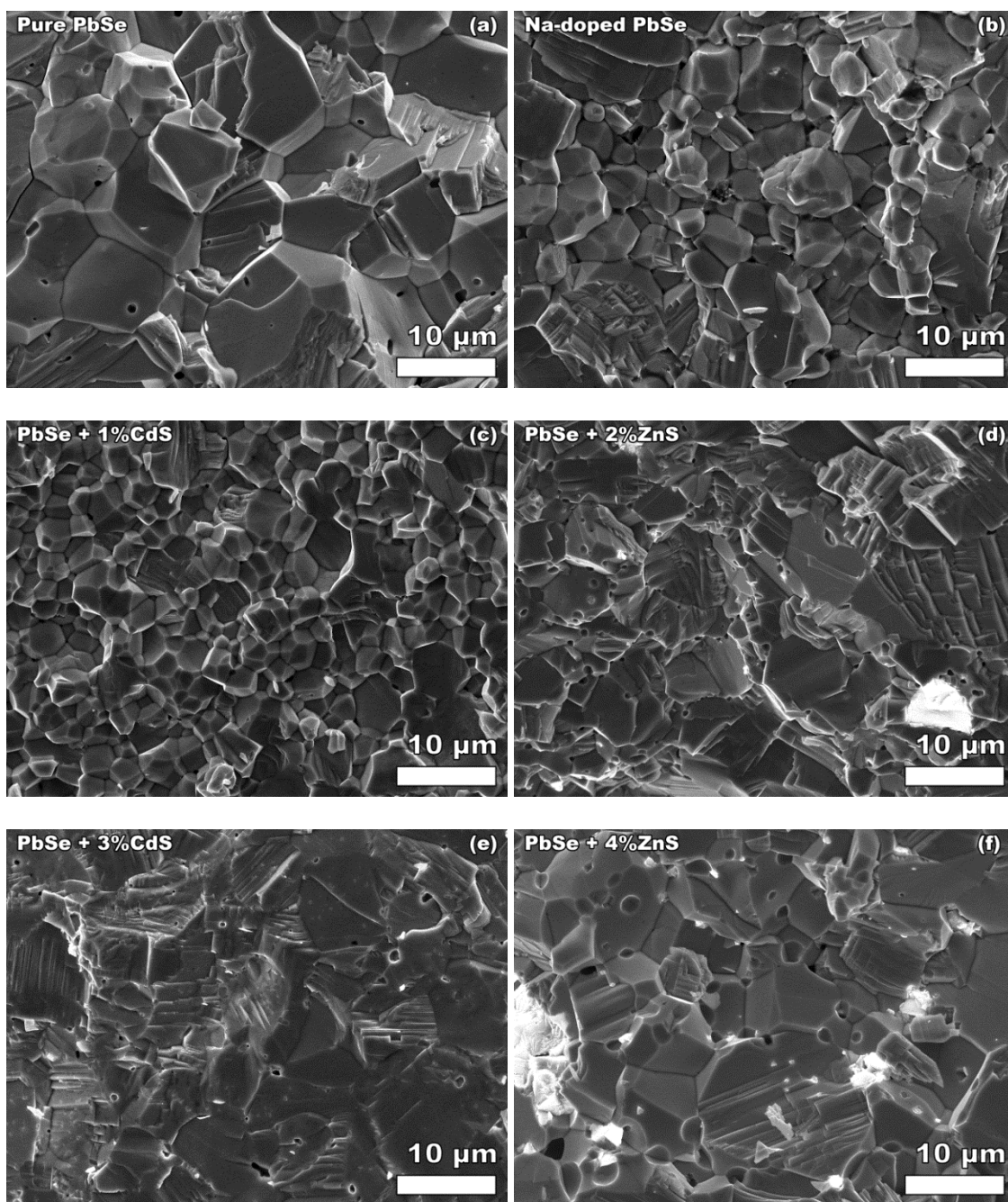


Figure 8.3. Fracture surfaces of PbSe specimens indicate primarily intergranular fracture for the pure PbSe specimen, the Na-doped PbSe specimen, and the specimens with 1% addition of CdS or ZnS (a-c). With 2% to 4% addition of CdS or ZnS, the fracture mode changes to primarily transgranular fracture (d-f), although significant intergranular fracture was also observed in the specimen with 4% ZnS (f). Note the bright areas in images (d) and (f) are the ZnS precipitates.

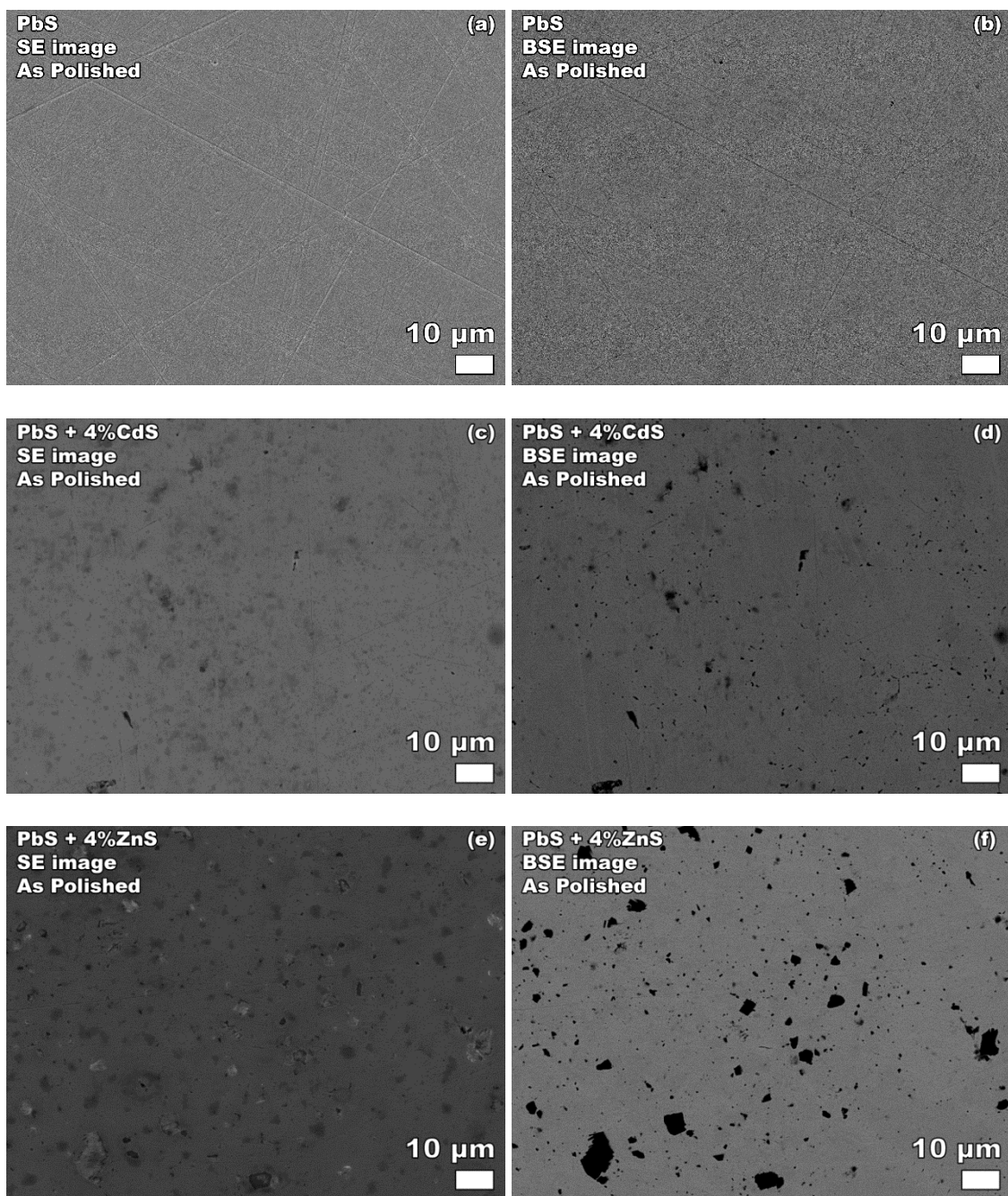
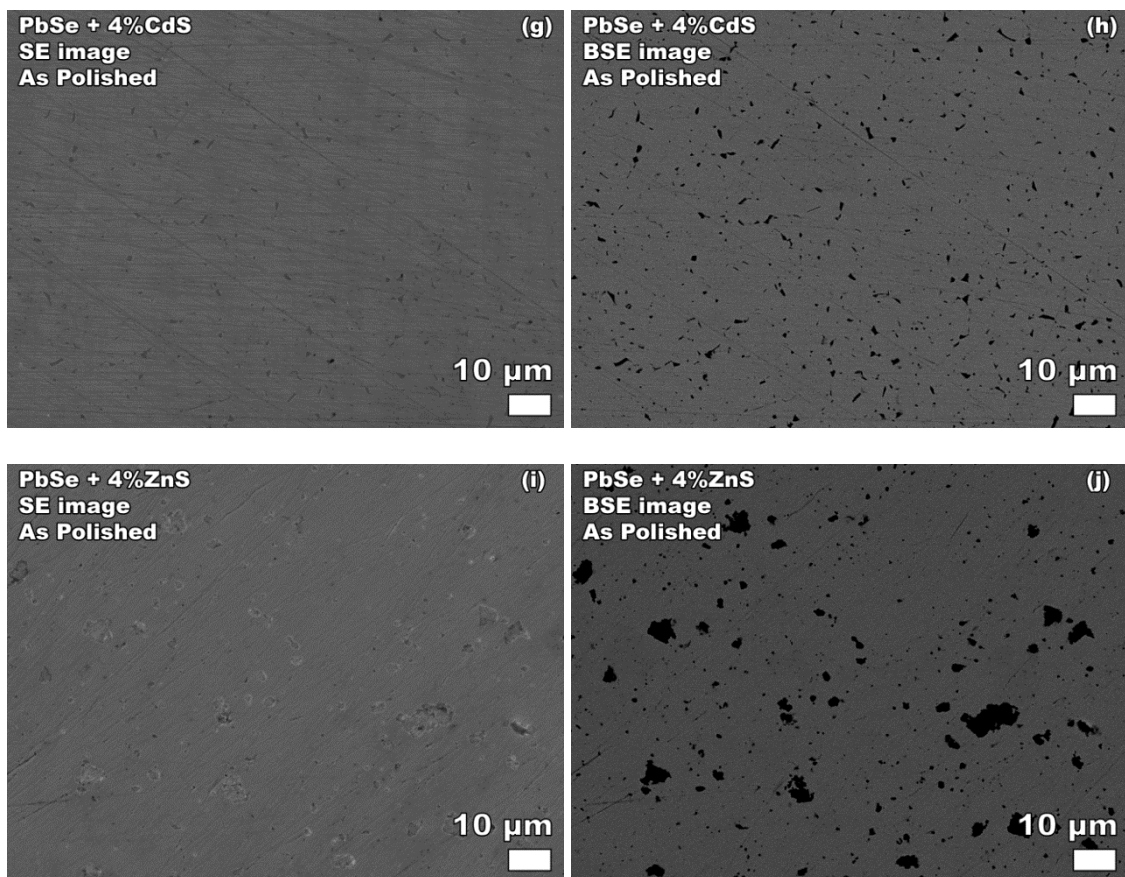


Figure 8.4. Secondary images of the polished specimens show isolated, micron scale spherical porosity and minor scratches from polishing. In the specimens with 4% CdS or ZnS, precipitates of sub-micron up to approximately 15 μm were observed, particularly in backscattered electron (BSE) mode. The images of polished PbS in both secondary electron (SE) and BSE mode (a and b) only exhibit spherical pores ~1 μm, with no evidence of precipitates, consistent with the material having no additions of CdS or ZnS.

Figure 8.4 (cont'd)



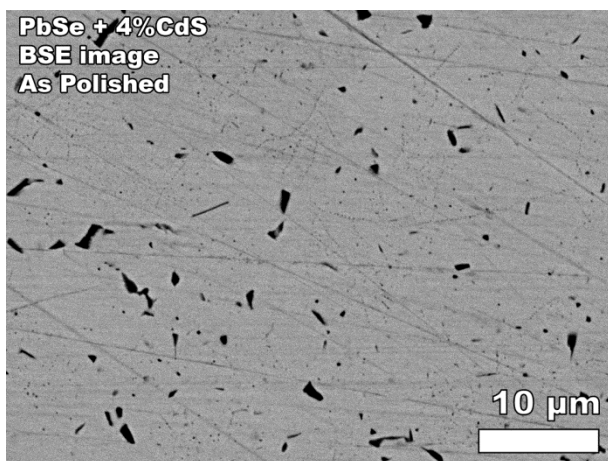


Figure 8.5. Observed in backscatter, precipitates of CdS were up to $\sim 4\ \mu\text{m}$, with some micron scale precipitates with geometry of rods or plates and sharp facets consistent with crystallographic alignment.

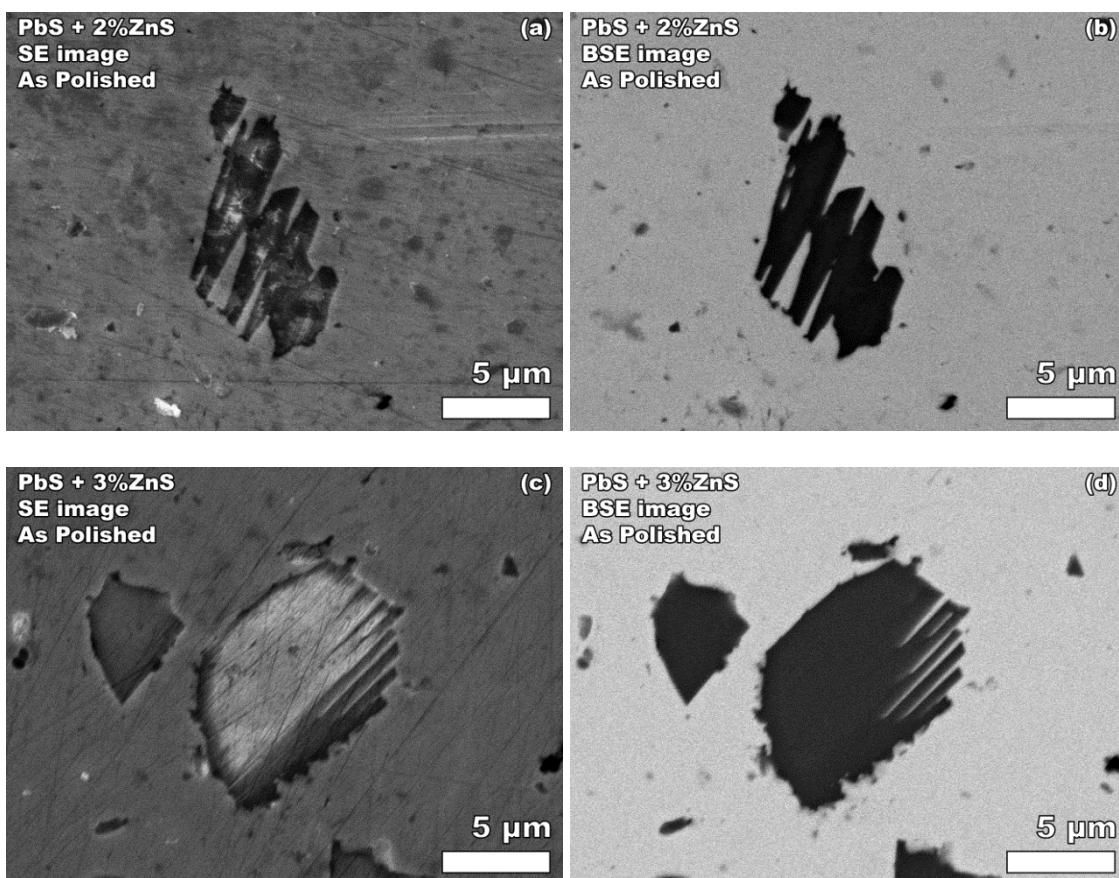


Figure 8.6. Some ZnS inclusions in PbS resembled stacked plates.

(Figure 8.5). In addition, the ZnS precipitate morphology included stacked plates, particularly in the PbS matrix (Figures 8.4 and 8.6).

The fracture mode changed from primarily intergranular fracture in Na-doped PbS and PbSe to primarily transgranular fracture when additions of up to 4 at% CdS or ZnS were added to either Na-doped PbS (Table 8.1, Figure 8.2) or PbSe (Table 8.2, Figure 8.3). Mode mixity, M , was examined to determine the fraction of transgranular fracture, with $M = 0$ indicating pure intergranular fracture and $M = 1$ indicating pure transgranular fracture. Undoped PbS exhibited primarily transgranular fracture, $M = 0.91$, while the Na-doped PbS changed to primarily intergranular, $M = 0.14$. The PbSe specimens without CdS or ZnS exhibited primarily intergranular fracture, with both Na doped and pure PbSe specimen M values ranging from 0.07 to 0.28. M increased to 0.51 to 0.98 for PbS and PbSe specimens with additions of 2 at% to 4 at% CdS or ZnS, as compared to the doped PbS and PbSe specimens. Generally, M was higher for specimens with additions of CdS than with additions of ZnS (Tables 8.1 and 8.2). In both the PbS with ZnS (Table 8.1) and the PbSe with ZnS (Table 8.2), M reaches a maximum at 3 at% ZnS. In contrast, there was no observed maximum in M for CdS additions to PbS and PbSe. EDS analysis of the polished surface of PbS indicated a deficiency of S (Table 8.3). The lattice parameter from XRD of the PbS specimen was 5.941 Å for the bulk, as-sintered specimen (Figure 8.7). The measured lattice parameters for sintered PbS are larger than the lattice parameter of 5.932 Å for the same PbS material prior to sintering [Zhao 2012a], and consistent with a change in the concentration of S, as indicated by EDS analysis.

Table 8.3. EDS results from four area scans of a polished PbS specimen, indicating a higher concentration of Pb than S.

Location ID	Atomic %	
	S	Pb
1	49.6	50.4
2	49.6	50.4
3	49.1	50.9
4	49.5	50.5
5	49.2	50.8

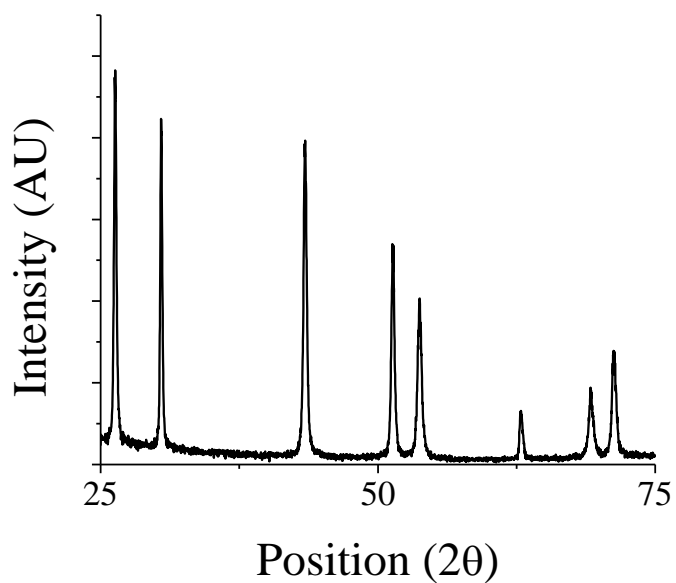


Figure 8.7. XRD pattern of the sintered PbS specimen.

The undoped PbS specimen required a higher sintering temperature (873 K) than the Na-doped PbS specimens (723 K). An undoped PbS specimen produced at a sintering temperature of 723 K was too porous for comparison to the nearly dense Na-doped specimens, with a density of 6.27 g/cm^3 , and a P of 0.18, far exceeding the maximum of $P < 0.05$ for all other specimens in this study. Therefore, the porous undoped PbS specimen was excluded from the elasticity and hardness testing.

8.3.2 Elasticity results

For the PbS-based specimens, the elastic moduli, E and G , were not sensitive to the addition of CdS or ZnS, with a mean and standard deviation of E of $63.38 \pm 2.25 \text{ GPa}$ (Figure 8.8a) and G was $24.69 \pm 0.93 \text{ GPa}$ (Figure 8.8c). The undoped PbS specimen had a much lower porosity, $P = 0.008$, than all the other Na-doped PbS-based specimens, $P = 0.031$ to 0.050 (Table 8.1), likely due to the higher sintering temperature of the PbS specimen (see section 8.2.1 for sintering procedures). This difference in P likely explains the higher E and G of the undoped PbS specimen relative to the other PbS-based specimens (Figure 8.8a), and not a sensitivity to Na doping, as discussed in section 8.4.2.

In contrast, the moduli of the PbSe-based specimens are sensitive to Na doping, but not CdS or ZnS additions. Both the E and G of the PbSe specimens decreased with the addition of Na dopant, from $64.29 \pm 0.16 \text{ GPa}$ and $25.29 \pm 0.02 \text{ GPa}$ for pure PbSe, to $60.33 \pm 0.26 \text{ GPa}$ and $23.66 \pm 0.04 \text{ GPa}$ for Na-doped PbSe (Figure 8.8b and 8.8d). No change in modulus was observed in the Na-doped PbSe specimens as a function of increasing additions of 1 at% to 4 at% CdS or ZnS except for a slight decrease in G and a corresponding increase in ν . The mean of E for the PbSe specimens with either CdS or

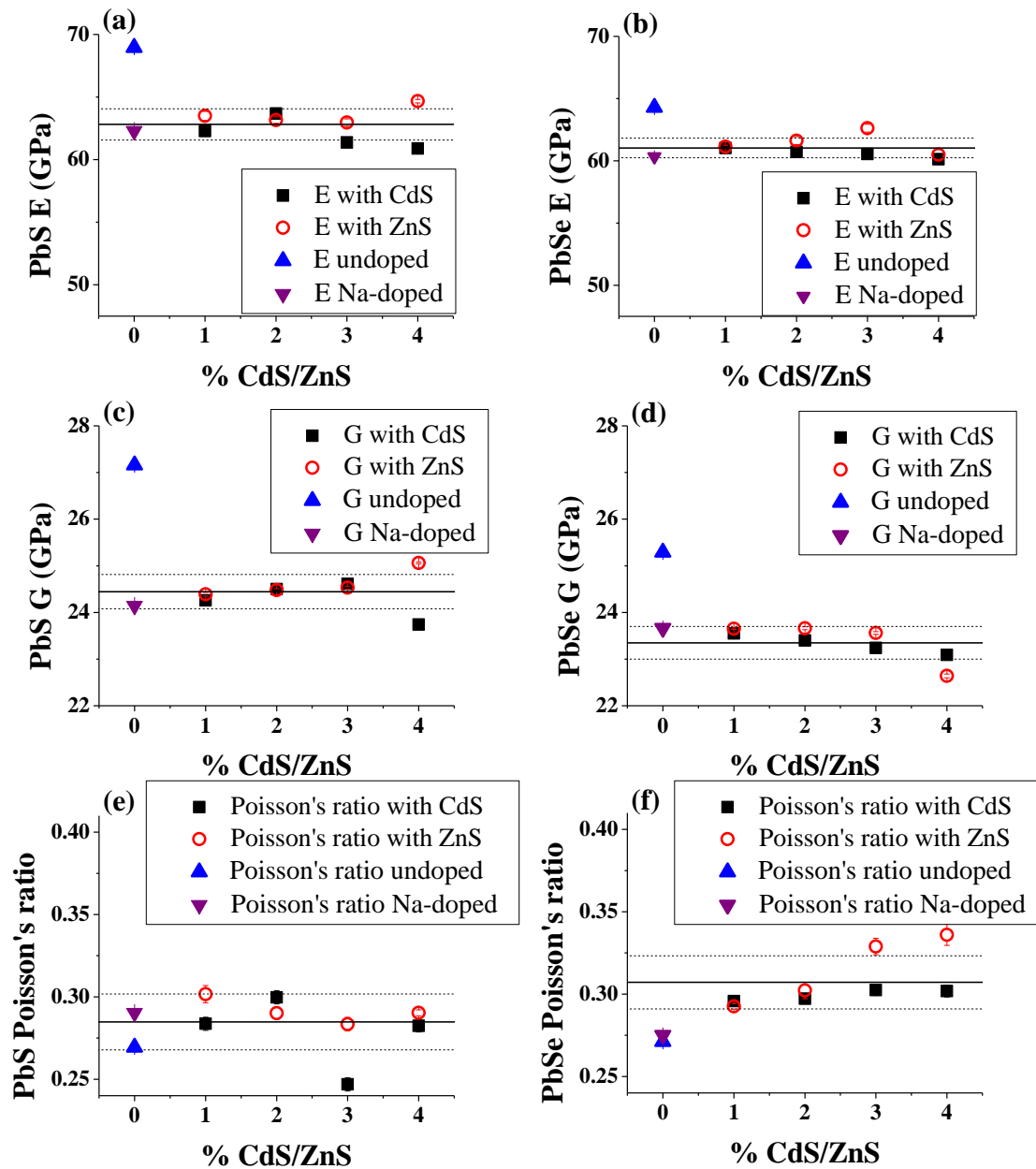


Figure 8.8. The E and G of the undoped PbS and PbSe were higher than the Na-doped PbS and PbSe. The E and G of undoped PbS are likely higher due to reduced porosity (pure PbS $P = 0.008$, all other PbS $P = 0.031$ to 0.050), while the E and G of undoped PbSe are likely higher due to doping effects. Only small changes in E and G were noted in Na-doped PbS and PbSe with addition of up to 4% CdS or ZnS, with. Only small variability in the ν noted in PbS with addition of CdS or ZnS. The ν of PbSe increased with the addition of CdS or ZnS. Solid line is average and dotted line is standard deviation of the specimens with 1% to 4% CdS or ZnS addition.

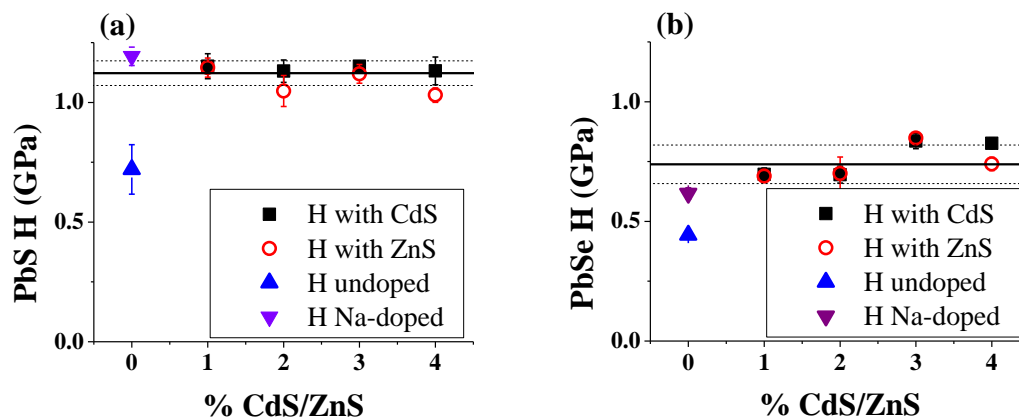


Figure 8.9. The hardness of both PbS and PbSe increased with the addition of Na dopant. No measurable change in hardness was noted in PbS with addition of up to 4% CdS or ZnS. Hardness of PbSe increased from 0.6 GPa to 0.8 GPa with the addition of either CdS or ZnS.

ZnS was 61.03 ± 0.79 and the mean of G was 23.35 ± 0.35 GPa) (Figure 8.8b, 8.8d, 8.8f).

(Note: each of the specimens with additions of CdS or ZnS were Na-doped.)

8.3.3 Hardness results

The hardness of PbS and PbSe increased with 2.5 at% or 2.0 at% Na-dopant additions, respectively, but were largely unaffected by the addition of 0 to 4 at% CdS or ZnS (Figure 8.9). The hardness of the pure PbS was 0.72 ± 0.10 , and the average of the Na-doped PbS with additions of 0 to 4 at% CdS or ZnS was 1.12 ± 0.05 (Figure 8.9a). Similarly, the hardness of the pure PbSe was 0.44 ± 0.02 GPa, but increased to 0.62 ± 0.02 GPa when doped with 2.0 at% Na, and averaging 0.74 ± 0.08 GPa for specimens with 0 to 4 at% CdS or ZnS (Figure 8.9b).

8.4 Discussion

8.4.1 Microstructural analysis

The observation of ZnS precipitates of up to 10 μm to 15 μm in diameter (Tables 8.1 and 8.2), as compared to CdS precipitates of up to 1.5 μm to 4 μm in both the PbS matrix (Table 8.1, Figure 8.4) and the PbSe matrix (Table 8.2, Figure 8.4), may be related to the much lower solubility limit of ZnS in the matrix [Zhao 2013]. More specifically for PbSe, “no solid solubility of Zn in PbSe was observed” [Zhao 2013]. Zhao et al. expected a continuous change in band gap up to the solubility limit for additions of CdS or ZnS in PbSe [Zhao 2013]. The band gap increased with up to 2% addition of CdS in PbSe, but with ZnS in PbSe, “no band gap changes are observed, suggesting a much lower solubility limit” of ZnS in PbSe [Zhao 2013].

Transmission electron microscopy observations of nanoprecipitates of CdS and ZnS in PbS and PbSe matrices have shown endotaxial crystallographic alignment with

the matrix [Zhao 2013; Zhao 2012a]. The morphology of the observed micron-scale precipitates with rod or plate geometry and sharp facets (Figure 8.4), particularly in the samples with CdS addition (Figure 8.5), are consistent with the observations of nanoprecipitate morphology.

The change in fracture mode observed between specimens with and without CdS or ZnS addition (Tables 8.1 and 8.2) is often associated with a change in fracture toughness. A change from intergranular to transgranular fracture has been associated with either an increase [Mukhopadhyay 2010; Kawabata 1977; Karakasidis 2011] or decrease [Yamada 2010; Jang 2010]. The fracture toughness of the material was not determined in this study, but may be an area for future studies of PbS and PbSe with additions of CdS or ZnS.

For PbS-based specimens sintered at 723 K, the P for the undoped material was 0.18, while the P of each of the Na-doped specimens was less than 0.05. A nearly dense ($P = 0.01$) undoped PbS specimen was sintered for this study, but only by increasing the sintering temperature to 873 K. The enhanced densification of the Na-doped PbS specimens may indicate the Na dopant acts as a sintering aid. A previous study on a different TE material, $\text{Ba}_{0.3}\text{Co}_4\text{Sb}_{12}$, showed the addition of metal particles, specifically 0.5 wt% Ag nanoparticles, may act as sintering aid [Schmidt 2014]. In $\text{Ba}_{0.3}\text{Co}_4\text{Sb}_{12}$, the Ag had a eutectic or peritectic reaction with Sb in the $\text{Ba}_{0.3}\text{Co}_4\text{Sb}_{12}$ [Schmidt 2014] and a similar eutectic reaction may explain the enhanced densification in the Na-doped PbS specimens.

The Na-S system has eutectics at 513 K and 61.5 at% Na, 522 K and 70 at% Na, and at 525 K and 72.5 at% Na [Sangster 1997]. All three of these eutectic points are well

below the sintering temperature used for the Na-doped PbS samples, 723 K. In the closely related PbTe material system, the Na in Na-doped PbTe partially segregates in a layer less than 10 nm thick at the grain boundaries [Biswas 2012]. A similar Na-rich layer may also form during sintering in the PbS-based material in this study, and this Na-rich layer may act as a liquid-phase sintering aid for the PbS-based system that accounts for the enhanced sintering. The sintering behavior of Na-doped PbS has not been explored and may be a topic for future work.

8.4.2 Elasticity analysis

For the PbS-based specimens, the undoped PbS specimen exhibited higher E and G relative to the other PbS-based specimens (Figure 8.8a). The difference in elastic moduli between PbS-based specimens likely a function of porosity, as the porosity of the undoped PbS specimen is $P = 0.008$, much lower than all the other Na-doped PbS-based specimens, $P = 0.031$ to 0.050 (Table 8.1), and not because of a sensitivity to the Na doping.

In general, the elastic modulus of TE materials and other brittle materials is a linear function of porosity [Schmidt 2013a; Ni 2009b; Rice 1998; Ni 2011],

$$E = E_0(1 - b_E P) \quad (4)$$

where E_0 is the Young's modulus at $P = 0$, and b_E is a measure of the decrease in E with increasing P . For two previously studied TE materials, YbAl_3 and LAST (lead–antimony–silver–tellurium), b_E is 2.34 [Schmidt 2013a] and 3.6 [Ni 2009b]. Based on these values of b_E , the difference between the undoped PbS and the Na-doped specimens with 0 to 4 at% addition of CdS or ZnS is expected to be between 4 GPa and 11 GPa, and consistent with the measured difference of approximately 6 GPa (Figure 8.8a).

The elastic moduli for the doped TE materials with nanoprecipitates in this study have not been reported, however the moduli of the undoped PbS [Dalven 1969; Bhagavantam 1951] and PbSe [Lippmann 1971; Dalven 1969; Hellwege 1979] are known for single crystal specimens. The aggregate average of the Hashin and Shtrikman bounds, $\langle H-S \rangle$, [Simmons 1971] allow a direct comparison of the single crystal specimen moduli to the moduli of a dense polycrystalline specimen (Table 8.4). Comparing this study to the $\langle H-S \rangle$ averages, the polycrystalline PbS specimen in this study (which has a volume fraction porosity, P of 0.008) were lower than the single crystal values by 12% to 18%, with the measured E of 68.95 ± 0.10 GPa in this study, and the single crystal $\langle H-S \rangle E$ of 78.05 GPa [Dalven 1969] and 83.61 GPa [Bhagavantam 1951] (Table 8.4). The elastic moduli of PbSe in this study ($P = 0.016$), with E of 64.29 ± 0.16 GPa, generally agrees with previous studies, with $\langle H-S \rangle E$ between 61.68 GPa and 70.69 GPa [Lippmann 1971; Dalven 1969; Hellwege 1979] (Table 8.4).

The reader may ask, “why are the moduli of PbS lower than those reported in literature?” The two most likely causes would be (i) porosity and (ii) doping or composition differences.

Porosity is not sufficient by itself to explain the difference between the literature values of $\langle H-S \rangle E$ and the measured E in this study. The contribution from porosity may be estimated using equation 4 and applying the measured b_E from two previously studied

Table 8.4. The Young's modulus, E , the shear modulus, G , and the Poisson's ratio measured in this study for the polycrystalline undoped PbSe and undoped PbS specimens compared with the aggregate average values of E and G computed from the Hashin and Shtrikman bounds, <H-S> [Simmons 1971] for single crystal elasticity from the literature [Dalven 1969, Bhagavantam 1951, Lippmann 1971, Hellwege 1979].

Material	Bulk material form	E (GPa)	G (GPa)	Poisson's ratio	Density (g/cm ³)	Reference
PbS	Polycrystalline	68.95	27.16	0.269	7.53	This study
PbS	Single crystal	78.05	29.98	0.302	7.5 (P=0.01)	[Dalven 1969]
PbS	Single crystal	83.61	32.53	0.277	NA	[Bhagavantam 1951]
PbSe	Polycrystalline	64.29	25.29	0.271	8.13	This study
PbSe	Single crystal	66.83	23.76	0.298	8.26	[Lippmann 1971]
PbSe	Single crystal	70.69	24.11	0.466	8.16 (P=0.01)	[Dalven 1969]
PbSe	Single crystal	61.68	23.76	0.294	NA	[Hellwege 1979]

NA: Not available from literature

TE materials, YbAl_3 ($b_E = 2.34$) [Schmidt 2013a] and LAST ($b_E = 3.6$) [Ni 2009b].

Based on these values of b_E and the observed porosity in the PbS specimen ($P = 0.046$), the E_0 of PbS in this study would likely be in the range of 70.3 GPa to 71.0 GPa, which is still 12% to 15% less than the average of literature values (Table 8.4).

After accounting for porosity, the remaining differences between the moduli of the polycrystalline PbS specimen in this study and the literature may be related to composition or doping and vacancies. To examine this possibility, a cut surface of the PbS specimen was examined by EDS to determine an approximate composition (Table 8.3). The EDS surface composition of a polished surface of the specimen was $\text{PbS}_{0.98}$, averaged over 5 separate sites, where the area of each site was approximately 0.05 mm^2 . The surface composition of the PbS specimen is thus consistent with sulfur vacancies (Table 8.3). In this study, the PbS was densified by PECS in an argon atmosphere using a starting powder milled from an ingot. During the initial stage of sintering before densification occurs, the surfaces of the PbS powder particles are exposed to the sintering atmosphere at elevated temperature, 873 K, providing a pathway for S loss. Prior to sintering, the powder was single phase in XRD, with a lattice parameter of 5.932 \AA [Zhao 2012a]. After sintering, the specimen was single phase in XRD, but with a lattice parameter of 5.941 \AA for the sintered specimen (Figure 8.7). The increase in lattice parameter is consistent with a change in vacancy concentration. The observed reduction in the elastic moduli by roughly 12% to 15% in this study may be caused by sulfur vacancies introduced during sintering, as indicated by EDS analysis.

A change in elastic moduli by roughly 12% to 15% due to vacancies is not unique to PbS. Another thermoelectric, SnTe_{1+x} , exhibits a decrease of E by 12% with

increasing Te content from $x = 0$ to 0.016 and a subsequent rise in the number of cation vacancies [Schmidt 2013b]. In addition, the elastic modulus of a set of nitrides decreases with increasing N vacancies. The E of TiN_x coatings decreases by 23% [Shin 2003] or 41% [Portnoi 1968] for a change in x from 1 to 0.67, decreases ~20% [Jiang 1991] or 50% [Portnoi 1968] for x from 1 to 0.5, and by 5% for a small change of x from 0.98 to 0.94 [Portnoi 1968]. Similarly, the E of ZrN_x decreased 12% for a change in x from 1 to 0.85 [Portnoi 1968]. For CeO_{2-x} -based compounds, increasing O vacancies (x from approximately 0 to approximately 0.11, at O_2 partial pressure of 0.22 atm and 4.50×10^{-22} atm) reduced the E of ceria by 11% and gadolinium doped ceria by 6% [Wang 2007].

8.4.3 Hardness analysis

Hardness values for single crystal PbS [Bloem 1955] and polycrystalline specimens of PbS and PbSe [Darrow 1969] are available in the literature (Table 8.5), but no hardness data is available in the literature for PbS and PbSe specimens optimized as TE materials by the inclusion of Na dopant and CdS or ZnS nano/micro precipitates.

The hardness of PbS specimens included in this study was not observed to be a function of addition of precipitates or the dopant (Table 8.5, Figure 8.9a). The hardness of PbS is higher than reported in the literature [Bloem 1955; Darrow 1969], but hardness is known to be a function of grain size, and would be expected to be higher for the powder processed specimens in this study than for single crystal specimens of the same composition [Rice 1994].

Table 8.5. In general, hardness, H , is grain size dependent, and the single crystal hardness results from Bloem and Kröger [Bloem 1955] are expected to have a lower hardness than the other, polycrystalline specimens in this table. The grain size for the PbS and PbSe was not listed by Darrow [Darrow 1969]. Average grain sizes for all specimens in this study are between 1.8 μm and 18.7 μm , listed in Tables 8.1 and 8.2.

Material	Bulk material form	H (GPa)	Indentation Load (N)	Reference
PbS	Polycrystalline	1.09 ± 0.14	1.96	This study
PbS	Single crystal	0.4 to 0.7 (dependent on vacancy concentration)	0.98	[Bloem 1955]
PbS	Polycrystalline	0.72 to 0.92	1.41	[Darrow 1969]
PbS	Polycrystalline	0.73	3.92	[Darrow 1969]
PbSe	Polycrystalline	0.44 ± 0.02	1.96	This study
Na-doped PbSe	Polycrystalline	0.62 ± 0.02	1.96	This study
PbSe	Polycrystalline	0.56 to 0.57	1.41	[Darrow 1969]

Although the hardness was not observed to be a function of Na doping in this study, the hardness of PbS is a function of the vacancy concentration [Bloem 1955]. On single crystal specimens of PbS, Bloem and Kroger reported a minimum hardness of 0.4 GPa is reported when there is a minimum of vacancies [Bloem 1955]. In this study, the PbS was S-deficient (Table 8.3), implying S vacancies were present, regardless of the Na doping and regardless of whether or not CdS or ZnS was added to the matrix. The difference between the constant H in this study and the minimum reported by Bloem and Kroger [Bloem 1955] is likely because there are likely a large number of S vacancies (Table 8.3) in each of the PbS specimens in this study. For future work with different processing conditions or Na doping concentrations, the vacancy concentration may approach a value where a minimum in H is possible, and the value of H should be reexamined.

For PbSe, there may be a similar relationship between vacancies and hardness as was observed by Bloem and Kroger in PbS [Bloem 1955]. Without CdS or ZnS additions, the hardness increased from 0.44 ± 0.02 GPa to 0.62 ± 0.02 GPa with the addition of 2.0 at% Na dopant (Table 8.5, Figure 8.9b). After the addition of Na, the hardness was only a weak function, if any, of CdS or ZnS addition, averaging 0.75 ± 0.07 GPa for all the specimens with CdS or ZnS addition (Figure 8.9b).

Fracture toughness was not measured in this study. For each of the specimens included in this study, Vickers indentation produced an impression with a set of typically 8 to 15 or more cracks surrounding and extending out from the sides of the indentation impression, rather than a set of radial or Palmquist cracks that extend from the corners of the indentation impression. The lack of well-defined radial cracks

precluded making an estimate of the fracture toughness for the materials in this study. These cracks may develop as a result of many mechanisms, such as the environment, microstructural toughening, surface stress, or preferred crystallographic cleavage planes [Cook 2003]. Future studies may examine fracture toughness by a method other than Vickers indentation.

8.5 Conclusions

For PbS + x at%(CdS, ZnS), neither the elastic moduli, with E averaging 63.38 ± 2.25 GPa, nor the H , averaging 1.12 ± 0.05 GPa, are a function of addition of 2.5 at% Na dopant and 0 to 4 at % CdS or ZnS, but the elastic moduli of the sintered pure PbS is lower than previous reports. The lower elastic modulus is partially accounted for by porosity, but may also be related to S vacancies.

For PbSe + x at%(CdS, ZnS), the elastic moduli and hardness of PbSe are a function of 2.0 at% Na dopant, but not a function of addition of 0 to 4 at% CdS or ZnS. Without Na dopant, the E was 64.29 ± 0.16 GPa and H was 0.44 ± 0.02 GPa. With the Na dopant, the E averaged 61.03 ± 0.79 and the H averaged 0.75 ± 0.07 GPa.

The elastic moduli are required material properties to model stresses of a TE material in a module or device, and stress modeling is necessary for designing or fabrication of a mechanically reliable device. Hardness is related to wear characteristics for a material. As the transport properties of a TE material are optimized, the mechanical properties may change, potentially requiring a redesign of a module or device.

The continuing work on optimization of PbS- [Zhao 2012a] or PbSe-based [Zhao 2013] TE materials carries implications on changing the mechanical properties of these materials required for designing and modeling a TE module or device. The effects on

mechanical properties from two aspects of optimization were examined in this study, (i) addition of a precipitate phase, namely CdS or ZnS, and (ii) changes based on Na doping or S deficiency. Optimizing either PbS or PbSe by addition of up to 4 at% CdS or ZnS may be performed without concern for changing elastic moduli or H , nor the mechanical design of TE devices reliant upon the elastic moduli or H , although a change in fracture mode may indicate a change in fracture toughness.

The addition of 1 at% to 4 at% CdS or ZnS to either a PbS or PbSe matrix changes the fracture mode of the specimen, from primarily intergranular fracture to primarily transgranular fracture. A change in mode mixity is often associated with a change in fracture toughness. Fracture toughness could not be determined by Vickers indentation in this study, but may be measured by an alternative method in future work. The CdS and ZnS additions were observed as precipitates, with the range of precipitate diameter generally not a function of concentration or if the matrix was PbS or PbSe. The maximum diameter of CdS precipitates is up to 4 μm , and the maximum size of ZnS precipitates up to 15 μm .

ACKNOWLEDGEMENTS

The authors acknowledge the financial support of the Department of Energy, Revolutionary Materials for Solid State Energy Conversion Center, an Energy Frontiers Research Center funded by the U.S. Department of Energy, Office of Science, Office of Basic Energy Sciences under award number DE-SC0001054.

REFERENCES

REFERENCES

- [Alleno, Chen, Chubilleau, Lenoir, Rouleau, Trichet, Villeroy 2009] Alleno, E., Chen, L., Chubilleau, C., Lenoir, B., Rouleau, O., Trichet, M.F., Villeroy, B. Thermal Conductivity Reduction in CoSb₃–CeO₂ Nanocomposites. *Journal of Electronic Materials* 39 (2009) 1966–1970.
- [Androulakis, Lin, Kong, Uher, Wu, Hogan, Cook, Caillat, Paraskevopoulos, Kanatzidis 2007] Androulakis, J., Lin, C.-H., Kong, H.-J., Uher, C., Wu, C.-I., Hogan, T., Cook, B.A., Caillat, T., Paraskevopoulos, K.M., Kanatzidis, M.G. Spinodal decomposition and nucleation and growth as a means to bulk nanostructured thermoelectrics: enhanced performance in Pb(1-x)Sn(x)Te-PbS. *Journal of the American Chemical Society* 129 (2007) 9780–8.
- [Beattie 1969] Beattie, A.G. Temperature Dependence of the Elastic Constants of Tin Telluride. *Journal of Applied Physics* 40 (1969) 4818.
- [Bhagavantam, Rao 1951] Bhagavantam, S., Rao, T. Elastic constants of galena. *Nature* 168 (1951) 42.
- [Bhattacharya, Hermann, Keppens, Snyder 2006] Bhattacharya, S., Hermann, R.P., Keppens, V., Snyder, G.J. Effect of disorder on the thermal transport and elastic properties in thermoelectric Zn₄Sb₃. *Physical Review B* 74 (2006) 1–5.
- [Biswas, He, Blum, Wu, Hogan, Seidman, Dravid, Kanatzidis 2012] Biswas, K., He, J., Blum, I.D., Wu, C.-I., Hogan, T.P., Seidman, D.N., Dravid, V.P., Kanatzidis, M.G. High-performance bulk thermoelectrics with all-scale hierarchical architectures. *Nature* 489 (2012) 414–8.
- [Bloem, Kröger 1955] Bloem, J., Kröger, F. A Relation between Hardness and Stoichiometry in Lead Sulphide Single Crystals. *Nature* 175 (1955) 861.
- [Cline, Dunegan, Henderson 1967] Cline, C.F., Dunegan, H.L., Henderson, G.W. Elastic Constants of Hexagonal BeO, ZnS, and CdSe. *Journal of Applied Physics* 38 (1967) 1967.
- [Cook 2003] Cook, R.F. Microstructural Control of Indentation Crack Extension under Externally Applied Stress. *Fracture mechanics of ceramics* 14 (2003) 57–67.
- [Dalven 1969] Dalven, R. A review of the semiconductor properties of PbTe, PbSe, PbS and PbO. *Infrared physics* 9 (1969) 141–184.

- [Darrow, White, Roy 1969] Darrow, M., White, W., Roy, R. Micro-indentation hardness variation as a function of composition for polycrystalline solutions in the systems PbS/PbTe, PbSe/PbTe, and PbS/PbSe. *Journal of Materials Science* 4 (1969) 313–319.
- [Fan, Case, Lu, Morelli 2013] Fan, X., Case, E.D., Lu, X., Morelli, D.T. Room temperature mechanical properties of natural-mineral-based thermoelectrics. *Journal of Materials Science* 48 (2013) 7540–7550.
- [Gelbstein, Gotesman, Lishzinker, Dashevsky, Dariel 2008] Gelbstein, Y., Gotesman, G., Lishzinker, Y., Dashevsky, Z., Dariel, M.P. Mechanical properties of PbTe-based thermoelectric semiconductors. *Scripta Materialia* 58 (2008) 251–254.
- [Haxel, Hedrick, Orris 2002] Haxel, G.B., Hedrick, J.B., Orris, G.J. Rare Earth Elements — Critical Resources for High Technology. *USGS Fact Sheet fs087-02*, (2002) . <http://pubs.usgs.gov/fs/2002/fs087-02>.
- [Hellwege 1979] Landolt-Bornstein numerical data and functional relationships in science and technology, new series, Volume 11. Springer-Verlag, Berlin, 1979.
- [Heremans, Jovovic, Toberer, Saramat, Kurosaki, Charoenphakdee, Yamanaka, Snyder 2008] Heremans, J.P., Jovovic, V., Toberer, E.S., Saramat, A., Kurosaki, K., Charoenphakdee, A., Yamanaka, S., Snyder, G.J. Enhancement of thermoelectric efficiency in PbTe by distortion of the electronic density of states. *Science (New York, N.Y.)* 321 (2008) 554–7.
- [Houston, Strakna, Belson 1968] Houston, B., Strakna, R.E., Belson, H.S. Elastic Constants, Thermal Expansion, and Debye Temperature of Lead Telluride. *Journal of Applied Physics* 39 (1968) 3913.
- [Hsu, Loo, Guo, Chen, Dyck, Uher, Hogan, Polychroniadis, Kanatzidis 2004] Hsu, K.F., Loo, S., Guo, F., Chen, W., Dyck, J.S., Uher, C., Hogan, T., Polychroniadis, E.K., Kanatzidis, M.G. Cubic AgPb(m)SbTe(2+m): bulk thermoelectric materials with high figure of merit. *Science (New York, N.Y.)* 303 (2004) 818–21.
- [Jang, Kim, Han, Seo, Hong, Woo, Sakka 2010] Jang, B.-K., Kim, S.-Y., Han, I.-S., Seo, D.-W., Hong, K.-S., Woo, S.-K., Sakka, Y. Influence of uni and bi-modal SiC composition on mechanical properties and microstructure of reaction-bonded SiC ceramics. *Journal of the Ceramic Society of Japan* 118 (2010) 1028–1031.
- [Ji, He, Alboni, Su, Gothard, Zhang, Tritt, Kolis 2007] Ji, X., He, J., Alboni, P., Su, Z., Gothard, N., Zhang, B., Tritt, T.M., Kolis, J.W. Thermal conductivity of CoSb₃ nano-composites grown via a novel solvothermal nano-plating technique. *physica status solidi RRL – Rapid Research Letters* 1 (2007) 229–231.

- [Jiang, Wang, Schmidt, Dunlop, Haupt, Gissler 1991] Jiang, X., Wang, M., Schmidt, K., Dunlop, E., Haupt, J., Gissler, W. Elastic constants and hardness of ion-beam-sputtered TiN_x films measured by Brillouin scattering and depth-sensing indentation. *Journal of Applied Physics* 69 (1991) 3053–3057.
- [Karakasidis, Charitidis 2011] Karakasidis, T.E., Charitidis, C. a. Influence of nano-inclusions' grain boundaries on crack propagation modes in materials. *Materials Science and Engineering: B* 176 (2011) 490–493.
- [Kawabata, Izumi 1977] Kawabata, T., Izumi, O. The relationship between fracture toughness and transgranular fracture in an Al-6.0% Zn-2.5% Mg alloy. *Acta Metallurgica* 25 (1977) 505–512.
- [Kvetková, Duszová, Kašiarová, Dorčáková, Dusza, Balázs 2013] Kvetková, L., Duszová, A., Kašiarová, M., Dorčáková, F., Dusza, J., Balázs, C. Influence of processing on fracture toughness of Si₃N₄+graphene platelet composites. *Journal of the European Ceramic Society* 33 (2013) 2299–2304.
- [Lippmann, Kastner, Wanninger 1971] Lippmann, G., Kastner, P., Wanninger, W. Elastic constants of PbSe. *physica status solidi (a)* 159 (1971) 159–161.
- [Mi, Zhao, Zhu, Tu 2008] Mi, J.L., Zhao, X.B., Zhu, T.J., Tu, J.P. Thermoelectric properties of Yb 0.15 Co 4 Sb 12 based nanocomposites with CoSb 3 nano-inclusion. *Journal of Physics D: Applied Physics* 41 (2008) 205403.
- [Migliori, Sarrao 1997] Migliori, A., Sarrao, J.L. *Resonant Ultrasound Spectroscopy: Applications to Physics, Materials Measurements, and Nondestructive Evaluation*. Wiley-Vch, New York, 1997.
- [Milekhine, Onsøien, Solberg, Skaland 2002] Milekhine, V., Onsøien, M.I., Solberg, J.K., Skaland, T. Mechanical properties of FeSi (e), FeSi₂ (za) and Mg₂Si. *Intermetallics* 10 (2002) 743–750.
- [Möchel, Sergueev, Wille, Voigt, Prager, Stone, Sales, Guguchia, Shengelaya, Keppens, Hermann 2011] Möchel, a., Sergueev, I., Wille, H.-C., Voigt, J., Prager, M., Stone, M.B., Sales, B.C., Guguchia, Z., Shengelaya, a., Keppens, V., Hermann, R.P. Lattice dynamics and anomalous softening in the YbFe₄Sb₁₂ skutterudite. *Physical Review B* 84 (2011) 184306.
- [Morrison, Case, Ren, Baumann, Kleinow, Ni, Hogan, D'Angelo, Matchanov, Hendricks, Karri, Cauchy, Barnard, Kanatzidis 2012] Morrison, a. Q., Case, E.D., Ren, F., Baumann, a. J., Kleinow, D.C., Ni, J.E., Hogan, T.P., D'Angelo, J., Matchanov, N. a., Hendricks, T.J., Karri, N.K., Cauchy, C., Barnard, J., Kanatzidis, M.G. Elastic modulus, biaxial fracture strength, electrical and thermal transport properties of

thermally fatigued hot pressed LAST and LASTT thermoelectric materials.
Materials Chemistry and Physics 134 (2012) 973–987.

- [Mukhopadhyay, Chakravarty, Basu 2010] Mukhopadhyay, A., Chakravarty, D., Basu, B. Spark Plasma-Sintered WC-ZrO₂-Co Nanocomposites with High Fracture Toughness and Strength. *Journal of the American Ceramic Society* 93 (2010) 1754–1763.
- [Ni, Ren, Case, Timm 2009a] Ni, J., Ren, F., Case, E., Timm, E. Porosity dependence of elastic moduli in LAST (lead–antimony–silver–tellurium) thermoelectric materials. *Materials Chemistry and Physics* (2009) .
- [Ni, Case, Khabir, Stewart, Wu, Hogan, Timm, Girard, Kanatzidis 2010] Ni, J.E., Case, E.D., Khabir, K.N., Stewart, R.C., Wu, C.-I., Hogan, T.P., Timm, E.J., Girard, S.N., Kanatzidis, M.G. Room temperature Young's modulus, shear modulus, Poisson's ratio and hardness of PbTe–PbS thermoelectric materials. *Materials Science and Engineering: B* 170 (2010) 58–66.
- [Ni, Case, Schmidt, Wu, Hogan, Trejo, Lara-Curzio, Kanatzidis 2013] Ni, J.E., Case, E.D., Schmidt, R.D., Wu, C.-I., Hogan, T.P., Trejo, R.M., Lara-Curzio, E., Kanatzidis, M.G. Fracture mode, microstructure and temperature-dependent elastic moduli for thermoelectric composites of PbTe–PbS with SiC nanoparticle additions. *Philosophical Magazine* 93 (2013) 4412–4439.
- [Ni, Case, Stewart, Wu, Hogan, Kanatzidis 2011] Ni, J.E., Case, E.D., Stewart, R., Wu, C.-I., Hogan, T.P., Kanatzidis, M.G. Bloating in (Pb_{0.95}Sn_{0.05}Te)_{0.92}(PbS)_{0.08-0.055}PbI₂ Thermoelectric Specimens as a Result of Processing Conditions. *Journal of Electronic Materials* 41 (2011) 1153–1158.
- [Ni, Ren, Case, Timm 2009b] Ni, J.E., Ren, F., Case, E.E.D., Timm, E.J.E. Porosity dependence of elastic moduli in LAST (lead–antimony–silver–tellurium) thermoelectric materials. *Materials Chemistry and Physics* 118 (2009) 459–466.
- [Portnoi, Mukaseev, Gribkov, Levinskii 1968] Portnoi, I., Mukaseev, A.A., Gribkov, V.N., Levinskii, Y. V. Modulus of normal elasticity of porosity-free titanium and zirconium nitrides. *Soviet Powder Metallurgy and Metal Ceramics* 7 (1968) 406–408.
- [Ren, Case, Ni, Timm, Lara-Curzio, Trejo, Lin, Kanatzidis 2009] Ren, F., Case, E.D., Ni, J.E., Timm, E.J., Lara-Curzio, E., Trejo, R.M., Lin, C.-H., Kanatzidis, M.G. Temperature-dependent elastic moduli of lead telluride-based thermoelectric materials. *Philosophical Magazine* 89 (2009) 143–167.
- [Ren, Case, Timm, Lara-Curzio, Trejo 2010] Ren, F., Case, E.D., Timm, E.J., Lara-Curzio, E., Trejo, R.M. Anomalous temperature-dependent Young's modulus of a

- cast LAST (Pb–Sb–Ag–Te) thermoelectric material. *Acta Materialia* 58 (2010) 31–38.
- [Ren, Case, Timm, Schock 2007] Ren, F., Case, E.D., Timm, E.J., Schock, H.J. Young's modulus as a function of composition for an n-type lead–antimony–silver–telluride (LAST) thermoelectric material. *Philosophical Magazine* 87 (2007) 4907–4934.
- [Ren, Hall, Ni, Case, Sootsman, Mercouri 2008] Ren, F., Hall, B.D., Ni, J.E., Case, E.D., Sootsman, J., Mercouri, G. Mechanical Characterization of PbTe-based Thermoelectric Materials. *1044* (2008) .
- [Rice 1998] Rice, R.W. *Porosity of Ceramics*. Marcel Dekker, New York, 1998.
- [Rice, Wu, Borchelt 1994] Rice, R.W., Wu, C.C., Borchelt, F. Hardness–Grain-Size Relations in Ceramics. *Journal of the American Ceramic Society* 77 (1994) 2539–2553.
- [Rogl, Rogl 2011] Rogl, G., Rogl, P. Mechanical Properties of Skutterudites. *Science of Advanced Materials* 3 (2011) 517–538.
- [Salvador, Yang, Shi, Wang, Wereszczak, Kong, Uher 2009] Salvador, J.R., Yang, J., Shi, X., Wang, H., Wereszczak, a. a., Kong, H., Uher, C. Transport and mechanical properties of Yb-filled skutterudites. *Philosophical Magazine* 89 (2009) 1517–1534.
- [Sangster, Pelton 1997] Sangster, J., Pelton, A. The Na-S (sodium-sulfur) system. *Journal of phase equilibria* 18 (1997) 89–96.
- [Schmidt, Case, Giles, Ni, Hogan 2012a] Schmidt, R.D., Case, E.D., Giles, J., Ni, J.E., Hogan, T.P. Room-Temperature Mechanical Properties and Slow Crack Growth Behavior of Mg₂Si Thermoelectric Materials. *Journal of Electronic Materials* 41 (2012) 1210–1216.
- [Schmidt, Case, Lehr, Morelli 2013a] Schmidt, R.D., Case, E.D., Lehr, G.J., Morelli, D.T. Room temperature mechanical properties of polycrystalline YbAl₃, a promising low temperature thermoelectric material. *Intermetallics* 35 (2013) 15–24.
- [Schmidt, Case, Lobo, Thompson, Sakamoto, Zhou, Uher 2014] Schmidt, R.D., Case, E.D., Lobo, Z., Thompson, T.R., Sakamoto, J.S., Zhou, X.-Y., Uher, C. Influence of silver nanoparticle addition, porosity, and processing technique on the mechanical properties of Ba_{0.3}Co₄Sb₁₂ skutterudites. *Journal of Materials Science*(2014) .
- [Schmidt, Case, Ni, Sakamoto, Trejo, Lara-Curzio 2012b] Schmidt, R.D., Case, E.D., Ni, J.E., Sakamoto, J.S., Trejo, R.M., Lara-Curzio, E. Temperature-dependent Young's modulus, shear modulus and Poisson's ratio of p -type Ce_{0.9} Fe_{3.5} Co_{0.5} Sb₁₂

and n -type Co_{0.95}Pd_{0.05}Te_{0.05}Sb₃ skutterudite thermoelectric materials. *Philosophical Magazine* 92 (2012) 727–759.

- [Schmidt, Case, Ni, Trejo, Lara-Curzio, Korkosz, Kanatzidis 2013b] Schmidt, R.D., Case, E.D., Ni, J.E., Trejo, R.M., Lara-Curzio, E., Korkosz, R.J., Kanatzidis, M.G. High-temperature elastic moduli of thermoelectric SnTe_{1±x} – y SiC nanoparticulate composites. *Journal of Materials Science* 48 (2013) 8244–8258.
- [Schmidt, Ni, Case, Sakamoto, Kleinow, Wing, Stewart, Timm 2010] Schmidt, R.D., Ni, J.E., Case, E.D., Sakamoto, J.S., Kleinow, D.C., Wing, B.L., Stewart, R.C., Timm, E.J. Room temperature Young's modulus, shear modulus, and Poisson's ratio of Ce_{0.9}Fe_{3.5}Co_{0.5}Sb₁₂ and Co_{0.95}Pd_{0.05}Te_{0.05}Sb₃ skutterudite materials. *Journal of Alloys and Compounds* 504 (2010) 303–309.
- [Shin, Gall, Hellgren, Patscheider, Petrov, Greene 2003] Shin, C.-S., Gall, D., Hellgren, N., Patscheider, J., Petrov, I., Greene, J.E. Vacancy hardening in single-crystal TiN[sub x](001) layers. *Journal of Applied Physics* 93 (2003) 6025–6028.
- [Simmons, Wang 1971] Simmons, G., Wang, H. *Single Crystal Elastic Constants and Calculated Aggregate Properties: A Handbook*. The M.I.T. Press, Cambridge, Massachusetts, 1971.
- [Toprak, Stiewe, Platzek, Williams, Bertini, Muller, Gatti, Zhang, Rowe, Muhammed 2004] Toprak, M.S., Stiewe, C., Platzek, D., Williams, S., Bertini, L., Muller, E., Gatti, C., Zhang, Y., Rowe, M., Muhammed, M. The Impact of Nanostructuring on the Thermal Conductivity of Thermoelectric CoSb₃. *Advanced Functional Materials* 14 (2004) 1189–1196.
- [Tritt 2011] Tritt, T.M. Thermoelectric Phenomena, Materials, and Applications. *Annual Review of Materials Research* 41 (2011) 433–448.
- [Wang, Duncan, Wachsman, Ebrahimi 2007] Wang, Y., Duncan, K., Wachsman, E., Ebrahimi, F. The effect of oxygen vacancy concentration on the elastic modulus of fluorite-structured oxides. *Solid State Ionics* 178 (2007) 53–58.
- [Whitten, Chung, Danielson 1965] Whitten, W., Chung, P., Danielson, G. Elastic constants and lattice vibration frequencies of Mg₂Si. *Journal of Physics and Chemistry of Solids* 26 (1965) 49–56.
- [Yamada, Sekine, Kumazawa, Tanabe 2010] Yamada, M., Sekine, K., Kumazawa, T., Tanabe, Y. Relationship between the cone crack and fracture mode in ceramics under high-velocity-projectile impact. 96 (2010) 903–908.
- [Zhang, Rogl, Grytsiv, Puchegger, Koppensteiner, Spieckermann, Kabelka, Reinecker, Rogl, Schranz, Zehetbauer, Carpenter 2010] Zhang, L., Rogl, G., Grytsiv, A.,

- Puchegger, S., Koppensteiner, J., Spieckermann, F., Kabelka, H., Reinecker, M., Rogl, P., Schranz, W., Zehetbauer, M., Carpenter, M.A. Mechanical properties of filled antimonide skutterudites. *Materials Science and Engineering: B* 170 (2010) 26–31.
- [Zhao, Hao, Lo, Wu, Zhou, Lee, Li, Biswas, Hogan, Uher, Wolverton, Dravid, Kanatzidis 2013] Zhao, L.-D., Hao, S., Lo, S.-H., Wu, C.-I., Zhou, X., Lee, Y., Li, H., Biswas, K., Hogan, T.P., Uher, C., Wolverton, C., Dravid, V.P., Kanatzidis, M.G. High thermoelectric performance via hierarchical compositionally alloyed nanostructures. *Journal of the American Chemical Society* 135 (2013) 7364–70.
- [Zhao, He, Hao, Wu, Hogan, Wolverton, Dravid, Kanatzidis 2012a] Zhao, L.-D., He, J., Hao, S., Wu, C.-I., Hogan, T.P., Wolverton, C., Dravid, V.P., Kanatzidis, M.G. Raising the thermoelectric performance of p-type PbS with endotaxial nanostructuring and valence-band offset engineering using CdS and ZnS. *Journal of the American Chemical Society* 134 (2012) 16327–36.
- [Zhao, He, Wu, Hogan, Zhou, Uher, Dravid, Kanatzidis 2012b] Zhao, L.-D., He, J., Wu, C.-I., Hogan, T.P., Zhou, X., Uher, C., Dravid, V.P., Kanatzidis, M.G. Thermoelectrics with earth abundant elements: high performance p-type PbS nanostructured with SrS and CaS. *Journal of the American Chemical Society* 134 (2012) 7902–12.
- [Zhao, Lo, He, Li, Biswas, Androulakis, Wu, Hogan, Chung, Dravid, Kanatzidis 2011] Zhao, L.-D., Lo, S.-H., He, J., Li, H., Biswas, K., Androulakis, J., Wu, C.-I., Hogan, T.P., Chung, D.-Y., Dravid, V.P., Kanatzidis, M.G. High performance thermoelectrics from earth-abundant materials: enhanced figure of merit in PbS by second phase nanostructures. *Journal of the American Chemical Society* 133 (2011) 20476–87.
- [Zhao, Zhang, Li, Zhou, Liu, Liu 2008] Zhao, L.-D., Zhang, B.-P., Li, J.-F., Zhou, M., Liu, W.-S., Liu, J. Thermoelectric and mechanical properties of nano-SiC-dispersed Bi₂Te₃ fabricated by mechanical alloying and spark plasma sintering. *Journal of Alloys and Compounds* 455 (2008) 259–264.
- [Zhou, Li, Kita 2008] Zhou, M., Li, J.-F., Kita, T. Nanostructured AgPb(m)SbTe(m+2) system bulk materials with enhanced thermoelectric performance. *Journal of the American Chemical Society* 130 (2008) 4527–32.
- [Zhu, Lee, Lan, Wang, Joshi, Wang, Yang, Vashaee, Guilbert, Pillitteri, Dresselhaus, Chen, Ren 2009] Zhu, G., Lee, H., Lan, Y., Wang, X., Joshi, G., Wang, D., Yang, J., Vashaee, D., Guilbert, H., Pillitteri, a., Dresselhaus, M., Chen, G., Ren, Z. Increased Phonon Scattering by Nanograins and Point Defects in Nanostructured Silicon with a Low Concentration of Germanium. *Physical Review Letters* 102 (2009) 196803.

9 Summary and Conclusions

9.1 Porosity dependence and processing method independence of elastic moduli

From the results of Chapter 3 on properties of YbAl_3 and Chapter 6 on $\text{Ba}_{0.3}\text{Co}_4\text{Sb}_{12}$ skutterudites, we conclude that the Young's modulus, E , shear modulus, G , and bulk modulus, B , of bulk porous YbAl_3 and $\text{Ba}_{0.3}\text{Co}_4\text{Sb}_{12}$ are a function primarily of the volume fraction of natural porosity, P . In this work, natural porosity refers to porosity that occurs when powder processing and sintering a brittle material, as opposed to introduced porosity such as that formed when a second material is mixed and then burned out during sintering or when pores are formed via bloating. Two powder processing and sintering methods, (i) grinding and sieving and hot press (HP) sintering, and (ii) vibratory milling and pulsed electric current sintering (PECS), were used to produce sets of specimens with a range of porosity for each of YbAl_3 and $\text{Ba}_{0.3}\text{Co}_4\text{Sb}_{12}$. The powder processing method, sintering method, or different natural porosity size and distribution are not a significant factor in determining the mechanical properties of E , G , and H for YbAl_3 and $\text{Ba}_{0.3}\text{Co}_4\text{Sb}_{12}$. The properties may be accurately estimated with only a knowledge of P .

The elastic moduli, E , G , and B , of many brittle materials have been shown follow the empirical relationship [Rice 1998]

$$A = A_0(\exp(-b_A P)) \quad (1)$$

where A represents E , G , or B , A_0 represents E_0 , G_0 and B_0 , the $P = 0$ intercepts, and b_A is a unitless, material-dependent parameter. If $b_A P$ is small, equation (1) may be linearized [Ni 2009b] by using the first two terms of the Taylor series expansion of equation (1).

$$A = A_0(1 - b_A P) \quad (2)$$

For both YbAl_3 and $\text{Ba}_{0.3}\text{Co}_4\text{Sb}_{12}$, the linear form has been used.

Rice [Rice 1998] has shown that the porosity dependence, b_A , of the elastic moduli for a variety of brittle materials typically lies between 2 and 6. Prior to this work, the b_E and b_G values for only one TE material was in the literature, LAST (lead–antimony–silver–tellurium) [Ni 2009a].

9.1.1 Grain size and processing method independence of elastic moduli

Processing conditions may lead to a change in grain size (GS), but a change in GS does not change the elastic moduli for specimens with GS greater than approximately 20 nm [Kim 1999]. This was consistent with the results for the $\text{Ba}_{0.3}\text{Co}_4\text{Sb}_{12}$ specimens, where processing method changed the $\text{Ba}_{0.3}\text{Co}_4\text{Sb}_{12}$ GS from bimodal, with most grains $>1 \mu\text{m}$ in diameter for the HP, to unimodal with an average GS of $0.14 - 0.17 \mu\text{m}$. The elastic moduli results for the different GS $\text{Ba}_{0.3}\text{Co}_4\text{Sb}_{12}$ specimens in section 6 further support the result that only the P dependence is required to predict the E , G , or B of a TE material.

9.2 Sintering aids and TE materials

Sintering aids have generally not been considered for TE materials, despite the numerous benefits, such as reduced sintering time, temperature and cost [German 1985]. A new possible sintering aid was determined for Sb-based skutterudites and other Sb-containing TE materials, as well as a method to identify possible sintering aids for other TE materials (chapter 6).

In examining the increased density of $\text{Ba}_{0.3}\text{Co}_4\text{Sb}_{12}$ with 0.5 wt% Ag additions, the Ag in the composite was determined to react with excess Sb and form an Ag_3Sb phase

(chapter 6). Examining the binary phase diagram, this Ag_3Sb phase likely formed in a eutectic/peritectic reaction during sintering, and a liquid was likely present at 873 K, and possibly at 773 K. This liquid acted as a sintering aid, and the reaction to form the Ag_3Sb phase may also act as a beneficial scavenger of excess Sb. The use of Ag as a sintering aid may likely be expanded to other Sb-containing TE materials. Furthermore, the use of a binary or ternary phase diagram between constituent elements of a TE material and a possible addition may indicate materials with a possibly beneficial eutectic/peritectic reactions.

9.3 Elastic moduli of TE materials with nanoparticle or nanoprecipitate additions

In general, if the addition of nanoparticles or nanoprecipitates does not change the composition of the matrix TE material, the elastic moduli of the composite exhibits only a weak dependence on the addition, and may be effectively modeled by the Hashin or Halpin-Tsai models.

For nanoparticle or nanoprecipitate additions that are typically considered in TE materials (less than 4 vol%), SiC_{NP} additions in Mg_2Si (chapter 5) or SnTe (chapter 7), Ag_{NP} additions in skutterudites (chapter 6), or precipitates of CdS or ZnS in PbS or PbSe (chapter 8), the elastic moduli are weak functions of the volume fraction of the additions. The weak dependence of the elastic moduli is poorly described by a rule of mixtures approximation (chapters 7 and 8),

$$E_C = V_m E_m + V_r E_r \quad (3)$$

but may be reasonably described by either the Hashin particulate composite [Hashin 1962] (chapters 7 and 8)

$$E_C = E_m \left(\frac{E_m V_m + E_r \{V_r + 1\}}{E_r V_m + E_m \{V_r + 1\}} \right) \quad (4)$$

or the Halpin-Tsai model [Halpin 1992] (chapters 7 and 8)

$$E_C = E_m \left(\frac{1 + 2(a/b)qV_r}{E_r V_m + E_m \{V_r + 1\}} \right) \quad (5a)$$

where the boundary condition parameter, q , is

$$q = \frac{\left(\frac{E_r}{E_m} \right) - 1}{\left(\frac{E_r}{E_m} \right) + 2 \left(\frac{a}{b} \right)} \quad (5b)$$

These models for the Young's modulus of the composite, E_C , depend on the Young's modulus of the matrix material and reinforcing material (nanoparticle or nanoprecipitates), E_m and E_r , and the volume fraction of the matrix and reinforcing materials, V_m and V_r . For the Halpin-Tsai model, the length/thickness ratio, a/b , for roughly equiaxed particles or precipitates was set to 1.

9.4 Fracture toughness and slow crack growth in Mg_2Si and other TE materials

The fracture toughness, K_C , of TE materials is low, typically less than $1.5 \text{ MPa}\cdot\text{m}^{1/2}$, and must be considered carefully when designing at TE module. Despite the importance of K_C , it has not been measured for many TE materials. The K_C for both unreinforced Mg_2Si (chapter 4) and up to 4 vol% SiC_{NP} -reinforced Mg_2Si (chapter 5) was measured, as well as for YbAl_3 (chapter 3) and $\text{Ba}_{0.3}\text{Co}_4\text{Sb}_{12}$ (chapter 6).

Fracture toughness is a function of both the reinforcing material and the powder processing/sintering conditions. Planetary ball milled Mg_2Si with addition of SiC_{NP} reached a maximum K_C at 1 – 2 vol% SiC_{NP} , increasing 33% over no addition, but

vibratory milled Mg_2Si exhibited no improvement in K_C with 0 – 2 vol% SiC_{NP} addition (chapter 5).

The ball milled Mg_2Si with 1 – 2 vol% SiC_{NP} may not be the best choice for highest strength, despite having the highest K_C , ~ 30% higher than without SiC_{NP} or the vibratory milled material (chapter 5). The fracture stress, σ_{fract} , is a function of K_C , the flaw size, a , and shape factor, Y , where [Rice 1998]

$$\sigma_{\text{fract}} = \frac{YK_C}{\sqrt{a}} \quad (6)$$

When fracture occurs, the critical flaw, a_{crit} , is typically the largest flaw in a region of high stress, and this flaw can be from a variety of sources, such as the pores and cracks that form within a material or scratches and cracks at the surface from machining.

Typically, the largest flaw not caused by machining scales with GS. Vibratory milled Mg_2Si specimens exhibited an average GS (0.4 – 0.8 μm) roughly 1/5 the average GS of planetary milled specimens (2 – 4 μm). If the critical flaw scales directly with GS, the fracture stress would be ~70% higher with the vibratory milled Mg_2Si than the ball milled Mg_2Si with 1 – 2 vol% SiC_{NP} , even with the lower K_C . If, however, the critical flaw does not scale directly with GS, as might happen with flaws from machining or other external sources, the highest K_C would be the more desirable material.

In addition, slow crack growth is a particular concern for low fracture toughness materials such as most TE materials. With slow crack growth, a flaw, such as from cutting or grinding to fabricate a leg, may grow to a large flaw that leads to failure in the minutes or hours after machining. Slow crack growth was examined for unreinforced Mg_2Si in dry room air and determined to not be a concern. However Mg_2Si does react with water and a humid or other environment may remain a concern (chapter 4).

REFERENCES

REFERENCES

- [German 1985] German, R.M. *Liquid phase sintering*. Springer Science+Business Media, Inc., Troy, New York, 1985.
- [Halpin 1992] Halpin, J.C. *Primer on composite materials analysis*. Technomic Publishing Company, Inc., Lancaster, Pennsylvania, 1992.
- [Hashin 1962] Hashin, Z. The Elastic Moduli of Heterogeneous Materials. *Journal of Applied Mechanics* 29 (1962) 143–150.
- [Kim, Bush 1999] Kim, H.S., Bush, M.B. The effects of grain size and porosity on the elastic modulus of nanocrystalline materials. *Nanostructured Materials* 11 (1999) 361–367.
- [Ni, Ren, Case, Timm 2009a] Ni, J., Ren, F., Case, E., Timm, E. Porosity dependence of elastic moduli in LAST (lead–antimony–silver–tellurium) thermoelectric materials. *Materials Chemistry and Physics*(2009) .
- [Ni, Ren, Case, Timm 2009b] Ni, J.E., Ren, F., Case, E.E.D., Timm, E.J.E. Porosity dependence of elastic moduli in LAST (lead–antimony–silver–tellurium) thermoelectric materials. *Materials Chemistry and Physics* 118 (2009) 459–466.
- [Rice 1998] Rice, R.W. *Porosity of Ceramics*. Marcel Dekker, New York, 1998.

10 Future work

In the examination of the mechanical properties of YbAl_3 , there were considerable differences between the experimental measurements of elastic moduli and published models, and even between the models themselves (chapter 3). These were stated to possibly be related to “complexities in modeling and understanding the nature of the intermediate valence nature of the Yb ion in YbAl_3 .” As such, a closer examination of the modeled and measured elastic moduli of other Yb-based materials may be investigated.

For Mg_2Si , slow crack growth in a dry environment does not occur (chapter 4). However, machining fluids may be water-based or contain dissolved water or other polar molecules required for slow crack growth, and storage of machined components may not be in a dry environment. Additional measurements of Mg_2Si and other TE materials in a humid environment or with machining oil on the surface should be investigated to determine if environmental assisted crack growth may occur in other common environments in which the TE materials may be stored.

The fracture strength of Mg_2Si specimens has shown improvement when SiC_{NP} was added to ball milled powder, but not vibratory milled powder (chapter 5). The difference in the behavior between these two processing techniques may be related to grain size, but requires further exploration. For non-cubic materials, K_C may reach a maximum at a critical grain size [Bennison 1989], although this is not shown for cubic materials. The composite thermoelectric (TE) materials may warrant further

investigation to determine if an improved model for fracture toughness of cubic matrix materials with addition of nanoparticles may be observed.

Additional work on discovery and use of sintering aids can benefit both the cost and development of TE materials (chapter 6). Use of Ag_{NP} in other Sb-containing TE materials may enhance sintering, and the use of binary or ternary phase diagrams should be employed to discover other candidate materials for liquid phase sintering aids.

The functional relationship between elastic moduli of SnTe_{1+x} as a function of x has only been partially addressed (chapter 7), especially since the stoichiometry of the SnTe is not in the previous elasticity literature [Beattie 1969; Baughman 1969].

The differences between the measured PbS (chapter 8) and the literature values are a concern and should be further explored. The doping effect of contaminants and/or excess Pb on the elastic moduli of PbS is significant in the measured results.

REFERENCES

REFERENCES

- [Baughman, Lefever 1969] Baughman, R., Lefever, R. Czochralski encapsulation growth of GeTe, SnTe and PbTe single crystals. *Materials Research Bulletin* 4 (1969) 721–726.
- [Beattie 1969] Beattie, A.G. Temperature Dependence of the Elastic Constants of Tin Telluride. *Journal of Applied Physics* 40 (1969) 4818.
- [Bennison, Lawn 1989] Bennison, S.J., Lawn, B.R. Role of interfacial grain-bridging sliding friction in the crack-resistance and strength properties of nontransforming ceramics. *Acta Metallurgica* 37 (1989) 2659–2671.

APPENDICES

APPENDIX A. Effect of nanoparticle addition on the elastic modulus of a composite material

The effect of the nanoparticle additions on the Young's modulus, E_C , of a nanocomposites material can be predicted from numerous models. In this appendix, we list relationships for four composite models, namely rule of mixtures (ROM), Reuss constant strain (RCS), Hashin particulate (HP) and Halpin-Tsai (HT) [Schmidt 2013]. For each model, the Young's modulus of the composite, E_C , is the based on E_r , the elastic modulus of the nanoparticle reinforcement phase, V_r , the volume fraction reinforcement phase, E_m , the Young's modulus of the matrix phase, and V_m , the volume fraction matrix phase. Expressions for the four models can be written as:

$$\textbf{ROM: } E_C = V_m E_m + V_r E_r \quad (9)$$

$$\textbf{RCS: } \frac{1}{E_C} = \frac{V_m}{E_m} + \frac{V_r}{E_r} \quad (10)$$

$$\textbf{HP: } E_C = E_m \left(\frac{E_m V_m + E_r \{V_r + 1\}}{E_r V_m + E_m \{V_r + 1\}} \right) \quad (11)$$

$$\textbf{HT: } E_C = E_m \left(\frac{1 + 2(a/b)qV_r}{E_r V_m + E_m \{V_r + 1\}} \right) \quad (12)$$

In the HT model, a/b is the aspect ratio (length/thickness) for the reinforcing phase and q is a boundary condition parameter given by

$$q = \frac{\left(\frac{E_r}{E_m} \right) - 1}{\left(\frac{E_r}{E_m} \right) + 2 \left(\frac{a}{b} \right)} \quad (13)$$

Table A.1. For spherical metallic particle additions to brittle matrices [Fujieda 2012; Hasselman 1965], comparison of the measured composite modulus, E_C , with the values predicted by the four models given in this appendix (rule of mixtures, ROM, Reuss constant strain, RCS, Hashin particulate, HP, and Halpin-Tsai, HT [Schmidt 2013]). E_m is the Young's modulus of the matrix material [Fujieda 2012; Hasselman 1965] and E_r is the Young's modulus of the reinforcing material [Lowrie 1967; Macfarlane 1965; Neighbours 1958; Chang 1966].

Material [Reference]	E_m (GPa)	E_r (GPa)	V_r (%)	E_C (GPa)	ROM (GPa)	RCS (GPa)	HP (GPa)	HT (GPa)
Sodium boro-silicate glass + W [Hasselman 1965]	80.5 [Hasselman 1965]	409.8 [Lowrie 1967]	10	90.9 ± 1.4	113.4	87.5	92.1	96.2
Sodium boro-silicate glass + W [Hasselman 1965]	80.5 [Hasselman 1965]	409.8 [Lowrie 1967]	20	105.5 ± 1.1	146.4	95.9	105.5	114.1
Sodium boro-silicate glass + W [Hasselman 1965]	80.5 [Hasselman 1965]	409.8 [Lowrie 1967]	30	118.0 ± 0.2	179.3	106.1	121.1	134.7
Sodium boro-silicate glass + W [Hasselman 1965]	80.5 [Hasselman 1965]	409.8 [Lowrie 1967]	40	137.5 ± 0.3	212.2	118.6	139.6	158.7
Sodium boro-silicate glass + W [Hasselman 1965]	80.5 [Hasselman 1965]	409.8 [Lowrie 1967]	50	159.9 ± 0.5	245.2	134.6	161.9	186.8
Dental porcelain + Pt _{NP} [Fujieda 2012]	60.1 [Fujieda 2012]	177.6 [Macfarlane 1965]	11.7	67.2 ± 1.6	73.9	65.2	67.5	69.7
Dental porcelain + Ag _{NP} [Fujieda 2012]	60.1 [Fujieda 2012]	82 [Neighbours 1958; Chang 1966]	21.4	67.8 ± 4.3	64.8	63.7	64.2	65.0

Table A.1 summarizes the Young's modulus change due to the addition of both micron-sized and nanosized-metallic particles to brittle matrices in studies by Hasselman [Hasselman 1965] and by Fujieda et al. [Fujieda 2012]. Table A.1 gives the measured composite modulus, E_C , for the addition of 0.10, 0.20, 0.30 and 0.40 volume fraction of tungsten particles with diameters of approximately 30 μm to a borosilicate glass [Hasselman 1965], along with the predicted values of modulus calculated by the ROM, RCS, HP, HT models and the modulus of tungsten [Lowrie 1967]. In addition, Table A.1 lists the measured E_C for composite specimens from Fujieda et al. [Fujieda 2012], who measured the elastic modulus change induced by adding either 26 wt% platinum nanoparticles (Pt_{NP}) [Macfarlane 1965] or 26 wt% Ag_{NP} [Neighbours 1958; Chang 1966] to a dental porcelain, where the mean diameters of the Pt_{NP} and Ag_{NP} nanoparticles were 5 nm and 10 nm, respectively. The measured composite moduli, E_C , (Table A.1) [Fujieda 2012; Hasselman 1965] agree quite well with the moduli calculated in this study using the Halpin-Tsai model (HT). Since the metal particles were spherical in both the Hasselman [Hasselman 1965] and Fujieda et al. [Fujieda 2012] studies, for the purposes of the calculations we set $a/b = 1$ in equation 12, where a/b is the particle aspect ratio.

The amounts of particle addition in the studies by Fujieda et al. [Fujieda 2012] and Hasselman [Hasselman 1965] were significantly greater than the 0.0068 volume fraction (0.5 wt%) Ag_{NP} added in this study. The four composite models given in this Appendix predict a decrease in E_C of about 0.39% with the 0.5 wt% Ag_{NP} addition to the Ba-skutterudite in this study. In recent research by Schmidt et al. [Schmidt 2013] applied the four modulus-composite models to a thermoelectric system consisting of a brittle matrix and a brittle reinforcing phase, namely with 0.00, 0.01, 0.02, 0.03, and 0.04

volume fraction of added SiC nanoparticles (SiC_{NP}) in the brittle thermoelectric matrix SnTe_{1+x} , (where $x = 0.0$ or 0.016), Hashin and the Halpin-Tsai models best described the elastic modulus data. Thus, for the Hasselman [Hasselman 1965] and Fujieda et al. [Fujieda 2012] studies in which the volume percentage of micro and nano particles added was relatively high (from 0.10 to 0.40 volume fraction), as well as the SnTe_{1+x} (with 0.00 to 0.04 volume fraction SiC_{NP} added), the Halpin-Tsai model agrees with the experimental modulus data relatively well. In particular, for 0.5 wt% Ag_{NP} in this study, the Halpin-Tsai model predicts a change in E of only 0.35%, which is consistent with the E values measured in this study for the Ba-skutterudite with and without added Ag_{NP} .

APPENDIX B. Standard operating procedure for HT-RUS furnace

Note: This SOP describes operation of the furnace, not the operation of the RUS computer or software. The furnace controller and power supply was designed and constructed by Brian Wright and Gregg Mulder of the Electrical and Computer Engineering Shop.

Precautions

Do not operate the furnace with the bell jar removed and the heating element leads exposed. When the bell jar has been removed, if the high voltage is turned on, the line voltage leads and the ends of the SiC heating elements are exposed and are an electrocution hazard.

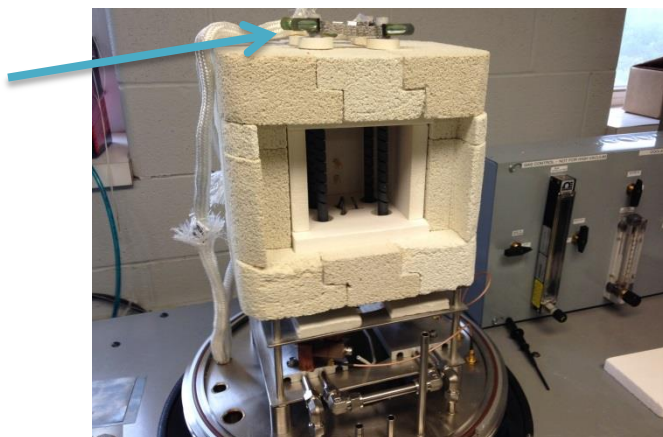


Figure B.1. The top of the furnace has exposed leads to power the heating elements with up to 120 VAC electricity. Do not operate the furnace with these leads exposed.

The furnace cools through the outside of the bell jar. When in operation, the bell jar may get extremely hot and cause burns. Additional cooling for the bell jar may be required.

The specimen will be exposed to elevated temperatures. Verify that there are no concerns with specimen decomposition or reaction at the temperatures it will be exposed to.

1 Furnace Preparation

1.1 Wear gloves and do not use oils. Oils, especially in the inner furnace, will be burned off during operation. For this reason, do not introduce oils to the furnace. Keep the inner

furnace clean, remove any finger oils from the specimen and wear gloves when adjusting furnace components to keep them clean.

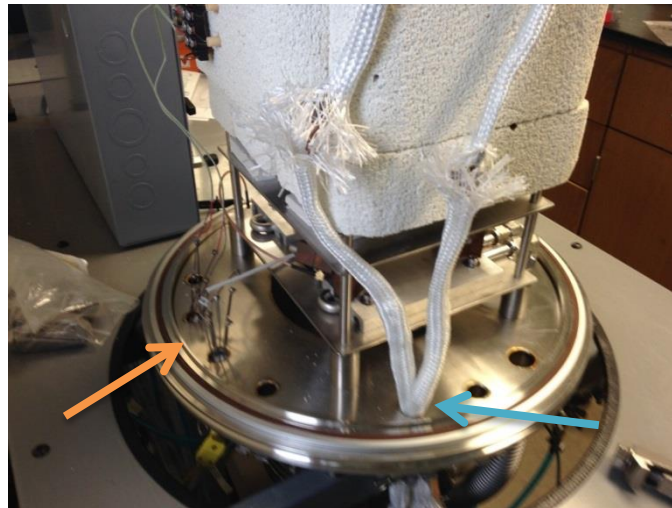


Figure B.2. Note feedthroughs for the thermocouples (left arrow) and heating element power (right arrow). These feedthroughs and the wires from them should not touch the base or the sides of the bell jar when closed.



Figure B.3. Braided insulation must be in place around the conductors to the heating elements to prevent a short.

1.2 Clean dust and debris. The furnace is composed of several refractory bricks that let off a significant amount of abrasive dust and debris. For this reason, a thorough cleaning is required prior to operation to ensure the proper sealing and operation of the furnace. Particular attention is required with the feed-through connections for the power and thermocouples, to ensure no shorts are created. Power is supplied through a feed-through with two copper conductors, capable of handling the 20A current to the furnace heating elements (Figure B.3). These copper conductors are shielded with high temperature braided ceramic insulator material, and the insulator must be in place to protect from a potentially dangerous short between the bell jar and the power supply. There are two types of thermocouples, one K-type thermocouple for the lower temperature sensing near the transducers to sense if the transducers are over the maximum design temperature, and a pair of R-type thermocouples to measure the temperature within the furnace. All the thermocouples make connections to the bare wires of the feed-throughs.

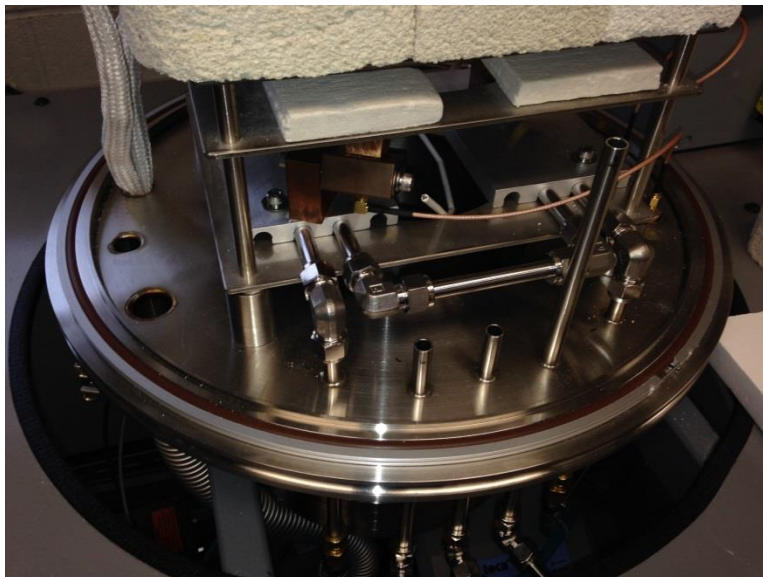


Figure B.4. The o-ring and the base of the bell jar may have some debris, particularly from the furnace refractories. The debris is abrasive, and may inhibit a proper seal between the bottom and side of the bell jar. The debris should be removed and appropriate grease reapplied to the o-ring prior to operation.

1.3 Clean and reapply vacuum grease. Clean off the centering ring and o-ring at the base of the bell jar (Figure B.4). The o-ring will have Apiezon or equivalent low volatile organic compound (VOC), high temperature vacuum grease on it that may have debris embedded that should be removed. Reapply a thin layer of Apiezon or equivalent low VOC, high temperature vacuum grease.

1.4 Check for electrical shorts. Verify the power connections are properly shielded with braided insulation (Figure B.3) and that they will not be touching the bell jar or any uninsulated components when closed. Turn on the 120 V power for the temperature controllers (NOT the high voltage for the heating elements) and check for room temperature readings from each of the three thermocouples (Figure B.5). Inspect all cables for any damage.

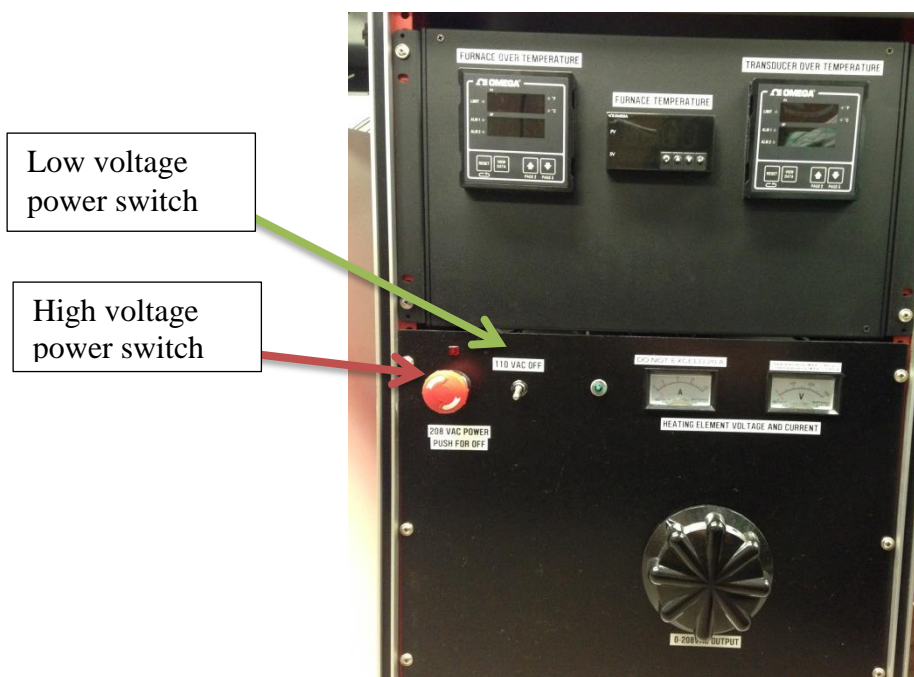


Figure B.5. Controls and power supply for furnace. Note the high voltage power supply is activated with the red button, and indicated with a red light. Power for the transducers is provided by a 110 VAC circuit, turned on with a toggle switch and indicated with a green light.

1.5 Inspect the hoses. Check the coolant lines to and from the RUS mount assembly (Figure B.6). Check the chiller for proper operation, and to verify the tank is properly filled with water. Turn on the chiller pump to verify no leaks. Turn off after inspection to avoid a buildup of condensation inside the furnace. Inspect the compressed gas hoses for any damage (Figure B.6). Verify the compressed gas cylinder has sufficient pressure to run for the duration of the experiment. Verify the pressure regulator setting does not exceed the pressure rating of the hoses and connectors, typically set much less than 100 psi (for example, 30 psi).

1.6 Set up the bubbler for proper operation. Verify the end of the gas out line that is in the bubbler is below the liquid level (Figure B.7). Adjust the end of the gas out line if necessary to be near the bottom of the bubbler. Refill with water if necessary.

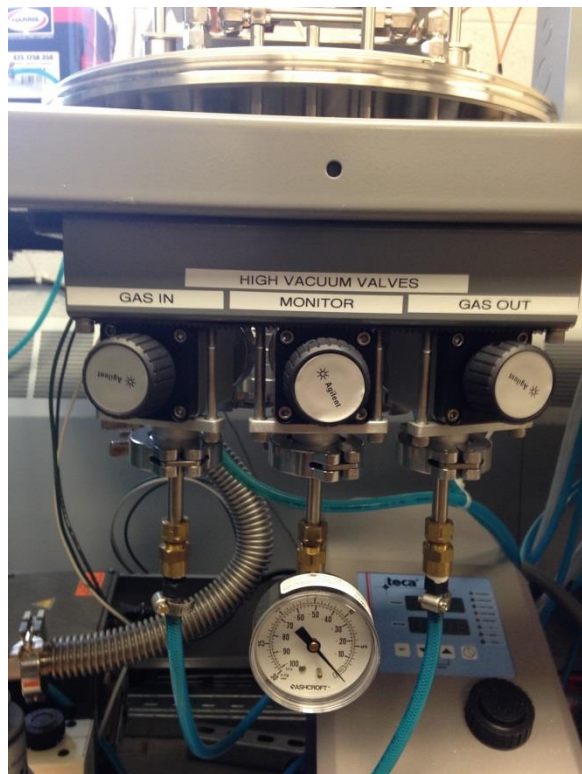


Figure B.6. Blue hoses for gas in and gas out (front bottom) and for coolant water in and out (behind valves) should be inspected for damage such as abrasion or holes.



Figure B.7. The bubbler (arrow), with the hose extending out, should be filled to cover the end of the hose with liquid to prevent air from entering the hose.

1.7 Check the roughing pump. Verify oil is at proper level and is clean. Check for obstructions at inlet and outlet. Note the inlet at the base of the furnace has a screen to catch large debris before it may reach the pump (Figure B.8).

1.8 Check any additional equipment that may be attached or required for the experiment.

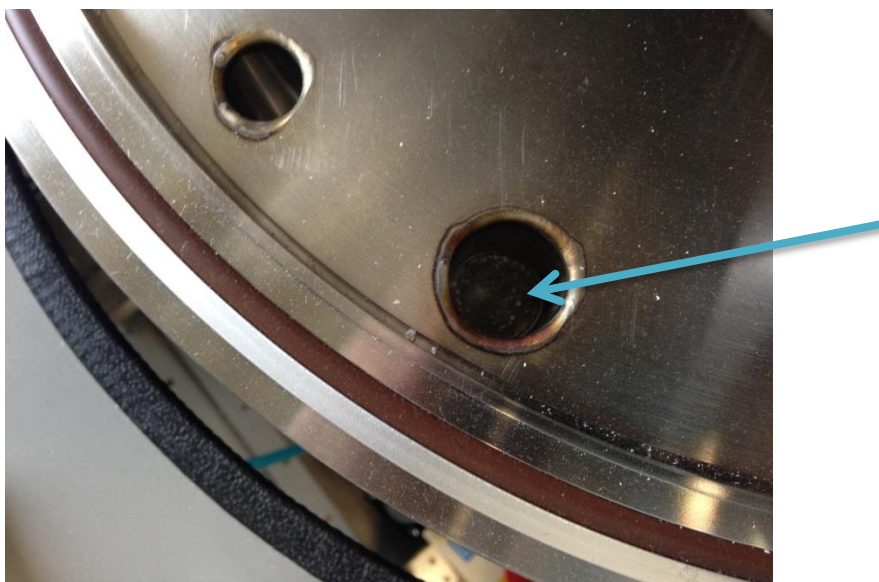


Figure B.8. Debris can be seen on the screen in the feed-through leading to the vacuum pump.

2 Furnace and sample preparation

The sample should be an appropriate specimen for RUS, either parallelepiped or cylinder and with no major chips or flaws. Small chips or flaws may be acceptable. Note the large buffer rods on the RUS transducer will limit the signal available and RUS signal will diminish with increasing temperature, thus a heavier specimen is typically required than for the room temperature setup to ensure sufficient signal. **Specimens have been examined with mass of 0.80 g, however a mass of at least 2 g would improve the signal.** A higher specimen mass will help keep the RUS signal transferring through the buffer rods.

2.1 Measure the specimen mass, dimensions, and determine the thermal expansion for the desired temperature range. The thermal expansion is required to calculate dimension changes for RUS analysis.

2.2 Note any apparent defects on the specimens.

2.3 Verify the RUS transducer rods do not touch the furnace and may be adjusted to the proper angle without hitting the furnace or any other components.



Figure B.9. The three transducers are mounted to copper blocks on the chiller plates underneath the furnace. The mount swivels to allow the angle of the transducer to be adjusted.

2.4 DO NOT MOVE TRANSDUCERS BY THE BUFFER ROD. Adjust the RUS transducers to support the edges of the specimen **by adjusting the angle of the copper mount that holds the base of the transducer.** The mount should allow rotation of the transducer with reasonable hand pressure. If the mount is (a) too difficult to move or (b) does not have sufficient tension to prevent movement, the screw on the swivel mount may be adjusted. Note there is a wave washer to maintain tension on the swivel mount without tightening the screw to fully tight.

2.5 Check for RUS signal. Place the specimen on the transducer and run a RUS scan to check for proper signal. Adjust specimen placement and transducer angle to maximize RUS signal. See RUS guide for setup of the RUS software and specimen placement.

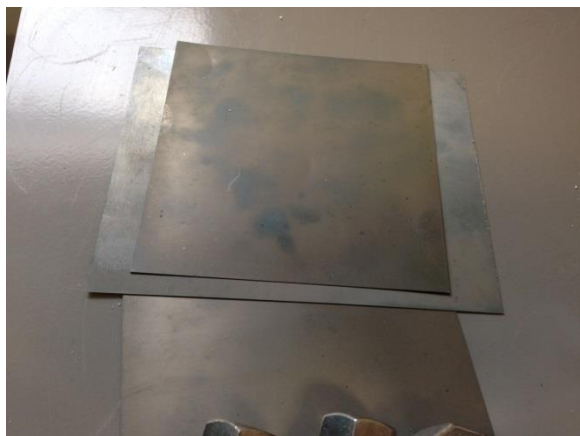


Figure B.10. Molybdenum sheets to be used as baffles.



Figure B.11. Molybdenum baffle being inserted around buffer rods.

2.6 Place molybdenum baffle sheets around the transducers (Figures B.10 and B.11). The specimen may need to be removed during baffle sheet placement. The molybdenum sheets are placed on the second (of three) shelf on the furnace and RUS support, under the insulators that support the heating elements. These should be placed as near as reasonably possible to the RUS transducer rods without touching the transducer rods in order to deflect heat from the furnace before it reaches the transducer base. Verify the RUS signal is maintained.

2.7 Close the front of the furnace with refractories. Fit the front SALI board into position (Figures B.12 and B.13). Fit the front refractory bricks into position (Figures B.14 and B.15). The top of the furnace may need to be slightly lifted to allow the refractories to fit. Verify the RUS signal is maintained.

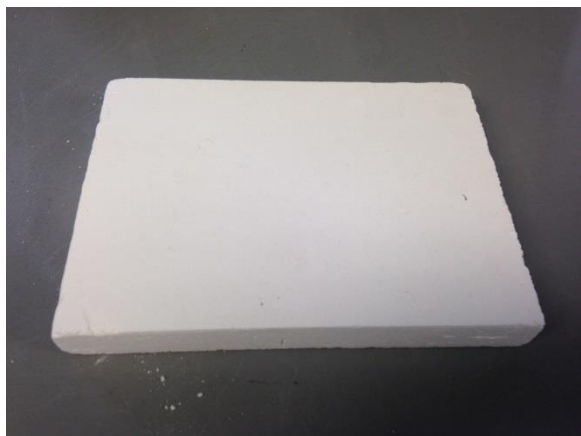


Figure B.12. Front SALI board of inner furnace.

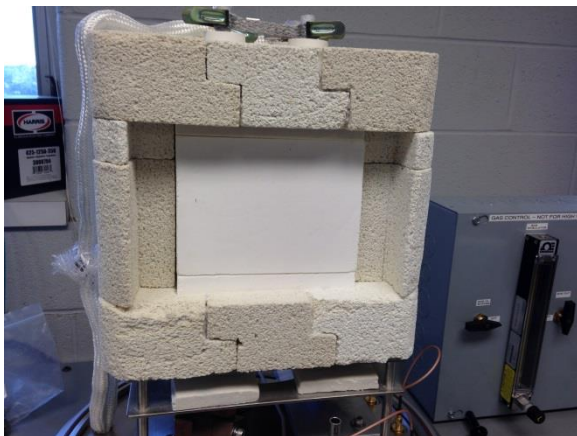


Figure B.13. Front SALI board of inner furnace, inserted into position

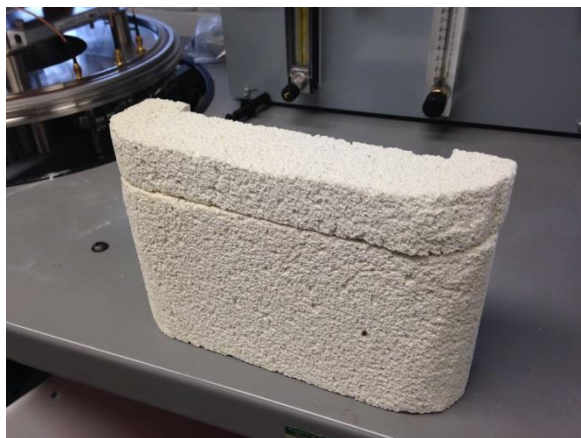


Figure B.14. Front refractory bricks of outer furnace.

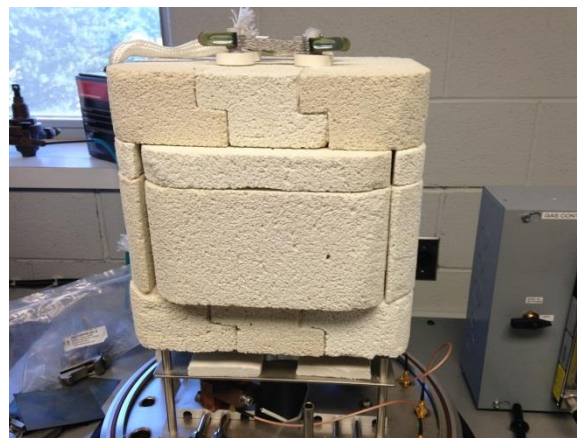


Figure B.15. Front refractory bricks of outer furnace, inserted into position

2.8 DO NOT PLACE HANDS OR BODY UNDER SUSPENDED BELL JAR. Place the bell jar on the furnace. This is a two-person job. Use the hoist to lift the bell jar higher than the furnace, then slide the bell jar into position with the gantry. One person must guide the bell jar by the sides while the second person operates the hoist. Operate the hoist up or down with the remote control wired to the hoist. Guide the bell jar down on the furnace o-ring seal. Bring the hoist down sufficiently that there is some slack in the chain. Verify the RUS signal is maintained.



Figure B.16. Hoist and controls to operate up and down. Note the hoist is mounted to a rail for movement left and right, and that the chain has some slack when the bell jar is in position.

3 Evacuation of furnace

3.1 Clamp the bell jar to the base with the 12 clamps (Figure B.17) and tighten with a wrench.



Figure B.17. Clamps for the bell jar. The same clamps are used to secure the top and base of the bell jar.

3.2 Verify all gas inlet and outlet valves are closed.

There are three high vacuum gas valves mounted to the underside of the table, two of which are for inlet and outlet. Close the gas inlet and outlet to snug against the valve seat. The middle valve is for use with a pressure gauge. This middle valve should be left open. Currently, there is no oxygen monitor on the furnace. If a different configuration of the furnace is used that employs an oxygen monitor, then the valve should be closed.



Figure B.18. High vacuum valves below the furnace. The gas in and gas out valves should be closed before pumping down the bell jar chamber.

3.3 Pump down the bell jar. Turn on the pump and run until the vacuum chamber has been evacuated, typically about 10 minutes. Verify with pressure gauge.

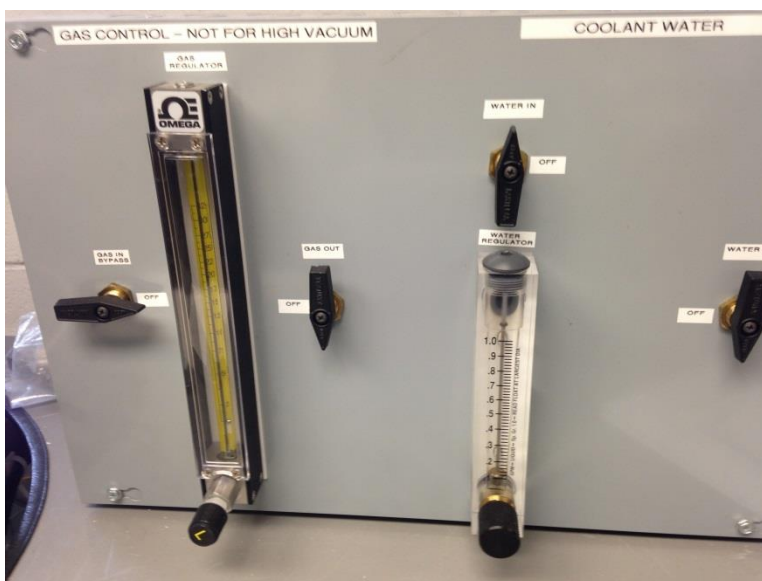


Figure B.19. Flow control panel, with flow controls and bypass for the inert gas in and out of the bell jar and the coolant water from the chiller to the base of the transducers.

3.4 Backfill the bell jar with inert gas. Open the cylinder valve for the compressed gas cylinder containing inert gas and verify the pressure reading on the regulator is less than 100 psi. Verify the gas in bypass valve, located on the flow control panel to the right of the furnace, is closed. Open the high vacuum inlet valve below the furnace. If desired, the chamber may be refilled by opening the refill bypass valve, being careful to avoid disturbing the RUS specimen by the gas. Backfill with inert gas until the chamber is at atmospheric pressure. Verify the RUS signal is maintained.

3.5 Repeat steps 3.3 and 3.4 until at least three inert gas purges of the furnace chamber have been performed.

4 Operation of furnace

4.1 Turn on chiller. On the chiller unit, set to appropriate temperature (typically 20°C) and flow (typically 0.5 gal/min).

4.2 Set gas flow. Fill bell jar with gas to slightly above atmospheric pressure to prevent back flow. Open the high vacuum valve below the furnace for outlet gas to the bubbler. Open the gas out valve on the flow control panel. Verify bubble flow through the bubbler. Adjust inlet gas flow control to desired gas flow.

4.3 Set monitor. If an oxygen monitor is attached, open valve to monitor and set oxygen monitor for operation according to manufacturer instructions. (No oxygen monitor is currently attached).

4.4 Set temperature limit controllers. Both temperature controllers are Omega CN3101 series controllers with temperature limits that may be set with the arrow keys. If the controller is tripped, the controller may be reset with the RESET button. The furnace temperature limit controller is typically set to 25° to 50° above the maximum temperature for the experiment. The transducer temperature limit controller is typically set to 80°C. Do not allow the transducers to exceed 80°C to avoid irreparable damage to the transducers or cabling.



Figure B.20. From left, the furnace over temperature limit controller, furnace temperature controller, and the transducer over temperature limit controller.



Figure B.21. Furnace temperature controller, from left, in run mode, selecting set point 1, and setting set point 1 to 60°C.



Figure B.22. 208 VAC power switch with red indicator light on, and 110 VAC power switch with green indicator on.

4.5 Set first desired temperature. Set the furnace temperature controller for the desired first temperature. Use the scroll key on the controller to change to set point 1, use the enter key to select, then use the arrows to choose the desired temperature and enter the selected temperature with the enter key. Use the scroll key to return to run mode. Turn the variac all the way to the left. Turn on the 208/240VAC supply for the heating elements. Increase the variac up to a maximum of 60 V. Verify the amperage on the ammeter to the heating elements is less than 20 A. If the heating rate is insufficient, the variac may be increased up to a maximum of 20 A current. The voltage may be increased up to 120 V for older heating elements until a maximum of 20 A of current. If a higher voltage is required, the heating elements must be replaced (see section 6). Note two set points may be set on the controller at a time, although set point 1 (SP1) is set up to run currently.

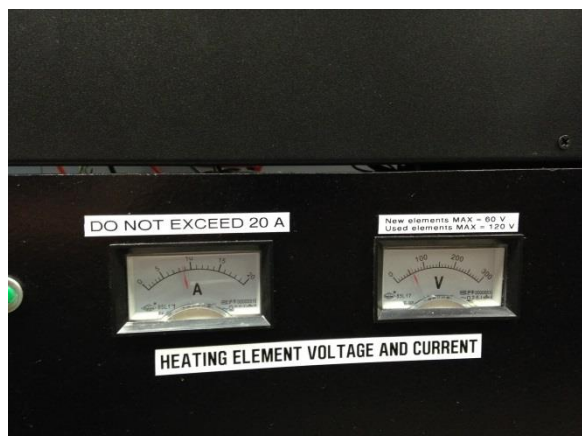


Figure B.23. Ammeter and voltmeter for heaters. Resistance decreases with temperature, and the current should be monitored to not exceed 20 A. Operate heater elements at less than 60 V for new elements, less than 120 V for elements that have aged due to use.



Figure B.24. Heater ammeter, heater voltmeter, and variac output knob on control box.

4.6 Hold at desired temperature. Allow the specimen to soak at the desired temperature until it is uniformly heated, typically 5 minutes soak. Run a RUS scan. Record the settings and time. Do not hold at high temperatures for excessively long time to avoid heating the top of the bell jar excessively.

4.7 Set next desired temperature. Set the temperature controller for the desired next temperature. Verify the amperage to the heaters does not exceed 20 A. Note the resistance of the heating elements changes with temperature so that as the furnace temperature changes, the current through the heating elements changes even when the voltage is fixed.

4.8 Repeat steps 4.6 and 4.7 until RUS scans are gathered for all desired temperatures.

4.9 Turn off 208/240 VAC power to heating elements. Allow furnace to cool below 50°C. Turn off oxygen monitor, if applicable. Turn off gas at regulator. The gas out valve should remain open to allow for excess pressure to escape. Note that the gas will initially have some pressure to continue a flow through the bubbler unit, but as the furnace cools the pressure

inside the furnace will drop which could cause the water from the bubbler to be drawn back into the furnace. There is excess hose to reduce the chance of water from the bubbler reaching the furnace, but monitor the bubbler to verify no water reaches the furnace.

5 Opening of furnace

5.1 Turn off chiller and turn off power to the temperature controllers. To prevent a buildup of condensation on the transducers once the furnace is open, the chiller should be turned off just before opening the chamber. To eliminate the chance of electrical energy in the chamber, turn off power to the temperature controllers.



Figure B.25. Bell jar at rest on side table and furnace opened. There should be some slack in the chain, allowing all the weight of the bell jar to rest on the table.

5.2 Open chamber. When the bell jar is cooled sufficiently to safely handle, detach the clamps from the bottom of the bell jar with care. Even with the outlet open, there may be a small amount of pressure in the chamber. With one person to guide the bell jar, raise the hoist to lift the bell jar above the top of the furnace. Slide the bell jar to the side table and lower onto the table.

5.3 Verify the furnace is cool, then open the furnace. With gloves, remove the front refractory bricks on the furnace and the front SALI inner furnace board.

5.4 Measure the specimen mass and dimensions.

5.5 Note any apparent defects on the specimens.

5.6 Verify all furnace equipment is properly turned off and stowed.

6 Replacement of service parts

6.1 Replacement of RUS transducer. If the RUS transducer is no longer providing a proper signal, it may require replacement. Turn all power off. Disconnect the cable from the transducer. Move molybdenum baffle sheets away from the transducer to allow the transducer to be removed. Remove the transducer from the copper mounting block by loosening the clamp screw on the swivel mount, then carefully lift the transducer out of the mounting block. Remove the cold cap from the transducer (Figure B.26). Apply Apeizon or equivalent low VOC vacuum grease to transducer near the top of the brass body to allow heat transfer between the body and the cold cap. Apply a thin layer of grease to the base of the cold cap to allow heat transfer between the cold cap and the swivel mount. Insert the replacement transducer into furnace through the furnace chamber and seat into the swivel mount. Tighten the swivel mount screw. Reconnect the transducer cable.

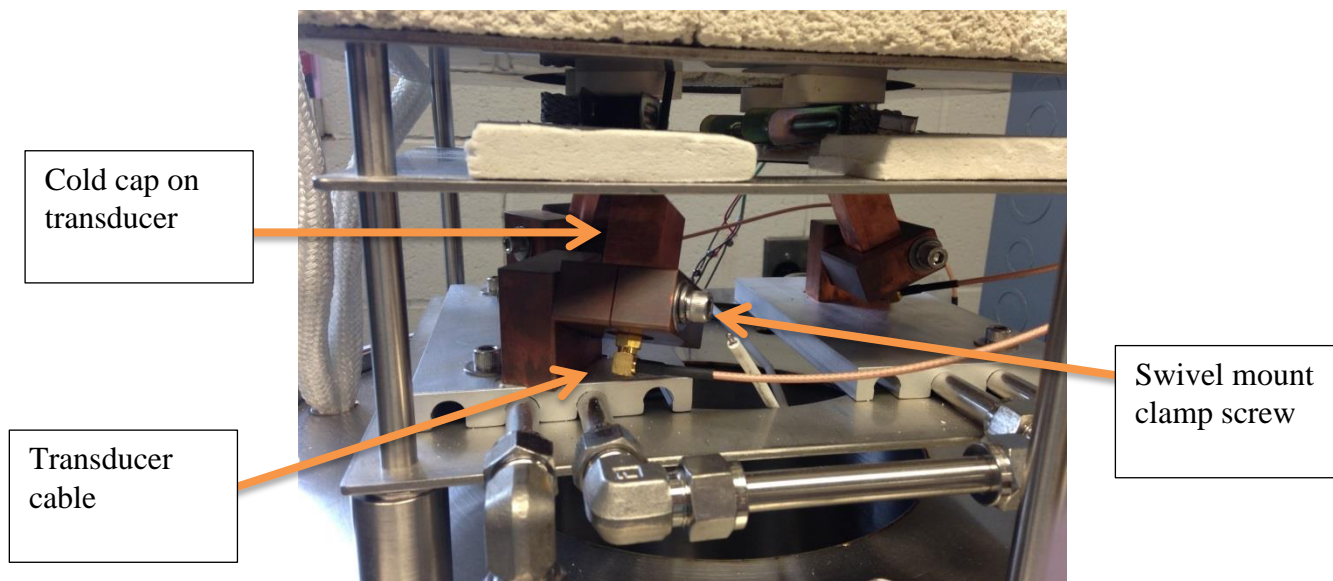


Figure B.26. RUS transducer mount components.

6.2 Replacement of heating elements. The heating elements should be changed only as a full set, as the resistance of the elements changes as they are used. Do not replace individual heating elements. Disconnect the clamps and the flat braided cables from the four heating elements. Lift the heating elements out of the furnace. Replace with new heating elements. Reconnect the flat braided cable and clamps to the new heating elements. The elements should be wired together in series, supported on the base by an insulating material, and the hot zone should be completely within the inner furnace.



Figure B.27. The spiral cut hot zone of the heating elements should be completely contained within the furnace. The power connections to the heating elements should be outside the furnace.

6.3 Replacement of furnace thermocouples. The furnace thermocouples are bare wire type R platinum thermocouples and should only be handled with gloves. Disconnect the old thermocouple from the terminal strip and remove. Thread the new thermocouple through the holes, noting which is the positive and which is the negative side. Connect to the appropriate terminal and trim the excess wire.

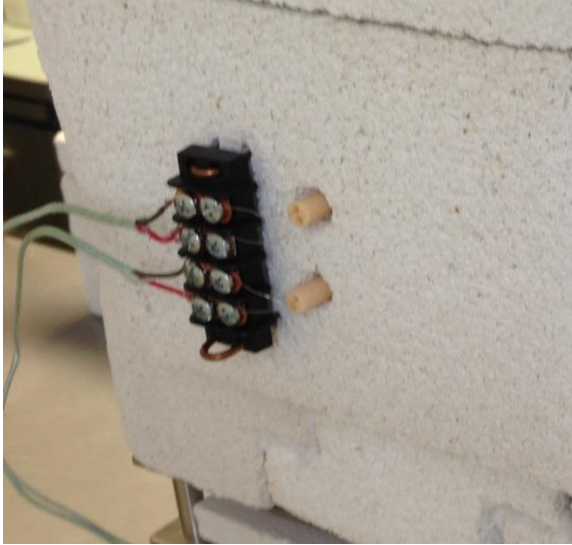


Figure B.28. Terminal strip on back of furnace for R-type thermocouples, with thermocouple wires extending into the furnace.

Isometric drawing of a gantry system with numbered callouts 1 through 6. Callout 1 points to the top horizontal beam, 2 to the vertical support beam, 3 to the base frame, 4 to the motor unit, 5 to the pulley system, and 6 to the cable. The drawing shows a gantry with a motor, pulley, and cable assembly.

303

Item Number	File Name (no extension)	Author	Quantity
1	Gantry	case353leb	1
2	Full Assy	case353leb	1
3	Diff Pump	case353leb	1
4	Chiller	case353leb	1
5	RUS Temp Controller	case353leb	1
6	RUS Computer	case353leb	1

Figure C.2. Gantry and full assembly BOM

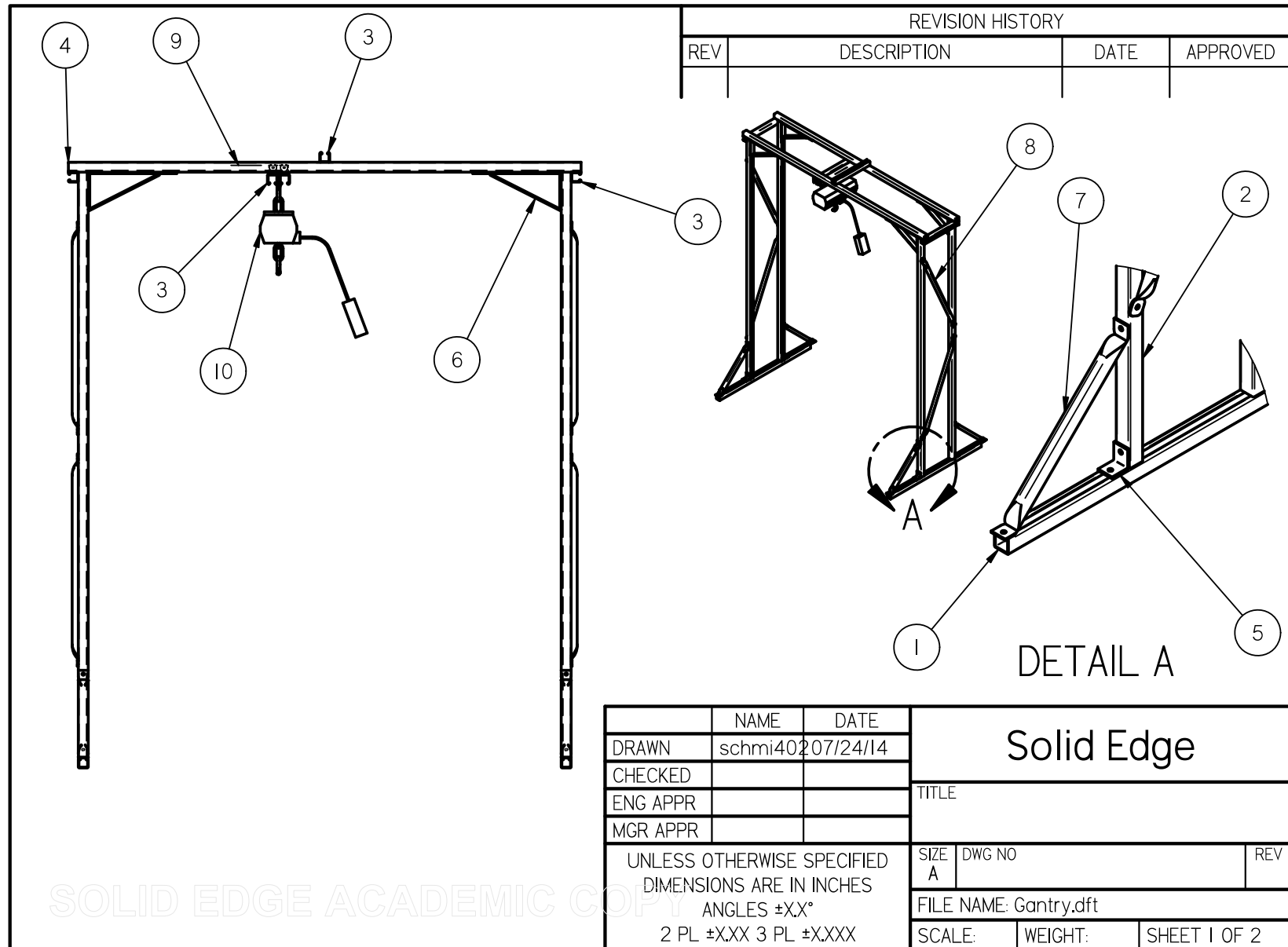


Figure C.3. Gantry.

Item Number	File Name (no extension)	Author	Quantity
1	Unistrut PI000 x 42	case353leb	2
2	Unistrut PI000 x 96	case353leb	4
3	Unistrut PI000 x 16	case353leb	5
4	Unistrut PI000 x 84	case353leb	2
5	Unistrut I026	case353leb	4
6	Unistrut I775	case353leb	4
7	Unistrut 2458-18	case353leb	4
8	Unistrut 2459-36	case353leb	4
9	Unistrut 2750	case353leb	2
10	Dayton 4GU70	case353leb	1

Figure C.4. Gantry BOM.

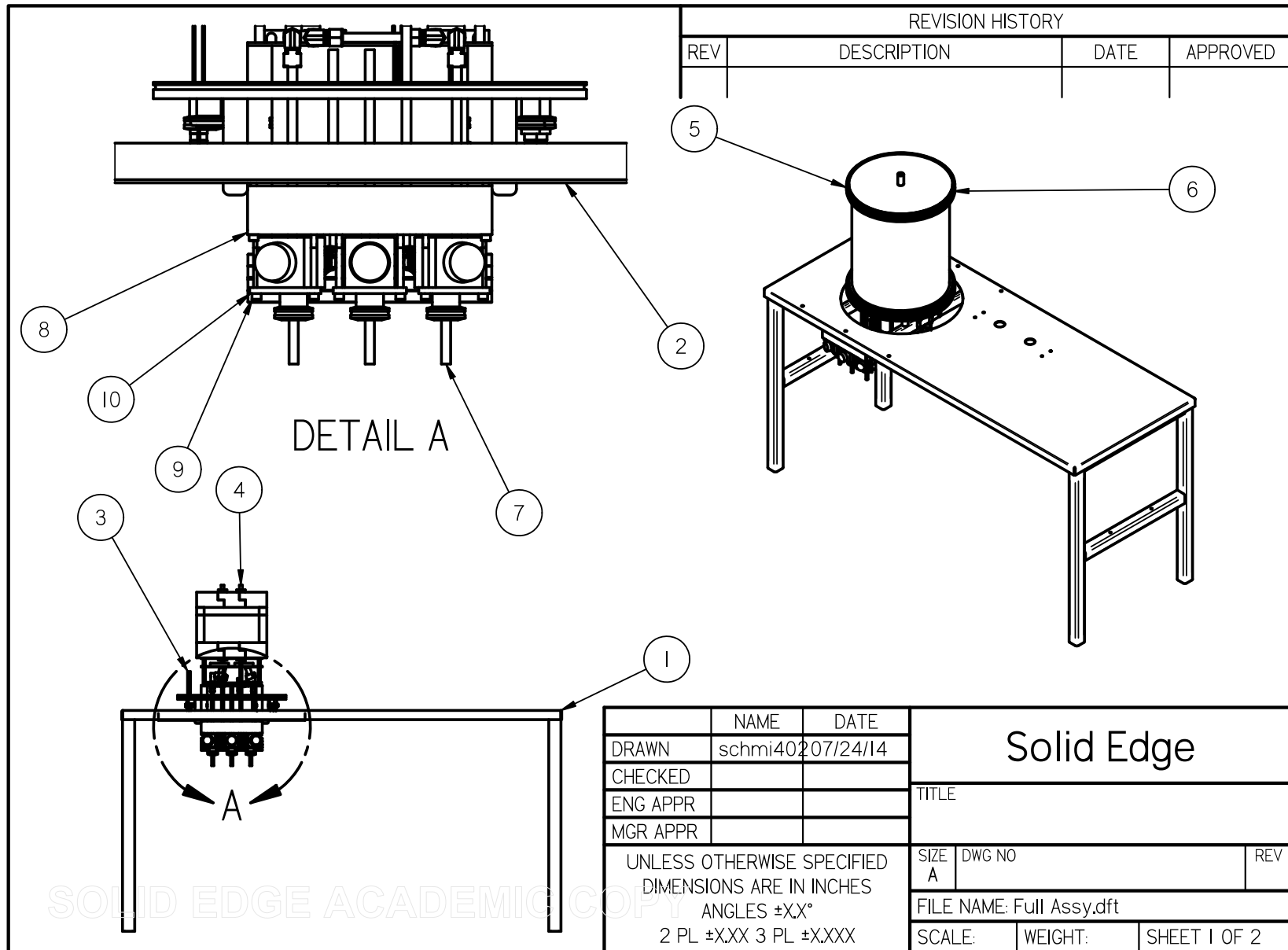


Figure C.5. Full assembly.

Item Number	File Name (no extension)	Author	Quantity
1	Table	case353leb	1
2	BaseMountWDMT	case353leb	1
3	BellJarBaseASSY	case353leb	1
4	RUS and Furnace	case353leb	1
5	BellJarSide	case353leb	1
6	BellJarTop	case353leb	1
7	Valve assy	Robert	3
8	Vlv Mt	case353leb	1
9	0.25-20x3.00 SHCS	case353leb	8
10	Bar Clamp	case353leb	3

Figure C.6. Full assembly BOM.

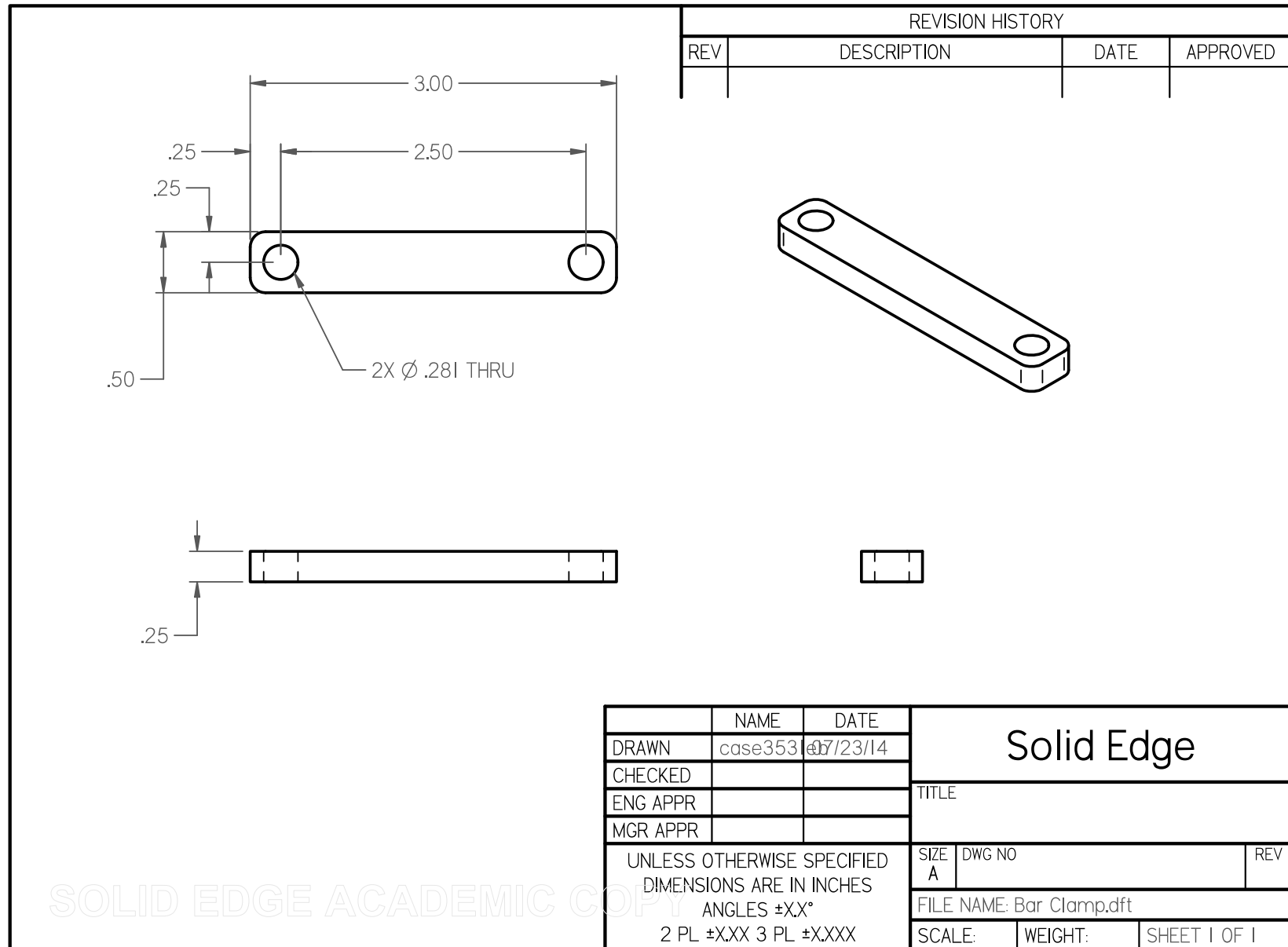


Figure C.7. Bar clamp.

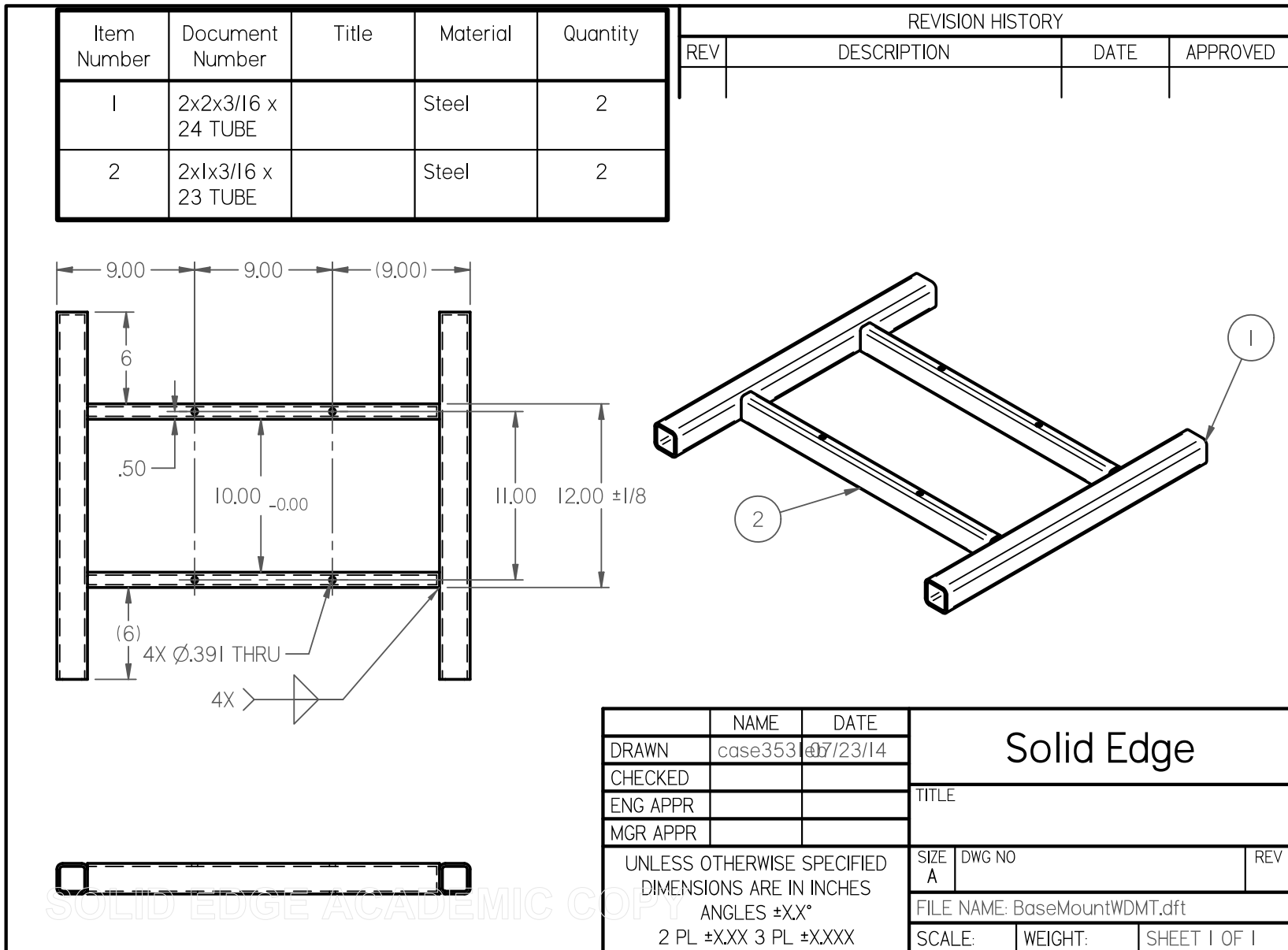


Figure C.8. Base mount weldment.

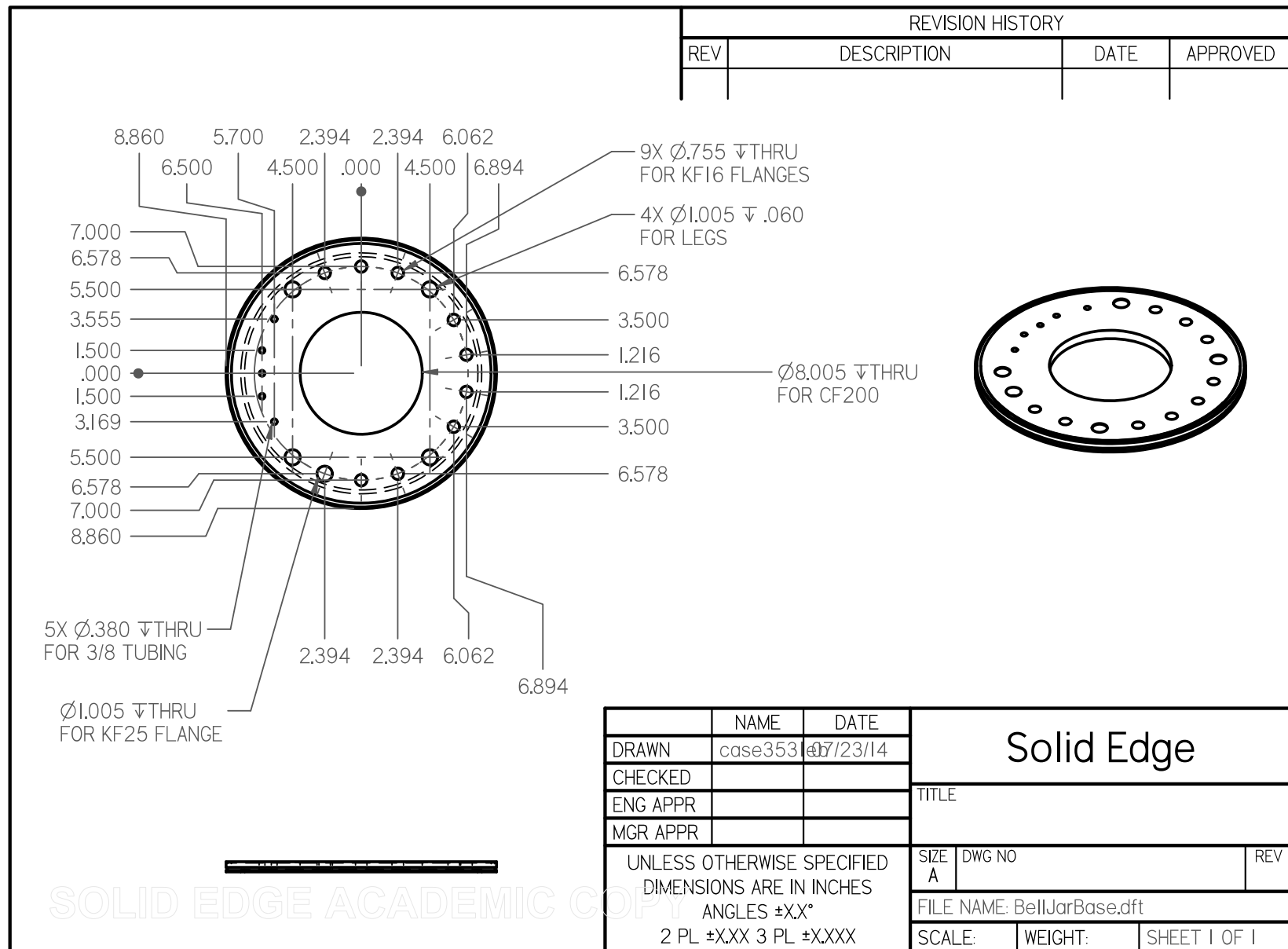


Figure C.9. Bell jar base.

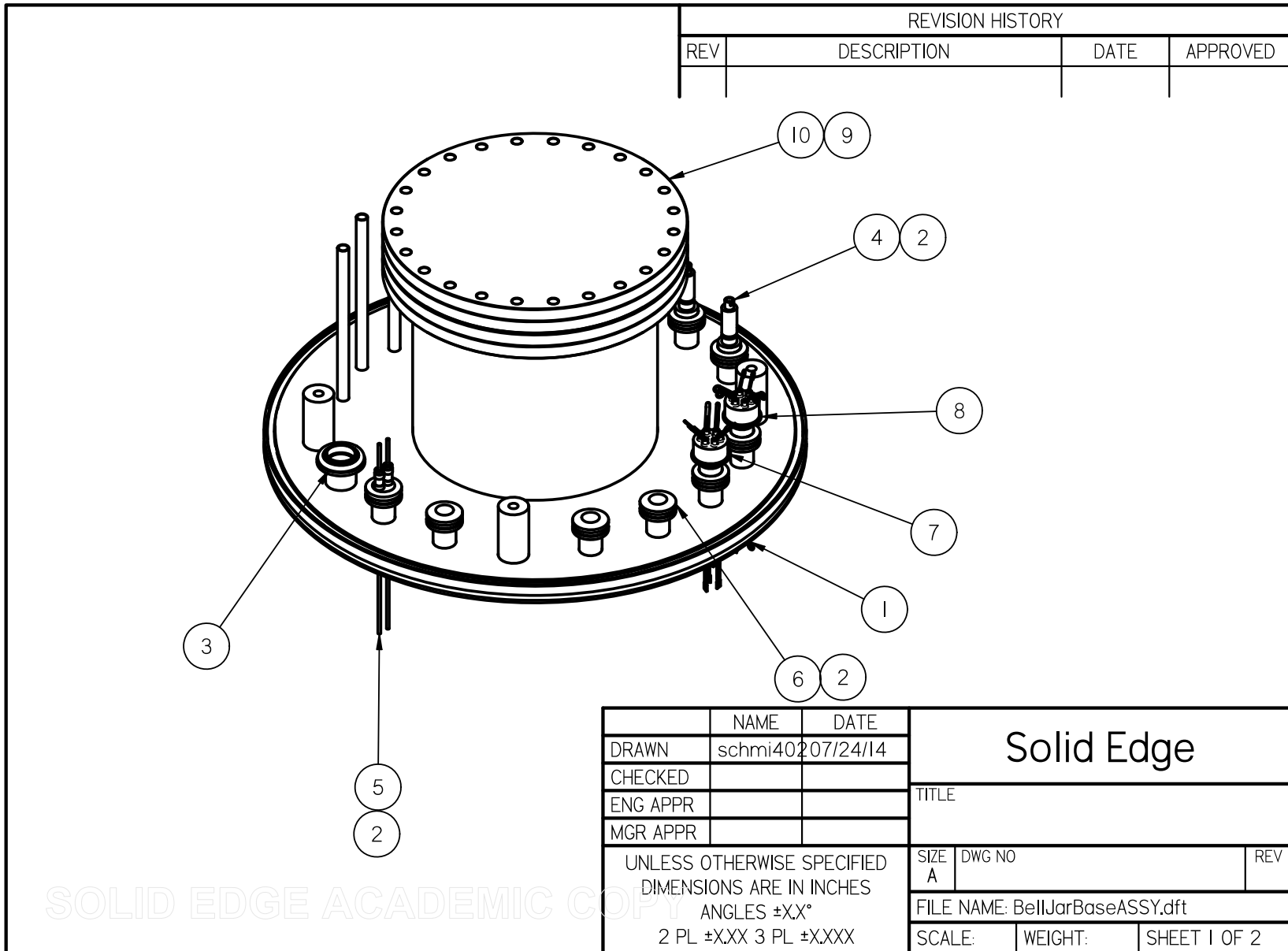


Figure C.10. Bell jar base assembly.

Item Number	File Name (no extension)	Author	Quantity
1	BellJarBaseWDMT	case353leb	1
2	QF16-075-ARB	case353leb	9
3	QF25-100-SRV	case353leb	1
4	IFDBG012038	case353leb	3
5	EFT0523098	case353leb	1
6	QF16-075-SB	case353leb	3
7	tft3ky00008	schmi402	1
8	tft3rn00008	schmi402	1
9*	ga-1000	schmi402	1
10	f1000x000n	schmi402	1

SOLID EDGE ACADEMIC COPY
Figure C.11. Bell jar base assembly BOM.

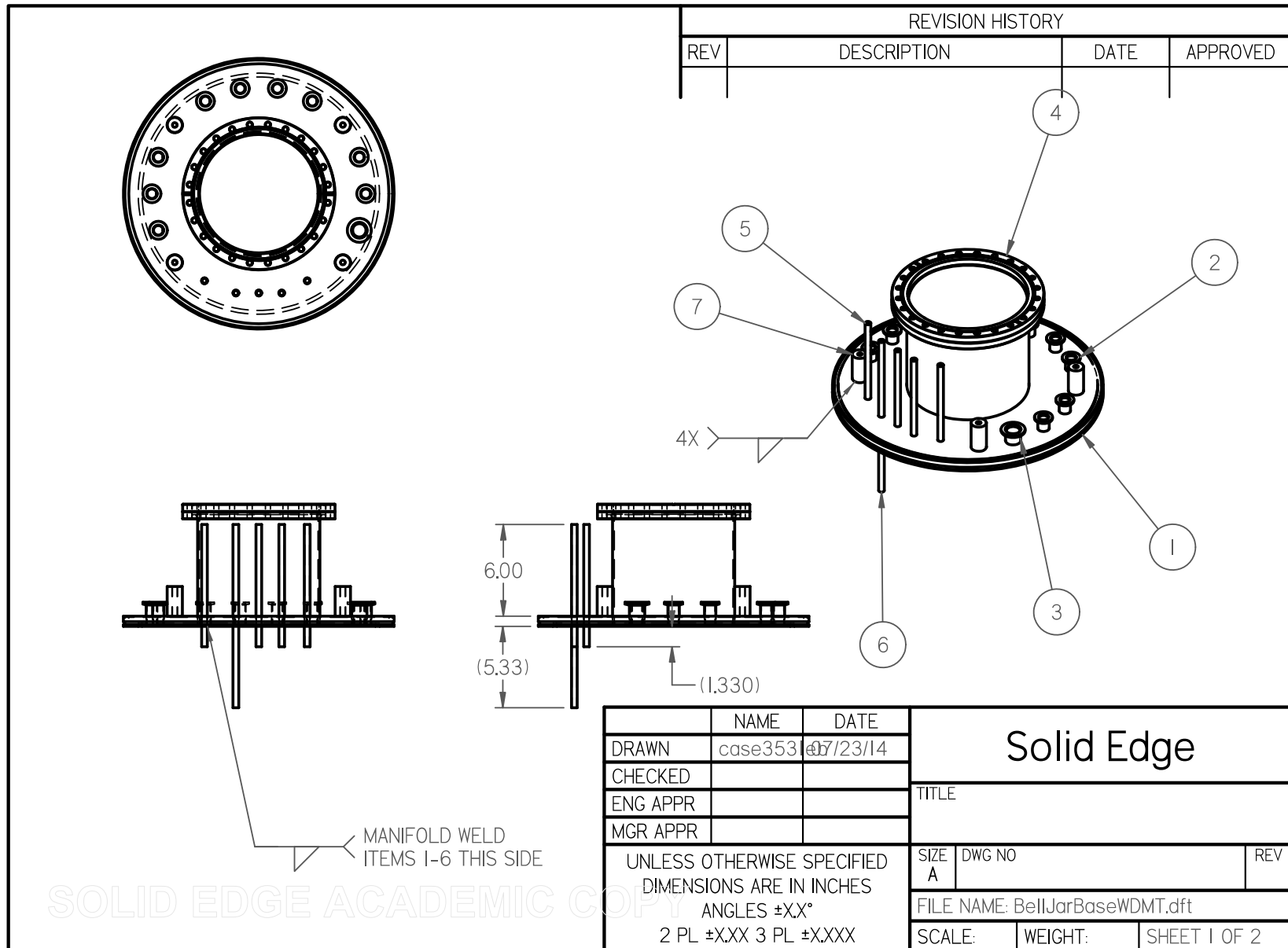


Figure C.12. Bell jar base weldment.

BOM
BellJarBaseWDMT

Item Number	Document Number	Title	Material	Quantity
1	BellJarBase		Stainless Steel, 316	1
2	QF16-075-LF		Stainless Steel, 316	9
3	QF25-100-LF		Stainless Steel, 316	1
4	HN-1000R		Stainless Steel, 316	1
5	TUBE0.38X0.028 x8.00		Stainless Steel, 316	4
6	TUBE0.38X0.028 x12.00		Stainless Steel, 316	1
7	Standoff		Stainless Steel, 316	4

Figure C.13. Bell jar base weldment BOM.

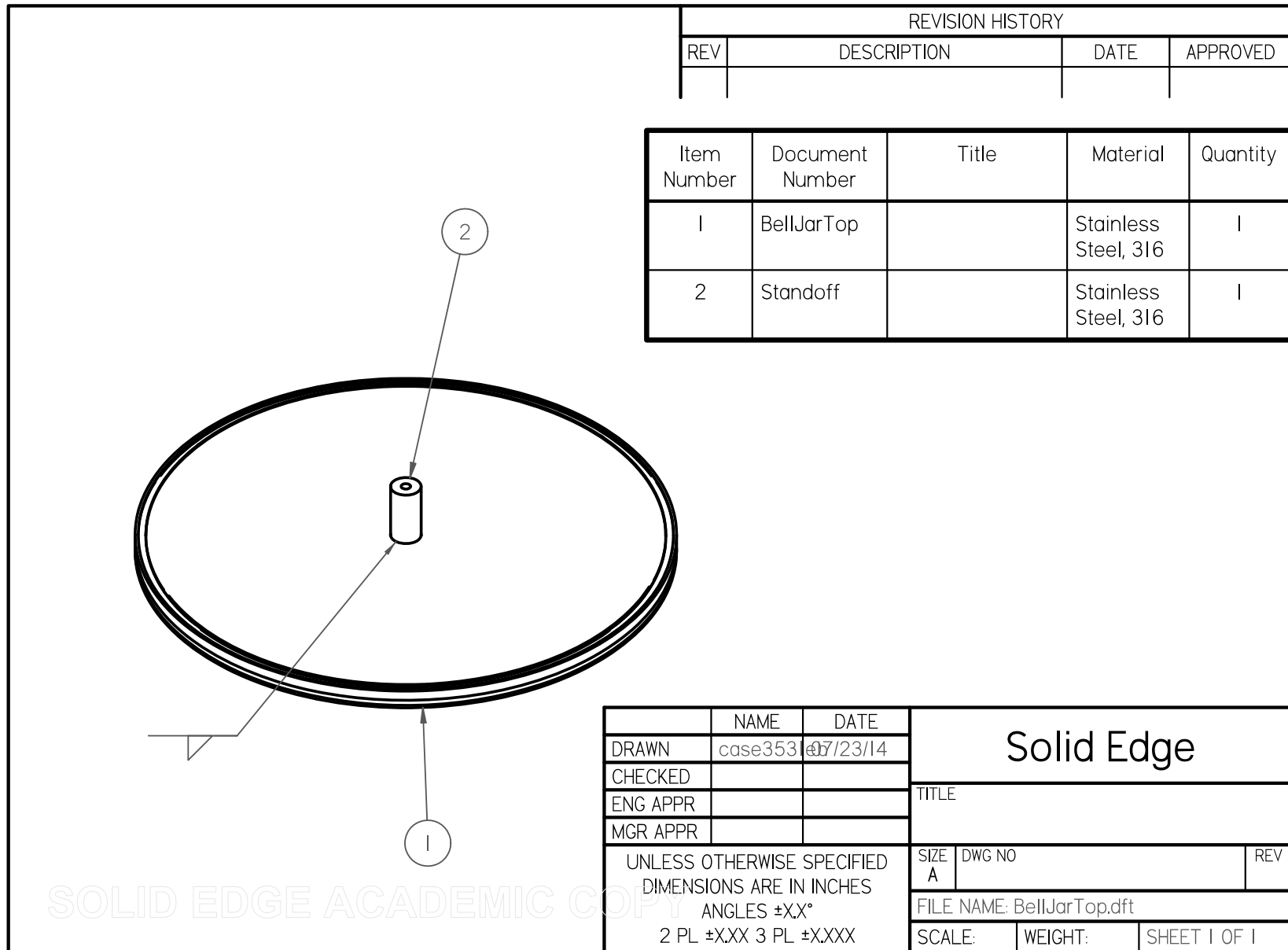


Figure C.14. Bell jar top.

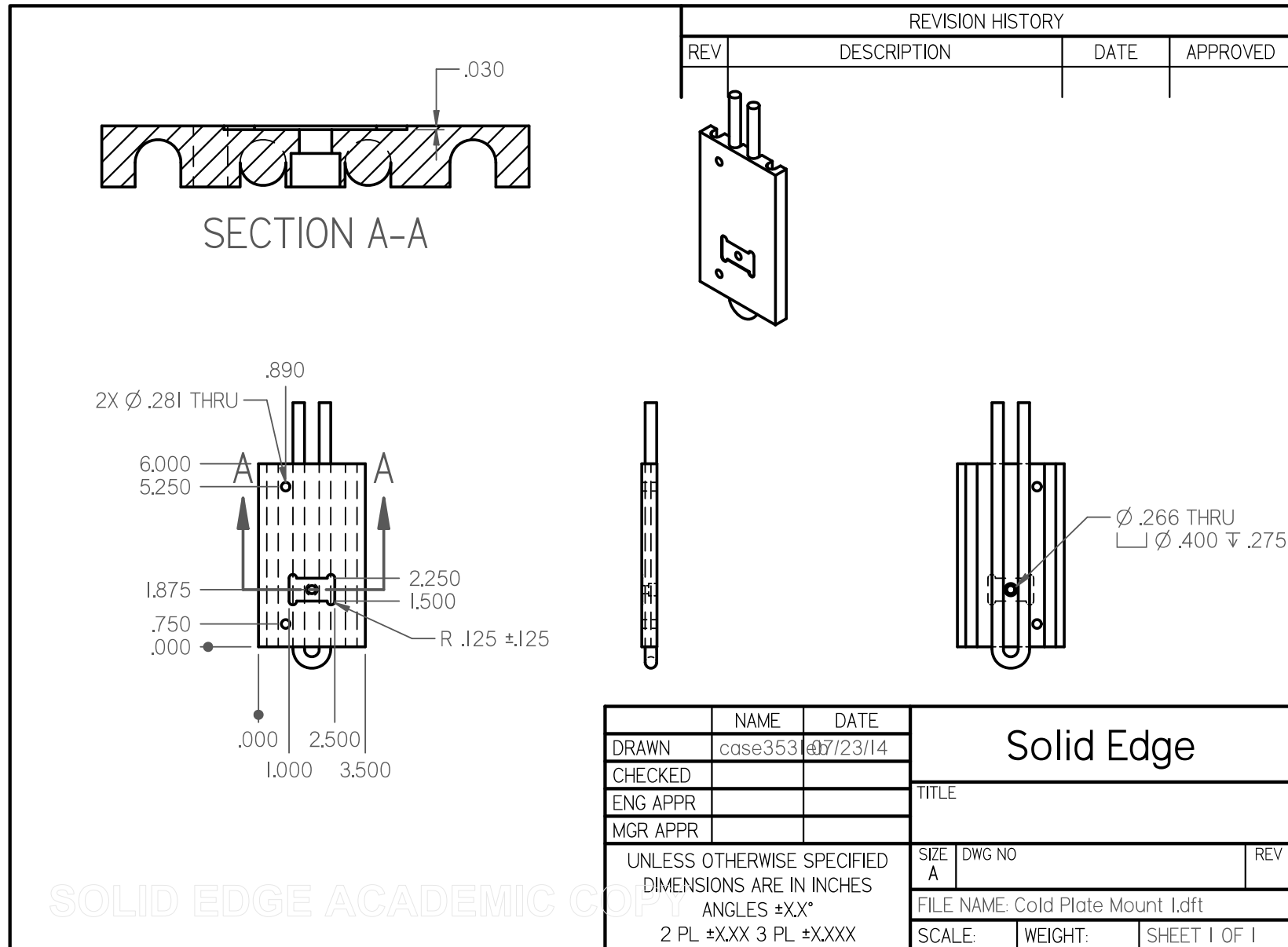


Figure C.15. Cold plate mount 1.

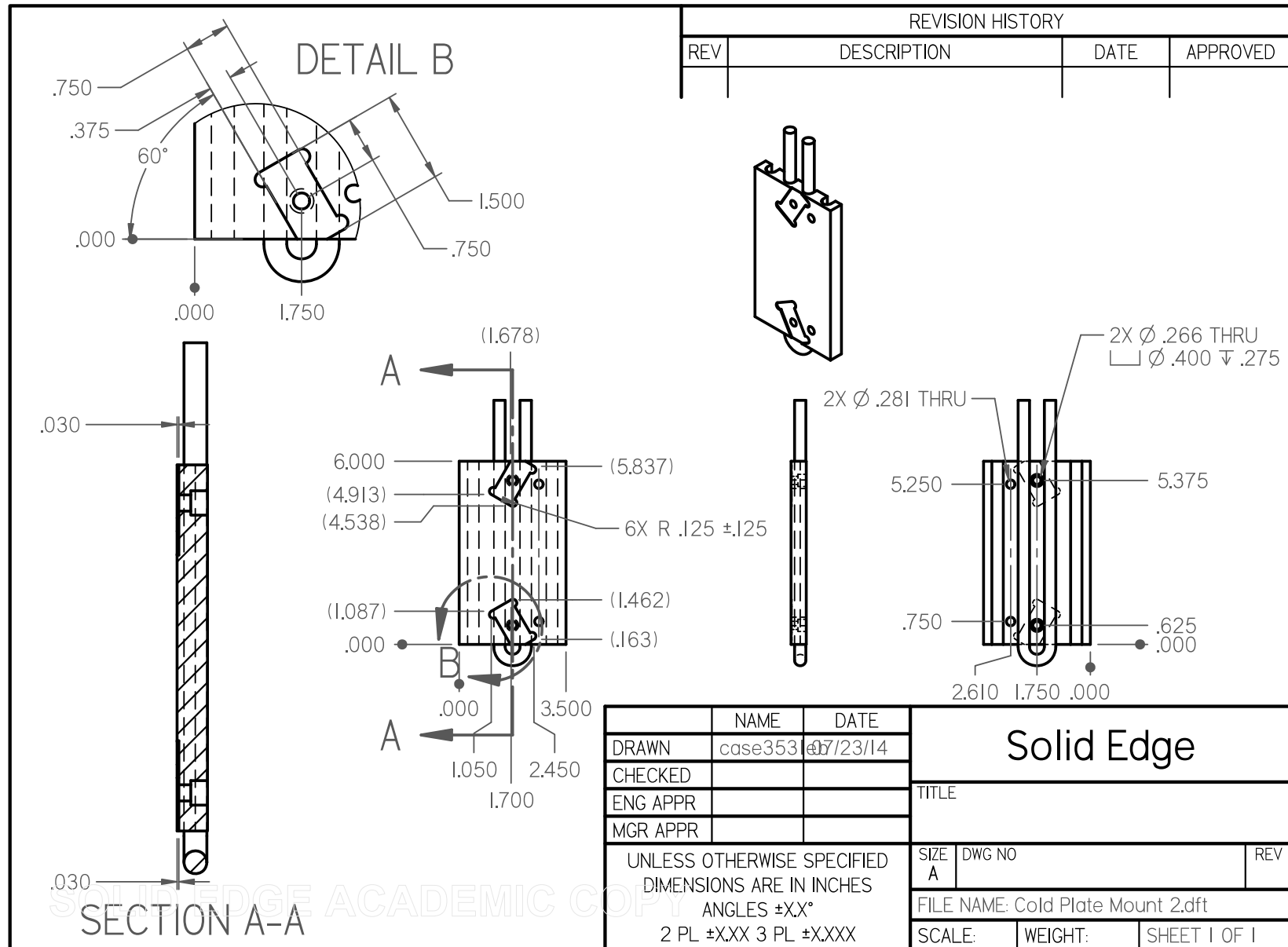
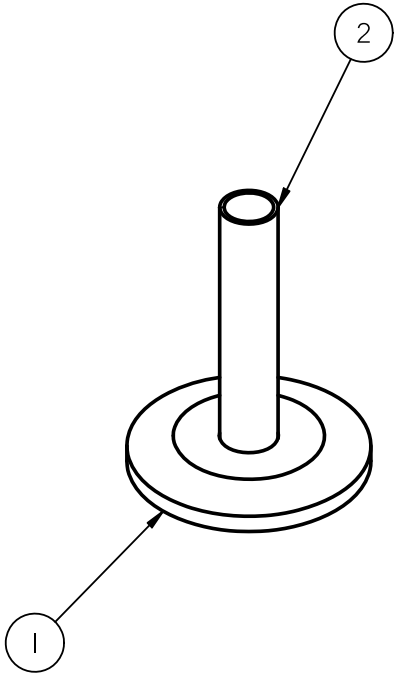


Figure C.16. Cold plate mount 2.

REVISION HISTORY			
REV	DESCRIPTION	DATE	APPROVED



Item Number	File Name (no extension)	Author	Quantity
1	QF25-037-SBB	Robert	1
2	038x0028x02tube	Robert	1

	NAME	DATE	Solid Edge									
DRAWN	schmi402	07/24/14										
CHECKED												
ENG APPR												
MGR APPR												
UNLESS OTHERWISE SPECIFIED DIMENSIONS ARE IN INCHES ANGLES ±X.X° 2 PL ±X.XX 3 PL ±X.XXX			<table border="1" style="width: 100%; border-collapse: collapse;"> <tr> <td style="width: 10%;">SIZE A</td> <td style="width: 60%;">DWG NO</td> <td style="width: 30%;">REV</td> </tr> <tr> <td colspan="3">FILE NAME: Flange Tube.dft</td> </tr> <tr> <td>SCALE:</td> <td>WEIGHT:</td> <td>SHEET 1 OF 1</td> </tr> </table>	SIZE A	DWG NO	REV	FILE NAME: Flange Tube.dft			SCALE:	WEIGHT:	SHEET 1 OF 1
SIZE A	DWG NO	REV										
FILE NAME: Flange Tube.dft												
SCALE:	WEIGHT:	SHEET 1 OF 1										

Figure C.17. Flange tube.

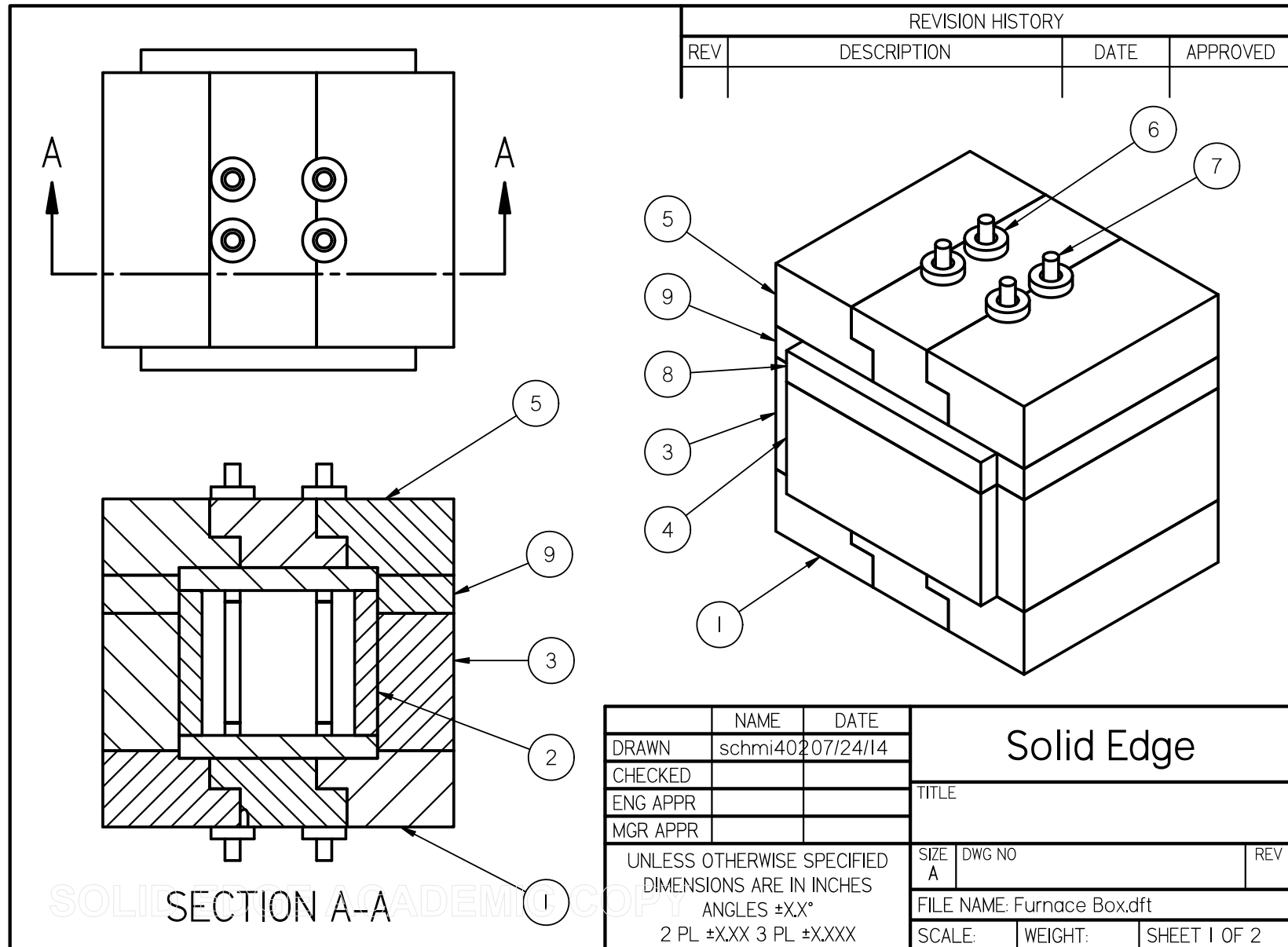


Figure C.18. Furnace box.

Item Number	File Name (no extension)	Author	Quantity
1	Outer Furnace Base	case353leb	1
2	Inner Furnace	case353leb	1
3	Outer Furnace Side	case353leb	2
4	Outer Furnace Front	case353leb	2
5	Outer Furnace Top	case353leb	1
6	Globar lead-in sleeve	case353leb	8
7	Globar Element SG 100mmHZx330mm	case353leb	4
8	Outer Furnace Front 2	case353leb	2
9	Outer Furnace Side 2	case353leb	2

SOLID EDGE ACADEMIC COPY
Figure C.19. Furnace box BOM.

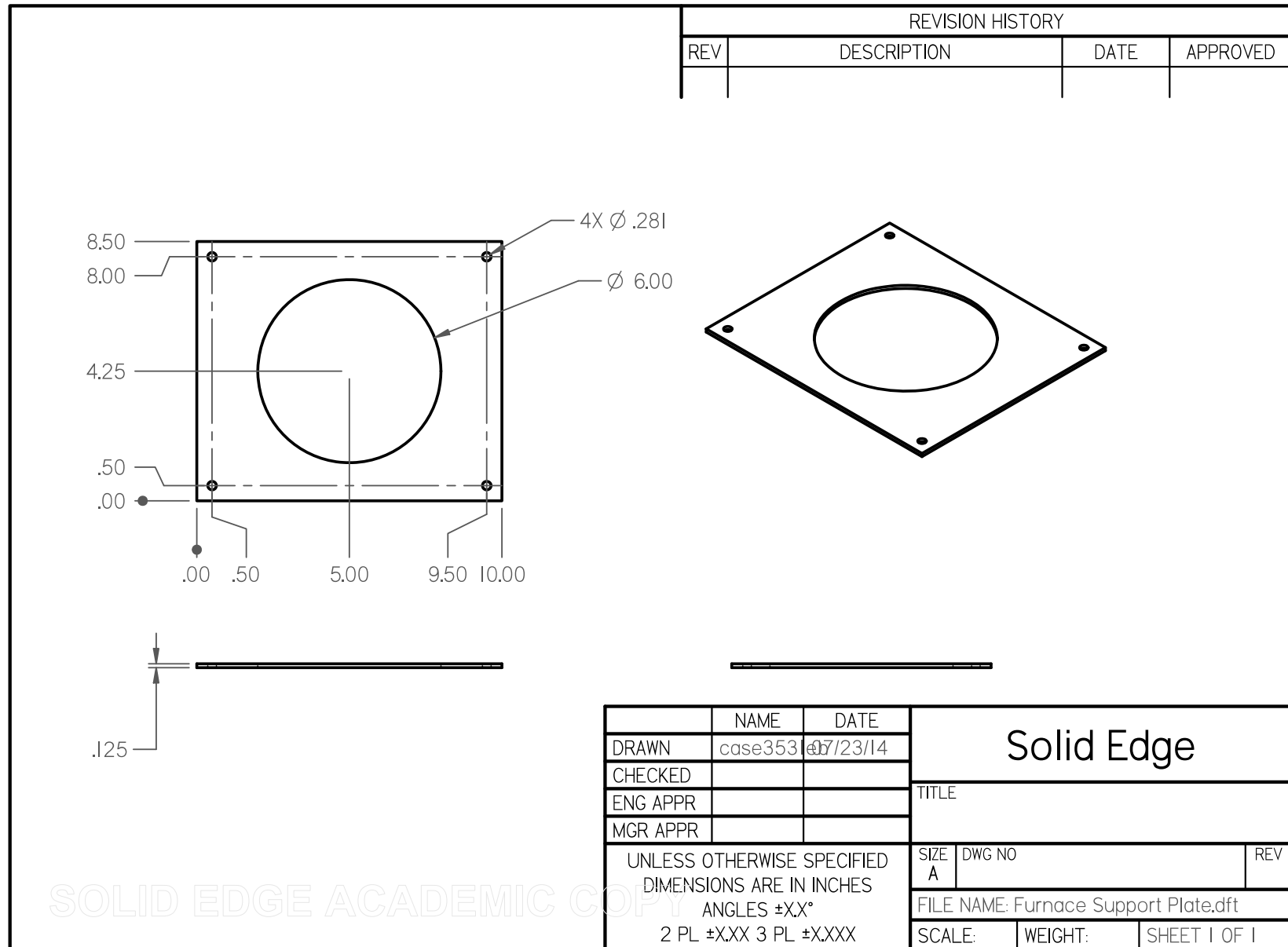


Figure C.20. Furnace support plate.

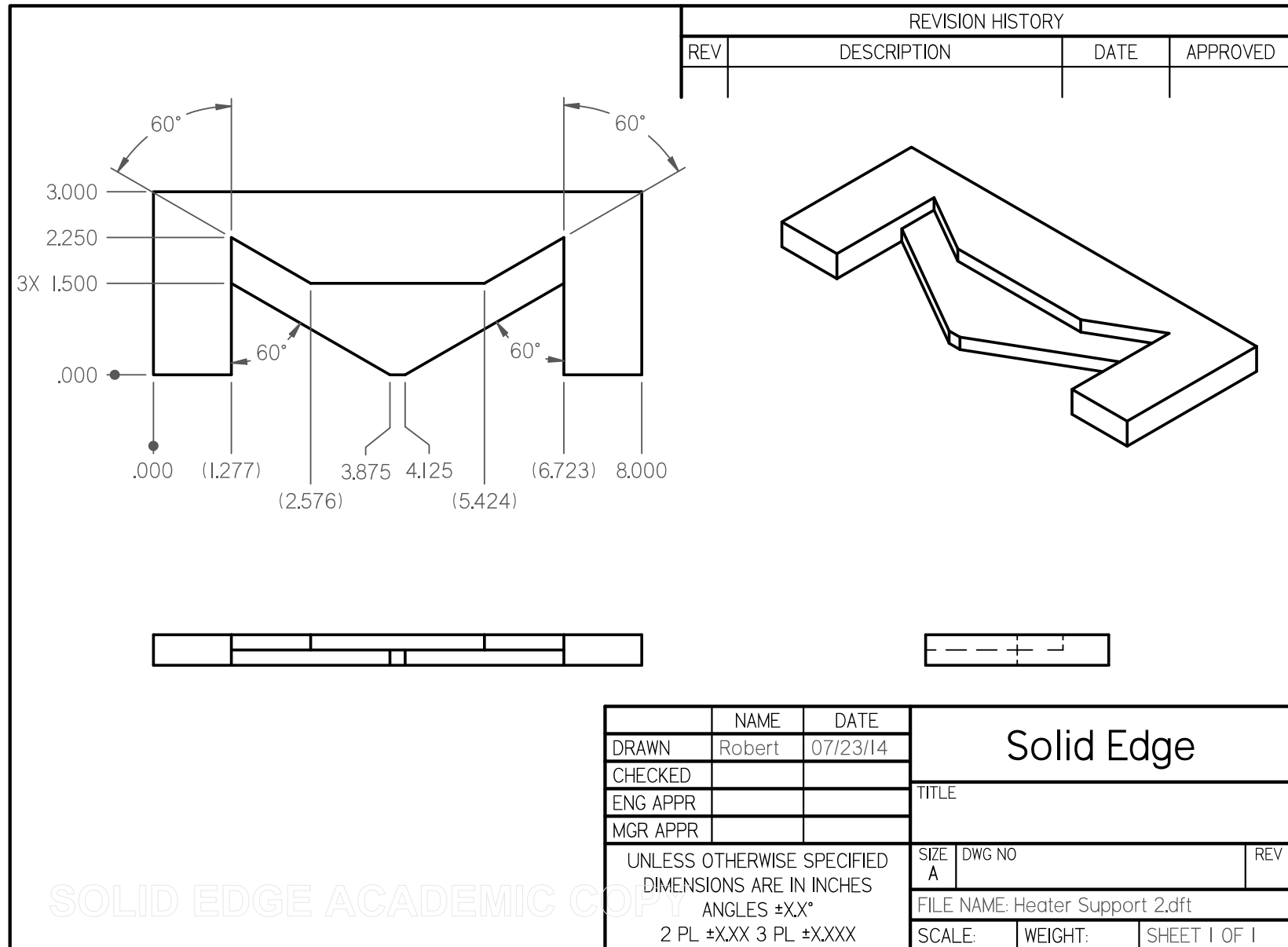


Figure C.21. Heater support 2.

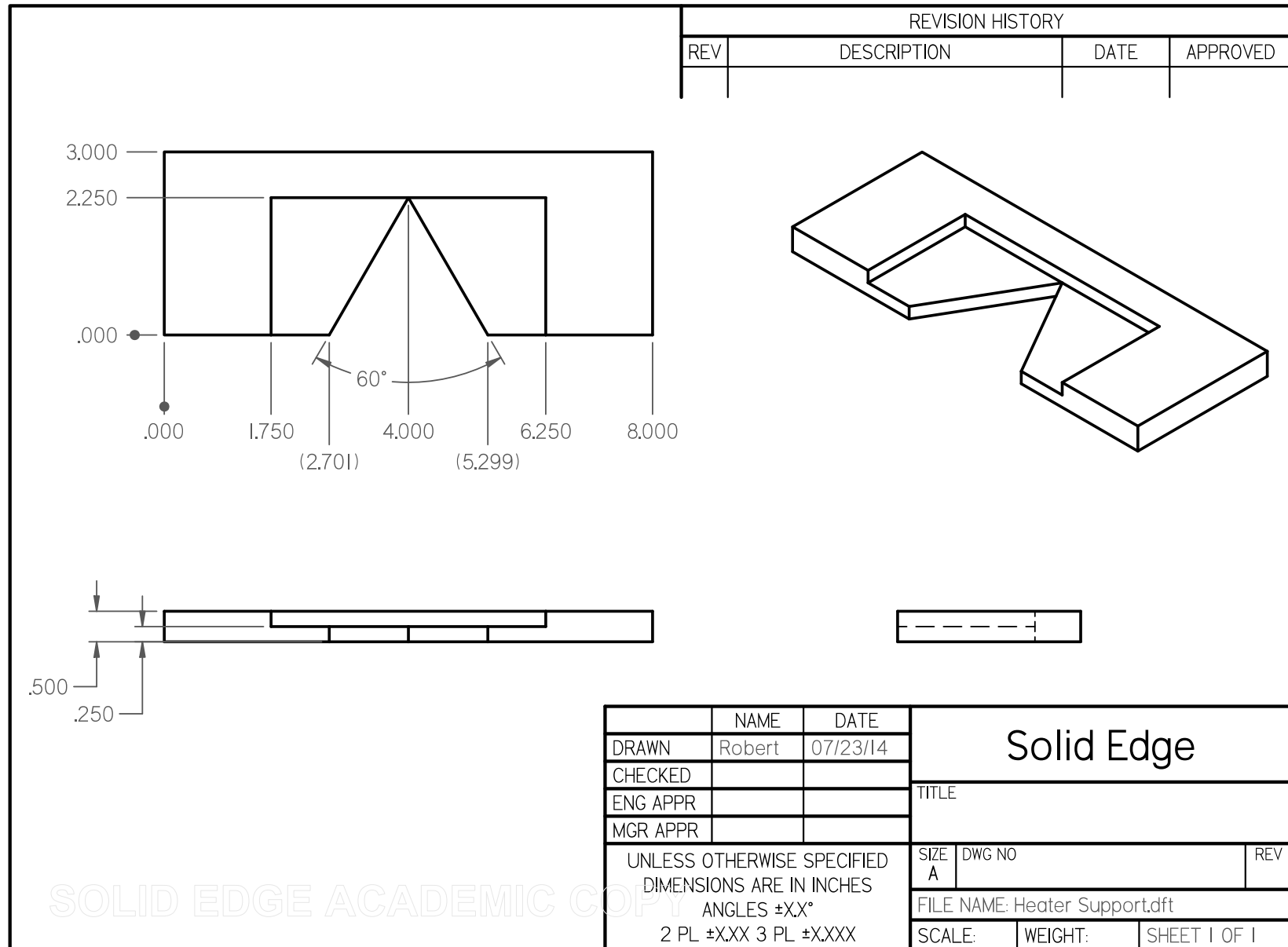


Figure C.22. Heater support.

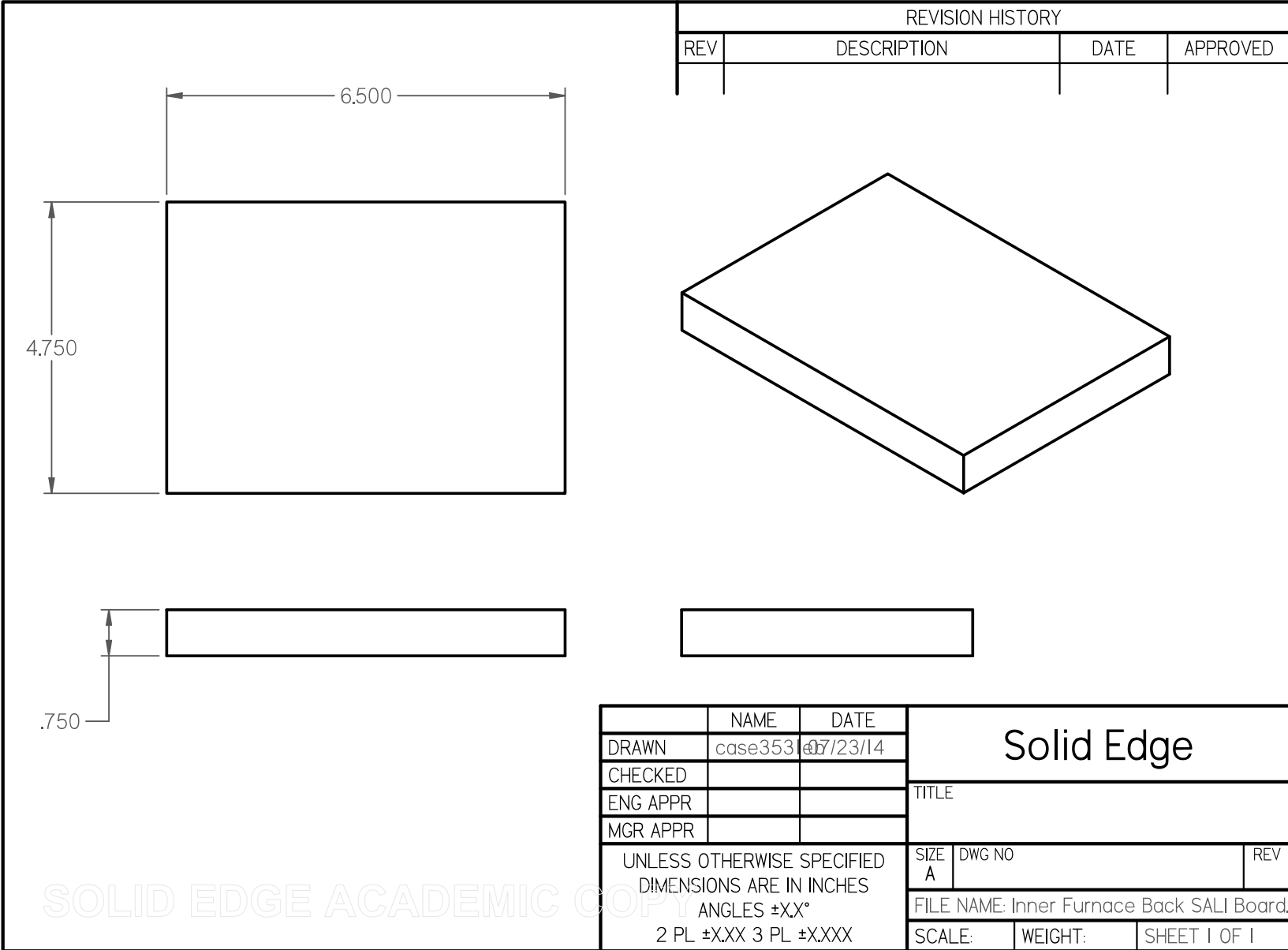


Figure C.23. Inner furnace back SALI board.

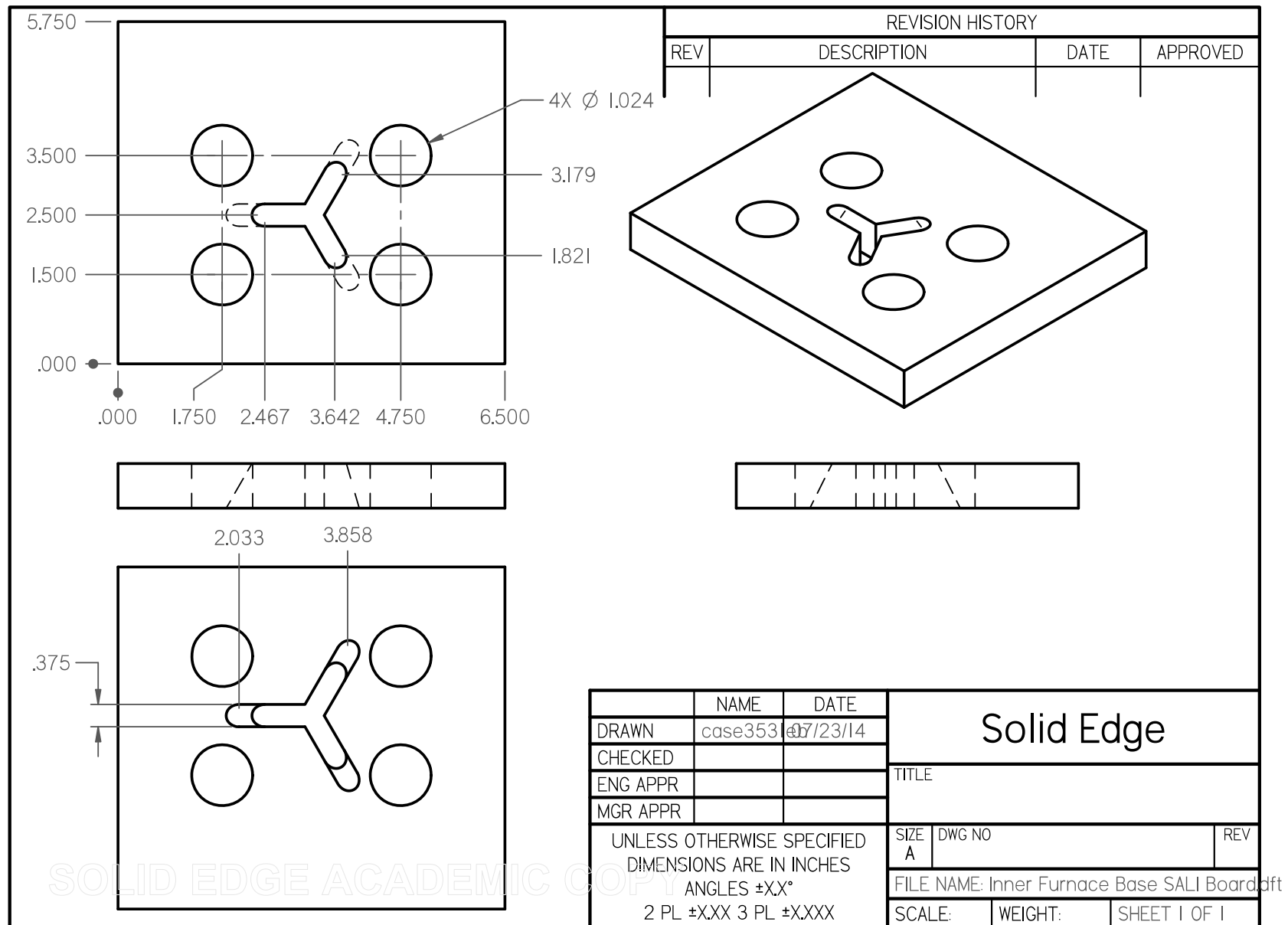


Figure C.24. Inner furnace base SALI board.

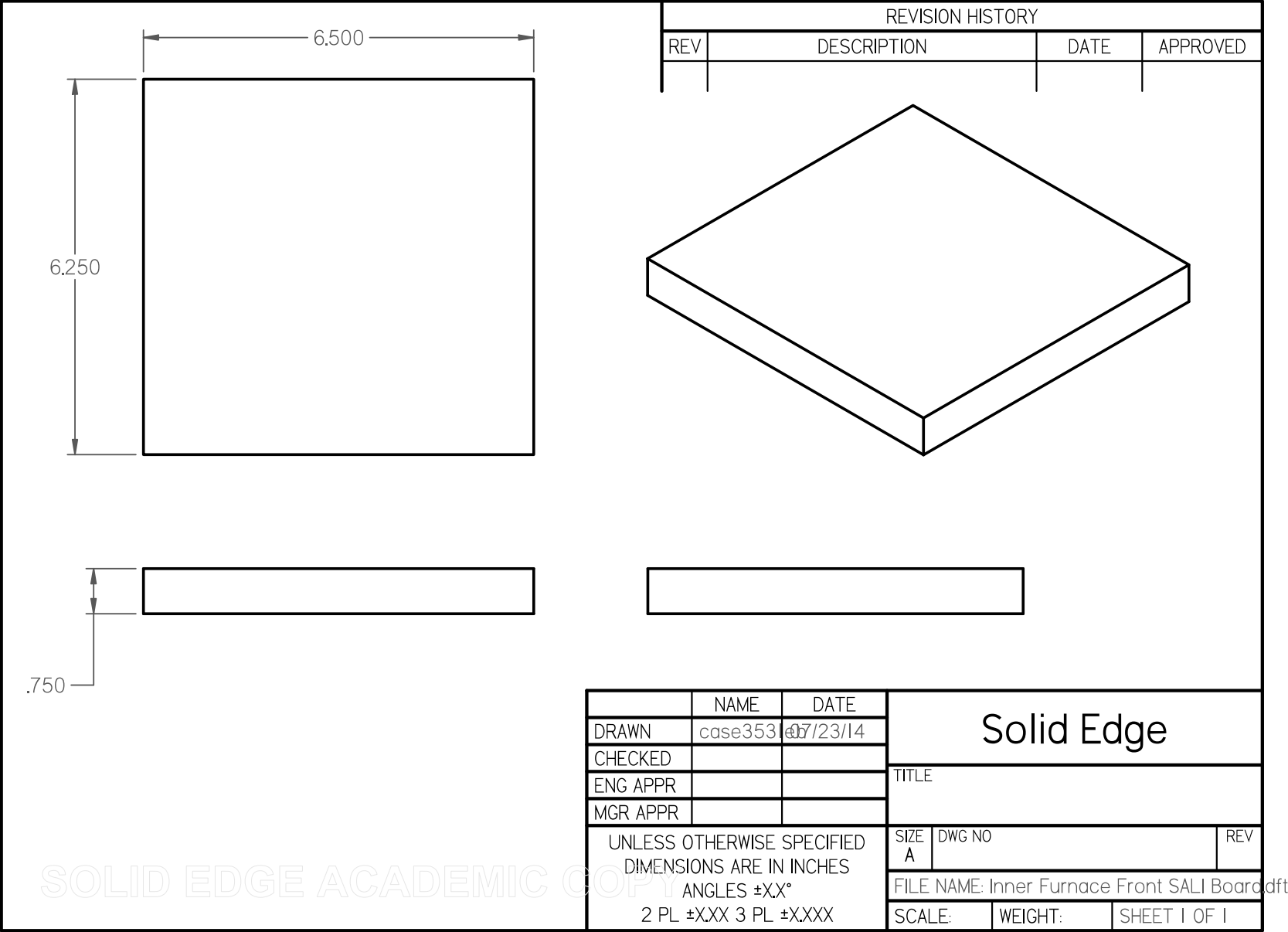


Figure C.25. Inner furnace front SALI board.

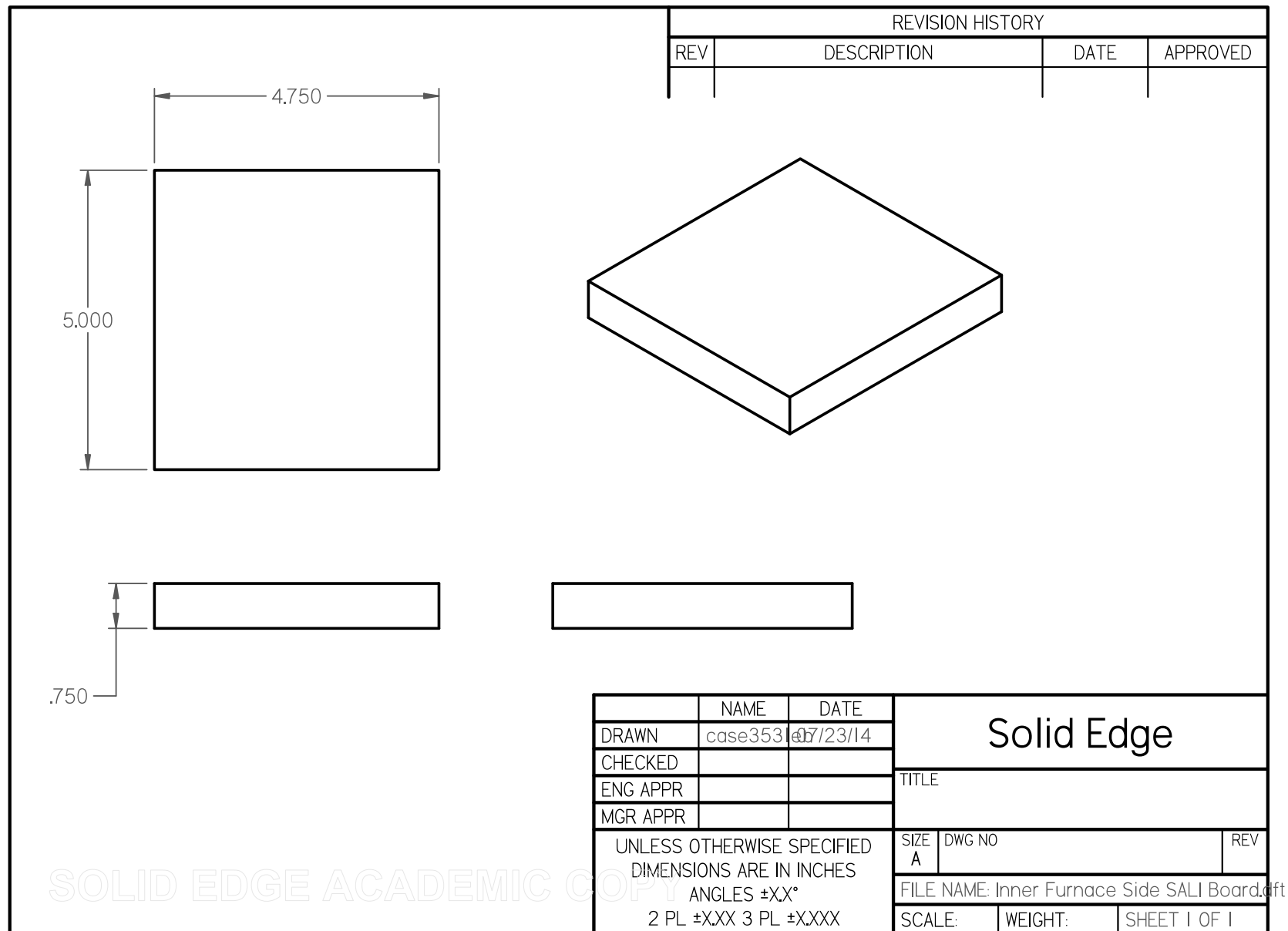


Figure C.26. Inner furnace side SALI board.

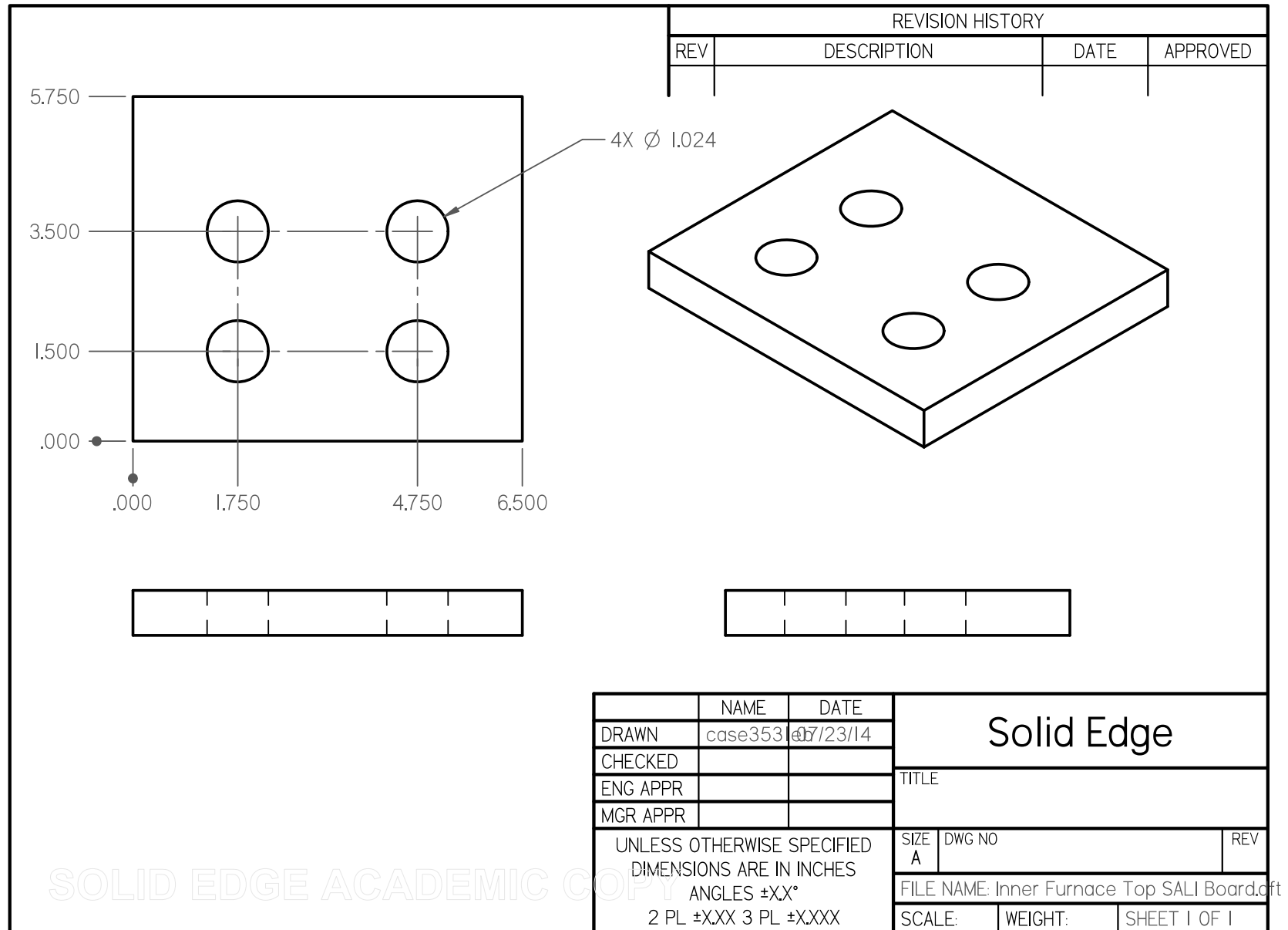


Figure C.27. Inner furnace top SALI board.

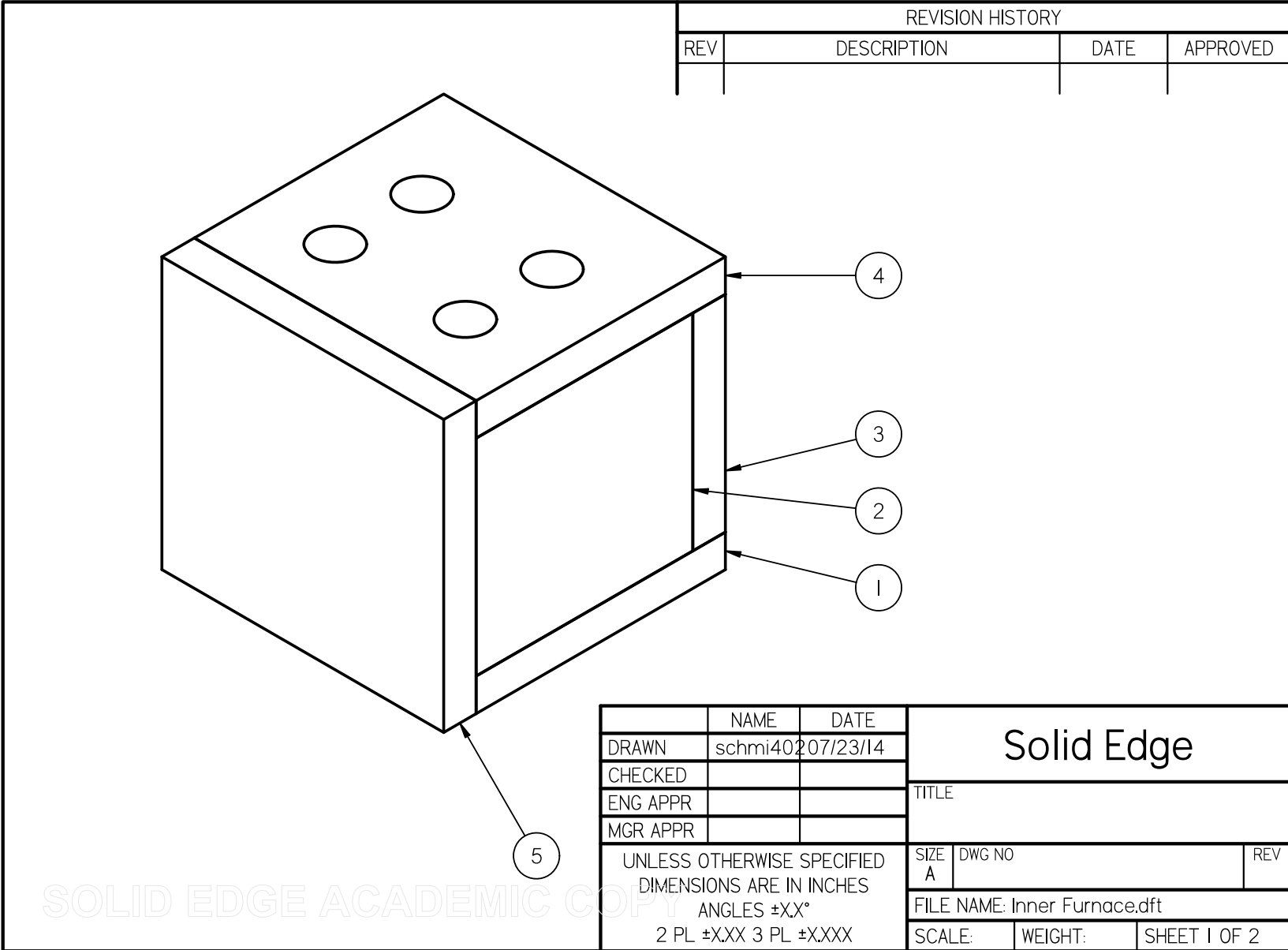


Figure C.28. Inner furnace.

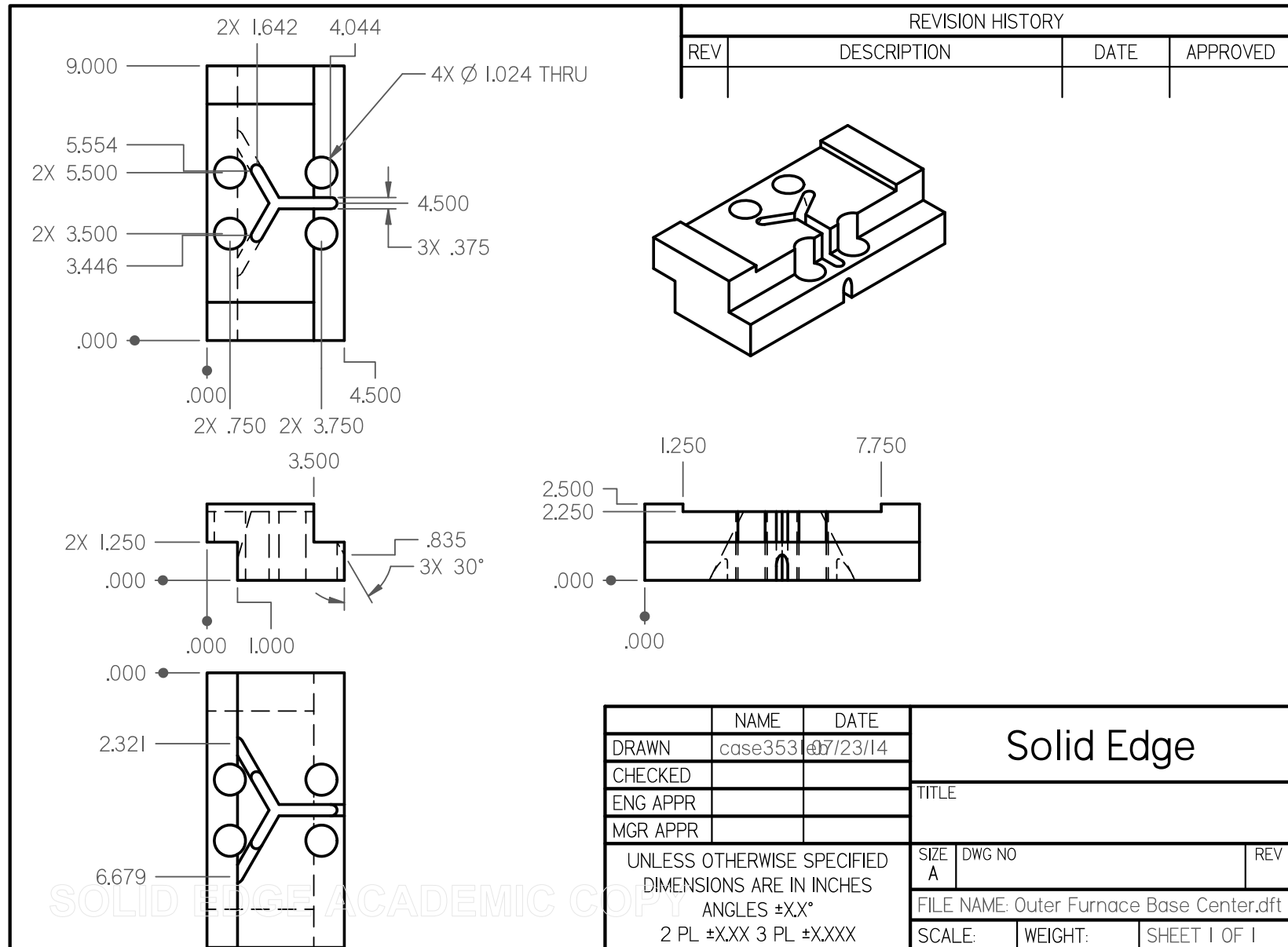


Figure C.30. Outer furnace base center.

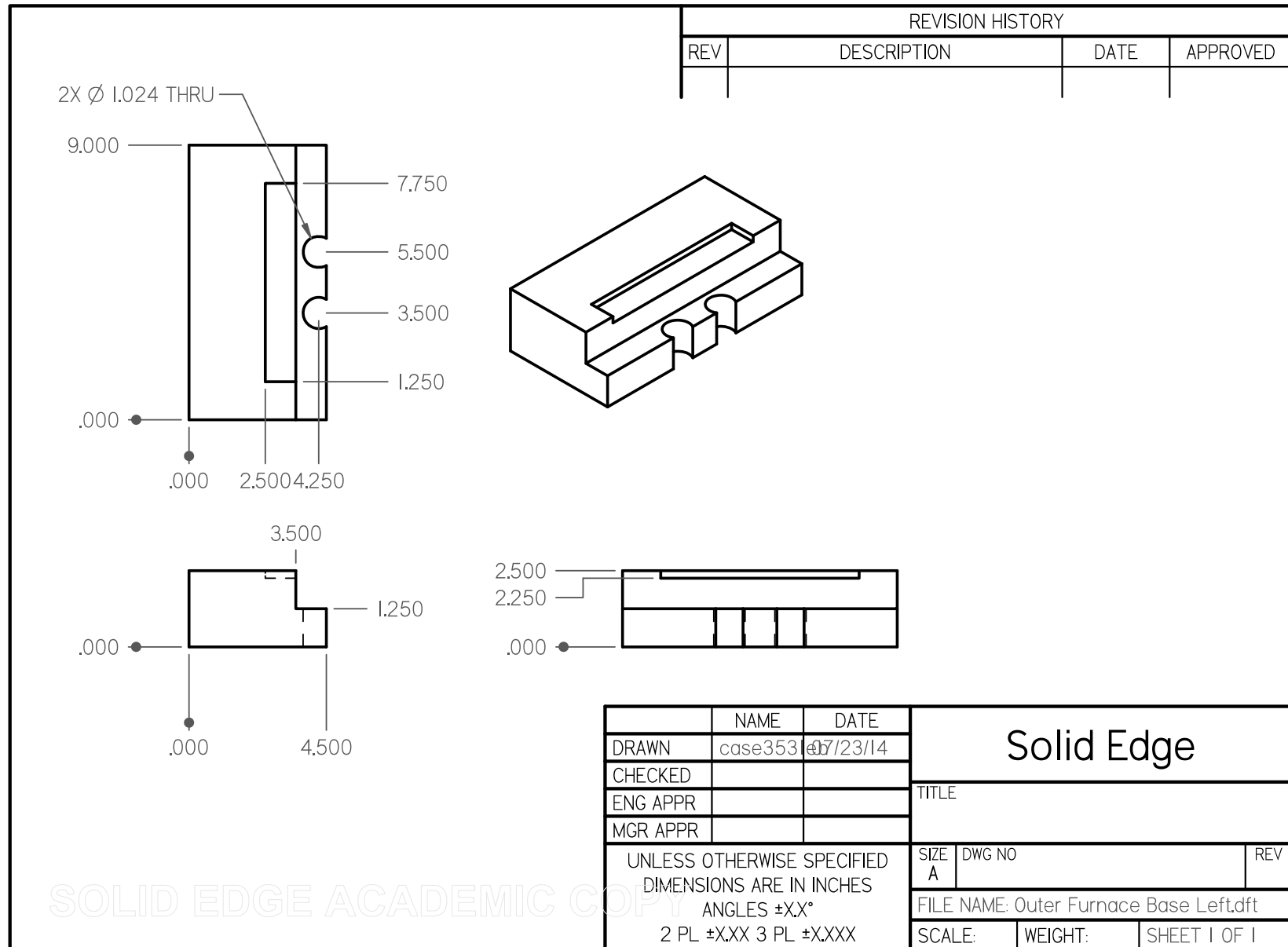
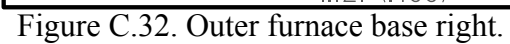


Figure C.31. Outer furnace base left.



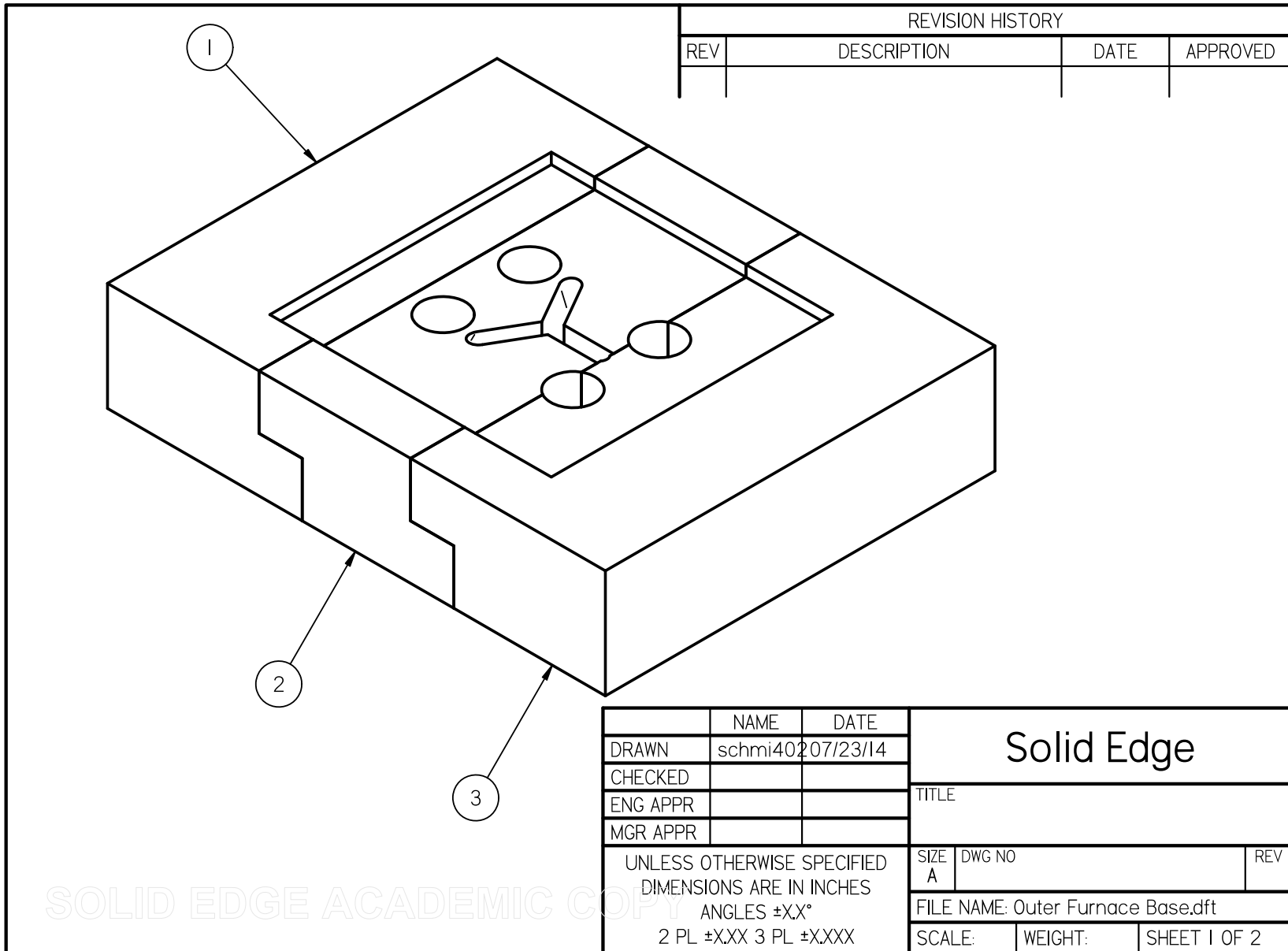


Figure C.33. Outer furnace base.

Item Number	File Name (no extension)	Author	Quantity
1	Outer Furnace Base Left	case353leb	1
2	Outer Furnace Base Center	case353leb	1
3	Outer Furnace Base Right	case353leb	1

SOLID EDGE ACADEMIC COPY
Figure C.34. Outer furnace base BOM.

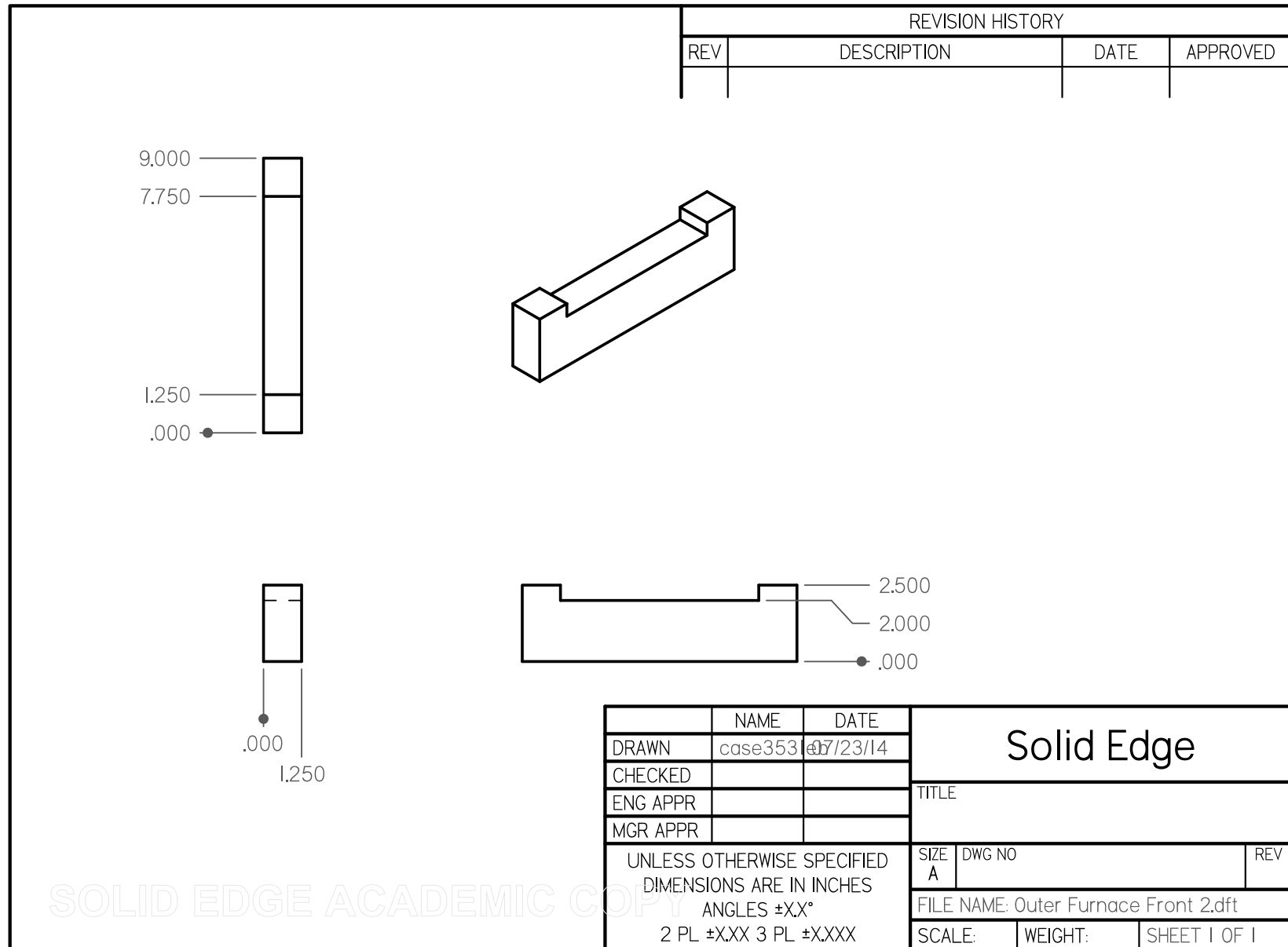


Figure C.35. Outer furnace front 2.

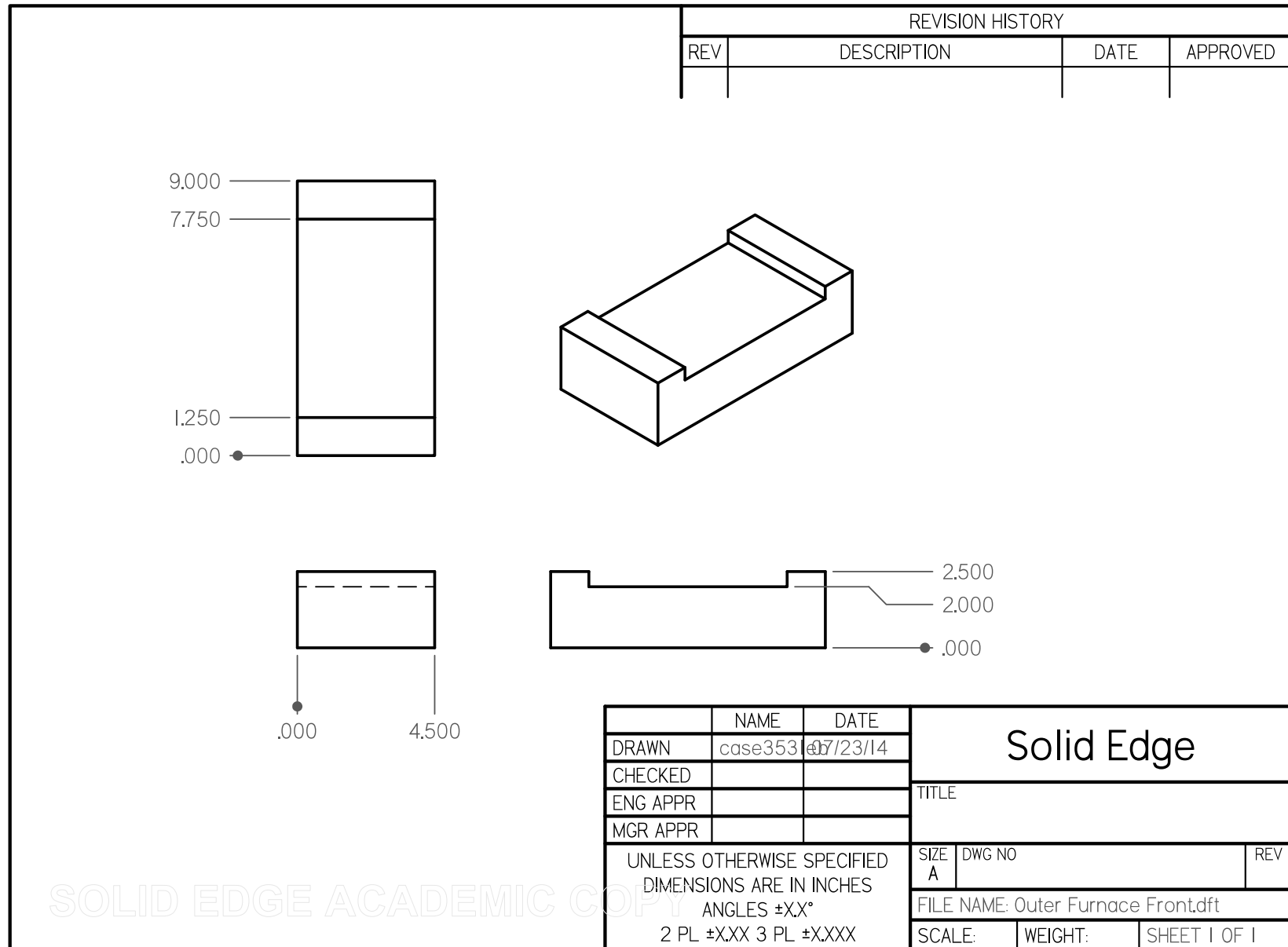


Figure C.36. Outer furnace front.

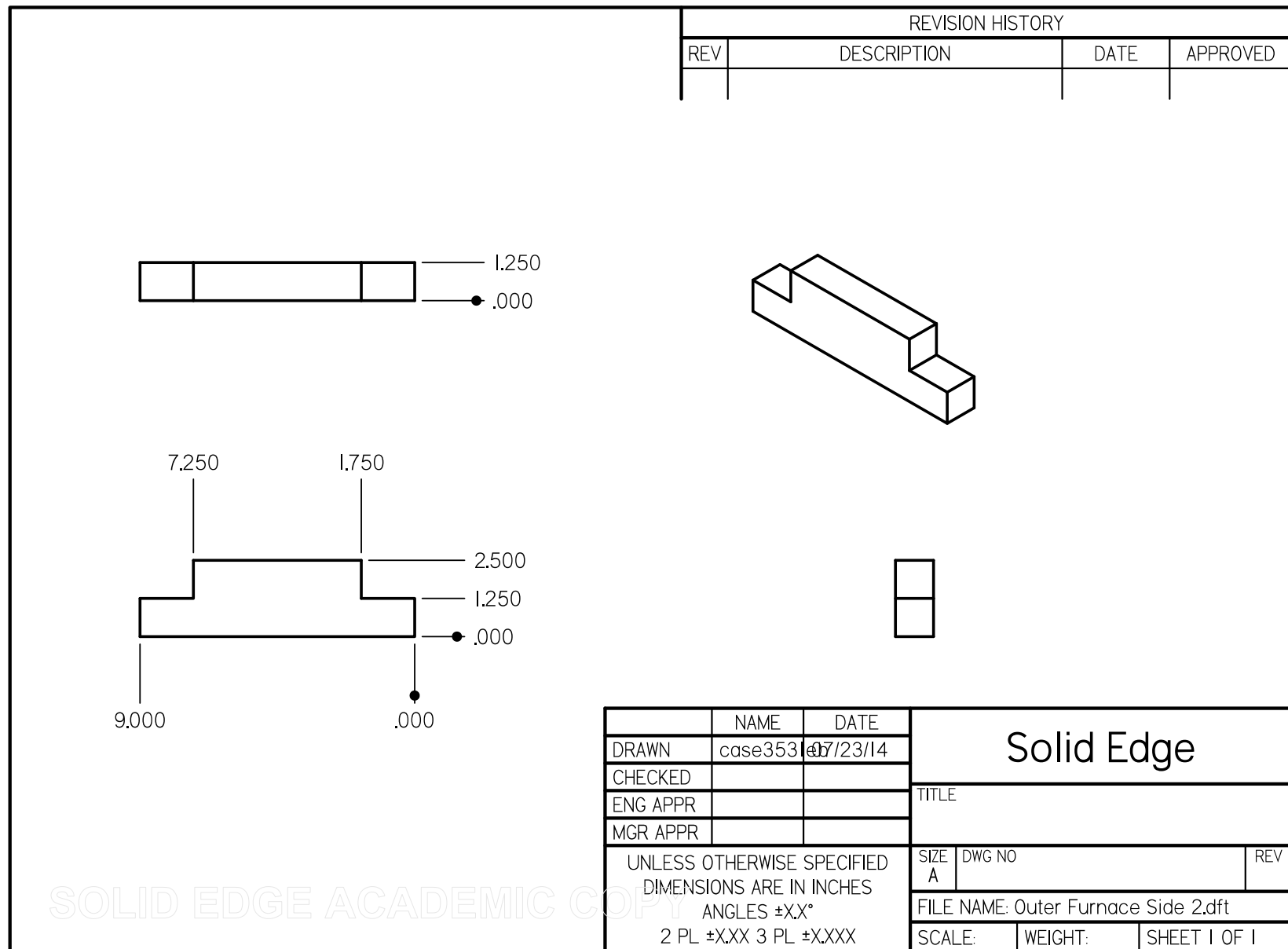


Figure C.37. Outer furnace side 2.

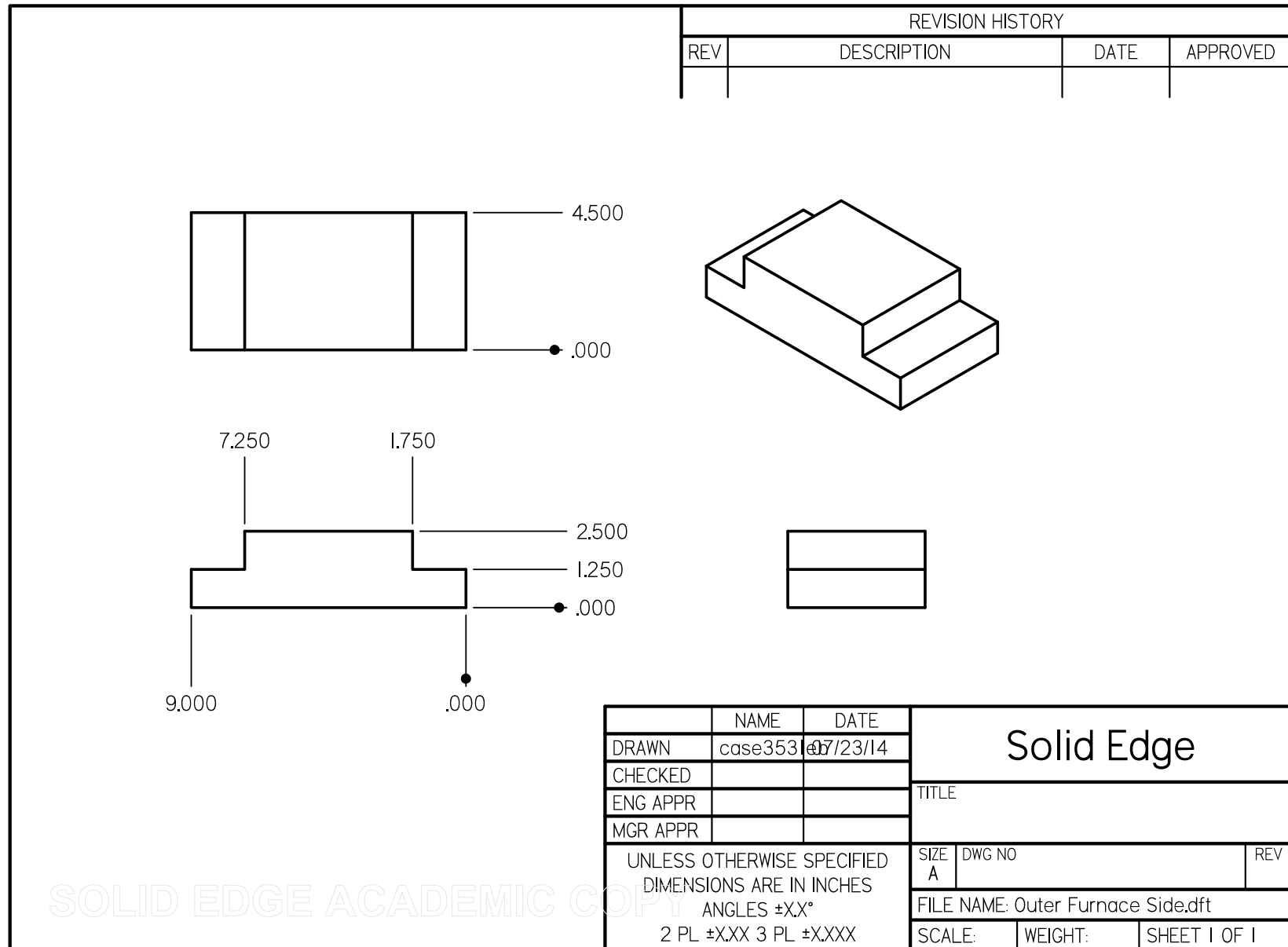


Figure C.38. Outer furnace side.

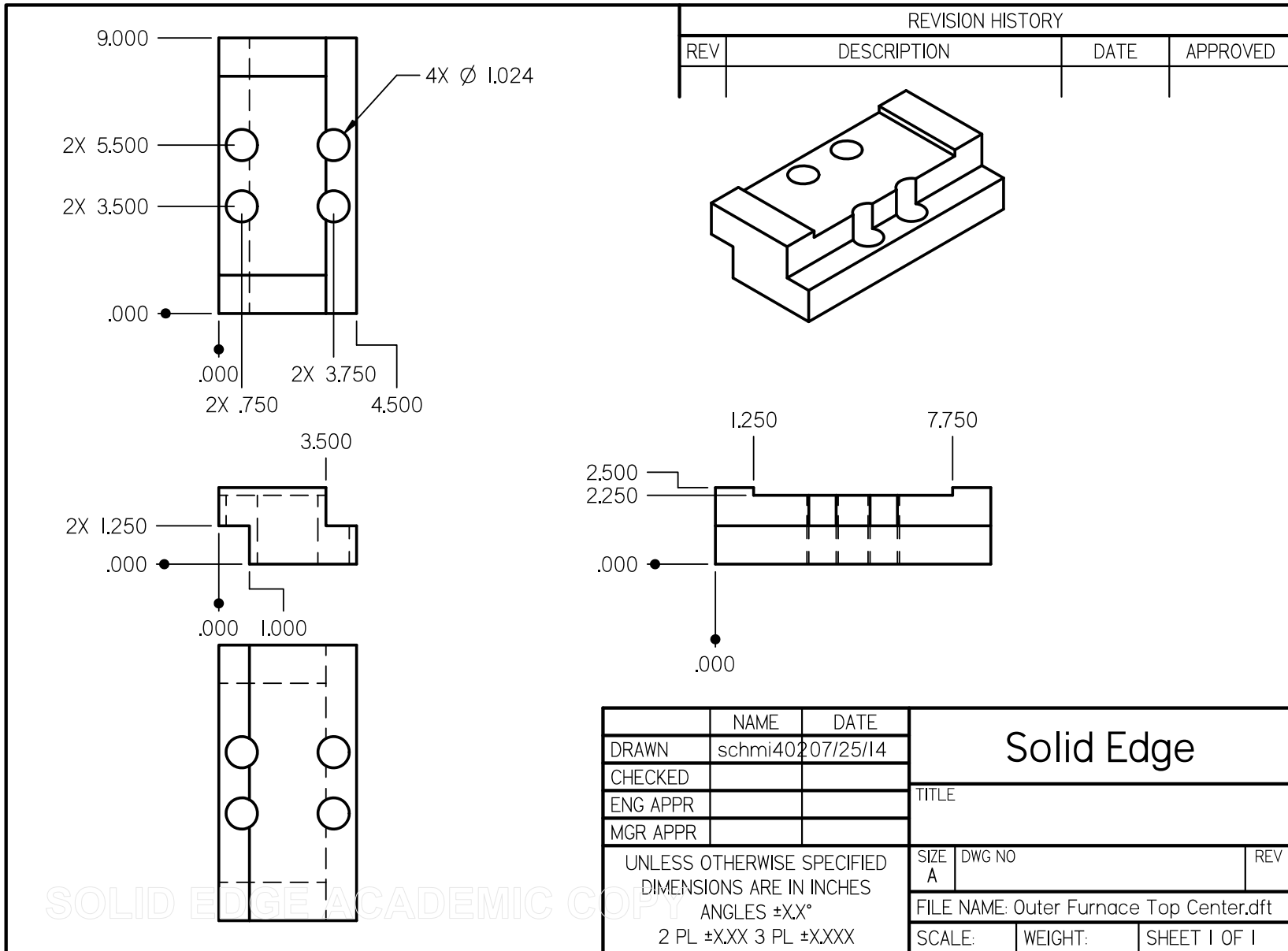


Figure C.39. Outer furnace top center.

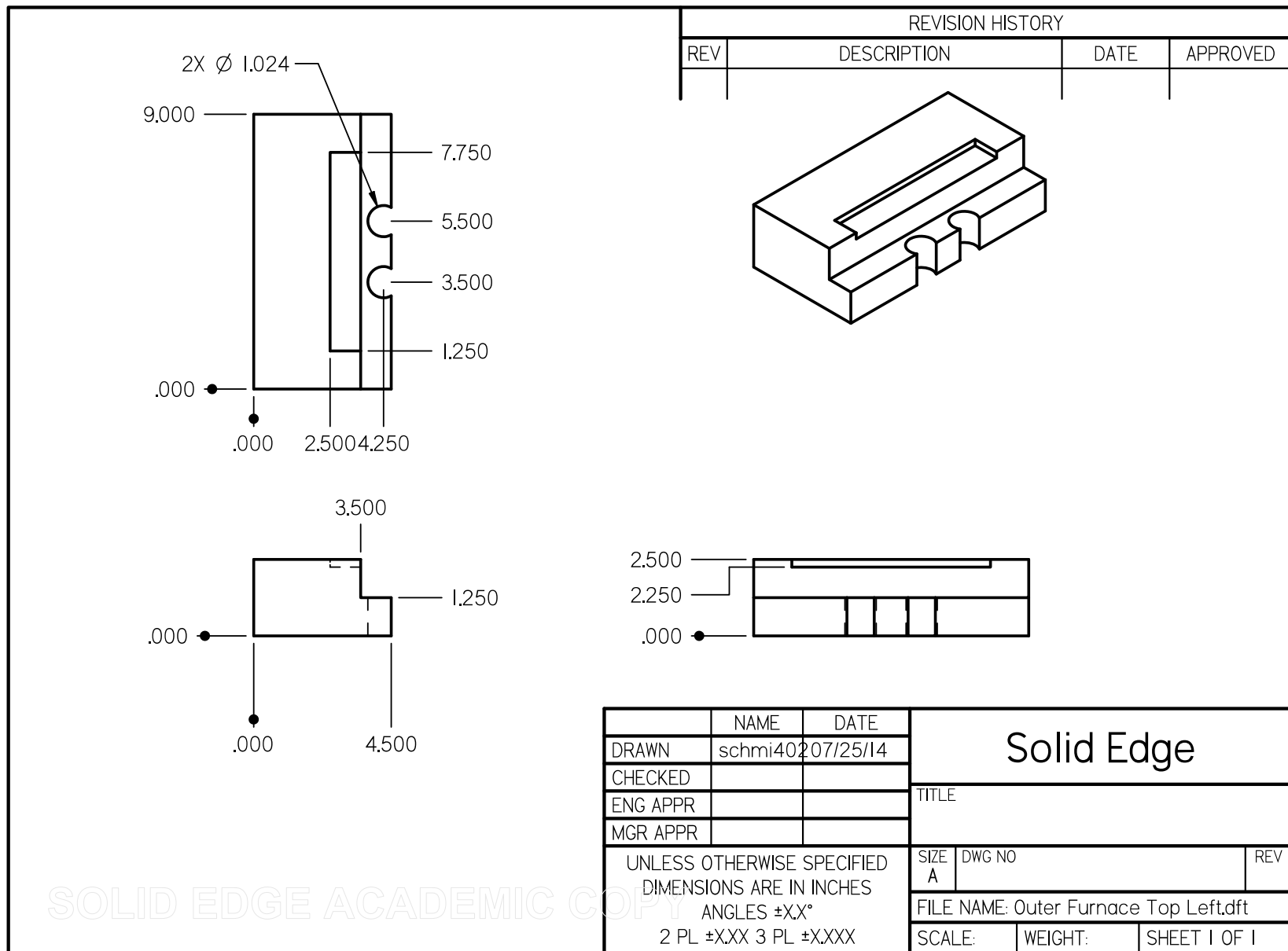


Figure C.40. Outer furnace top left.

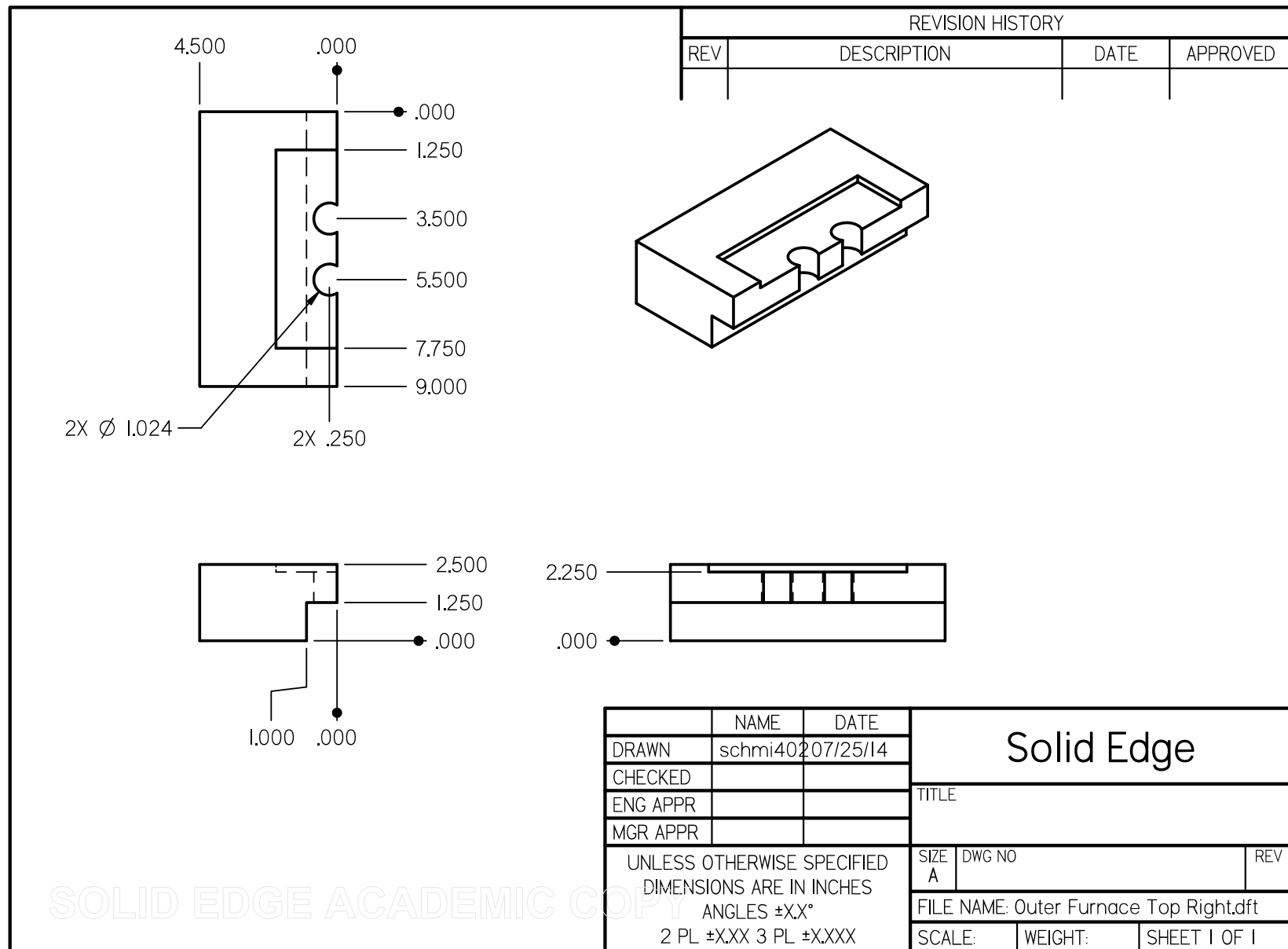


Figure C.41. Outer furnace top right.

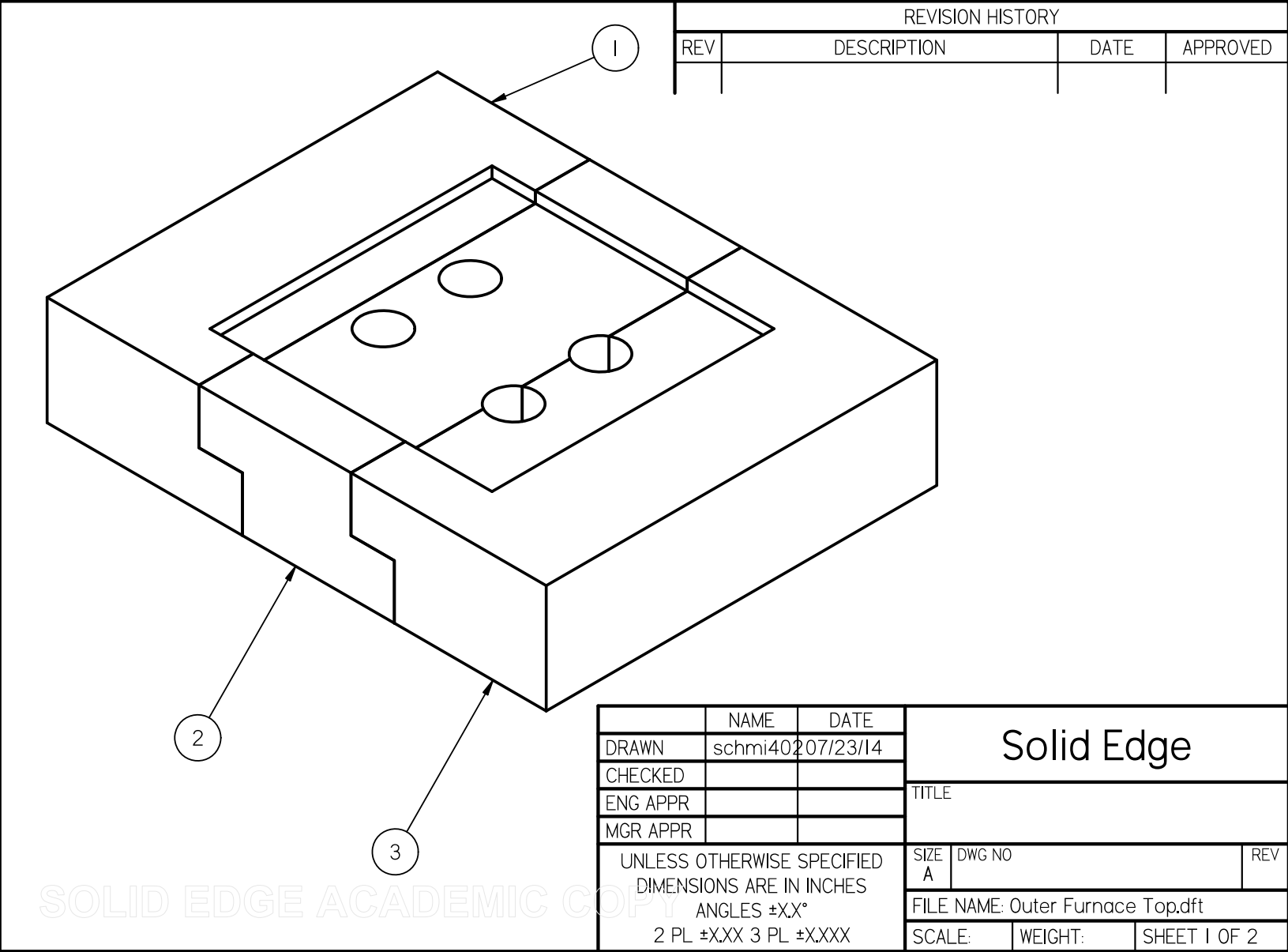


Figure C.42. Outer furnace top.

Item Number	File Name (no extension)	Author	Quantity
1	Outer Furnace Top Left	case353leb	1
2	Outer Furnace Top Center	case353leb	1
3	Outer Furnace Top Right	case353leb	1

SOLID EDGE ACADEMIC COPY
Figure C.43. Outer furnace top BOM.

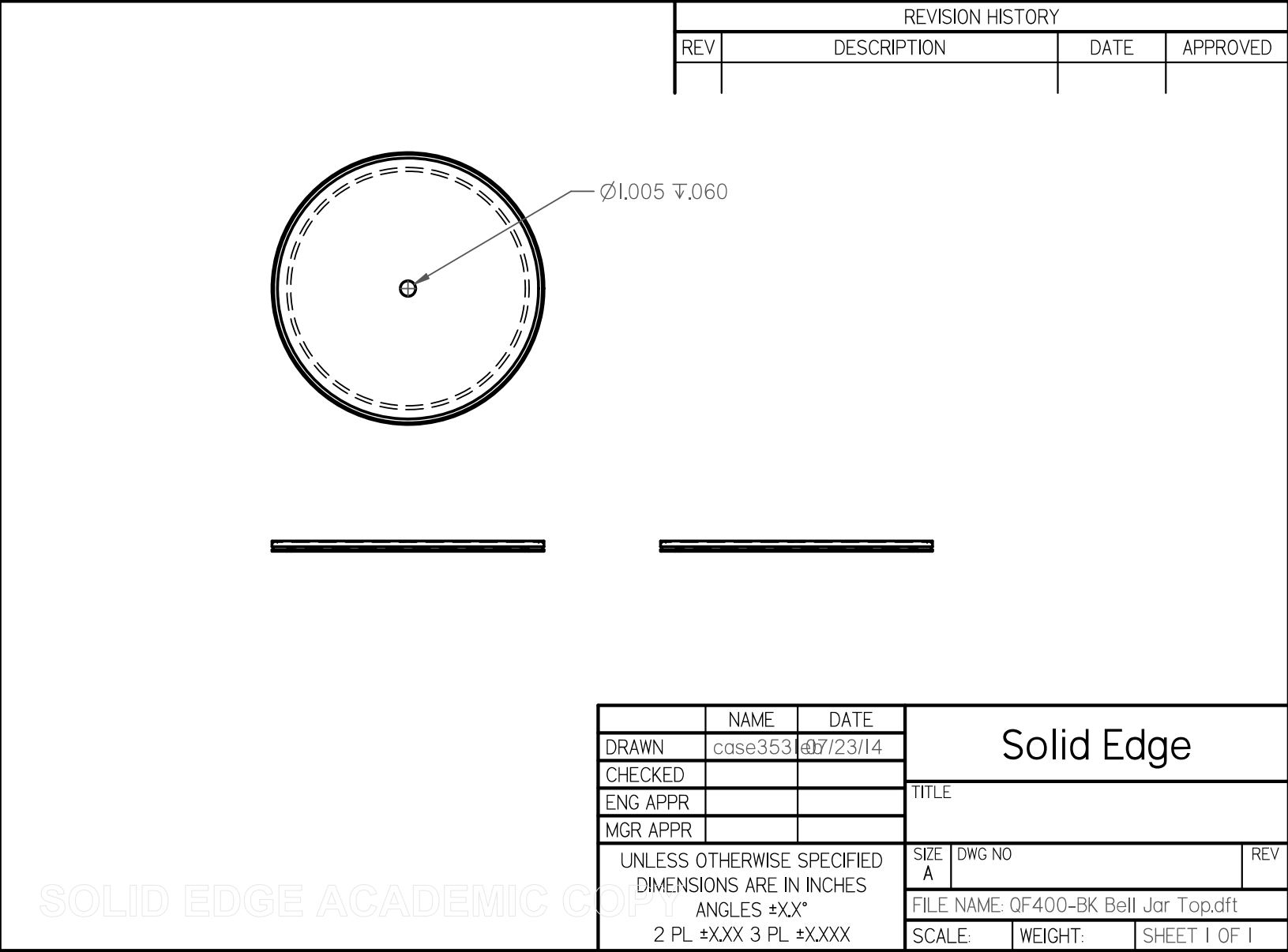


Figure C.44. Bell jar top.

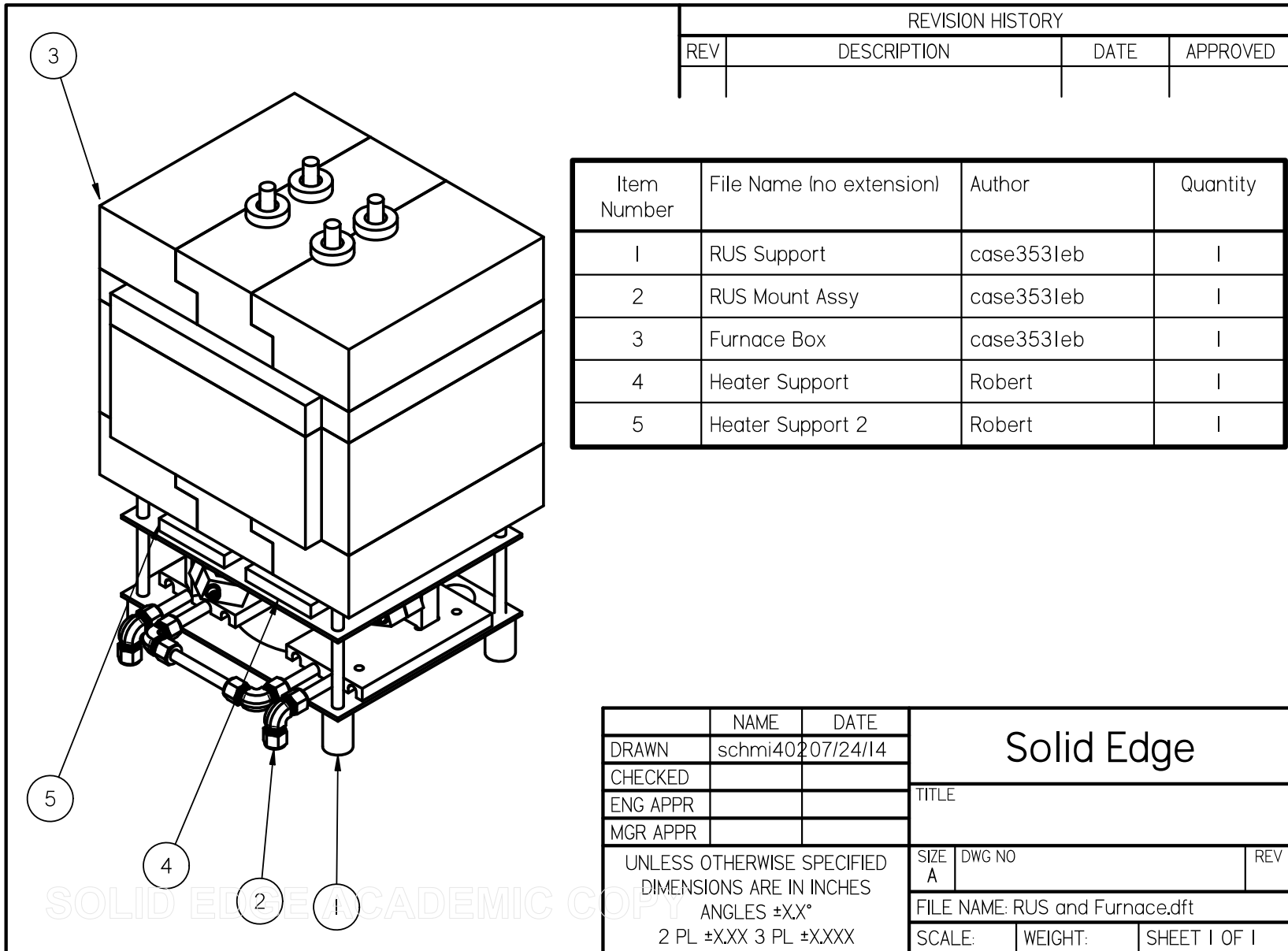


Figure C.45. RUS and furnace.

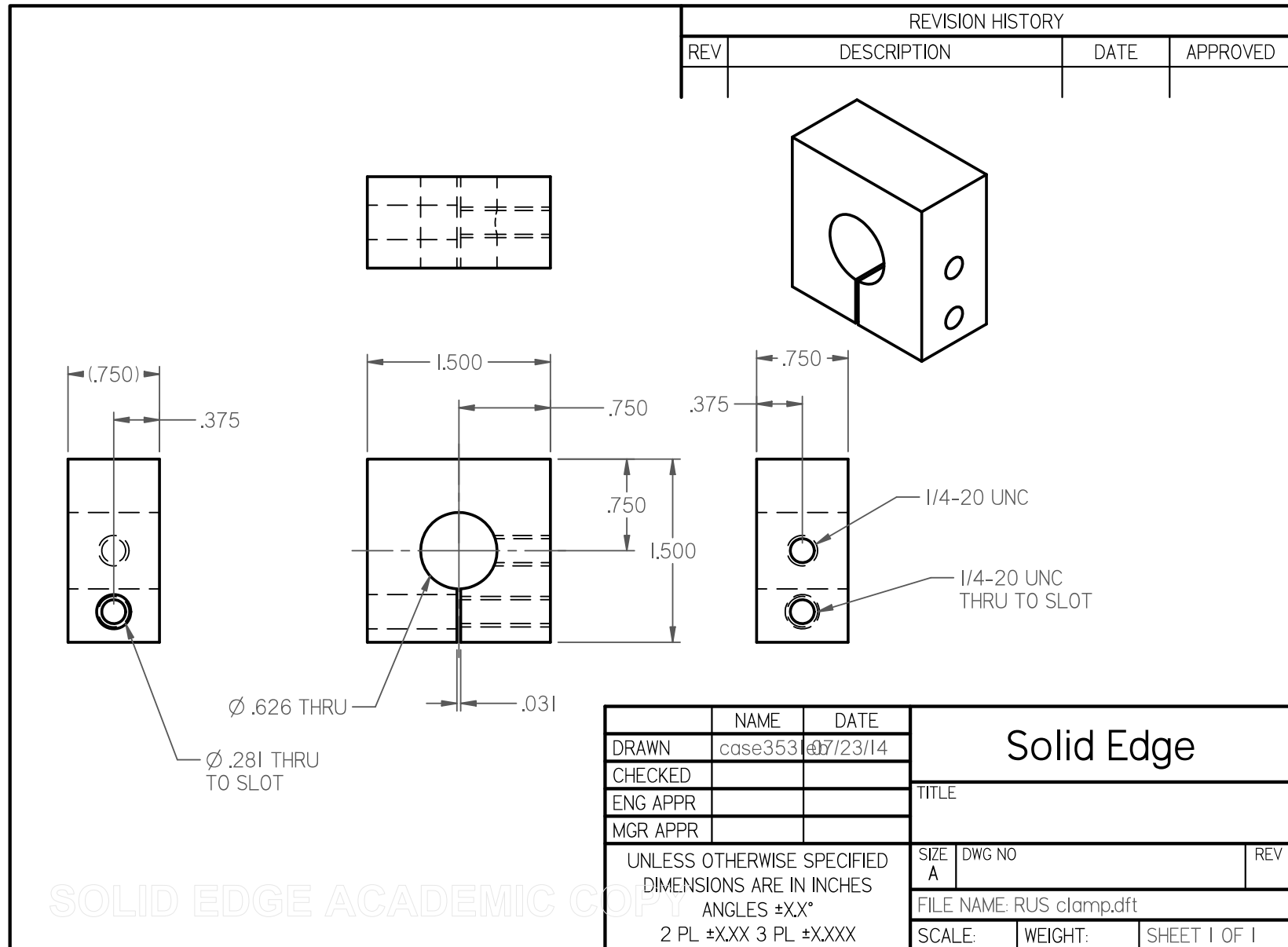


Figure C.46. RUS clamp.

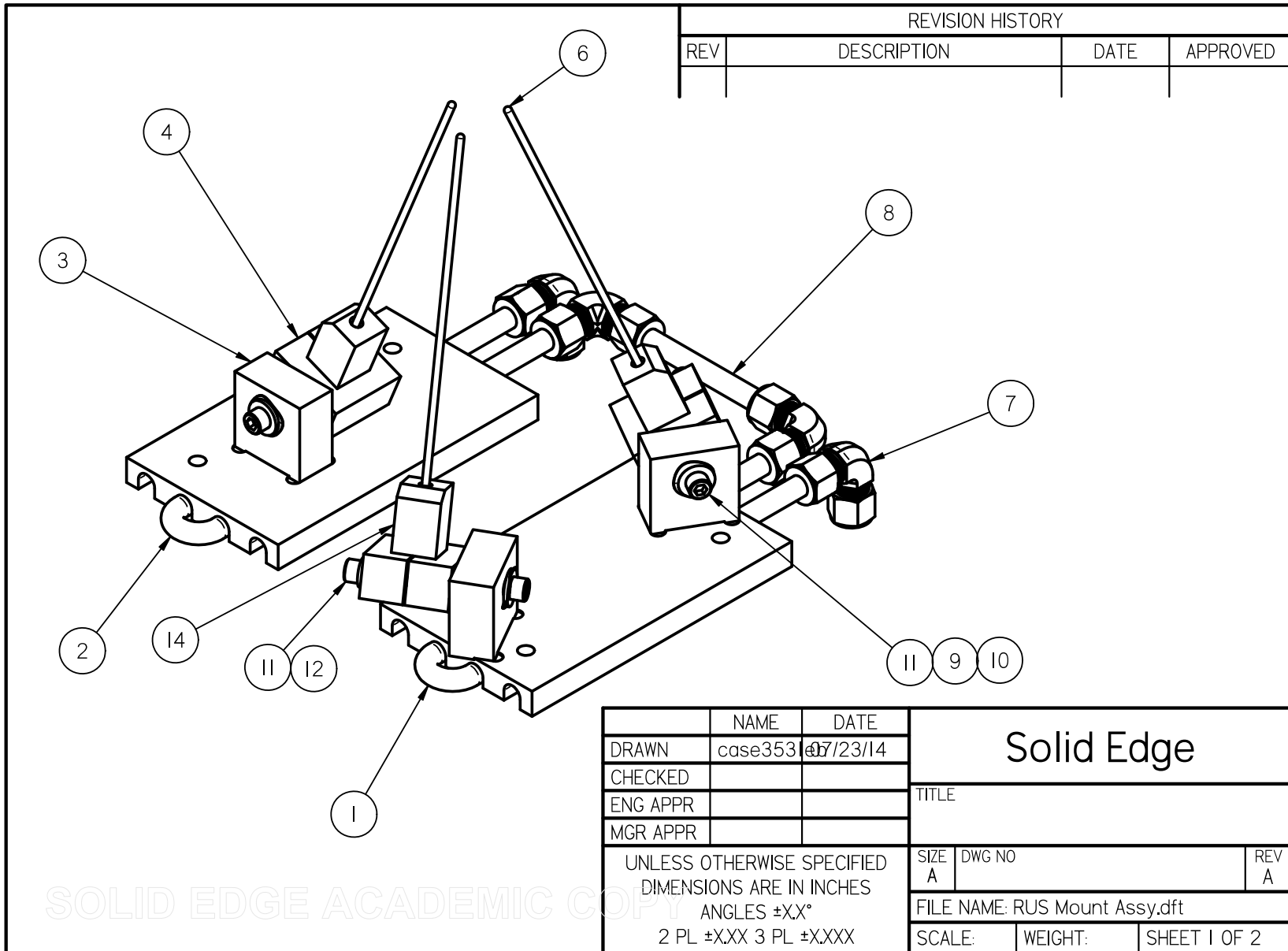


Figure C.47. RUS mount assembly.

BOM, RUS MOUNT ASSY

Item Number	Document Number	Title	Material	Quantity
1	COLD PLATE MT 2			1
2	COLD PLATE MT			1
3	RUS Mount		Copper	3
4	RUS Clamp I		Copper	3
6	RUS TRANSDUCER		Brass, yellow brass	3
7	FTG, 90 EL 0.38 T 5182K416		Stainless steel	4
8	TUBE, 0.38X0.028 X 3.75 SS			1
9	WSHR, 0.25 SS		Stainless steel	3
10	WSHR, Wave 92161A029			3
11	0.25-20x1.25 SHCS		Stainless steel	6
12	LOCK WSHR, 0.25 SS		Stainless steel	3
13*	0.25-20x0.75 SHCS		Stainless steel	3
14*		Transducer Cold Cap	Copper	3

Figure C.48. RUS mount assembly BOM.

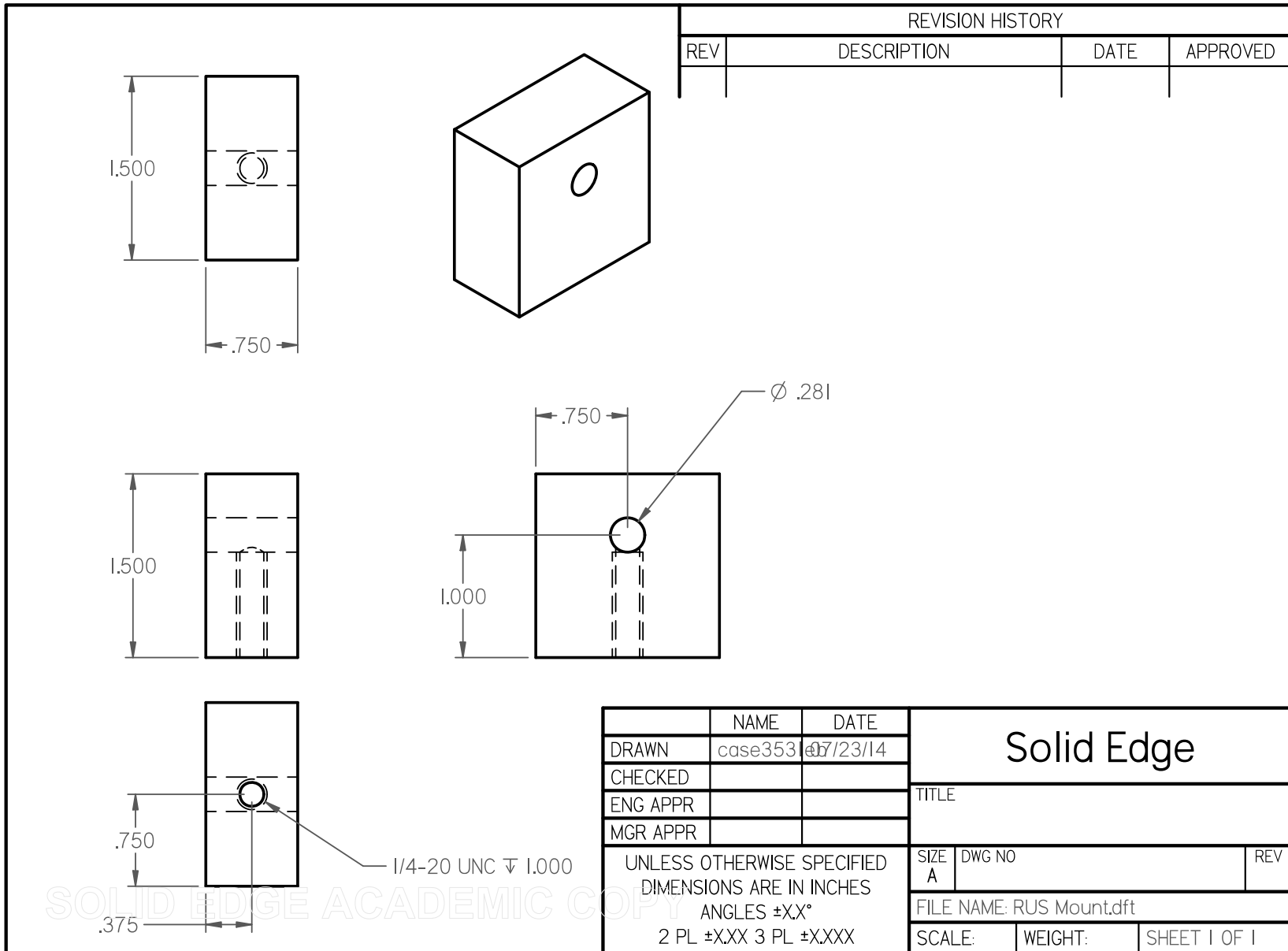


Figure C.49. RUS mount.

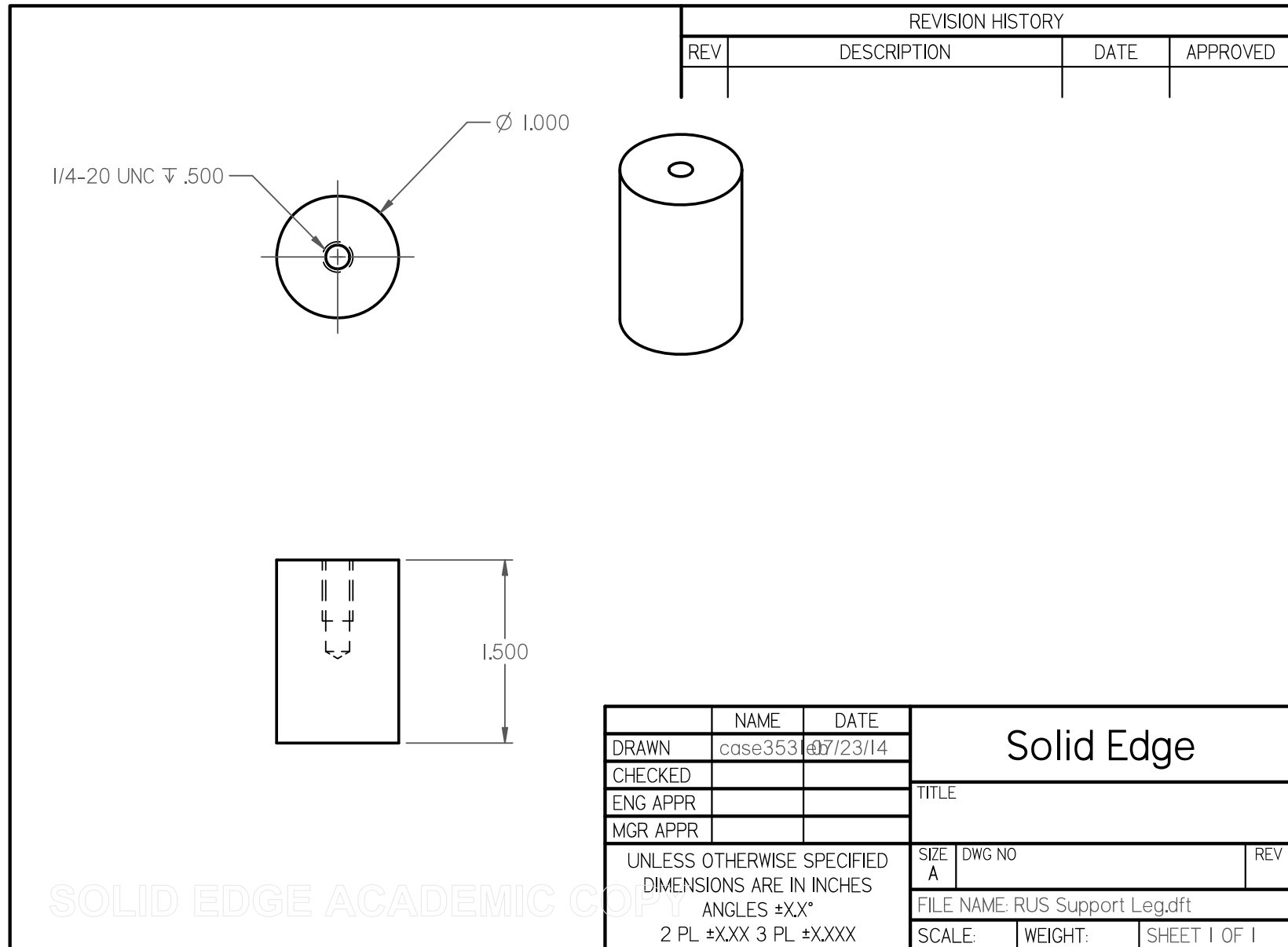


Figure C.50. RUS support leg.

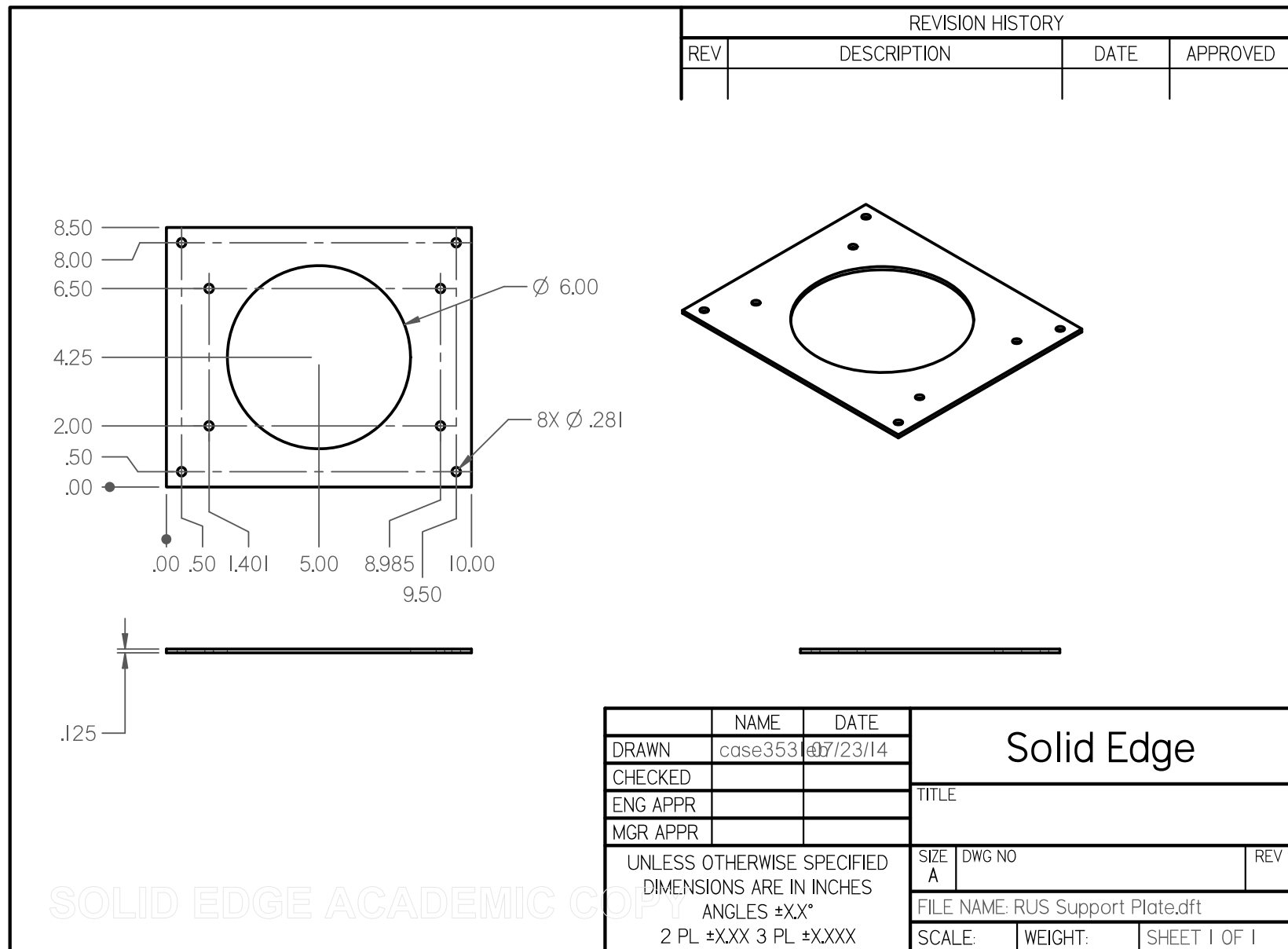


Figure C.51. RUS support plate.

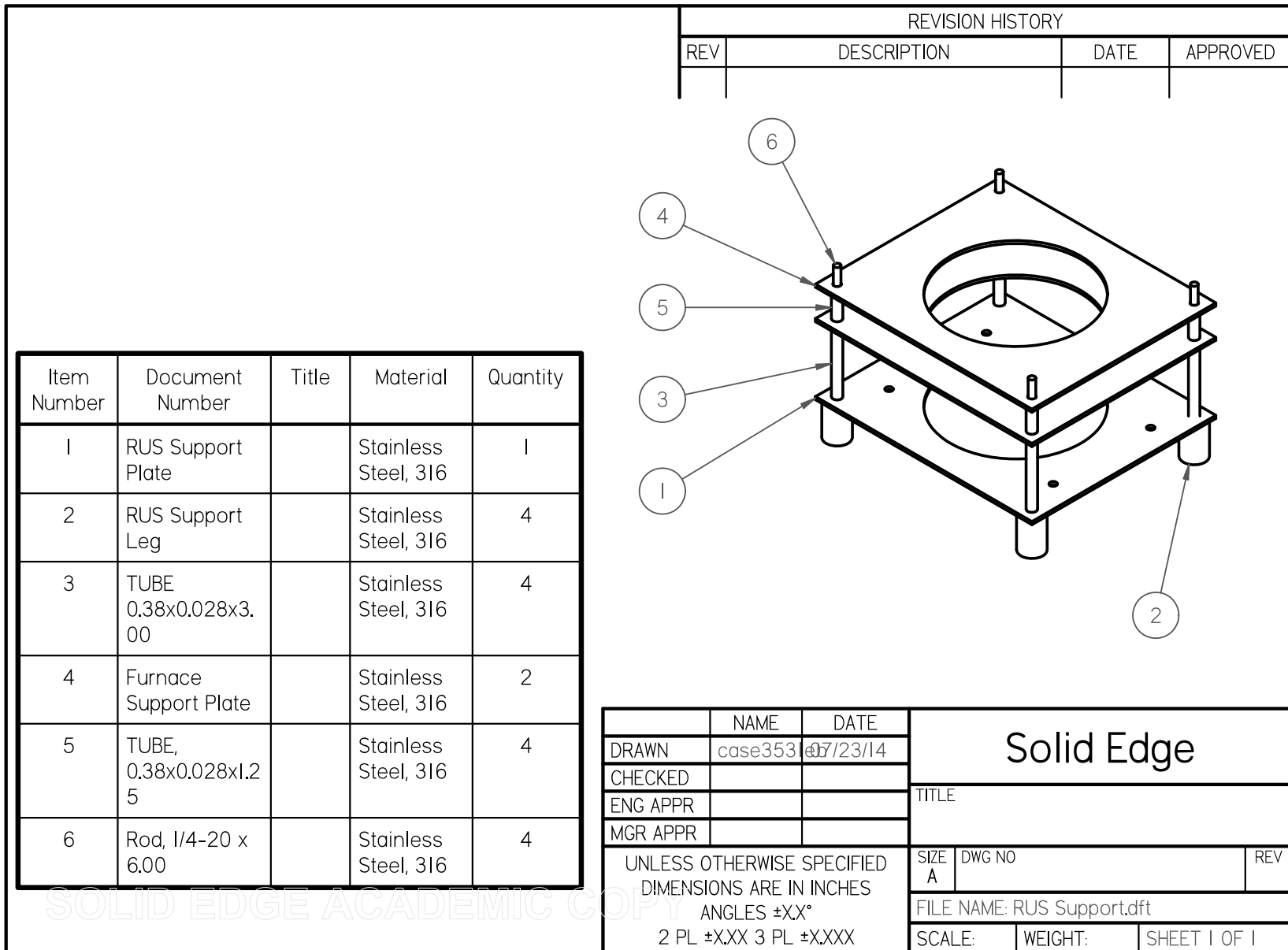


Figure C.52. RUS support.

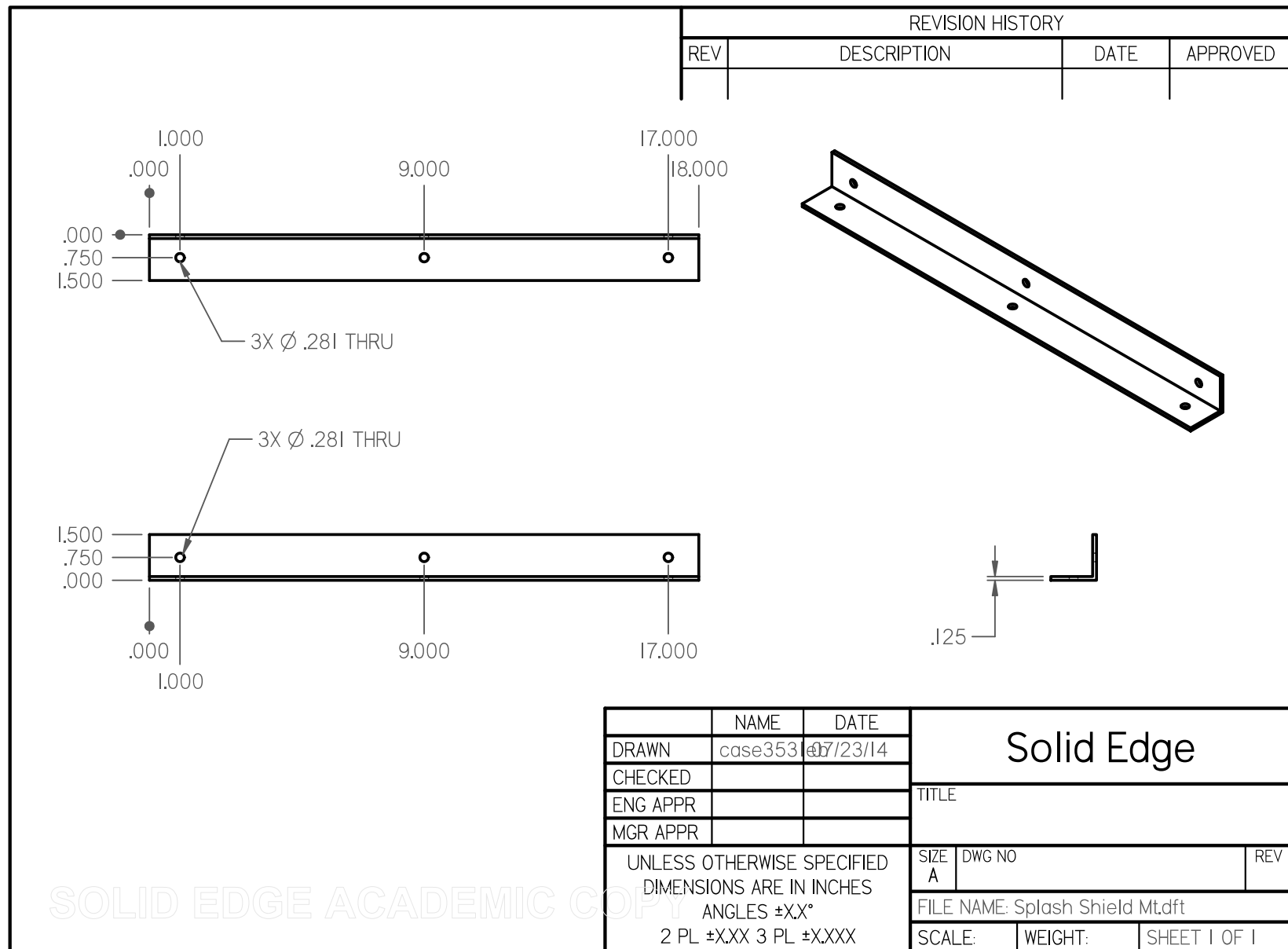


Figure C.53. Splash shield mount.

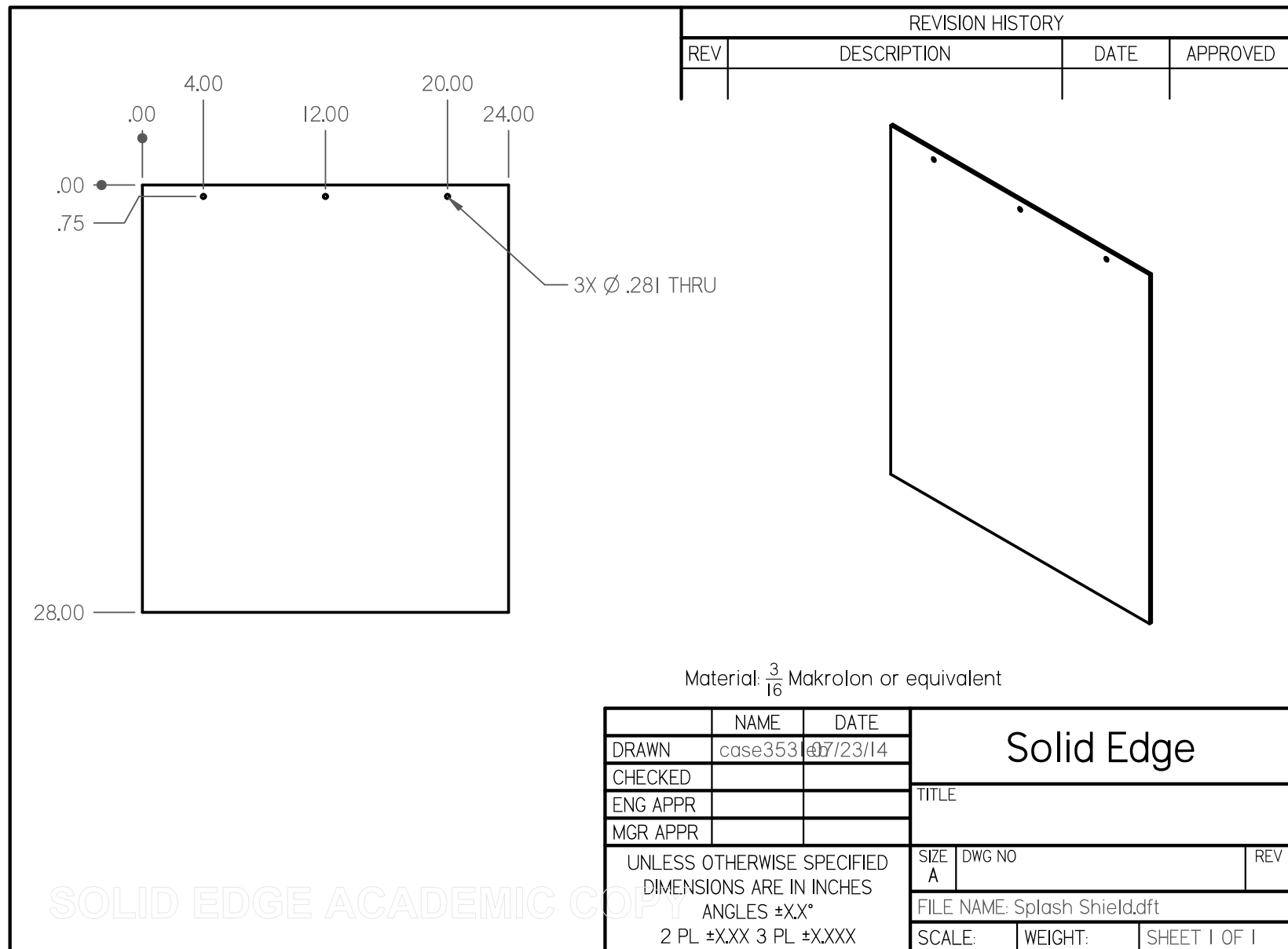


Figure C.54. Splash shield.

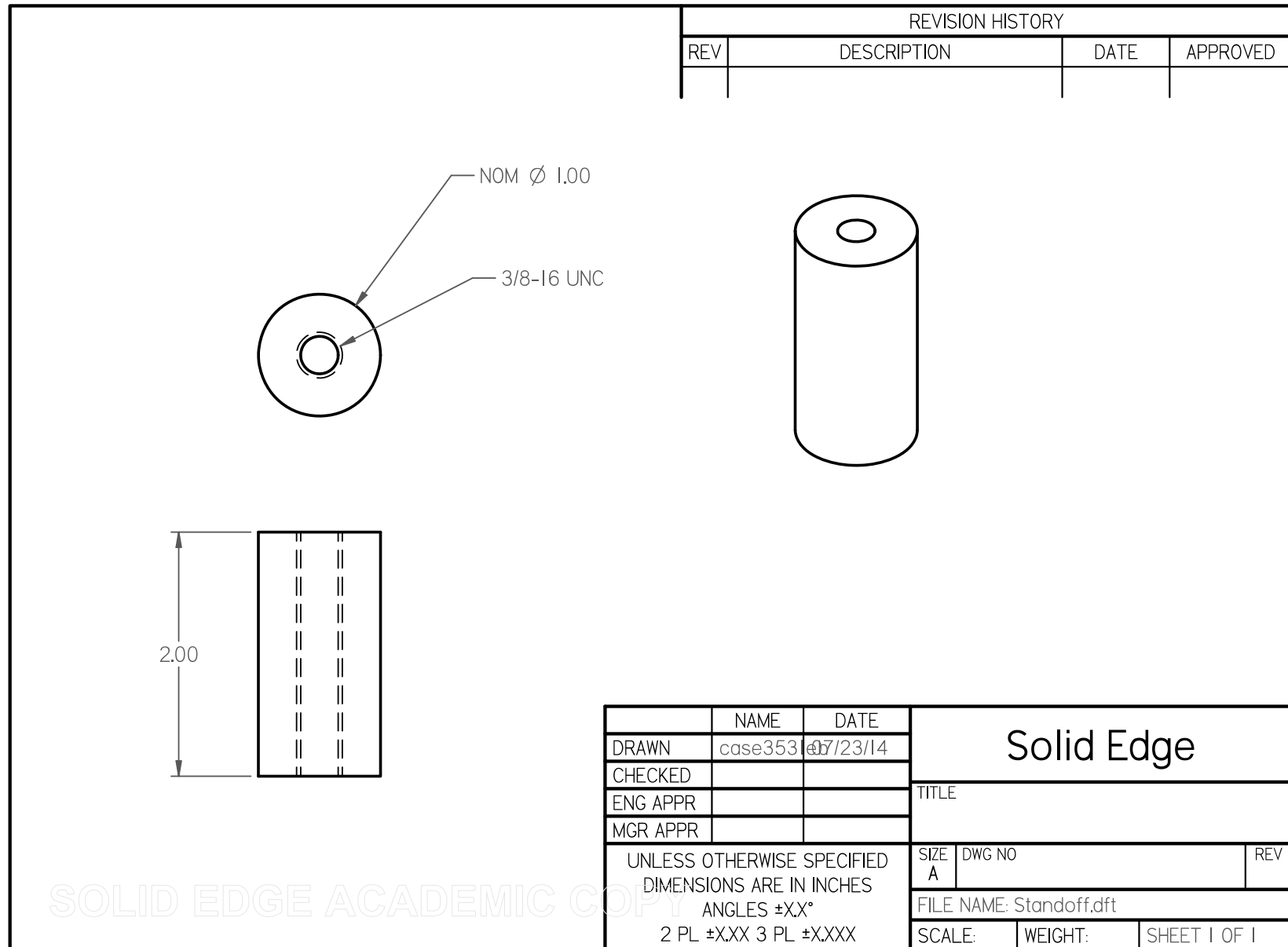


Figure C.55. Standoff.

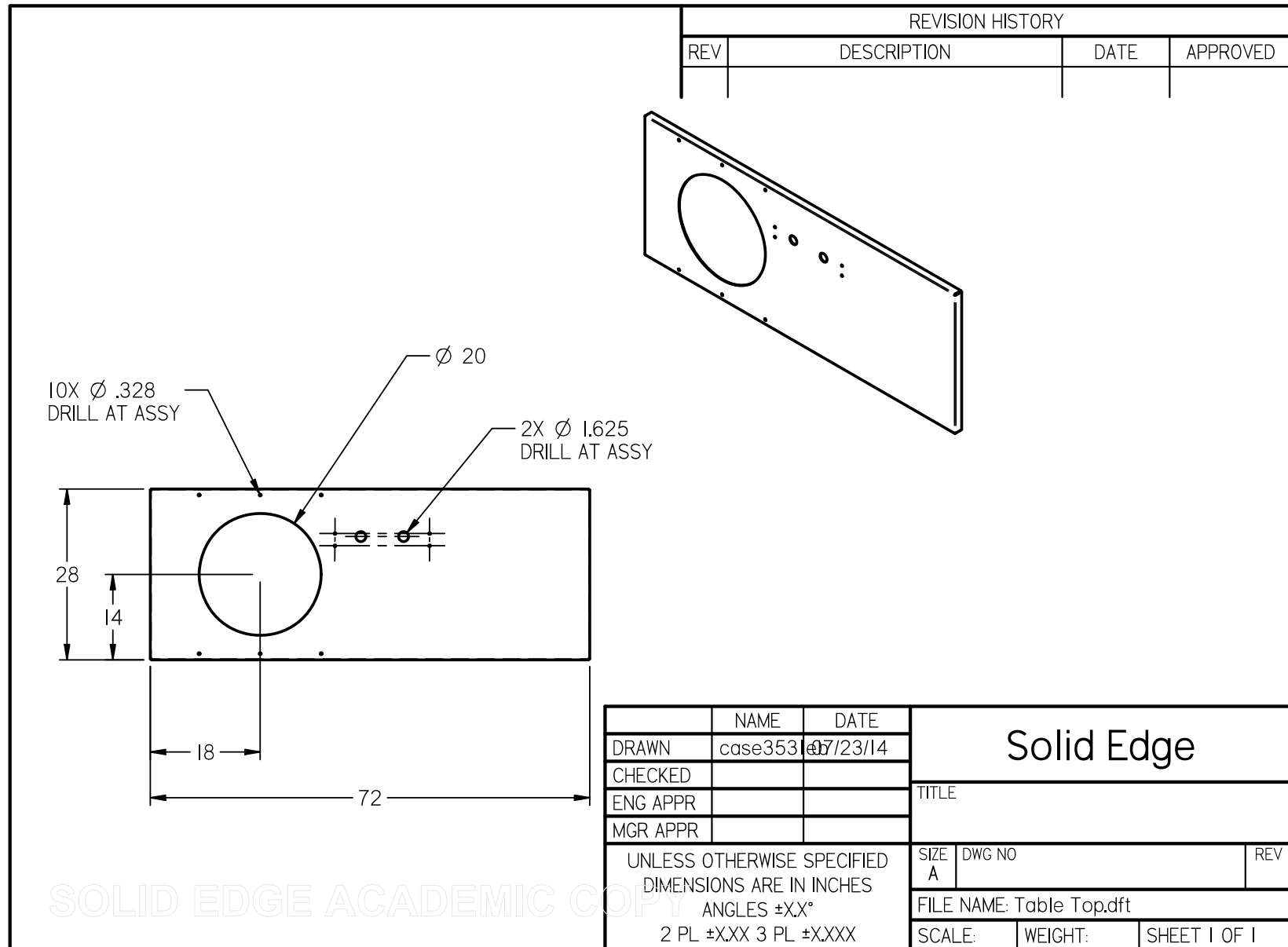


Figure C.56. Table top.

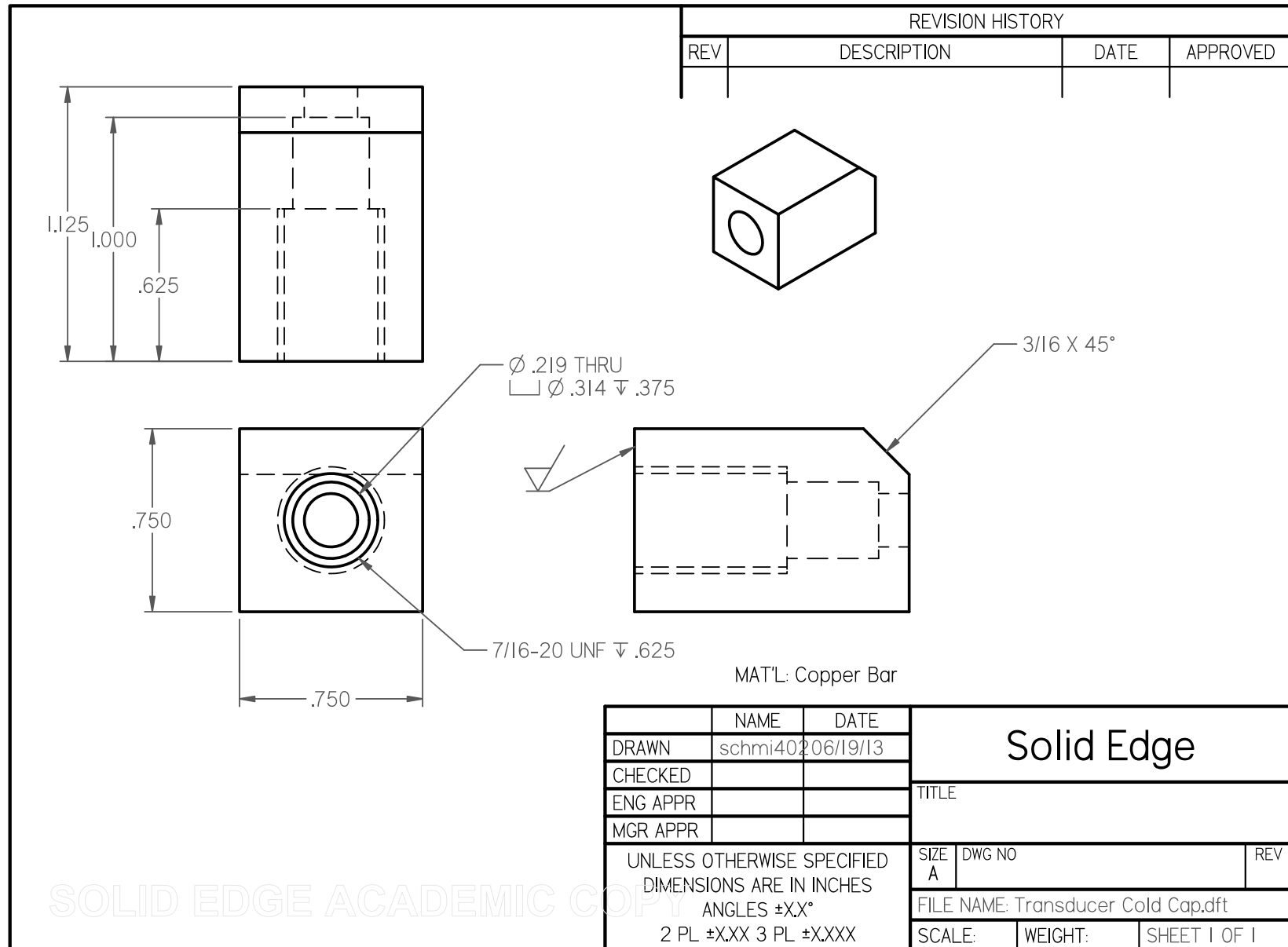


Figure C.57. Transducer cold cap.

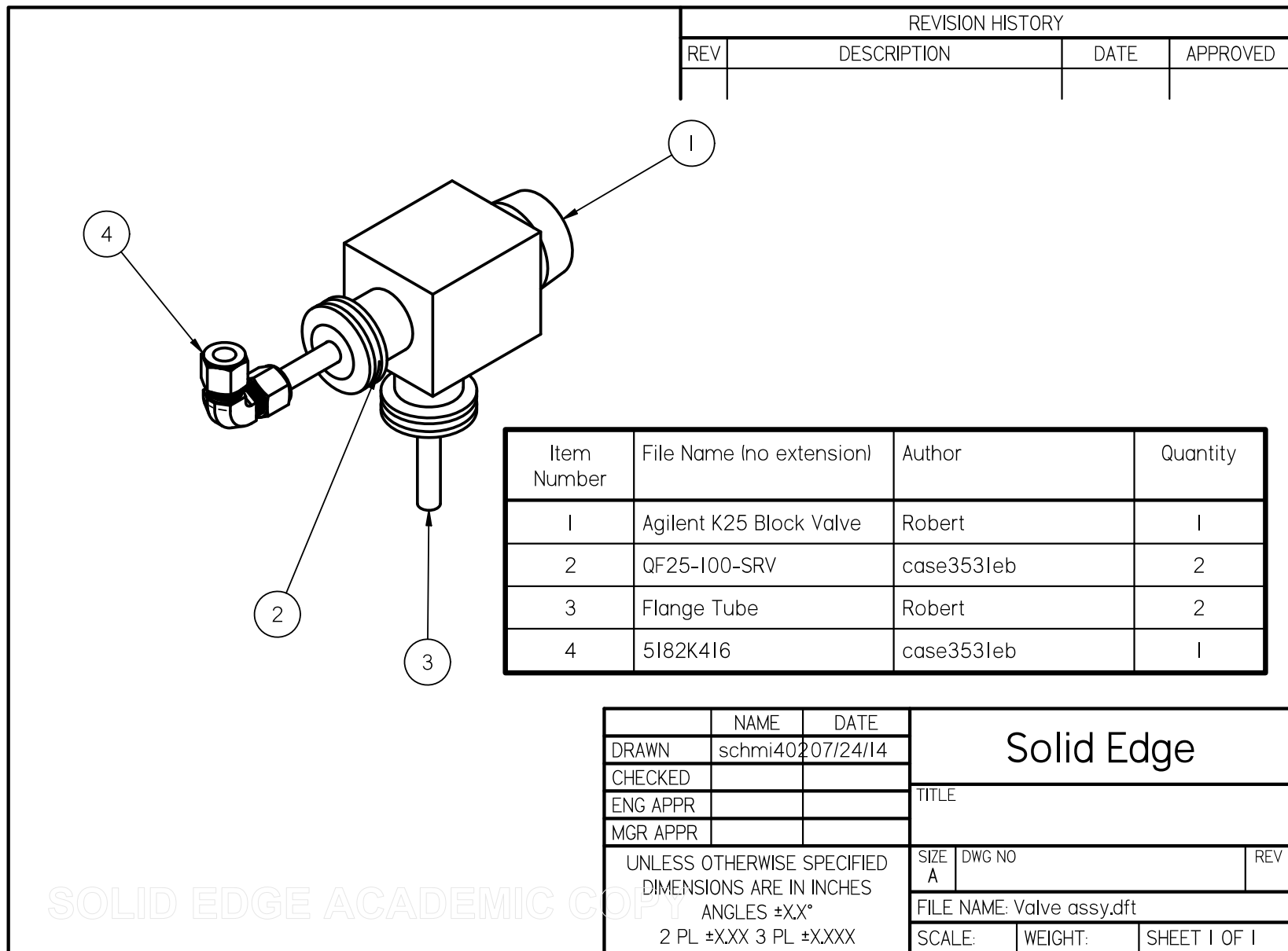


Figure C.58. Valve assembly.

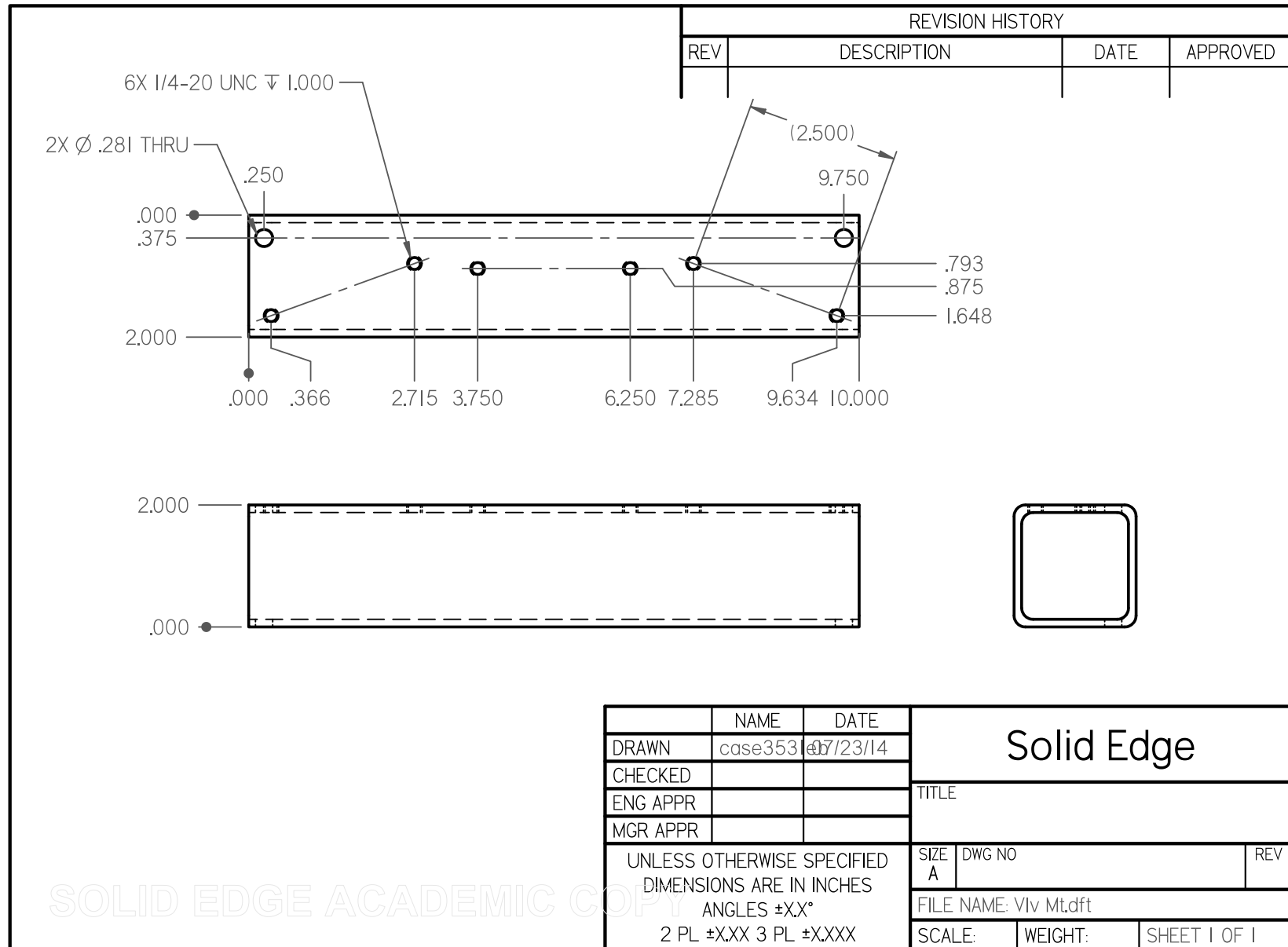


Figure C.59. Valve mount.

REFERENCES

REFERENCES

- [Chang, Himmel 1966] Chang, Y.A., Himmel, L. Temperature Dependence of the Elastic Constants of Cu, Ag, and Au above Room Temperature. *Journal of Applied Physics* 37 (1966) 3567–3572.
- [Fujieda, Uno, Ishigami, Kurachi, Wakamatsu, Doi 2012] Fujieda, T., Uno, M., Ishigami, H., Kurachi, M., Wakamatsu, N., Doi, Y. Addition of platinum and silver nanoparticles to toughen dental porcelain. *Dental Materials Journal* 31 (2012) 711–716.
- [Hasselman, Fulrath 1965] Hasselman, D., Fulrath, R. Effect of spherical tungsten dispersions on Young's modulus of a glass. *Journal of the American Ceramic Society* 48 (1965) 548–549.
- [Lowrie 1967] Lowrie, R. Single-Crystal Elastic Properties of Tungsten from 24° to 1800°C. *Journal of Applied Physics* 38 (1967) 4505.
- [Macfarlane, Rayne, Jones 1965] Macfarlane, R.E., Rayne, J.A., Jones, C.K. Anomalous temperature dependence of shear modulus c_{44} for platinum. *Physics Letters* 18 (1965) 91–92.
- [Neighbours, Alers 1958] Neighbours, J., Alers, G. Elastic constants of silver and gold. *Physical Review* 88 (1958) 707–712.
- [Schmidt, Case, Ni, Trejo, Lara-Curzio, Korkosz, Kanatzidis 2013] Schmidt, R.D., Case, E.D., Ni, J.E., Trejo, R.M., Lara-Curzio, E., Korkosz, R.J., Kanatzidis, M.G. High-temperature elastic moduli of thermoelectric $\text{SnTe}_{1\pm x} - y \text{ SiC}$ nanoparticulate composites. *Journal of Materials Science* 48 (2013) 8244–8258.